

Improvement of Transonic Low Pressure Steam Turbine using High Performance Computation

A thesis submitted to attain the degree of
DOCTOR OF SCIENCES of ETH ZURICH
(Dr. sc. ETH Zurich)

presented by
Muhammad Asad Raheem
Master of Science ETH in Computational Science and Engineering
ETH ZURICH
born on 15.08.1983
citizen of Pakistan

Accepted on the recommendation of
Prof. Dr. Reza S. Abhari, examiner
Prof. Dr. Patrick Jenny, co-examiner

2019

Abstract

Steam turbines hold the largest share of electricity production worldwide. In order to meet growing energy demands, steam turbine designers strive for increased power output, improved efficiency, and longer operational lifespan. Modern steam turbine designs employ large exit annulus area with long blades of up to 60 inches in the last stage of a low-pressure steam turbine in order to achieve these objectives. Increase in last stage blade height introduces supersonic flows in the tip span of the last stage rotor inlet. Such flows are subject to high unsteadiness induced by shock waves. In addition, condensation, droplet formation and unsteady blade loads in the rotor transonic tip region introduce a very complicated flow for numerical computations. Therefore, optimization of blade stacking in the last stage of a transonic low-pressure steam turbine is one of the most delicate and time-consuming parts of the design process. This requires design modifications including blade sweep, lean or twist. The experiments for scaled geometries are nevertheless very expensive and designers have to rely on time accurate computational fluid dynamics. The accuracy of computations is extremely critical in order to guide optimization algorithms and designers to the most viable design. The time-accurate computations are an order of magnitude more expensive than steady state. During design optimization, detailed geometrical features are excluded in order to achieve realistic computational runtime at the cost of accuracy. The geometrical features mostly excluded are hub-tip cavities, seals, part span snubbers, full span shroud, blade count modification or exclusion of upstream or downstream stages. Full-scale multi-stage model with all-inclusive geometrical features results in very large meshes of up to one billion mesh nodes. The proposed meshes must have matching block interfaces throughout the mesh in order to keep a second-order accuracy in space and time posing additional requirements of a very fine mesh in order to resolve high blade twist, shroud connections, and cavities-seals in the flow path. In the case of low-pressure steam turbines, the steam transition from superheated to condense in penultimate and last stages. This necessitates the inclusion of steam modeling at the least for the prediction of wetness as well as numerical accuracy. This results in additional

computational resource requirements posing a very challenging computing problem. The recent widespread use of modern general-purpose graphics processing units (GPUs) for scientific computing provides a possibility to scale time-accurate computational fluid dynamic solvers for such challenging problems. A steady decline in graphics processing unit costs and at the same time improvements in throughput and onboard memory gradually allow hybrid high performance computing cluster as a viable option for the design engineering process. The key objective of this work is to improve the aerodynamic efficiency of a modern low-pressure steam turbine, using carefully tailored stator stacking, numerically on a cluster of GPUs and explain underlying time-resolved flow mechanisms. For this purpose, in-house unsteady Reynolds Averaged Navier-Stokes (URANS) solver MULTI3 is developed for multi-GPU supercomputing clusters with additional equilibrium steam modeling, able to handle full-scale model. In this work, the typical scale of about 386 million mesh nodes for a full annular four-stage model running on 114 Pascal P100 GPUs with time-resolved equilibrium steam modeling is reported with a convergence run-time of less than a week. For design optimization, a typical scale of 57 million mesh nodes including tip-cavities and seals for the last two stages is achieved within a week of run-time on 17 GPUs. Last two-stage computational model of 16.9 million mesh nodes excluding tip cavities converge within 21 hours of reported runtime on two GPUs. Further, a key understanding is developed on computational accuracy versus cost with each geometrical or modeling approximation and guidelines are proposed for a suitable compromise of numerical approximation in a low-pressure steam turbine design optimization process.

The results show the transonic tip region as the main source of entropy loss in the last stage of the transonic low-pressure steam turbine. The proposed stator stacking with an increase in tip axial gap (forward curved sweep) and throat-to-pitch ratio variation designs show aerodynamic total-to-total efficiency improvements of up to 1.3% and 1.1% respectively. The key improvements are seen in supersonic flow expansion in the last stage rotor tip driven by a reduction of relative inlet Mach. The flow unsteadiness in the transonic stator-rotor tip gap is primarily driven by leading edge bow shock, however as found in this work, also depends on the axial gap. Despite an increase in unsteadiness by the closing throat (stator twist design) in the last stage stator tip, a decrease in relative Mach improves efficiency by improvements in the flow expansion in the supersonic rotor tip airfoils. The control of throat-to-pitch ratio is found to be the most effective way to control reaction variation and mass flow redistribution in both the stator and rotor. The analysis shows that at least penultimate stage is compulsory in the computational model along with tip cavities and seals for the last stage optimization as any change in throat area as a result of stacking modification introduce a change in stage pressure ratio, workload, and reaction for both stages.

Zusammenfassung

Dampfturbinen haben weltweit den größten Anteil an der Stromerzeugung. Um den wachsenden Energiebedarf zu decken, streben die Dampfturbinenkonstrukteure eine höhere Leistung, einen verbesserten Wirkungsgrad und eine längere Lebensdauer an. Moderne Dampfturbinenkonzepte nutzen einen großen Austrittsring mit langen Schaufeln von bis zu 60 Zoll in der letzten Stufe der Niederdruck-Dampfturbine, um diese Ziele zu erreichen. Die Erhöhung der Schaufelhöhe der letzten Stufe führt zu Überschallströmungen an der Schaufelspitze des Rotoreinlasses der letzten Stufe. Solche Strömungen unterliegen einer hohen Instabilität, die durch Stoßwellen hervorgerufen wird. Darüber hinaus führen Kondensation, Tröpfchenbildung und instabile Schaufellasten im Rotorbereich der transsonischen Schaufelspitze zu einer sehr komplizierten Strömung für numerische Berechnungen. Daher ist die Optimierung der Schaufelprofile in der letzten Stufe einer transsonischen Niederdruck-Dampfturbine eine der schwierigsten und zeitaufwendigsten Abschnitte des Konstruktionsprozesses. Dies erfordert Schaufeldesign-Änderungen wie z.B. Schaufelschwung, Schräglage oder Verdrehung. Die Experimente für skalierte Geometrien sind jedoch numerisch sehr teuer und die Konstrukteure müssen sich auf eine zeitgenaue numerische Strömungssimulation verlassen. Die Genauigkeit der Berechnungen ist äußerst kritisch, um Optimierungsalgorithmen und Designer zum praktikabelsten Design zu führen. Die zeitaufgelösten Berechnungen sind um eine Größenordnung aufwändiger als die zeitgemittelten Berechnungen. Bei der Designoptimierung werden detaillierte geometrische Merkmale ausgeschlossen, um eine realistische Rechenlaufzeit auf Kosten der Genauigkeit zu erreichen. Die geometrischen Merkmale, die meist ausgeschlossen sind, sind Kavitäten, Dichtungen, Schaufeldämpfer, Schaufel-Deckbänder, Schaufelzahlmodifikationen oder Ausschluss von vor- oder nachgeschalteten Stufen. Ein mehrstufiges Modell in Originalgröße mit allumfassenden geometrischen Merkmalen führt zu sehr großen Netzen von bis zu einer Milliarde Netz-Knoten. Die vorgeschlagenen Netze müssen über passende Blockschnittstellen im gesamten Netz verfügen, um eine Genauigkeit zweiter Ordnung in Raum und Zeit zu gewährleisten, die zusätzliche Anforderungen an ein sehr feines Netz

stellt, um hohe Schaufeldrehungen, Deckbandanschlüsse und Hohlraumdichtungen im Strömungspfad zu lösen. Bei Niederdruck-Dampfturbinen erfolgt der Dampfübergang von überhitzt zu kondensierend in der vorletzten und letzten Stufe. Dies erfordert die Einbeziehung der Dampfmodellierung zumindest für die Vorhersage der Nässe sowie der numerischen Genauigkeit. Dies führt zu einem zusätzlichen Bedarf an Rechenressourcen, was zu einem sehr anspruchsvollen Rechenproblem führt. Der jüngste weit verbreitete Einsatz moderner Allzweck-Grafikverarbeitungseinheiten (GPUs) für wissenschaftliche Berechnungen bietet die Möglichkeit, zeitaufgelöste, strömungstechnische Löser für solche anspruchsvollen Probleme zu skalieren. Ein stetiger Rückgang der Kosten für die Grafikverarbeitungseinheit bei gleichzeitiger Verbesserung des Durchsatzes und des Onboard-Speichers ermöglicht nach und nach einen hybriden Hochleistungs-Computercluster als praktikable Option für den Konstruktionsprozess. Das Hauptziel dieser Arbeit ist die numerische Verbesserung der aerodynamischen Effizienz einer modernen Niederdruck-Dampfturbine unter Verwendung einer sorgfältig abgestimmten Statorschaufelprofil-Stapelung auf einem GPU-Cluster und die Erklärung der zugrunde liegenden zeitaufgelösten Strömungsmechanismen. Zu diesem Zweck wurde der hausinterne instationäre Reynolds Averaged Navier-Stokes (URANS)-Solver MULTI3 für einen Multi-GPU-Supercomputing-Cluster mit zusätzlicher Dampfmodellierung entwickelt, der in der Lage ist, ein Großmodell zu verarbeiten. In dieser Arbeit wird der typische Maßstab von etwa 386 Millionen Netz-Knoten für ein vollringförmiges, vierstufiges Modell, das auf 114 Pascal P100-GPUs mit zeitaufgelöster Gleichgewichtsdampfmodellierung läuft, mit einer Konvergenzlaufzeit von weniger als einer Woche präsentiert. Für die Designoptimierung wird innerhalb einer Woche nach der Laufzeit auf 17 GPUs eine typische Größe von 57 Millionen Mesh-Knoten einschließlich Schaufelspitzenkavitäten und Dichtungen für die letzten beiden Stufen erreicht. Das letzte zweistufige Rechenmodell von 16,9 Millionen Mesh-Knoten ohne Spitzenhohlräume konvergiert innerhalb von 21 Stunden nach der gemeldeten Laufzeit auf zwei GPUs. Darüber hinaus wird ein Schlüsselverständnis über die Rechengenauigkeit im Vergleich zu den Kosten mit jeder geometrischen oder modellierenden Annäherung entwickelt und Richtlinien für einen geeigneten Kompromiss der numerischen Annäherung in einem Niederdruck-Dampfturbinen-Design-Optimierungsprozess vorgeschlagen.

Die Ergebnisse zeigen den transsonischen Schaufelspitzenbereich als Hauptursache für den Entropieverlust in der letzten Stufe der transsonischen Niederdruck-Dampfturbine. Die vorgeschlagene Statorprofilstapelung mit einer Erhöhung des axialen Spitzenspalts (vorwärts gekrümmte Wölbung) und der Variation des Verhältnis von Schaufelverengung zu Schaufeldistanz zeigt aerodynamische Verbesserungen des Gesamtwirkungsgrades von bis zu 1,3% bzw. 1,1%. Die wichtigsten Verbesserungen sind in der Überschallströmungsexpansion in der Rotorspitze der letzten Stufe zu sehen, die durch eine Reduzierung des relativen Eintritts-Mach-Zahl angetrieben wird. Die instationäre Strömung im transsonischen Stator-Rotor-Spalt wird in erster Linie durch den Bugstoß der Vorderkante angetrieben, hängt aber, wie in dieser Arbeit gezeigt wird, auch vom Axialspalt ab. Trotz einer Zu-

nahme der Strömungsinstabilität durch die Schaufelverengung (Statordrallkonstruktion) in der Statorspitze der letzten Stufe verbessert eine Abnahme der relative Mach-Zahl den Wirkungsgrad durch Verbesserungen in der Strömungsexpansion in den Überschallrotorspitzen. Die Steuerung des Verhältnisses der Schaufelverengung zu Schaufeldistanz erweist sich als der effektivste Weg, um Turbinen Reaktionsschwankungen und Massenstromverlagerungen sowohl im Stator als auch im Rotor zu kontrollieren. Die Analyse zeigt, dass zumindest die vorletzte Stufe im Berechnungsmodell zusammen mit den Spitzenhohlräumen und Dichtungen für die Optimierung der letzten Stufe zwingend erforderlich ist, da jede Änderung in der Schaufelverengung als Folge der Stapelmodifikation eine Änderung des Stufendruckverhältnisses, der Arbeitsbelastung und der Reaktion für beide Stufen mit sich bringt.

Acknowledgments

I would like to sincerely thank my supervisor, Professor Dr. Reza S. Abhari for giving me the opportunity to work on this challenging project and providing a professional and conducive learning environment at Laboratory for Energy Conversion (LEC). His intellectual support during uncertain times, uncertainty posed by the nature of scientific research topic, and especially during industrial collaborations and last year of my doctoral work. The high-performance computing aspect of the topic has been a very time-consuming part of this work. To ensure the developed solver is a complete solution and able to simulate all different possible designs of axial and radial turbomachinery with improved accuracy, not only in this work but also several other advance studies on a routine basis. His patience, trust, and constant support allowed us to achieve these objectives.

I would like to thank Prof. Dr. Patrick Jenny for accepting the request as co-examiner. Despite my background from software engineering and scientific computing, one of the reasons for undertaking this topic in turbomachinery, has been one of the lectures in turbulence modeling by Prof. Jenny during my master's studies at ETH. I can recall the lecture, as he discussed the cross-section of a turbofan (aircraft engine) and explained the challenging nature of the design for turbulence modeling and computational fluid dynamics in general.

I would like to thank Dr. Shigeki Senoo for numerous discussions on the intellectual context of the presented work. His support throughout research collaboration and providing all necessary details of the designs required for successful completion of this work. His in-depth knowledge of steam turbines and discussions helped me expand my understanding of this topic.

I would like to thank LEC colleagues and friends. I have known some of the brightest and finest individuals. This work is incomplete without the mention of my colleagues Altug Basol, Ilias Papiagiannis and Ilias Bosdas for the countless discussions and hours

working together. I thank Rainer Schädler, Alexandros Chasoglou, Carsten Degendorfer, Dominic Hänni, Vahid Iranidokht for countless discussion on my work and thesis. Thanks to Marco Pagani and Marcello Marini for making our shared office a fun workspace.

In particular, I would like to thank Marlene Hegner for constant support during my stay at LEC and helping with all the administrative matters. I cannot forget the constant support of Dr. Ndaona Chokani on numerous occasions.

The years in doctoral study and research has been one of the most difficult and busy years in my life. The people who sacrificed and stood by my side in difficult times, my parents Khurshid Ahmed, Mussarat Jabeen, my wife Sehrish Anjum and my brothers especially Fahd Rahim. I thank you for your support.

This work was partially supported by a grant from the Mitsubishi Hitachi Power Systems Japan (MHPS). I would like to thank again for continuous support from Dr. Senoo from MHPS for providing necessary technical resources.

This work was also supported by the following grants from the Swiss National Supercomputing Centre (CSCS) under project ID d20, d34, s594, s677 and s822 for necessary computational resources.

Asad Raheem

Zürich, January 2019

Contents

Abstract	iii
Zusammenfassung	v
Acknowledgments	ix
Contents	xi
List of Tables	1
List of Figures	3
1 Introduction	9
1.1 Motivation	9
1.2 Theoretical background of loss mechanisms and flow aerodynamics of low-pressure steam turbines	11
1.2.1 Secondary flows in axial turbines	11
1.2.2 Last stage aerodynamics with a large annulus area	13
1.3 Source of errors in CFD for turbomachinery	17
1.4 Progress in GPU technology and applications in turbomachinery	19
1.5 Research objectives	20
1.6 Thesis outline	21
2 Numerical Methods	23
2.1 Compressible URANS solver "MULTI3"	23
2.2 Equilibrium steam modeling using "IAPWS 97" steam tables	26
2.2.1 Adaptation of the characteristic boundary conditions for equilibrium steam conditions	28

2.3	Multi-GPU architecture	29
3	Time-resolved aerodynamic analysis of MHPs low-pressure steam turbine with supersonic airfoils near the tip	37
3.1	10MW steam turbine test facility	37
3.2	Influence of equilibrium steam modeling on low-pressure last stage aerodynamics	39
3.3	Snubber aerodynamics in the last stage rotor blades of a low-pressure steam turbine	53
3.4	Influence of blade count modeling on flow aerodynamics	59
3.5	Influence of the tip cavity and seals modeling on efficiency and losses	62
3.6	Flow aerodynamics and loss mechanisms in the last two stages of a low-pressure steam turbine including tip cavities and seals	63
3.6.1	Computational setup and mesh	63
3.6.2	Spanwise entropy loss budget	72
3.6.3	Time-resolved aerodynamics and loss at L-0 stator exit	74
3.6.4	L-0 rotor flow aerodynamics and loss generation mechanisms	80
4	L-0 stator stacking redesign: Forward curved sweep	85
4.1	Forward curved sweep design	85
4.2	Stage efficiency and specific work	86
4.3	Spanwise aerodynamic performance analysis	88
4.3.1	Stage reaction variation and spanwise flow aerodynamics	88
4.3.2	Spanwise loss profiles	91
4.4	Time resolved flow analysis	95
4.4.1	L-0 Stator exit flow	95
4.4.2	Three-dimensional flow through L-0 stator tip passage	103
4.4.3	L-0 rotor aerodynamic improvements	107
4.5	Concluding summary and remarks	115
5	L-0 stator stacking redesign: Blade twist-controlling throat to pitch ratio	119
5.1	Stator twist design	119
5.2	Stage efficiency and specific-work	120
5.3	Spanwise aerodynamic performance analysis	121
5.3.1	Stage reaction variation and spanwise flow aerodynamics	121
5.3.2	Spanwise loss profiles	123
5.4	Time resolved flow analysis	126
5.4.1	L-0 Stator exit flow	126
5.4.2	L-0 rotor aerodynamic improvements	129

5.5	Comprehensive flow model - Reduction of losses in supersonic rotor tip airfoils in the low-pressure steam turbine by controlling stator throat-to-pitch ratio	133
5.6	Concluding summary and remarks	133
6	Conclusions and outlook	135
6.1	Impact of thermodynamic properties of steam on computational accuracy .	135
6.2	Impact of geometrical model on computational accuracy	136
6.3	Aerodynamic improvements of low-pressure steam turbine by last stage stator stacking	137
6.3.1	Forward curved sweep - Tip axial distance	137
6.3.2	Blade twist - controlling stage reaction by variation of the throat to pitch ratio	139
6.4	Future work	141
	Bibliography	143
	A. Nomenclature	149
	B. List of publications	151
	C. Curriculum Vitae	153

List of Tables

3.1	Operating tested full load conditions for MHPS low-pressure steam turbine experiments.	39
3.2	Mesh size for GPU sub-domains for equilibrium versus dry ideal steam case study	41
3.3	GPU domain decomposition and mesh size for L-0 stage including snubber . .	55
3.4	Time-averaged stage efficiency and specific work percentage increase for the last two stages (30° sector - modified blade count) with respect to four stages half annular real blade count.	60
3.5	Time-averaged workload shift for stage L-1 and L-0 with respect to last two stages for 30° sector with modified blade count and four stages half annular real blade count.	62
3.6	Time-averaged stage efficiency and specific work percentage increase for without seals case (with respect to tip cavity and seal geometry case).	62
3.7	Last two stage computational model including tip cavities and seals mesh quality report	65
4.1	Stage efficiency improvements for forward curved sweep stacking. Calculations are time (30° of bucket rotation), circumferentially and radially mass averaged. Both total-to-total and total-to-static efficiency improve for modified FCS case.	87
4.2	Stage specific-work (Δh_o) load shift for datum and modified forward curved sweep design. Calculations are time (30° of bucket rotation), circumferentially and radially mass averaged.	88
4.3	L-0 stator: change in entropy loss, mass flow, and wetness in each hub to tip span region across the stator.	94
4.4	L-0 rotor: change in entropy loss, mass flow, and wetness from hub to tip radial span across the rotor.	94
4.5	L-0 diffuser: change in entropy loss, mass flow, and wetness from hub to tip radial span across part diffuser domain.	94

5.1	Stage efficiency improvements for stator twist stacking.	120
5.2	Stage specific-work (Δh_o) load shift for datum and modified design. Calculations are time (30° of bucket rotation), circumferentially and radially mass averaged.	121
5.3	L-0 stator: change in the loss, mass flow and wetness in each hub to tip span region	125
5.4	L-0 rotor: change in the loss, mass flow and wetness from hub to tip radial span	125
5.5	L-0 diffuser: change in the loss, mass flow and wetness from hub to tip radial span	125

List of Figures

1.1	Estimated fossil fuel energy share of global final energy consumption	10
1.2	Rankine cycle	10
1.3	Secondary flow model	12
1.4	Estimated radial profiles of static pressure and Mach number in the last stage of a low-pressure steam turbine	14
1.5	Limit diagram of 3600 rpm units	15
1.6	Loss generation mechanisms for L-0 rotor supersonic airfoil in the tip region .	16
1.7	Sources of error related to numerics in CFD	17
1.8	Sources of error related to modeling in CFD	18
2.1	The range of the steam tables in pressure P [bar] and internal energy e [J/kg].	27
2.2	Generated table for $P=f(\rho,e)$ derived from IAWPS-IF97.	27
2.3	Generated table for $T=f(\rho,e)$ derived from IAWPS-IF97.	28
2.4	The partial derivative of enthalpy with respect to pressure at a constant density for equilibrium and dry, ideal steam conditions.	29
2.5	The speed of sound for the equilibrium and dry steam conditions.	30
2.6	Schematic of Multi-GPU parallelization architecture.	31
2.7	Domain decomposition of full annular multi-stage computational setup for the first two stages of a low-pressure steam turbine.	32
2.8	MULTI3 multi-GPU framework scalability for single and multi-row master node parallelization	33
2.9	Subdomain decomposition of half annular multi-stage low-pressure steam turbine for scalability assessment of row master node framework optimization . .	34
2.10	Time per iteration versus length of computational run reported in number of solver iterations	35
2.11	Scalability assessment, time per iteration versus the size of computational mesh (number of GPUs)	36

3.1	Schematic of MHPS steam turbine (1000MW class, 4-flow configuration) and turbine output in MW	38
3.2	MHPS low-pressure steam turbine test facility for time-resolved FRAP-HTH measurements	38
3.3	Mesh details for equilibrium steam versus ideal gas assumption case study . . .	40
3.4	Convergence time history of mass flow for equilibrium steam versus dry steam case study	42
3.5	Instantaneous blade-to-blade contours of static pressure coefficient and entropy distribution at the different span-wise position for equilibriums team case . . .	43
3.6	Instantaneous static pressure and entropy contours at the axial cut plane in the stator-rotor axial gap for equilibrium steam case	44
3.7	Instantaneous static pressure coefficient contours at 90% span-wise position for dry and equilibrium-steam conditions	45
3.8	Instantaneous wetness mass fraction distribution at 90% blade-to-blade contour and averaged radial profile of wetness fraction at inlet and outlet of stator and rotor of a low pressure steam turbine	46
3.9	Radial profiles of circumferentially and the time-averaged difference in total-to-total stage efficiency for equilibrium and dry steam simulations	47
3.10	Instantaneous static pressure coefficient C_{ps} [-] distribution from equilibrium-steam simulation on the rotor pressure surface at $t/T=0$ in (a) and $t/T=0.625$ in (b).	47
3.11	Instantaneous rotor surface static pressure coefficient covering a time frame of one rotor passing at (a) 5%, (b) 50% and (c) 97% of span-wise positions for equilibrium-steam simulations.	48
3.12	Instantaneous stator surface static pressure coefficient covering a time frame of one rotor passing at (a) 5%, (b) 50% and (c) 97% of span-wise positions for equilibrium-steam simulations.	50
3.13	Time-averaged rotor surface static pressure coefficient at (a) 5%, (b) 50% and (c) 97% of span-wise positions for equilibrium and dry-steam simulations. . . .	51
3.14	L-0 snubber geometry, mesh and GPU domain decomposition	54
3.15	Circumferentially mass averaged and time-averaged relative yaw angle and relative Mach comparison at FRAP-HTH plane with experimental data, snubber and without snubber computations.	56
3.16	Radial profiles of circumferentially mass averaged and time-averaged total-to-total η_{tt} and total-to-static η_{ts} L-0 efficiency of snubber and without snubber case	57
3.17	Time averaged static pressure distribution C_{ps} at rotor wall surface at 41% (a) 60% (b) and 90% (c) radial span-wise location.	58

3.18	Circumferentially mass averaged and time-averaged relative flow yaw angle, relative Mach and absolute Total pressure comparison at FRAP-HTH plane with experimental data, last two-stage 30° with without seals and four stage half annular computations.	61
3.19	Schematic of L-1 and L-0 tip cavity and seals geometry in meridional view. Seals geometry not shown for confidentiality.	64
3.20	L-1 cavity schematic and mesh details	64
3.21	L-0 cavity schematic and mesh details	65
3.22	Mesh details and GPU domain decomposition of the last two stages computational model including tip cavities and seals	66
3.23	Last two stage including tip cavities and seals computational model mass flow convergence	67
3.24	[Last two stage including tip cavities and seals computational model mass flow error between inlet and outlet of each row	68
3.25	Schematic of last two stages of MHPS low pressure steam turbine with probe measurement locations marked with dotted lines.	69
3.26	Comparison of CFD and 5HP for absolute yaw angle (a) and total temperature (b) at rotor exit of L-1 stage (Papagiannis et al. [1]).	69
3.27	Comparison of CFD and time-averaged FRAP-HTH for delta flow yaw angle from the mean blade metal angle and relative Mach number at L-0 stator exit for the last two stage including tip cavities and seal computations.	70
3.28	CFD comparison with experiments for unsteady static pressure at the outlet at L-0 stator outlet (92% span)	71
3.29	CFD comparison with experiments for unsteady absolute Yaw angle relative to blade metal angle at L-0 stator outlet (92% span)	72
3.30	Radial profiles of the entropy loss coefficient for stator (a), rotor (b) and diffuser (c) for L-0 stage including tip cavities and seals.	75
3.31	Instantaneous contours for entropy loss and streamwise vorticity for two stator pitch at exit of L-0 stator from 70% to 100% of radial span.	76
3.32	Time-space plots for entropy loss, streamwise vorticity, total pressure coefficient C_{pt} and pitch angle for one stator pitch at the exit of L-0 stator 90% of radial span	78
3.33	Instantaneous blade to blade contours of static pressure coefficient, entropy loss and streamwise vorticity at 90% of radial span parallel to flared casing	79
3.34	Instantaneous entropy loss, streamwise vorticity ω_s for two circumferential pitch distance at L-0 stator exit from 0%-35% of radial span.	79
3.35	Time-resolved plots for entropy loss and streamwise vorticity Ω_s for one stator pitch at L-0 stator exit at 2% of radial span.	80
3.36	Time averaged relative Mach for (a) 91%, (b) 95% of the radial span.	81
3.37	Time averaged entropy loss $q[-]$ at 91% of the radial span.	81

3.38	Time averaged plots for (a) Entropy loss $q[-]$, (b) streamwise vorticity Ω_s for two rotor pitch at L-0 rotor exit from 70%-100% of radial span.	82
3.39	Time averaged plots for (a) Entropy loss $q[-]$, (b) streamwise vorticity Ω_s for one rotor pitch at L-0 rotor exit at 91% of radial span respectively.	82
3.40	Time averaged plots for (a) Entropy loss $q[-]$, (b) streamwise vorticity Ω_s for two rotor pitch at L-0 rotor exit from 0%-20% of radial span.	83
4.1	Spanwise schematic of L-1, L-0 stages combined with datum (red) and forward curved sweep (blue) stator modification is shown in (a), whereas 72%, 80%, 85% blade to blade schematic are shown in (b) respectively. Blade profiles at each spanwise position are moved axially away from L-0 rotor and throat area increased with blade twist in order to maintain overall constant annular throat area.	86
4.2	Circumferentially mass averaged and time-averaged spanwise reaction variation for L-1 (a) and L-0 (b) stages respectively for forward curved sweep design. . .	90
4.3	Circumferentially mass averaged and time-averaged spanwise Mach absolute, relative and static pressure coefficient C_{ps} in L-0 stator-rotor axial gap for forward curved sweep modification	90
4.4	Circumferentially mass averaged and time-averaged spanwise non-dimensional meridional mass flux $j_m = \rho C_m / \rho_{ref} C_{m,ref}$ in L-0 stator-rotor axial gap for forward curved sweep modification	91
4.5	Circumferentially mass averaged and time-averaged spanwise L-0 stage pressure ratio for modified forward curved sweep design	92
4.6	Circumferentially mass and time-averaged entropy loss, mass flow redistribution and wetness increase within the stator, rotor, and part diffuser respectively for forward curved sweep modification	93
4.7	Total pressure C_{pt} coefficient, Pitch and Yaw angle at the exit of L-0 stator tip (*-1) Datum on left and (*-2) Forward tip curved sweep design on the right column.	96
4.8	Streamwise vorticity and entropy loss at the exit of L-0 stator tip for (*-1) Datum on left and (*-2) Forward tip curved sweep design on the right.	98
4.9	Static pressure coefficient C_{ps} , incidence and Mach relative to rotor inlet at 90% of tip span for one stator pitch plotted for four rotor blade passing periods. Datum design is shown on the left (*-1) and forward curved sweep to the right (*-2).	100
4.10	Static pressure coefficient C_{ps} and relative Mach at 10% of stator pitch (high unsteadiness region) from 70-100% of tip span. Datum design is shown on the left (*-1) and forward curved sweep to the right (*-2).	102
4.11	Instantaneous blade-to-blade contours from L-0 stator tip region for datum and forward curved sweep case	104

4.12	Instantaneous contours for L-0 stator tip passage in axial ($r - \theta$) plane at 50% and 75% of axial chord length. The pressure side is on the left and suction side of stator airfoil is on the right in all the figures. Streamwise vorticity and entropy loss increase in tip passage and endwall flow for forward curved sweep design towards stator trailing edge.	105
4.13	The time-averaged and min/max envelope of blade static pressure loading C_{ps} for L-0 stator tip passage at 80%, 90% and 98% of radial span respectively. The forward curved sweep improves flow by reducing blade leading edge counter loading. L-0 stator C_{ps} loading is increased towards tip endwall at 98% of radial span and reduced towards hub span.	108
4.14	Time-resolved static pressure loading C_{ps} for L-0 stator tip passage at 98% of radial span respectively for datum and FCS design.	109
4.15	Time-averaged entropy loss $q[-]$ and streamwise vorticity $\Omega_s[Hz]$ contours (in relative frame of reference) for Datum on the left and forward curved sweep on the right at L-0 rotor exit tip region (70%-100%).	111
4.16	Time-resolved entropy loss $q[-]$ and relative Mach $M_{rel}[-]$ contours (in absolute frame of reference) for Datum on the left and forward curved sweep on the right at L-0 rotor exit (91% span).	112
4.17	Time-averaged and min/max envelop of static pressure C_{ps} distribution on a rotor wall surface at 90% and 95% respectively. Static pressure loading and airfoil lift are reduced in the tip region as a result of increased pressure ratio across rotor $P_e/P_{o,inl}$	113
4.18	Time-averaged relative Mach M_{rel} contours at 91% and 95% for datum on the left and FCS on the right respectively.	114
5.1	Spanwise throat to pitch ratio variation datum (red) and Reverse throat-to-pitch ratio (blue) stator modification in (a) whereas 5%, 50%, 90% blade to blade profile schematic (b) are shown respectively.	120
5.2	Circumferentially mass averaged and time-averaged spanwise reaction variation for L-1 (a) and L-0 (b) stages respectively for stator twist design	122
5.3	Circumferentially mass averaged and time-averaged spanwise Mach absolute, relative (a) and static pressure coefficient C_{ps} (b) in L-0 stator-rotor axial gap for stator twist design.	122
5.4	Circumferentially mass averaged and time-averaged spanwise non-dimensional meridional mass flux $j_m = \rho C_m / \rho_{ref} C_{m,ref}$ in L-0 stator-rotor axial gap for stator twist design.	123
5.5	Circumferentially mass and time-averaged entropy loss, mass flow redistribution and wetness increase within stator, rotor and part diffuser respectively for stator twist design	124
5.6	Instantaneous streamwise vorticity $\Omega_s[Hz]$ and entropy loss $q[-]$ at the exit of L-0 stator tip for (*-1) Datum on left and (*-2) Reverse design on the right.	127

5.7	Static pressure coefficient C_{ps} , incidence and Mach relative to rotor inlet at 90% of tip span for one stator pitch plotted for four rotor blade passing periods. Datum design is shown on the left (*-1) and Reverse design to the right (*-2).	128
5.8	Static pressure coefficient C_{ps} and relative Mach at 10% of stator pitch (high unsteadiness zone) from 70-100% of tip span. Datum design is shown on the left (*-1) and Reverse to the right (*-2).	130
5.9	Time-averaged entropy loss $q[-]$ and streamwise vorticity $\Omega_s[Hz]$ contours (in relative frame of reference) for Datum on the left and reverse stacking on the right at L-0 rotor exit tip region (70%-100%).	131
5.10	Time-averaged blade-to-blade contour of relative Mach and entropy loss coefficient at 91% of rotor tip span for stator twist design	132

Chapter 1

Introduction

1.1 Motivation

Steam turbines provide electric power generation in various types of power plants including combined cycle and coal-fired fossil power plants and nuclear power plants. The world's reported energy consumption by year 2016 as shown in Figure 1.1, rely 79.5% on fossil fuels. Since the use of fossil fuel is the major source of the increase in greenhouse gases [2], and in order to mitigate climate change and pollution, major efforts are underway to increase the use of renewables. Nevertheless, fossil fuel reserves are limited [3], and a long term solution to humanity's energy demands has to be addressed from alternative sustainable sources. The steam turbines are independent of the type of heat source and are able to utilize thermal energy from renewable sources including solar and geothermal. Recently, there has been a steady increase in concentrated solar thermal power (CSP) with a world total contribution of up to 4.9 GW (gigawatts) in 2017 and steadily increasing [4]. The total useful energy from geothermal power and heat is estimated to be 170 TW. However, the world geothermal power contributes to about 12.8 GW in 2017 [4]. The steam turbines are an essential and driving component in the world's energy market and will remain an important machine in the years to come. Therefore, in order to meet the world's increasing energy demands [3] and reduce carbon emissions, a consistent effort is required to improve efficiency and operational life-span of steam turbines. In addition, the integration of steam turbines to renewable heat sources such as solar and geothermal has to be boosted.

Steam turbines operate with Rankine cycle and convert heat into mechanical work. The schematic and temperature entropy T-S diagrams for Rankine cycle are shown in Figure 1.2. The steam is generated from water in a boiler (2) by using a heat source. The energy is added to water and steam in this step. The steam enters high-pressure steam turbine inlet (3) and expands to generate work on the rotating shaft. In this process of steam expansion, energy is transferred to rotor airfoils and steam changes its phase back

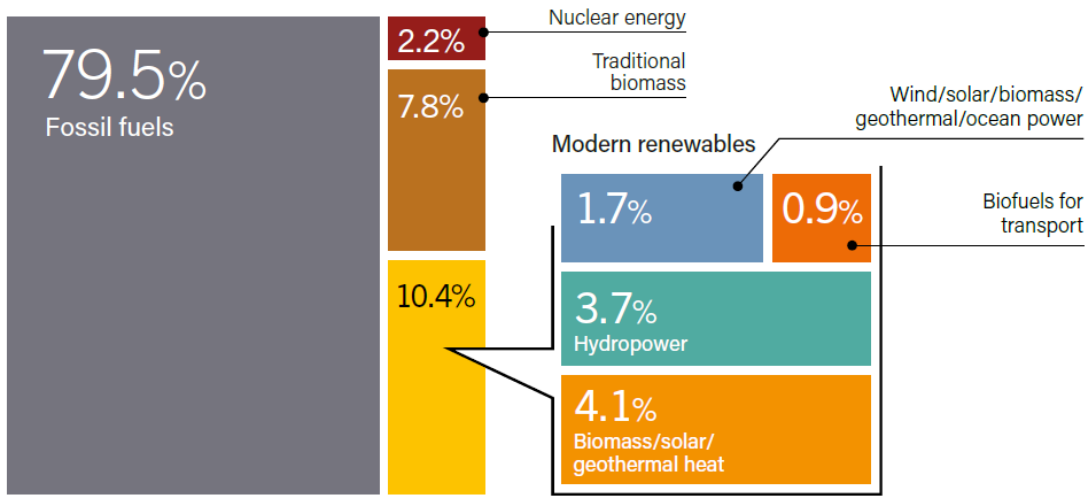


Figure 1.1: Estimated share of fossil fuels and renewable energy consumption in the year 2016 [4].

to water in the last stages of the low-pressure steam turbine. At this low temperature and pressure, a dense fog of water droplets with a diameter of up to $200\mu\text{m}$ is produced [5,6]. The condensed water and steam at the outlet are directed to the condenser (4), where the steam phase is completely changed to water (1) and pumped back to the boiler to complete the cycle.

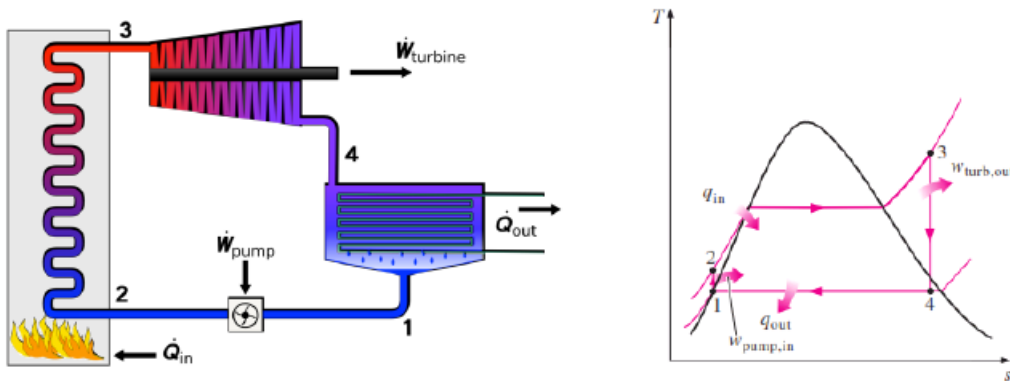


Figure 1.2: Rankine cycle (left) and temperature-entropy (T-S) diagram of a steam turbine (right) [7].

Computational fluid dynamics (CFD) has become an essential part of modern turbomachinery design process [8]. The experiments are necessary in order to obtain an accurate

description of flow aerodynamics. The high cost of experiments, however, require a design optimization process to rely on comprehensive CFD calculations in a first step and subsequently test most optimum design predicted by CFD with experiments. The accuracy of CFD predictions thus becomes of utmost importance in the design process. Numerical solution to Navier-Stokes equations can be obtained with reasonable accuracy only with well-resolved meshes. The inclusion of tip, hub cavities and multi-stage models increase the overall mesh size drastically. The turbomachinery flows are inherently unsteady and require an order of magnitude higher computational run-time to resolve unsteadiness in the numerical solution. The steam turbines, specifically low-pressure steam turbine component require additional steam modeling in the last two stages where steam phase transition occur. The inclusion of thermodynamic properties of steam (equilibrium steam) [9] or any non-equilibrium steam model [10, 11] further increase computational cost leading to unfeasible computational run-times. The unsteadiness introduced by last stage rotor blade leading edge shock of up to $\pm 22.5\%$ (for static pressure) [12] in transonic tip region requires advanced methods such as sliding mesh interface in order to accurately predict unsteady aerodynamics (in comparison to mixing plan interface treatment). The shock system in the transonic tip (relative to the rotor) and hub regions (relative to stator) further pose requirements of a well-resolved mesh. Time-resolved multi-stage computations including a hub, tip cavities, and seals with equilibrium steam modeling are required at the least during the design optimization process such as stator stacking in the last stage of a steam turbine. This level of computational detail is a minimum requirement for further modeling of film formation in the last stage stator, film breakup at stator trailing edge into droplets (Pietro and Raheem [13]) and impact on the downstream rotor (erosion problem to address turbine life span) as well vibration and structural analysis. The enormous computational runtime cost posed by these requirements can be addressed with the help of modern general purpose graphics processing unit (GPU) clusters with the aid of high-performance computing algorithms.

1.2 Theoretical background of loss mechanisms and flow aerodynamics of low-pressure steam turbines

1.2.1 Secondary flows in axial turbines

The secondary flows are present in all types of turbines. As reported by Sharma et al [14], the secondary flows may introduce aerodynamic loss of as high as 30-50% of total losses. The viscous effects generate low momentum fluid during the development of boundary layers at the end-walls. Secondary flows are generated by redistribution of this low momentum fluid within a blade passage induced by pressure field of the blades. The pressure field causes low momentum fluid to turn on a smaller radius than the main flow, also known as flow under turning and roll up to form structures like passage vortex. The size and

strength of secondary flows depend on inlet vorticity, blade turning, aspect ratio and pitch to chord ratio. The developed secondary flows are convected and cause additional losses as a result of flow angle deviation from design incidence angles of downstream blade rows. Nevertheless, the secondary flows do not follow a quasi-two-dimensional turbine primary flows and in order to mitigate aerodynamic losses require three-dimensional blade designs. The principle design approaches include blade sweep, twist and lean optimizations to control pressure field and blade loading within blade passage. These design optimizations require fully three-dimensional computations as a result of introduced large blade-to-blade stream surface twist [15]. Comprehensive research on understanding and improvements of secondary flows has been reported in the literature and a review of these studies is presented by Langston [16].

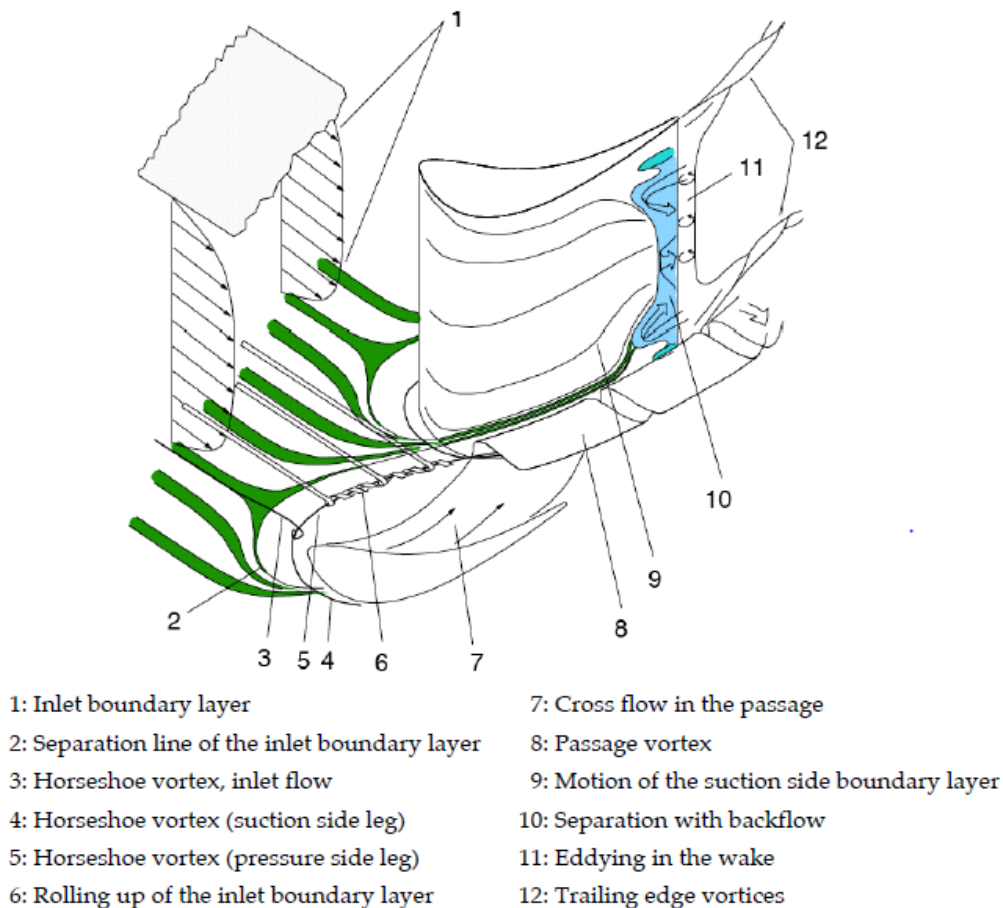


Figure 1.3: Secondary flow model described in [17].

Here, a brief summary of secondary flows is presented with the reported flow model of Vogt and Zippel [18], as shown in Figure 1.3. The flow features are labeled respectively.

The inlet end wall boundary layer (1) of incoming flow can be considered as a layer of tangential vorticity. This boundary layer rolls up into a system of two counter-rotating vortices approaching the leading edge of the blade known as horseshoe vortices. The pressure side leg of horseshoe vortex (5) has same rotation as passage vortex (clock-wise from the pressure side to suction side). The suction side leg (4) is counter rotating to passage vortex. The passage vortex (8) is formed under the influence of pressure gradient across passage caused by incoming flow turning. The end wall boundary layer, due to its low momentum, under the influence of this pressure gradient turns to a smaller radius than the main flow. Within the passage, an end wall cross passage flow from pressure to suction side (7) rolls up into passage vortex. Both pressure side horseshoe vortex (5) and passage vortex (8) merge within the passage and appear as one enhanced vortex downstream of the blade. The suction side vortex (4) stays close to the suction side of the blade and travels up the suction surface.

1.2.2 Last stage aerodynamics with a large annulus area

Steam turbines are the largest among all the turbomachinery designs. Modern day design of steam turbine incorporates long last stage blades in order to increase thermal efficiency, power output, and reduced axial lengths. Increase in the annulus area is beneficial in two aspects. If exit velocity is kept constant, power output is increased by a subsequent increase in mass flow rates. If mass flow rates are kept constants, a larger annulus area results in reduced averaged axial velocity at the exit. By reducing useless kinetic energy at the exit efficiency can be improved. The number of cylinders can also be reduced when increment in the annulus area compensate for the annulus area of the original blade. With increased annulus area, these machines are characterized by a large blade height to hub diameter ratio (H/D). The increased length of the blades is responsible for large pressure gradients from hub to tip at the inlet and exit of the long blades. The typical profile of static pressure, absolute and relative Mach numbers are shown in Figure 1.4. In order to satisfy radial equilibrium the static pressure increase from hub to tip progressively at rotor inlet as indicated by $P_{s,1}$. The absolute Mach Ma_a reduce from the hub (supersonic) to tip (subsonic). The relative Mach $Ma_{rel,1}$ at hub (near transonic) decrease near mid-span and progressively increase to transonic at tip span. With supersonic flow condition at hub $Ma_1 > 1$ and $Ma_{rel,1} > 1$ at the tip, the formation of shock waves are inevitable. The subsonic mid-span region at rotor inlet provides an ideal location for snubber in order to improve the structural integrity of long blades.

High loading at the hub is associated with a low degree of reaction and therefore supersonic Mach number resulting in high trailing edge shock losses as explained by Havakechian et al [20]. Transonic relative Mach at tip region generate a leading edge bow shock. The challenges in the design of low-pressure steam turbine with long blades involve improvements in the design for low mechanical vibrations, high aerodynamic efficiency and reduced

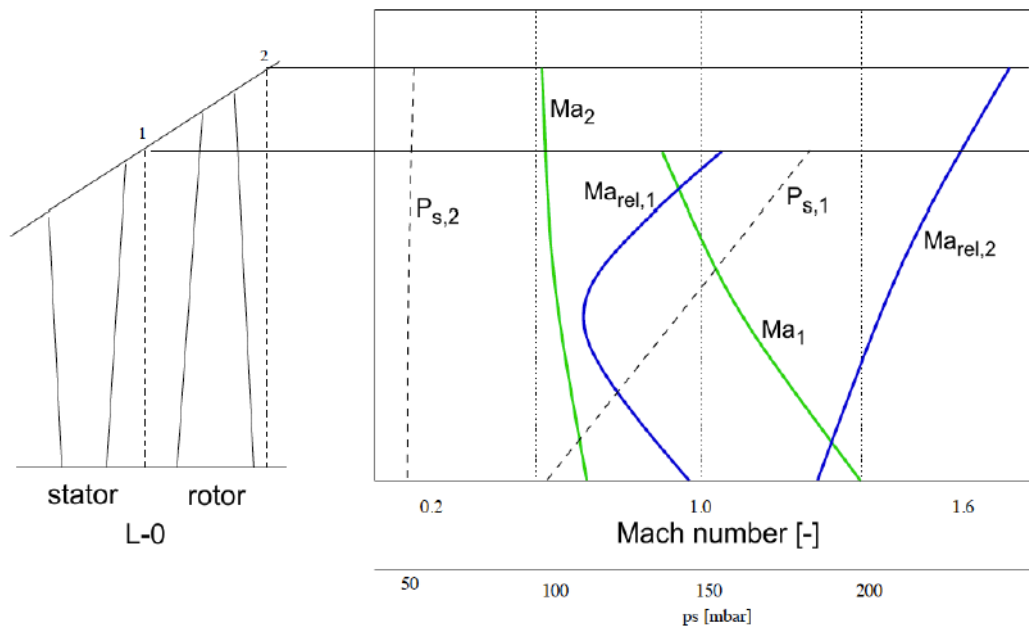


Figure 1.4: Estimated radial profiles of static pressure and Mach number in the last stage of a low-pressure steam turbine, Stüer et al [19].

erosion for a longer operational life span. Gyarmathy and Schlachter [21] proposed five design limit curves as the relationship between exhaust annulus area and hub tip radius ratio (boss ratio) based on simple mechanical engineering formula. This includes rotor stress, cascade geometry and blade stress, blade frequency, stage reaction, and erosion. The blade frequency limit can be overcome by shroud cover at tip and tie-boss (snubber) and mid-span. Too high or low stage reaction can be avoided by using three-dimensional stage design. A modified limit diagram proposed by Senoo et al [22] includes supersonic inflow limit curve as shown in Figure 1.5 for the long blade design. The supersonic inflow limitation restricts maximum relative inlet Mach at blade tip to avoid strong leading edge shock waves. Nevertheless, as indicated by limit curves a careful design optimization requires all three aspects, aerodynamics, blade stress, and erosion to be considered. The time-resolved and accurate CFD computations are necessary in order to predict all three aspects mentioned above.

Supersonic flows generate shock waves, which are responsible for high aerodynamic losses as reported by Stüer et al. [19]. The supersonic flow at the tip of long rotor blade requires a careful supersonic airfoil design in order to achieve smooth supersonic flow expansion and reduced shock losses as described by Senoo in [23]. The main loss mechanisms reported for the supersonic airfoil design is shown in Figure 1.6. Senoo et al. [24] report six loss generation mechanisms with supersonic wind tunnel cascade experiments as following.

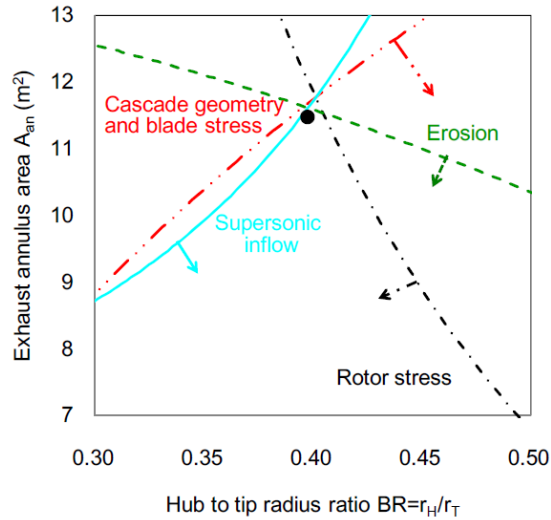


Figure 1.5: Limit diagram of 3600 rpm low-pressure steam turbine unit of a 1000 MW class steam turbine, Senoo et al. [22].

1. The upstream bow shock **S1** occurs due to blade blockage and results in relative total pressure loss.
2. This bow shock **S1** impinges on the pressure side of adjacent rotor airfoil and results in a boundary layer modulation loss.
3. The third loss is generated by reflected shock wave **Sr1** and interaction with suction side to increase boundary layer loss.
4. The trailing edge shock wave **S2** interact with suction side boundary layer of the adjacent airfoil to cause additional boundary layer loss.
5. The fifth loss is caused by an adverse pressure gradient by compression waves **C1** on suction side as a result of concave curvature near trailing edge.
6. The largest loss is trailing edge shock **S3**. The Mach number upstream of shock **S3** is largest as a result of supersonic flow expansion.

The flow field is highly unsteady as a result of the stator-rotor interaction in the last stage of a low-pressure steam turbine and presence of shock S1 at rotor leading edge enhances the flow unsteadiness and losses [25]. Comprehensive time-resolved experiments are reported by Bosdas [25] in the wet steam environment at last stage stator exit in the presence of bow shock S1. They report a static pressure unsteadiness of as much as $\pm 22.5\%$ from 85-100% of the transonic flow in the tip span stator-rotor gap. The shock S1 introduces a deviation angle (relative to stator exit) of $\pm 4.5^\circ$ and a dimensionless pitch angle of $\pm 11.9\%$. The experiments validate loss mechanism upstream of last stage rotor

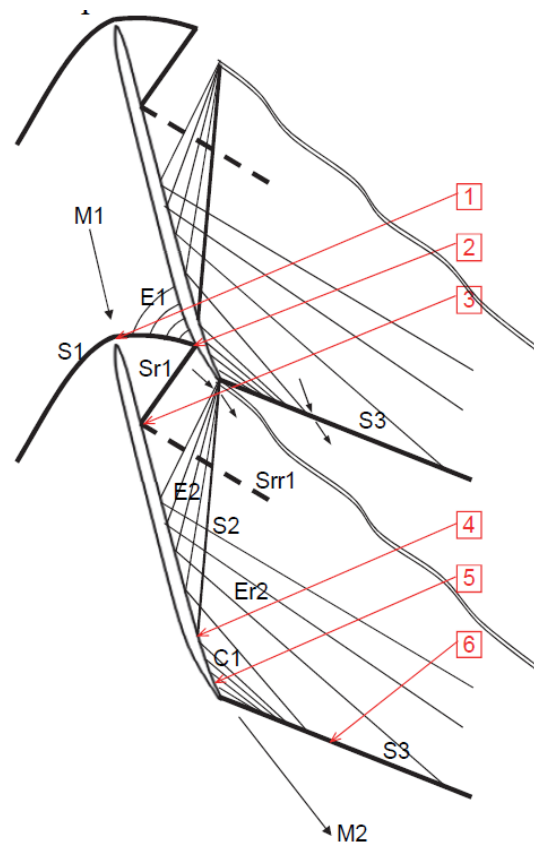


Figure 1.6: Loss generation mechanisms for L-0 rotor supersonic airfoil in the tip region as described by Senoo et al. [24]. Six loss generation mechanisms are identified in the linear cascade experiments.

reported by Senoo et al. [23] in the supersonic airfoil design and provide comprehensive details on wetness and coarse water droplet formation. These experiments also serve as key validation of all CFD calculations in the current work. Experiments report leading edge bow shock as a major contributing factor for flow unsteadiness in the transonic tip region. Further, in the realm of supersonic rotor tip airfoil design, an experimental investigation of the aerodynamic performance of such airfoils was performed by Parvizinia et al. [26]. They studied various pitch to chord ratios for different exit Mach numbers and reported interaction of trailing edge shock S2 (loss mechanism 4 in Figure 1.6) with suction side boundary layer. They report small pitch to chord ratios to introduce steady shock waves resulting in low aerodynamic losses. Similar to Senoo et al. [23] they performed experiments in a linear cascade wind tunnel and found the effect of unsteadiness on aerodynamic losses due to shock waves to be high. Stüer et al. [19] investigated rotor leading edge and stator trailing edge shock wave interaction using numerical computation. They report hub

region shock to introduce extremely high unsteady interactions with the downstream rotor. The suction side branch of the trailing edge shock interacts with the suction surface of the rotating blade and multiple reflections interact with both boundary layer of suction and pressure side of the rotor passage. This interaction introduce peak-to-peak fluctuations in the range of 30% of the mean value. The tip leading bow shock, however, is reported as steady with a reduced level of unsteadiness. The rotating bow shock weakens to about negligible before interacting with upstream forward swept stator.

1.3 Source of errors in CFD for turbomachinery

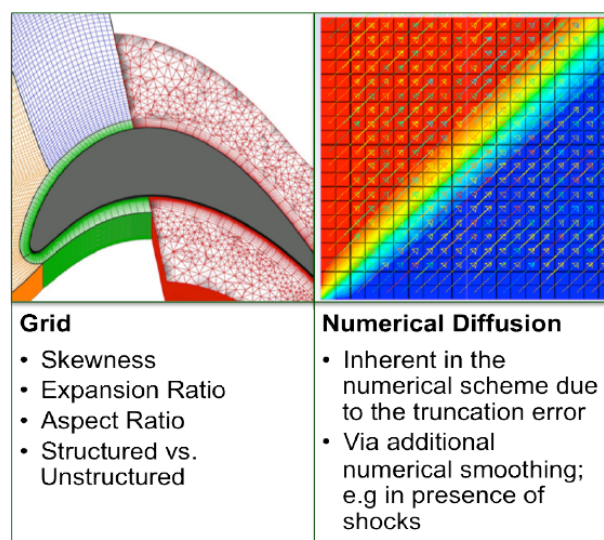


Figure 1.7: Sources of error related to numerics in CFD, Basol [27].

There are two types of known errors in turbomachinery CFD. Error related to numerics itself or the error introduced by modeling. Denton [28] has explained main sources of error in turbomachinery CFD in his work with detailed examples. The main sources of error, as explained by Basol [27] related to numerics itself are shown in Figure 1.7. Mesh size and quality itself plays a critical role in the accuracy of the solver. Cell skewness, high aspect, and expansion ratios decrease accuracy in numerics or even lead to instabilities during runtime. For a given mesh, only a theoretical accuracy of the solution can be achieved. Type of mesh, such as structured or un-structured also impacts the numerical accuracy of the solution. Multi-block structured meshes are more difficult to generate, especially for geometries such as low-pressure steam turbines with high blade twist from hub to the casing in the long blades, and presence of cavity and seals in the flow path. The full span shroud attachment to supersonic airfoils presence in the main flow path results

in very complicated mesh topologies and very skewed cells. The unstructured mesh can resolve such details with much less effort. Nevertheless, structured meshes are preferred for their favorable characteristics in reducing numerical diffusion. Coarse mesh also results in high numerical diffusion, and as a result, artificially smears flow features. A very fine mesh, however, introduce a high computational cost.

Errors associated with the modeling of the problem are listed in Figure 1.8. These are introduced by computational modeling of the physics, geometrical approximations or imposed boundary conditions. Error related to geometrical approximation is considerable. This is also related to the scope of the current thesis and an effort is made to understand computation resource requirements versus accuracy for different geometrical approximations to provide guidelines of a feasible model for a design optimization process. The part span connector (snubber) and tip span shroud provide structural stability to long rotor blades, however at the cost of aerodynamic losses and decrease in efficiency. The hub, tip leakage, and cavity flow not only reduce the work extraction through the stage but also decrease efficiency. In addition, leakage flow can alter secondary flows in the downstream stages to introduce additional aerodynamic losses. During operation of low-pressure steam turbines, droplet impact on the last stage rotor further erodes and alter blade geometry. All the above-mentioned uncertainties or approximations can mislead optimization algorithms and design engineers.

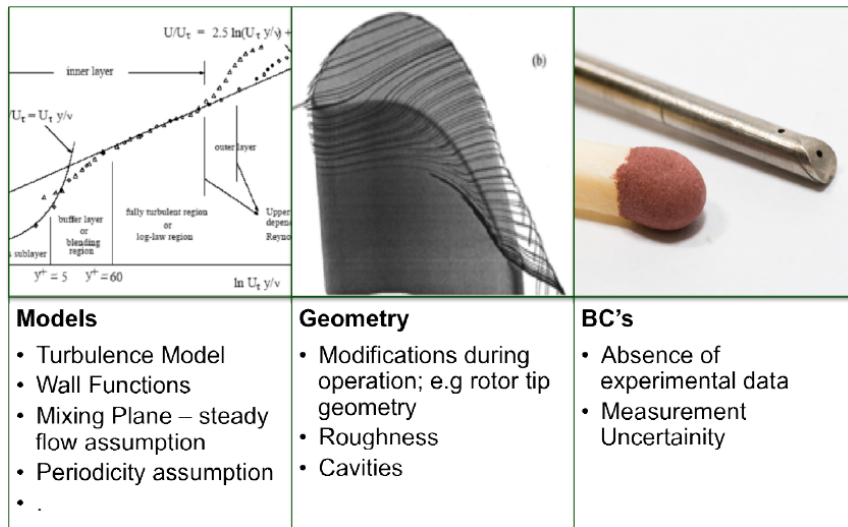


Figure 1.8: Sources of error related to modeling in CFD, Basol [27].

The imposed boundary conditions to a numerical setup are of critical importance. Unavailability of high-resolution experimental data is a very common problem in the initial design or in extreme flow conditions such as very high temperatures or wetness. In

such scenarios, designers rely on estimated boundary conditions. The errors associated with a periodicity of the domain such as periodic boundary conditions and blade count modification are also considerable. There are flow features in turbomachinery flows which do not show periodicity pattern especially in the presence of cavities. The periodicity assumption damps all non-periodic features in the computations. There are recent studies by Basol et al. [29] and Rainer et al. [30] on full annular numerical investigation enabled by MULTI3 for accurate predictions of non-periodic cavity modes as a result of multi-GPU parallelization discussed in this work. Change in blade count to integer ratio in order to fit in a sector sub-domain also results in a computational error.

Computational models within CFD are a major source of error. These models are required due to the unavailability of computational resources and longer run-time to the solution. For example, two-equation turbulence models replaced simplistic algebraic or one-equation models over the years with advances in computing technology. For multi-row computations, two-equation models improved the accuracy of computational results by modeling the convection. In addition, the simplistic mixing plane modeling approach across rows lose the necessary information of unsteady stator-rotor interaction. This can severely deteriorate the accuracy in highly unsteady environments such as stator-rotor interaction in the last stage of the transonic steam turbine. At the expense of computational resources, sliding mesh interface approach is adapted nowadays to overcome row interface treatment inaccuracies for time-resolved computations. The steam modeling itself is necessary in order to model the physics of steam. The ideal gas law with appropriate heat capacity ratio γ can be used in stages where the flow is either superheated and completely dry or completely wet. The regions where steam transition phase, thermodynamic properties of steam or even advance modeling of non-equilibrium steam condensation are required [10, 31–33]. Today, the availability of computational resources such as modern general-purpose graphics processing units (GPUs) and optimized parallel solvers allow a possibility to overcome the discussed computational inaccuracies and is one of the objectives of this work.

1.4 Progress in GPU technology and applications in turbomachinery

Today, progress in GPU technology enabled scientists and engineers to compute large scale of data in shorter computational run-times at a reduced cost. The fluid dynamic computations fit the parallelization paradigm of Single Instruction Multiple Data (SIMD) suitable for GPUs. A high theoretical output of up to 5.3 TeraFLOPS (floating point operations) is possible with a single Nvidia Pascal P100 GPU [34] available today. The onboard available memory of 16 GB allows a typical mesh size of 16 million mesh nodes for time-resolved computations for ideal gas and about 13 million mesh nodes for simulations with steam

modeling with the developed code in this work. The availability of a small cluster of GPUs in an affordable cost allows a possibility of full annular multi-stage simulations within the optimization and design process, not only to improve numerical accuracy but also understanding of time-resolved aerodynamics. CFD solvers can be parallelized with various approaches available including accelerator frameworks such as PGI [35], OpenACC [36] or more detailed CUDA [37] programming model. The directive based accelerator programming model generate underlying GPU kernels reducing the programming effort. However, for the most critical code sections, CUDA allows a flexible and detailed programming approach to generate the most optimum kernels. The communication across GPUs on different nodes require MPI (Message Passing Interface) programming frameworks such as OpenMPI [38]. With the availability of relevant technologies and hardware, one of the first works on the GPU parallelization of a turbomachinery CFD code was carried out by Brandvik and Pullen [39]. Their code has second-order accuracy in space and employs central discretization and Scree scheme with explicit time integration. A rather simplified smoothing algorithm was implemented with algebraic mixing length turbulence model. They demonstrated a 19x speedup on a single GPU (G80 series) versus quad-core CPU. The implementation shows linear scalability of up to 16 GPUs. In another study by Phillip et al. [40], in-house URANS CFD code based on Ni-Lax-Wendroff [41] and $k-\omega$ turbulence model is parallelized using the CUDA programming model. They developed code with multi-block unstructured mesh data formats. They obtained an order of magnitude speedup with Tesla Fermi GPU compared to the single CPU core. For the in-house developed URANS code MULTI3 for multi-block meshes (unstructured data format) and sliding row mesh interface approach a speedup of 13.6x is achieved on a Fermi-class GPU using double precision accuracy [27]. One of the objectives of this work is to extend MULTI3 with large scale computational capability able to handle full annular multi-stage configurations including cavities of an order of billion mesh nodes with linear scalability.

1.5 Research objectives

Steam turbines are widely used in power production, providing the world with more than 60% of the entire generated electrical power [42]. The design objectives include operational flexibility, increased power output, and improved efficiency in order to meet continuously increasing energy demands and reduce carbon emission. The increase in the annulus area of low-pressure steam turbines, specifically the last stage, enable increased power output and improved thermodynamic efficiency. Today's state of the art low-pressure steam turbines incorporates long last stage rotor blades of about 60 inch leading to complicated steam turbine aerodynamics, with highly three dimensional and unsteady flow field with the supersonic flow in the tip region. Therefore, in order to improve the current efficiency (60% in combined cycle) and reliability of these machines, the unsteady flow mechanisms responsible for the aerodynamic losses have to be investigated and understood well in detail.

Until now, the lack of time-resolved experimental data makes the analysis hardly feasible. Therefore, for understanding the unsteady flow environment unsteady numerical simulations with steam modeling are crucial. Due to the high computational cost of unsteady simulations, High Performance Computing (HPC) techniques, such as GPU acceleration and parallelization, need to be employed in order to harness the massive computational power offered by modern GPU supercomputing clusters.

Unsteady flow simulations have been conducted and gave insight to the unsteady stator-rotor interactions in the presence of a bow shock wave in a modern, transonic low-pressure steam turbine in this work. Numerical data have been successfully validated with unsteady flow measurements conducted in the same design operation configuration. There have been several ideas regarding the improvement by applying state-of-the-art stacking methods on the stator. However, there are no reports in open literature investigating stator stacking methods in a time-accurate manner, especially in the presence of a bow shock wave. This leads to the following research objectives of the current doctoral thesis:

- Develop necessary computational capability able to handle full annular multistage turbomachinery designs including hub/tip cavities and seals.
- Quantify computational cost versus accuracy by geometrical approximations such as excluding tip cavities, stages, blade count modification, snubber or thermodynamic properties of steam. Propose guidelines for acceptable computational accuracy in the design process of a low-pressure steam turbine.
- Identify major loss mechanisms in the last stage of a transonic steam turbine.
- Investigate the effect of stator stacking techniques, such as forward curve sweep or changing the throat-to-pitch ratio, on the loss generation and stage efficiency
- Describe the unsteady flow mechanisms present in the flow field and propose effective ways for designing the last stage of a modern steam turbine with very long blades.

1.6 Thesis outline

The chapters of this thesis are structured as follows. The first chapter is the motivation, while the second chapter describes the methods used in this computational study. Chapters three, four, and five present the simulations performed trying to identify the loss mechanisms and the improvements gained by different stator designs and chapter six provides the summary and conclusions of the current research work.

- **Chapter 1** presents the motivation of the thesis and the theoretical background on the flow field phenomena in the last stages of low-pressure steam turbines. The current use of state of the art GPU clusters to address computational requirements posed by turbomachinery design process is also discussed.

- **Chapter 2** describes the in-house developed CFD solver MULTI3 that was used during this computational study. Developments in the code that were necessary for the successful completion of the research objectives are discussed in detail. These are the adaptation of the solver for the wet steam environment and the development of two different parallelization frameworks for GPUs that enable large scale simulations.
- **Chapter 3** time-resolved flow and aerodynamic loss generation mechanism are identified and discussed for a modern low-pressure steam turbine with supersonic airfoils near the tip. A detailed understanding of computational cost versus accuracy is established for the introduction of geometrical simplification in computation such as the exclusion of steam modeling, snubber, tip cavities, blade count or upstream stages.
- **Chapter 4** details the effect that forward curve sweep of the stator on the unsteady flow field and loss generation, the differences in the shock development in the rotor and the gains that are achieved in terms of performance.
- **Chapter 5** presents an extensive analysis of the effect that a change in the throat-to-pitch ratio of the stator can have on loss generation and stage efficiency. Time-resolved data are presented and discussed in detail to describe the unsteady flow phenomena.
- **Chapter 6** summarizes and concludes the outcome of this research work. Suggestions for future work and some key design guidelines are provided as well.

Chapter 2

Numerical Methods

The in-house URANS solver MULTI3 is further developed for large scale multi-GPU computation with equilibrium steam modeling and used for all the numerical computations throughout this work. The necessary tools are developed for pre-processing including conversion from commercial meshing software including ICEM-CFD and NUMECA Auto-Grid. The procedure for the computational setup of multistage full annular computations is streamlined with necessary software modules and scripts for mesh conversion, initial guess and solver setup. The time-resolved data from multi-stage computations overwhelm disk storage and computer memory. Commercial post-processing software such as TECPLOT are able to handle only instantaneous and a sector sub-domain data consisting of a limited number of airfoils for analysis. Two sets of post-processing tools are developed in order to address this issue. First, transient (in-situ) post-processing is developed for run-time monitoring of simulation results and immediate availability of necessary time-averaged and time-resolved flow quantities for analysis. Secondly, for detailed time-resolved post-processing, a combination of TECPLOT macros, shell scripts, and Matlab plotting tools are developed in order to streamline detailed analysis. Necessary run-time checks are established to recover solution in case any cluster computing node or GPU failure during run-time. The solver is able to continue from the latest saved solution state after an abnormal exit. In this chapter, URANS solver MULTI3 is discussed with details on further development of thermodynamic properties of steam within the numerical code and multi-GPU parallelization. The scalability, runtime estimates, and viability of solver for multi-stage computations are also discussed.

2.1 Compressible URANS solver "MULTI3"

The in-house developed URANS solver "MULTI3" uses the Ni-Lax-Wendroff explicit time marching algorithm developed by Ni [41]. The unsteady compressible RANS equations

are solved with second-order accuracy in space and time. The time-dependent, three dimensional Navier-Stokes equations are written in conservative form as following.

$$\frac{\partial Q}{\partial t} + \frac{\partial F_{invisc}}{\partial x} + \frac{\partial G_{invisc}}{\partial y} + \frac{\partial H_{invisc}}{\partial z} + \frac{\partial F_{visc}}{\partial x} + \frac{\partial G_{visc}}{\partial y} + \frac{\partial H_{visc}}{\partial z} = 0 \quad (2.1)$$

The state vector is defined as follows.

$$Q = (\rho \ \rho u \ \rho v \ \rho w \ \rho E)^T \quad (2.2)$$

The inviscid and viscous flux vectors are defined as follows in the equation 2.3 and 2.4 respectively

$$F_{invisc} = \begin{pmatrix} \rho u \\ \rho u^2 + P \\ \rho uv \\ \rho uw \\ \rho uH \end{pmatrix}, G_{invisc} = \begin{pmatrix} \rho v \\ \rho v^2 + P \\ \rho vw \\ \rho vH \end{pmatrix}, H_{invisc} = \begin{pmatrix} \rho w \\ \rho w^2 + P \\ \rho wH \end{pmatrix} \quad (2.3)$$

$$F_{visc} = \begin{pmatrix} 0 \\ -\tau_{xx} \\ -\tau_{xy} \\ -\tau_{xz} \\ -\tau_{xx}u - \tau_{xy}v - \tau_{xz}w - q_x \end{pmatrix}, G_{visc} = \begin{pmatrix} 0 \\ -\tau_{xy} \\ -\tau_{yy} \\ -\tau_{yz} \\ -\tau_{xy}u - \tau_{yy}v - \tau_{yz}w - q_y \end{pmatrix} \quad (2.4)$$

$$H_{visc} = \begin{pmatrix} 0 \\ -\tau_{xz} \\ -\tau_{yz} \\ -\tau_{zz} \\ -\tau_{xz}u - \tau_{yz}v - \tau_{zz}w - q_z \end{pmatrix} \quad (2.5)$$

The ideal gas law assumption is used for pressure calculations defined in the equation 2.6.

$$P = (\gamma - 1)[\rho E - \frac{1}{2\rho}((\rho u^2) + (\rho v^2) + (\rho w^2))] \quad (2.6)$$

Computations in this work, however, use thermodynamic properties of steam as discussed in the later section 2.2. The time-dependent Navier-Stokes equations are discretized using the Ni's [41] Lax-Wendroff scheme for the inviscid fluxes and the central differencing for the viscous fluxes. The algorithm is adapted for multi-block unstructured data format.

Additionally, second order artificial dissipation is introduced in the vicinity of shocks and a fourth order artificial dissipation is added to prevent high-frequency oscillations. The numerical scheme is coupled with a JST type scalar, anisotropic artificial dissipation algorithm, which scales the smoothing coefficients, based on the local CFL number and also the local level of the modeled eddy viscosity. A dual time stepping method of Jameson [43] is used for time-resolved calculations and a local time stepping approach is utilized for steady simulations in order to speed up the convergence. Non-reflecting boundary conditions of Giles [44] are implemented to prevent spurious oscillations reflecting back from boundaries back into the domain. Further details of discretization scheme and implementation can be found in Burdet [45].

For the closure of RANS equations the zero-equation Baldwin-Lomax [46], one equation Spalart-Allmaras [47] a two-equation Wilcox [48] $k-\omega$ turbulence models have been implemented in the solver. In the scope of current work, only $k-\omega$ turbulence model is used with sliding mesh interface approach in order to retain second order accuracy and turbulence across rows. Time-dependent equations of $k-\omega$ turbulence model are defined in equation 2.7. The equations are written in three parts according to physics they represent. The convective, diffusive parts and source terms including production \mathbf{P} and destruction \mathbf{D} terms.

$$\frac{\partial Q}{\partial t} = - \left[\frac{\partial F_C}{\partial x} + \frac{\partial G_C}{\partial y} + \frac{\partial H_C}{\partial z} \right] + \left[\frac{\partial F_D}{\partial x} + \frac{\partial G_D}{\partial y} + \frac{\partial H_D}{\partial z} \right] + P - D \quad (2.7)$$

The equations are written in its conservative form and respective state vector Q_T is given as follows. Note that for RANS equations, density ρ and velocity \mathbf{u} , \mathbf{v} , \mathbf{w} are Favre averaged and pressure is Reynolds averaged.

$$Q_T = \begin{bmatrix} \rho k \\ \rho \omega \end{bmatrix} \quad (2.8)$$

The convective fluxes in three directions are given as follows in equation 2.9.

$$F_C = \begin{bmatrix} \rho u k \\ \rho u \omega \end{bmatrix}, G_C = \begin{bmatrix} \rho v k \\ \rho v \omega \end{bmatrix}, H_C = \begin{bmatrix} \rho w k \\ \rho w \omega \end{bmatrix} \quad (2.9)$$

The diffusive fluxes in three directions are given as follows in equation 2.10.

$$F_D = \begin{bmatrix} \left(\frac{\mu}{Re_{ref}} + \sigma^* \mu_t\right) \frac{\partial k}{\partial x} \\ \left(\frac{\mu}{Re_{ref}} + \sigma \mu_t\right) \frac{\partial \omega}{\partial x} \end{bmatrix}, G_D = \begin{bmatrix} \left(\frac{\mu}{Re_{ref}} + \sigma^* \mu_t\right) \frac{\partial k}{\partial y} \\ \left(\frac{\mu}{Re_{ref}} + \sigma \mu_t\right) \frac{\partial \omega}{\partial y} \end{bmatrix}, H_D = \begin{bmatrix} \left(\frac{\mu}{Re_{ref}} + \sigma^* \mu_t\right) \frac{\partial k}{\partial z} \\ \left(\frac{\mu}{Re_{ref}} + \sigma \mu_t\right) \frac{\partial \omega}{\partial z} \end{bmatrix} \quad (2.10)$$

The production terms are implemented and modified according to Kato and Launder [49]. This proposed modification prevents overproduction of turbulence at stagnation points.

$$P = \begin{bmatrix} \mu_T S \Omega \\ \alpha S \Omega \end{bmatrix}, D = \begin{bmatrix} \beta^* \rho \omega k \\ \beta^* \rho \omega^2 \end{bmatrix} \quad (2.11)$$

The definition of terms \mathbf{S} and Ω is given in equation 2.12.

$$S = \sqrt{\frac{1}{2} \left(\frac{\partial u_i}{\partial x_j} + \frac{\partial u_j}{\partial x_i} \right)^2}, \quad \Omega = \sqrt{\frac{1}{2} \left(\frac{\partial u_i}{\partial x_j} - \frac{\partial u_j}{\partial x_i} \right)^2} \quad (2.12)$$

For the low Reynolds version of the model, coefficients are used from Chima [50]. The equations are solved for turbulent state vector and calculated eddy viscosity is entered into the viscous flux calculations of momentum and energy equations. The eddy viscosity is calculated from equation 2.13.

$$\mu_T = \alpha^* \frac{\rho k}{\omega} \quad (2.13)$$

Further details of discretization scheme and implementation of k- ω turbulence model can be found in Basol [27].

2.2 Equilibrium steam modeling using "IAPWS 97" steam tables

A discrete version of the steam table is derived from standard IAWPS-IF97 formulation. The tables are generated using Matlab library XSteam [51]. Tables cover both the superheated and the saturated steam regions up to a wetness mass fraction of $\beta = 0.3$ as shown in Figure 2.1. The state of the condensed steam (temperature, pressure, enthalpy, entropy, wetness mass fraction) is read from the tables using a second-order accurate bi-linear interpolation scheme. As suggested by Senoo et. al. [9] internal energy and density are used as independent variables in the tables.

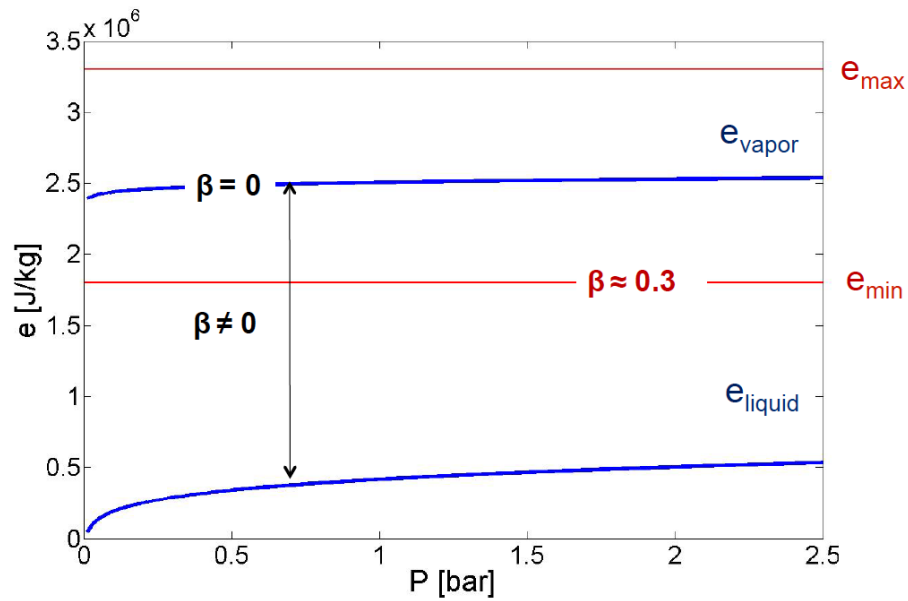


Figure 2.1: The range of the steam tables in pressure P [bar] and internal energy e [J/kg].

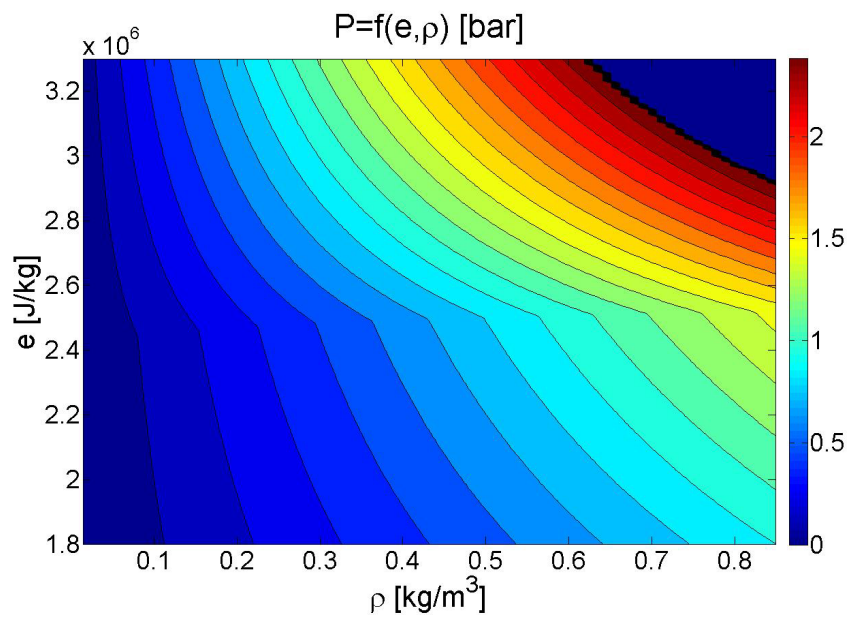


Figure 2.2: Generated table for $P=f(\rho,e)$ derived from IAWPS-IF97.

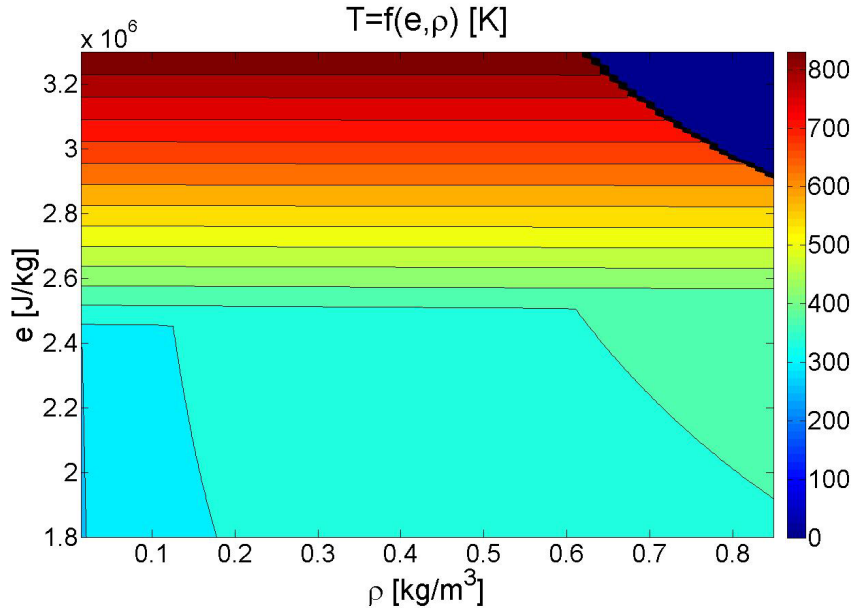


Figure 2.3: Generated table for $T=f(\rho,e)$ derived from IAWPS-IF97.

2.2.1 Adaptation of the characteristic boundary conditions for equilibrium steam conditions

A major modification required for equilibrium steam modeling is adapting the existing Giles [44] characteristic boundary conditions. In the implementation of Giles, the boundary conditions are imposed in terms of total enthalpy, entropy, and flow angles. The flow field at the inlet and outlet are updated such that the imposed level of enthalpy and the entropy hold. The implementation requires partial derivatives which can be analytically derived for the ideal gas law. However, for the equilibrium steam implementation, they all have to be read from the tables. Some of the required partial derivatives are given below.

$$\left. \frac{\partial h}{\partial \rho} \right|_p, \left. \frac{\partial h}{\partial p} \right|_\rho, \left. \frac{\partial S}{\partial \rho} \right|_p, \left. \frac{\partial S}{\partial p} \right|_\rho, \left. \frac{\partial e}{\partial \rho} \right|_p, \left. \frac{\partial e}{\partial p} \right|_\rho \quad (2.14)$$

The partial derivatives that are with respect to pressure have to be derived from partial derivatives with respect to internal energy and density since the generated tables have these two independent variables. The partial derivative of enthalpy with respect to pressure at constant density can be expressed as follows.

$$\left. \frac{\partial h}{\partial p} \right|_\rho = \left. \frac{\partial h}{\partial e} \right|_\rho / \left. \frac{\partial p}{\partial e} \right|_\rho \quad (2.15)$$

As shown in Figure 2.4, the partial derivative of enthalpy with respect to pressure is considerably different for the equilibrium steam than it is for the dry, ideal steam.

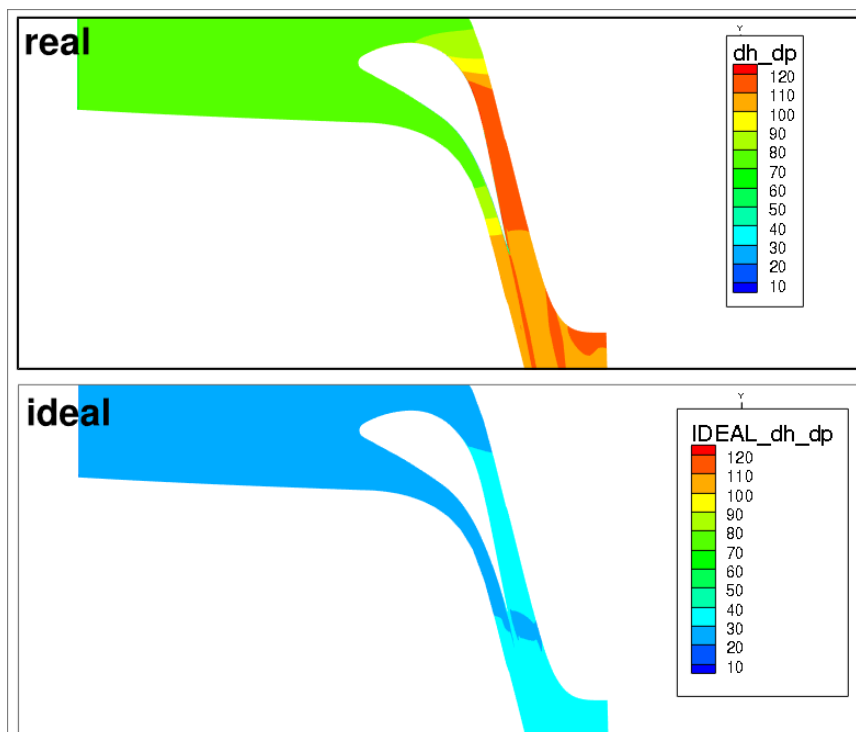


Figure 2.4: The partial derivative of enthalpy with respect to pressure at a constant density for equilibrium and dry, ideal steam conditions.

The speed of sound has to be derived differently for the equilibrium steam simulation. The formulation used for the calculation is given below and taken from Senoo et al. [9].

$$c = \frac{\partial p}{\partial \rho} \Big|_e + \frac{\partial p}{\partial e} \Big|_\rho \frac{p}{\rho^2} \quad (2.16)$$

Where \mathbf{e} , ρ , \mathbf{p} are internal energy, density and pressure respectively in equation 2.16. As shown in Figure 2.5, the speed of sound is 10% lower for the equilibrium steam conditions compared to the dry steam (ideal gas law).

2.3 Multi-GPU architecture

The GPU acceleration of the solver is based on the “PGI Accelerator” directives [35]. The single GPU implementation of laminar part of the solver is discussed in the work of Huber

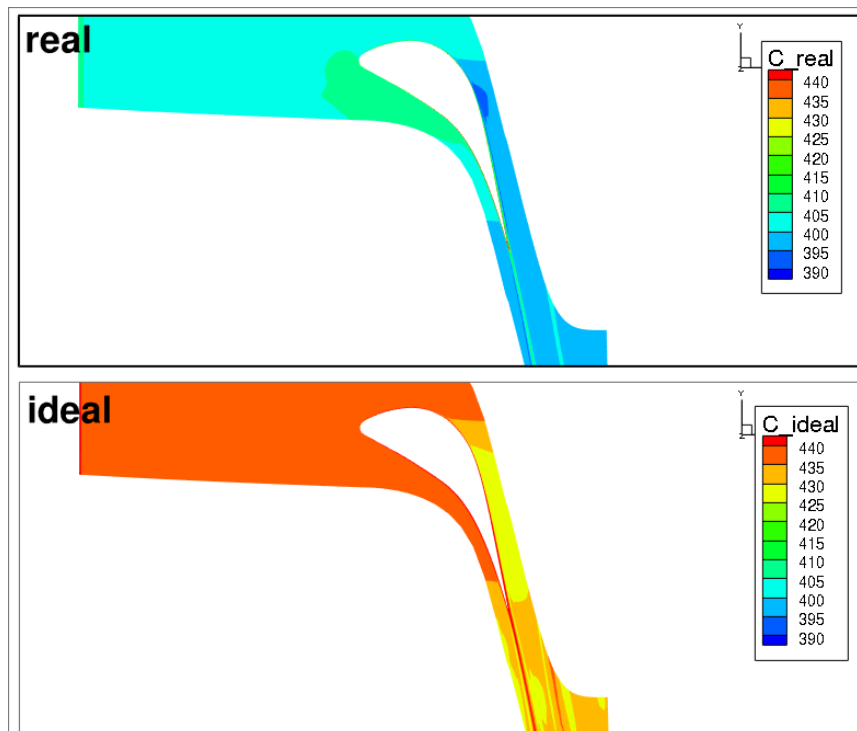


Figure 2.5: The speed of sound for the equilibrium and dry steam conditions.

[52]. For problems of bigger size than they would fit into a single graphics card, the domain is decomposed in the grid generation stage and distributed into separate graphics cards. The communication between the GPUs is handled using MPI (CRAY-MPICH for Piz Daint). Subdomain size is adjusted to fit the GPU memory available. Typically 5 million mesh nodes (equilibrium-steam model) for 6GB of GPU onboard memory is considered for NVIDIA Tesla K20X type graphics cards on Cray XC30 - Piz Daint [53]. A standard unit for the solver is 1 Gigabyte per 1 million mesh nodes for the turbomachinery designs that can be solved with ideal gas properties. The equilibrium steam model discussed in the previous section is necessary for the low-pressure steam turbines at the least in a multistage configuration where the steam transition from superheated to wet phase. The extended version of a solver for steam require additional memory for derivatives as discussed in the previous section.

In the current design, each GPU is paired with one CPU core. In the pre-processing stage, each subdomain is stored in a separate grid and flow file. MULTI3 framework is initialized with MPI parallel threads equal to the number of sub-domains and associates one GPU with each thread (CPU core). Each CPU-GPU pair reads sub-domain grid and flow files independently, and all of the computational data is transferred to GPU memory. A CPU-GPU pair performs computations on allocated sub-domain independently, except

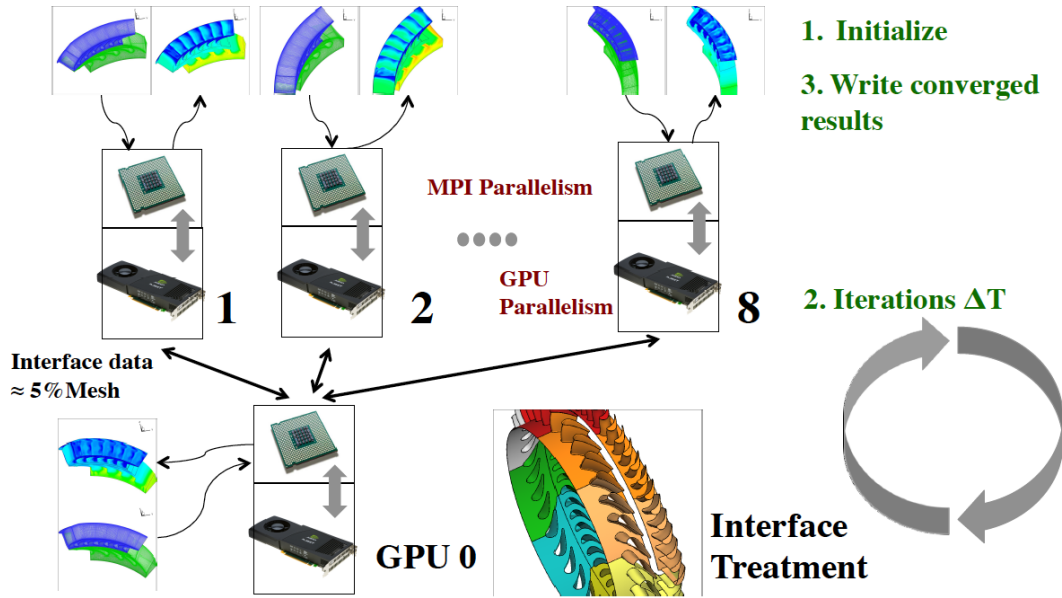


Figure 2.6: Schematic of Multi-GPU parallelization architecture. A CPU-GPU pair is responsible for sub-domain computations independently, except sub-domain boundaries (5% of mesh size) are computed at “GPU 0” master node.

operations on domain boundaries i.e. inner and periodic boundaries as well stator and rotor row interfaces. This interface data is measured to be about 5% of full domain mesh size. Interface data is first transferred from GPU to CPU memory for each sub-domain and assembled at Master node “GPU 0” via MPI synchronous calls as shown in Figure 2.6. Interface treatment is then performed at master node GPU, and results are communicated back to each sub-domain CPU-GPU pair. The standard single GPU implementation solves multi-row and multi-airfoil domain to fit into a single GPU. The code in the single GPU implementation has row loops throughout the code for multi-row treatment. The different models such as mixing plane, frozen rotor and sliding mesh interface are available to treat these row interfaces. The other type of boundaries includes inlet, outlet, wall and periodic. In order to minimize development time, annular multi-row domains are split into sector sub-domains. Each sub-domain consists of a multi-row or multi-stage turbine domain, with no domain splitting across the rows. This results in row loops in the code to be intact. The only change required in the code design is the treatment of periodic, inlet and outlet boundaries. This parallelization may introduce a theoretical bottleneck in scalability as the number of annular domains increase in problems with high-density mesh such as heat transfer simulations. Despite the theoretical limitations, simple design as proposed is well in use for mesh size up to 50 million mesh nodes. The discussed architecture applicability is demonstrated in numerous computational studies of full annular multistage geometries

such as reported by Rainer et al. [30], Basol et al. [29] and Papagiannis [54].

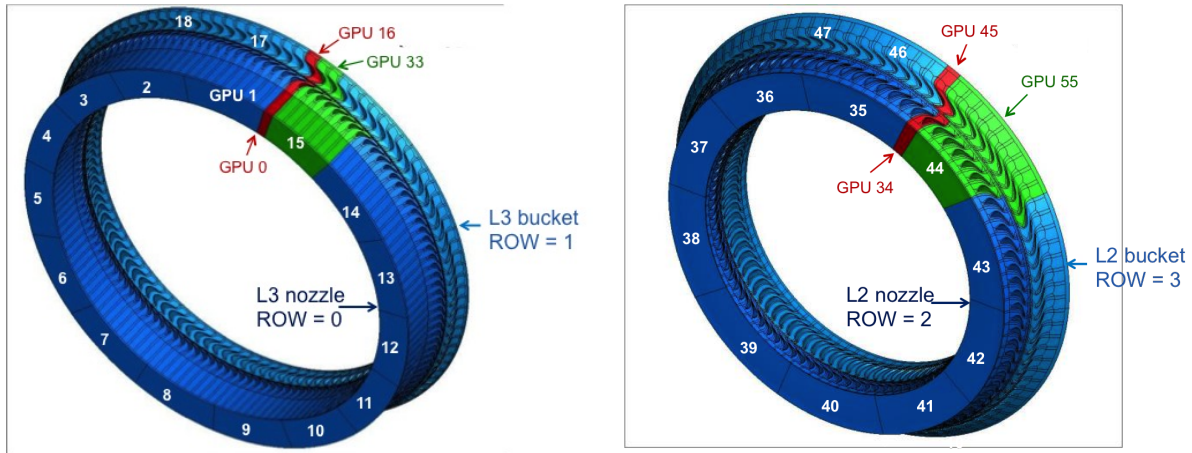


Figure 2.7: Domain decomposition of full annular multi-stage computational setup is shown, labeled with a unique GPU identification number. A master node for each row is shown in red, whereas domain nodes in blue represent GPUs with an equal number of mesh nodes each, and remaining mesh nodes for each row are fit into the last GPU of that particular row colored in green.

The solver, however, is limited with 6GB of onboard GPU memory for Nvidia Tesla K20 GPUs. In order to fit all 9 rows of a multistage low-pressure steam turbine (four stages and part diffuser) the mesh for a single airfoil per row assembled in a 9-row subdomain exceeds 6GB. This problem has been solved with the recent launch of Nvidia Pascal P100 with 16 GB of onboard memory, however, a robust architecture with a row split is necessary for a reduction of load on a single master node. To improve the scalability of the solver, parallelization framework optimizations have been successfully performed in terms of allocating one master per row and sub-domain split across rows. Improvements in the framework are briefly explained in this section. The test case considered for evaluation of the scalability of the improved framework consists of four full annulus blade rows (L-3, L-2 stage) of MHPS low-pressure steam turbine with a total mesh size of 225 million nodes divided into 56 sub-domains each treated by a single GPU as shown in Figure 2.7. This two-stage test case is setup only for development and code optimization test purpose. The low-pressure steam turbine design is discussed in detail in the next Chapter 3.

Parallelization framework before optimization for full annular multi-stage steam turbines consists of a single master node to treat the interface for all the blade rows, which was limiting the scalability of the solver for massively parallel 4-stage simulations. A mesh of 225 million nodes subdivided into 56 GPU's results in an overall interface domain data of about 11 million mesh nodes. This data cannot fit into the memory of the single GPU

at the master node. For this reason, the framework is efficiently re-structured to have a separate master node for each blade row to treat the row local interfaces. For the test case in discussion, which consists of four blade rows, four master nodes are assigned.

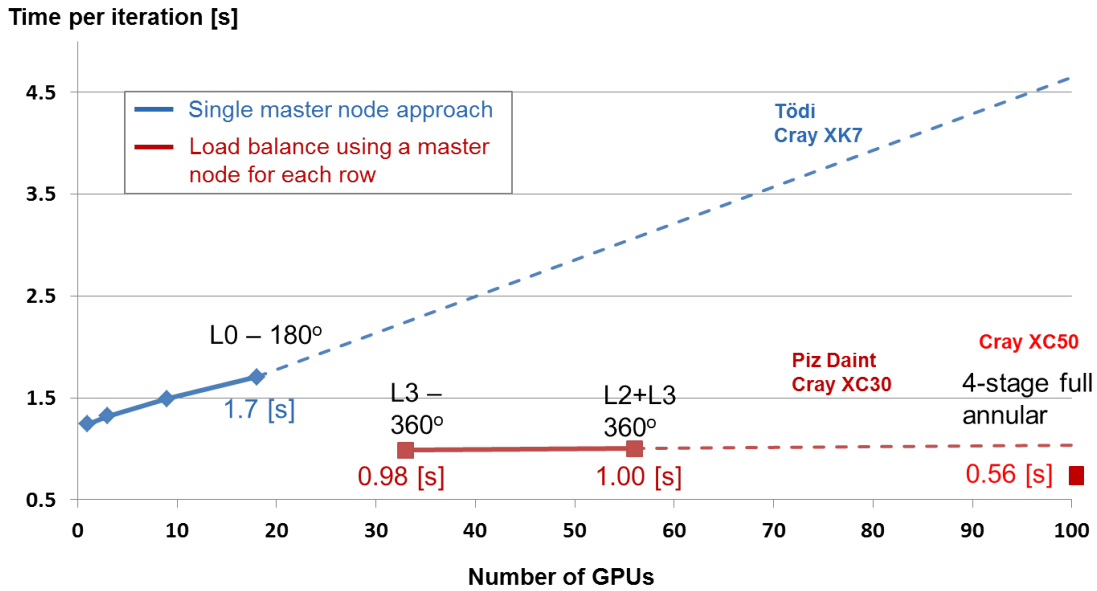


Figure 2.8: Comparison of MULTI3 solver single master node framework in blue and optimized framework with one master node for each row in red. The optimized framework shows good scalability as runtime remain constant even by adding additional computational mesh as well as additional GPUs for the added mesh. Performance improves with 1.84x speedup on new Piz-DAINT CRAY XC50 with Pascal P100 GPUs.

Two types of interfaces need to be treated for every time step during the simulation. The first type of interface is known as a periodic interface, between the blade passages in the circumferential direction, that are within the same blade row. The second type of domain interface is row interface between the stator and rotor row in the axial direction. For example, annular row outlet interface from GPU0-GPU15 requires sliding mesh interface treatment to inlet of GPU16-GPU33, as shown in Figure 2.7. Each master node is responsible for the treatment of periodic interfaces of the respective row and of row-interface of the adjacent row. With this flexibility of having a separate master node for each row, CFD solver handles additional rows approximately in the same runtime per iteration. As the problem size increases and accordingly new GPU's are added, computational run-time per iteration remains constant. The computational domain in Figure 2.9 with four rows, split into 56 GPUs, is run with the new framework optimizations and its scalability is compared with the previous single master node approach, as shown in Figure 2.8.

In Figure 2.8, the blue solid line represents the framework with a single master node approach where runtime measurements were performed with up to 18 GPUs on Todi CRAY XK7. This shows an increase in runtime with the addition of computational domains. On the other hand, the red line represents measurements on test case shown in Figure 2.7. The first measurement for 31 GPU domains shows a runtime of 0.98s per iteration. This measurement performed on Piz-DAINT appears to be faster than the computation with 18 GPU's performed on Tödi (CSCS old cluster CRAY XK7).

The important benefit of the new framework is highlighted by running all the four rows using 56 GPUs, which shows a runtime of 1 second per iteration. Dotted lines in Figure 2.8 are only a linear extrapolation of the expected runtime with addition of computational domains. In addition, the run-time per iteration improves by speedup of 1.84x on new Piz-DAINT CRAY XC50 with Pascal P100 GPUs for full annular multi-stage (114 GPUs) low-pressure steam turbine model running with equilibrium steam modeling.

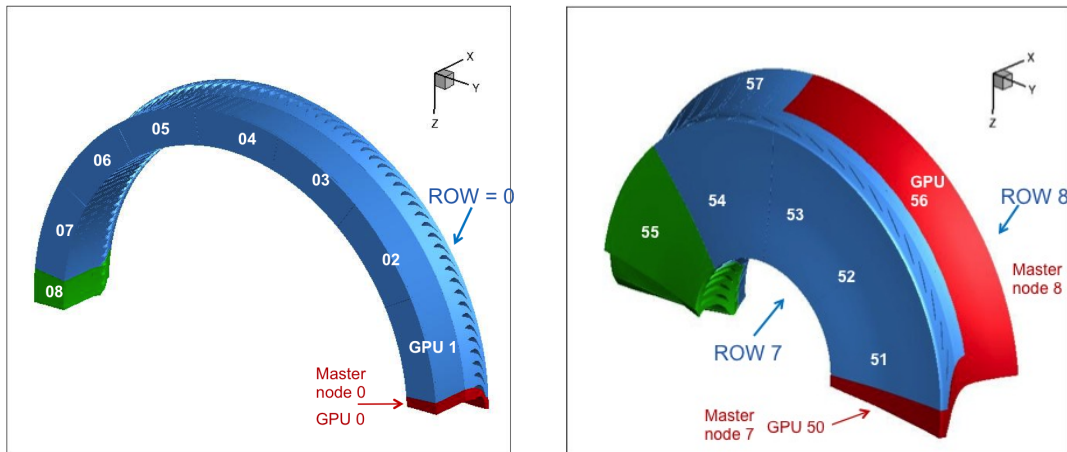


Figure 2.9: Subdomain and assigned GPU identification number of row 0 on left, and row 7 and 8 on the right. This test case consists of 57 GPUs and profiled for scalability assessment.

The scalability tests in the following section were performed on real supersonic steam turbine geometry under investigation, where the computational domain covers half of the full annulus of the turbine and consists of 8 blade rows and the diffuser. These (8+1) rows are decomposed into 57 sub-domains each running on a separate GPU. Sub-domains for the first row (0) and the last two rows (7 and 8) are shown in Figure 2.9 along with GPU numbers.

The scalability run-time measurements in this section have been performed as shown in Figure 2.10, the time per iteration for a problem size of 195.5 million mesh nodes, distributed into 57 GPUs, is about one second (1 [s]) per iteration along the duration of a

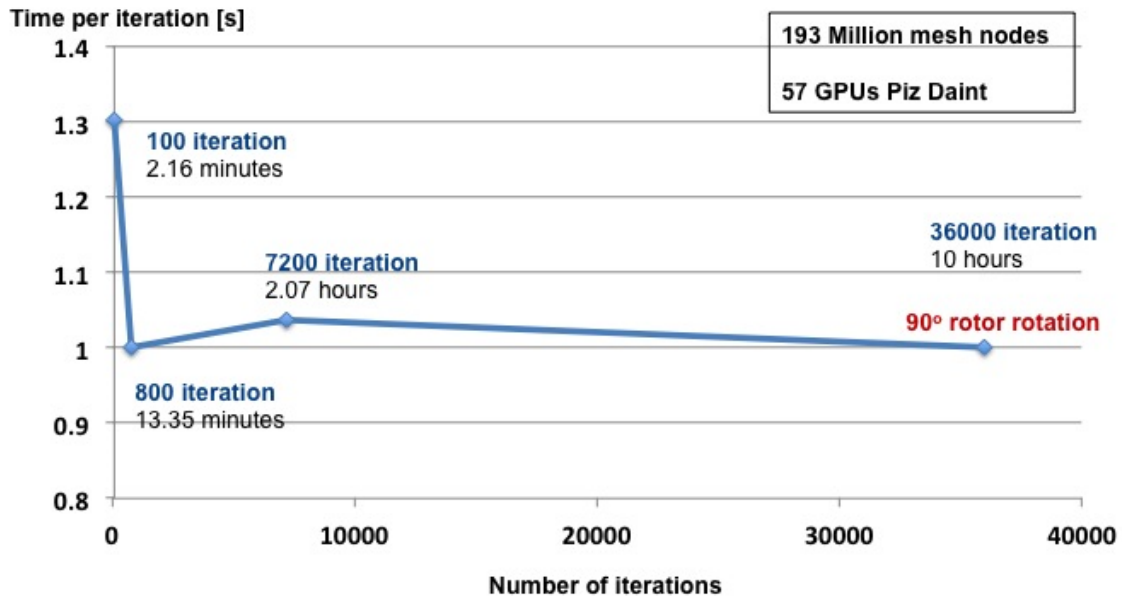


Figure 2.10: Time per iteration is measured with four separate runs of 100, 800, 7200 and 36000 iterations with reported wall clock runtimes.

10-hour job. Even for shorter runs, the iteration time stays constant at 1 [s].

To estimate the weak scalability of the solver, time per iteration has been measured for different runs having a range of mesh sizes distributed into the appropriate number of GPU's. As shown in Figure 2.11, there is a very slight variation in the iteration time between two runs with the same mesh sizes, which proves the homogeneity of the cluster. Increase in the iteration time by 11% is reported by full annulus setup (114 GPUs) compared to half annular setup (57 GPUs). Half annular setup with equilibrium-steam show 12% increase in run-time per iteration compared to dry steam. This test shows that the weak scalability of the solver is good enough to handle simulations in excess of 114 GPU's.

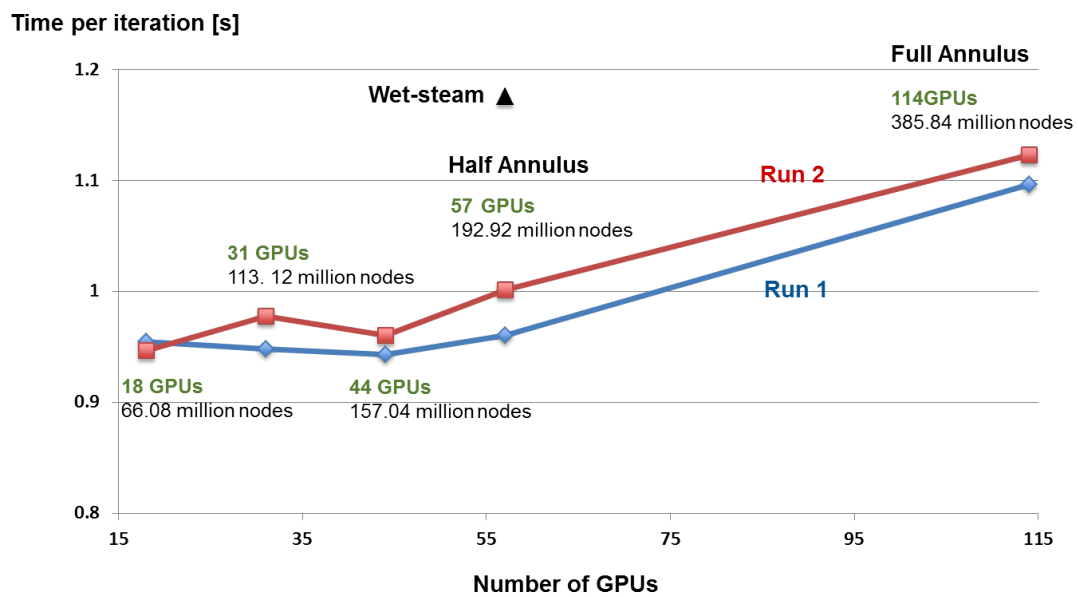


Figure 2.11: Scalability measurements using production run code. Each simulation run on curve consists of 800 iterations.

Chapter 3

Time-resolved aerodynamic analysis of MHPS low-pressure steam turbine with supersonic airfoils near the tip

The analysis in this work is focused on the MHPS 1000MW class steam turbine. The design employs long last stage blades of 50 inch specifically designed to realize a 1000MW-class steam turbine in the 4-flow configuration, as shown in Figure 3.1. When the rotational speed is 3600 rpm and the exhaust pressure is 5 kPa which is typical for sea-water-cooled units in Japan. The operating ranges are as shown in Figure 3.1 (b). The annulus areas of the last stage blade is increased to 11.5 m^2 , in order to realize these target operating ranges. The computational analysis in this work is performed on a one-third scale model of the low-pressure turbine component similar to the experimental model as discussed in section 3.1.

3.1 10MW steam turbine test facility

The experimental measurements are performed at MHPS' 10MW research steam turbine test facility in Hitachi, Japan. As shown in Figure 3.2 (a) and (b), low-pressure steam turbine rig consists of four-stages (L-3 to L-0) with a scale ratio of 1/3. The newly developed last stage rotor blades are a downscaled model of 50 inch steam turbine blades, with supersonic relative flow speeds in the tip region. Regarding the operation of the facility, the steam is generated in the boiler and directed into the turbine inlet. The inlet pressure and temperature are controlled in order to test different operating conditions and loads. At the exit of the last stage of the machine the condenser controls the exit absolute static pressure and the condensate water is guided back to the boiler to close the cycle. The facility also includes an inverter motor to drive the turbine shaft during low load

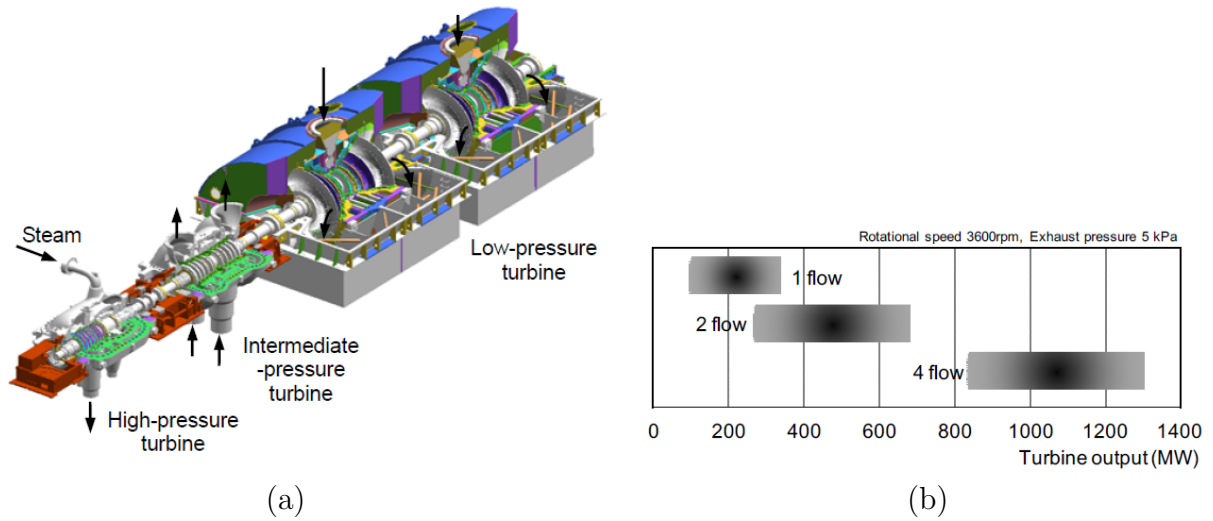


Figure 3.1: (a) MHPS steam turbine (1000MW class, 4-flow configuration) Senoo et al [22]. (b) Turbine output (MW)

tests. The inverter motor generator and a water brake dynamometer absorb the turbine’s generated power and control the rotational speed of the machine through a gearbox. The measurements were performed at a rated speed of 10,800rpm, which is representative of a 60Hz power plant mainly used in USA as well as in Korea and Japan. The design operating condition for full load experiments are summarized in Table 3.1.

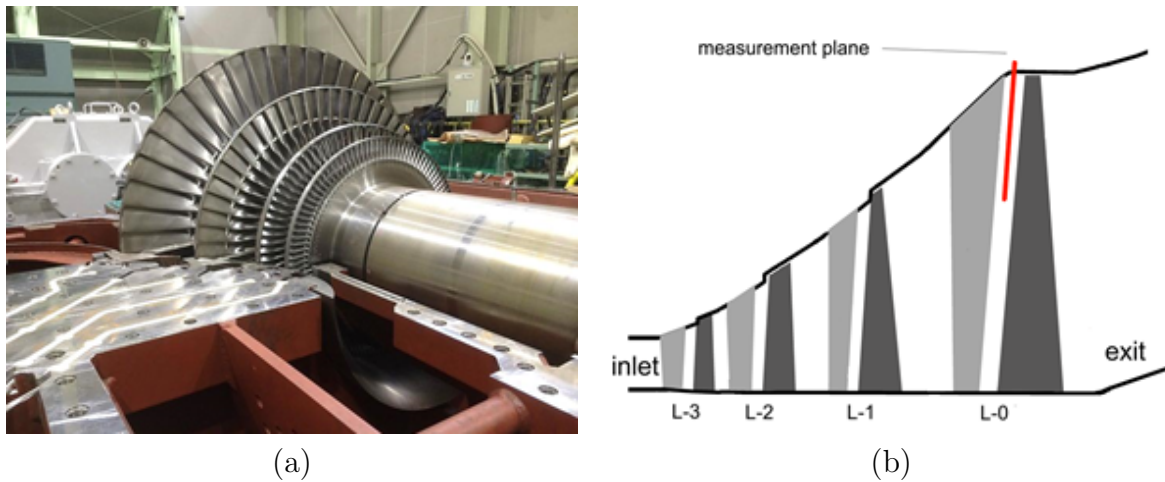


Figure 3.2: MHPS low-pressure steam turbine test facility where FRAP-HTH and FRAP-OB measurements were conducted (a). Schematic of the test facility, the measurement plane of the probe is marked in red (b), Bosdas [25].

Table 3.1: Operating tested full load conditions for MHPS low-pressure steam turbine experiments.

	OP-1
Massflow [t/h]	47.5
Exit pressure [kPa]	5
Inlet temperature [C°]	272
Calculated wetness mass fraction at L-0 stator exit @ 80% span [%]	4.0

FRAP-HTH time-resolved measurements were conducted at the stator exit of the last stage (L-0) in the 70% of tip span, as shown in Figure 3.2. The last stage of the LP steam turbine has 58 stator and 48 rotor blades respectively. The FRAP-HTH measurement plane is located at $\mathbf{x}/\mathbf{s}=\mathbf{0.35}$ between L-0 stator and rotor, where \mathbf{x} is distance downstream of stator trailing edge and \mathbf{s} is the measured distance from stator trailing edge to the rotor leading edge. In addition, 5-hole probe measurements are carried out at the inlet and exit of each stage for full radial span during the same rig operation. The 5-hole probe measurements provide time-averaged data that is used as experimental boundary conditions for computations throughout this work.

3.2 Influence of equilibrium steam modeling on low-pressure last stage aerodynamics

In this section, the computational model comprising of 5 stator and 4 rotor blades fitting in 30° sector for the last stage (L-0) is simulated. Time-resolved 3D computational fluid dynamics (CFD) simulations for design point operation are performed and then analyzed to understand unsteady aerodynamics flow field, blade surface pressure loading and shock wave interaction between stator and rotor. Thermodynamic properties of steam are applied in this work with the developed model explained in the previous chapter 2. The primary objective of this study is to understand error introduced in the reported efficiency, flow aerodynamics, and unsteady blade pressure loading by the approximation of ideal gas law assumption instead of thermodynamic properties of steam (equilibrium steam model). Simulations converge in 58 wall clock hours using four Tesla K20X GPUs with equilibrium steam. The reported time demonstrate the feasibility of unsteady CFD simulations in the design and engineering practice.

Geometry and computational domain: In this numerical study a simplified geometrical model with modified blade count of stator (Nozzle)¹ (58 to 60) is considered

¹Alternatively, terminology of Nozzle is used for stator and Bucket for rotor.

in order to fit integer blade count in 30° annular domain. The rotor (Bucket) blade count is unchanged. Geometry is scaled by $1/3$ to match the size of the test turbine facility described by Haraguchi et al. in [55].

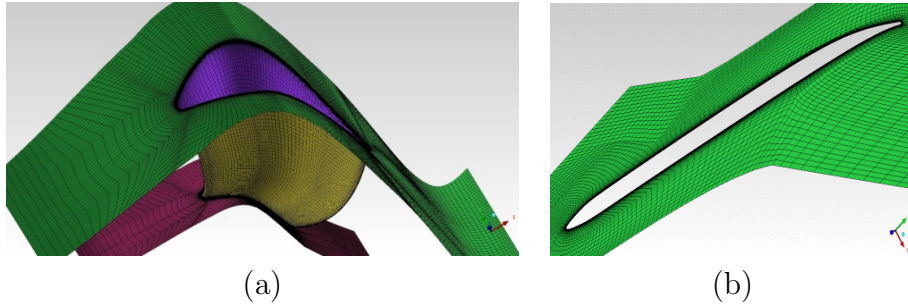


Figure 3.3: (a) Stator mesh consists of 1.4 million nodes per airfoil; wall mesh clustering shown on the left (b) Rotor mesh consists of 1.6 million mesh per blade; mesh clustering on tip-span is shown on the right.

A multi-block structured, body-fitted mesh is generated for each passage separately using Ansys ICEM-CFD. O-grids are placed around the airfoils, and wake blocks are attached to the leading and trailing edges. H-blocks are used in the areas between blade rows. High twist in blade geometry for improved mesh quality is resolved with additional span-wise generated surfaces which enabled control of mesh block edges at intermediate cuts. For the stator, only mid-span cut is required, whereas for the rotor six additional span-wise surfaces are needed. Size of the single stator and the single rotor is 1.4 and 1.6 million mesh nodes respectively. Mesh resolution on stator wall surface and rotor tip-shroud is shown in Figure 3.3. Mesh quality is ensured as laminar sublayer $y^+ < 5$.

A computational model of the turbine is constructed from the stator and rotor passages that are meshed separately. The model consists of five stators and four rotor blades. The computational domain is divided into three sub-domains, each handled by a separate graphics card and data is exchanged over the boundaries of the sub-domains between three graphics cards (GPUs). Table 3.2 shows blade count and total mesh size for each GPU.

Boundary conditions, simulation settings, and convergence: Uniform profiles of total pressure and total temperature are imposed at the inlet of L-0 domain across the span. Absolute yaw angles are set with estimated values whereas pitch angle is set as radial profiles in order to match flare angle of L-0 casing for realistic flow conditions. Turbulence intensity and length scales are set as uniform values of 1% and 0.03% of vane airfoil height respectively. A separate numerical study is conducted during the course of these simulation showing little observable effects of the turbulence intensity on the stator aerodynamics. Due to very high acceleration across the stator the turbulence intensity imposed at the inlet drops very rapidly along the passage. No-slip adiabatic wall boundary conditions

Table 3.2: Mesh size for GPU sub-domains; equilibrium versus dry ideal steam cases.

	Stator / Rotor	Number of Nodes [million]
GPU 0	2/1	4.3
GPU 1	12/	4.3
GPU 2	1/2	4.5
Total	5/4	13.1

are set for the walls. At the interface between the rows, the sliding interface approach is used. Outlet pressure at the hub is set to a representative value, with radial equilibrium imposed in order to match the desired pressure ratio across the L-0 stage. For dry steam simulations gas constant $R_{steam}=461.5$ [J/kg/K] and ratio of specific heats $\gamma_{steam}=1.32$ are used. For wet-steam simulations, the internal energy level at the stage inlet is adjusted to match the wetness fraction level of 3.4%, corresponding to the measured conditions.

Unsteady simulations are performed with dual time stepping approach, where the physical time is discretized based on 2nd order backward Euler scheme where four blades passing rotation of domain is divided into 120 equal time steps.

Simulations have been conducted with LEC's in-house solver MULTI3. Second order accuracy in space is ensured by matching mesh interface across blocks and row interfaces. To prevent artificial high-frequency oscillations anisotropic artificial dissipation algorithm is used which scales the smoothing coefficients, based on the local CFL number and also the local level of modeled eddy viscosity, as explained by Basol [27]. The eddy viscosity is calculated using the Wilcox's k-omega model [48], in its low Reynolds number form by Chima et al. [50]. For a robust implementation, the convective fluxes of turbulence model equations are calculated using non-oscillatory, second-order upwind space discretization with Kato & Launder [49] source term modification. For time-resolved simulations, Jameson's [43] dual time stepping scheme is utilized.

A computational study has been conducted using Tödi Cray XK7 hybrid computing system in Swiss National Supercomputing Centre CSCS Lugano Switzerland. The domain is distributed to three Nvidia Tesla K20X graphics cards. Using ideal, dry steam conditions, four rotor blade passing require 4.2 hours with an overall mesh size of 13.1 million mesh nodes. The same run took 7.2 hours, approximately 70% longer when wet-steam conditions are applied for the same simulation on the discussed computing architecture.

The convergence is evaluated with mass flow levels at stator inlet, rotor outlet and stator-rotor interface monitored over time as shown in Figure 3.4, for dry and wet steam simulations. As shown, the mass flow imbalances between the stator inlet and rotor outlet are about 0.2% for the dry and wet-steam simulations. The fluctuations in the mass flow

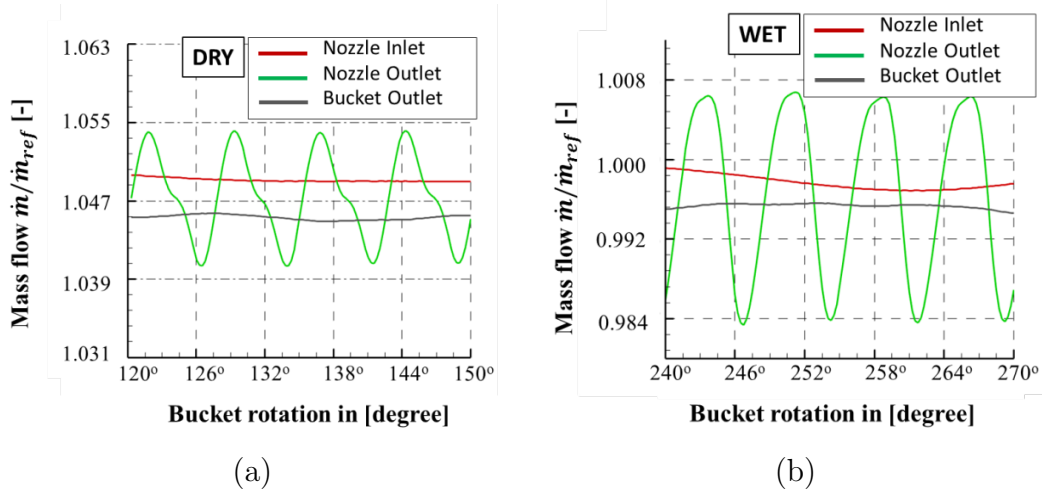


Figure 3.4: Time history of the mass flow for (a) dry-steam (b) wet-steam, in rotor rotational position.

rate at the stator-rotor interface shown in Figure 3.4 might be due to some inflow and outflow from periodic boundaries due to rotation of the rotor to adjacent GPU domains. The dry-steam simulation results in 5.5% higher mass flow rate than the wet steam simulation. For the wet-steam simulations, latent heat of evaporation is added on the internal energy distribution that was calculated for the dry steam simulation. The level of additional evaporation heat is set such that the wetness fraction at the stator inlet is 3.4%.

Dry steam simulation required 120° of rotor rotation to reach convergence with a total runtime of 17 hours. The wet-steam simulations require 240° of rotor rotation, double of that required by dry steam in 58 hours of wall clock runtime. In this section, inlet and outlet boundary conditions were taken from the design parameters. However with flow measurements by Bosdas et al. [25] available later, all subsequent studies in this work are conducted with experimental boundary conditions.

Unsteady results for wet steam condition: Static pressure coefficient distributions C_{ps} defined as equation 3.1 across six different span-wise positions are shown in Figure 3.5 (a).

$$C_{ps} = \frac{P_s - P_{s,exit}}{P_{t,inlet} - P_{s,exit}} \quad (3.1)$$

At stator-rotor gap near the hub section, a weak oblique shock wave is attached at the trailing edge of the stator. Downstream branch of stator trailing edge shock interacts with the rotor leading edge. Shock wave intensity from the stator reduces towards mid-span as the pressure ratio across the stator drops towards the tip region. On the other hand,

a bow shock wave **S1** starts to form at the leading edge of the rotor. These bow shock waves are moving with the rotor in the stationary frame of reference. At 90% of span bow shock wave at the leading edge of the rotor is clearly visible impinging on the suction side of the upstream stator blade as well pressure side of the neighboring rotor blade. Intensity of shock wave increases towards the shroud, as a result of higher rotational speed of the rotor near the tip.

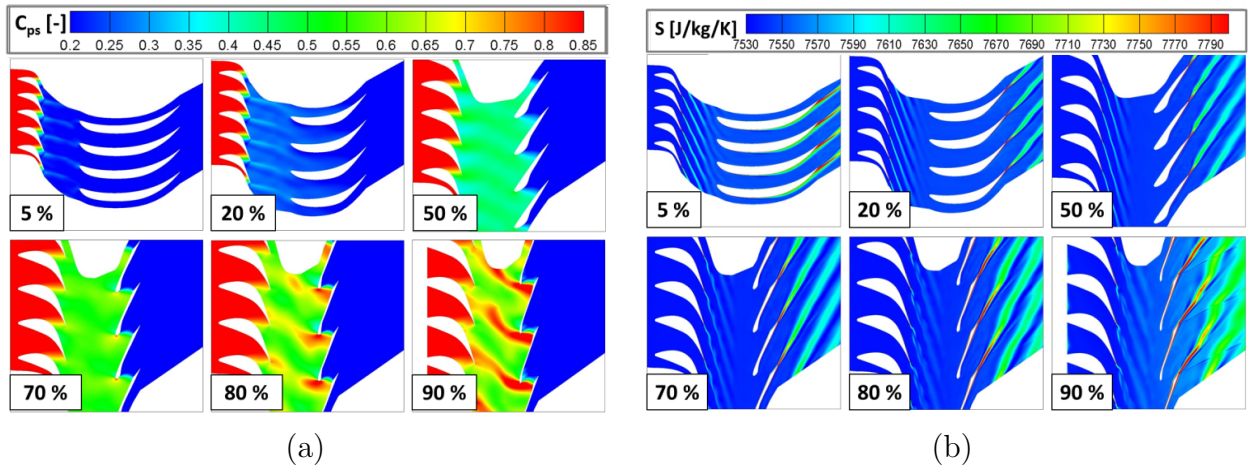


Figure 3.5: (a) Instantaneous static pressure coefficient C_{ps} [-] distribution at different span-wise positions based on equilibrium steam. (b) Instantaneous entropy distribution at different span-wise positions based on equilibrium steam.

Figure 3.5 (b) shows instantaneous entropy distribution across six different span-wise positions. No large loss is directly caused by both the weak oblique shock waves emanated from the stator trailing edge near the hub and the bow shock waves upstream of the rotor leading edge near the tip, but the stator wake starts to modulate at a span-wise position higher than 80%. This modulation is due to the unsteady interaction of bow shock wave with the stator suction side. Increased entropy levels are visible in the rotor boundary layer and wake from 70%-90% of span. The supersonic tip region shows high levels of entropy. This indicates an increased loss in supersonic tip region compared with hub and mid-span regions. The blade profile and wake loss dominate and presence of bow shock **S1** pronounce stator suction side boundary layer modulation.

Figure 3.6 shows the instantaneous pressure and the entropy distributions at the interface plane between the stator and rotor. The pressure distribution shows that the back pressure downstream of the stator is increased towards the tip shroud. From about 80%-100% of the tip span, the effect of the bow shock wave is visible at the interface. The entropy distribution at the interface plane shows an increase in the wake thickness close to the hub, presumably due to high absolute Mach numbers. It also shows that the level

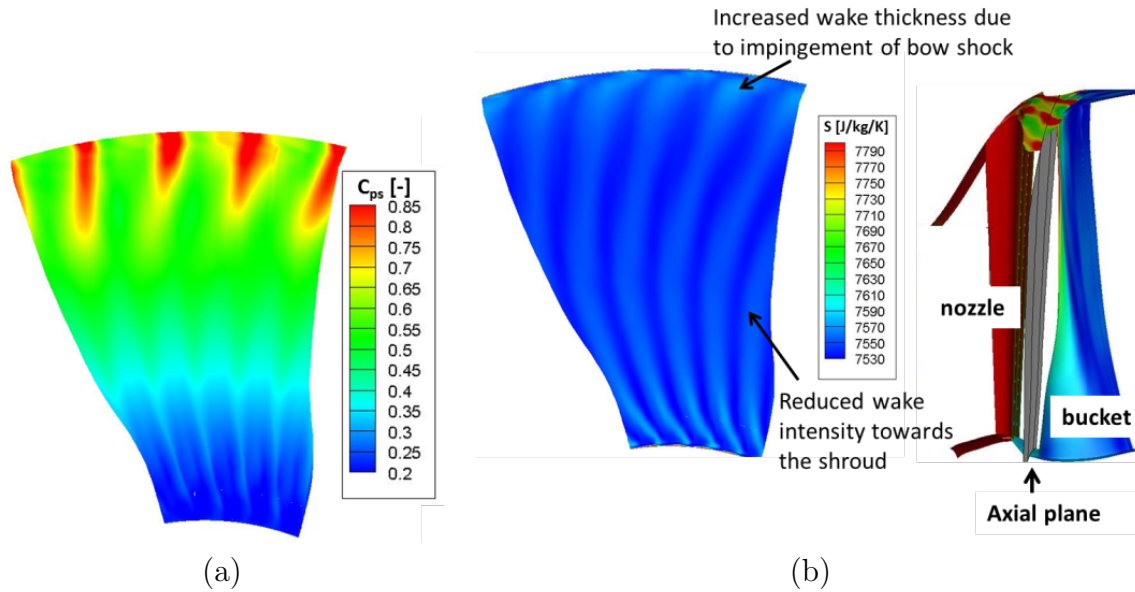


Figure 3.6: (a) Instantaneous static pressure coefficient C_{ps} [-] distribution, (b) entropy distribution S [J/kg/K], at the interface plane between the stator and rotor using equilibrium steam model.

of entropy reduces towards the 80% of span. From 80%-100% span in the vicinity of the casing, the thickness of the wake increases again due to the modulation of the boundary layer thickness on the stator suction side by the impingement of the bow shock wave.

Influence of wetness on shock dynamics: Figure 3.7 shows the instantaneous pressure distributions at 90% span for the simulations with dry steam properties assumed as the ideal gas and with equilibrium steam properties based on the steam tables IAPWS-IF97. Simulation with steam properties predicts a smaller subsonic region compared to those obtained with the dry steam properties.

The streamline is passing through two leading edge bow-shock waves ($S1$), see captions 1 and 2 in Figure 3.7. The bow shock wave (1) is upstream of the leading edge of the rotor as shown in the lower half of the Figure 3.7. This shock wave is generated due to the supersonic relative inflow to the moving rotor. The shock wave (2) impinges upstream of the throat on the pressure surface of the adjacent rotor blade. As shown in Figure 3.7, there are considerable differences between pressure levels and shock wave strength for the dry and wet conditions. In the shock, peak pressure levels are the same for dry and wet simulations; however, wet-steam predicts a smaller subsonic flow region. At the impinging position on the adjacent rotor blade (2), wet steam predicts the higher magnitude of peak pressure levels and a smaller subsonic flow region downstream the shock wave.

The instantaneous wetness mass fraction at the 90% span is given in Figure 3.8

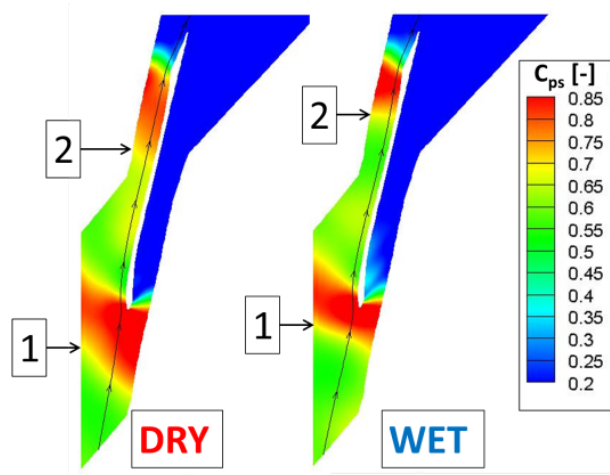


Figure 3.7: Instantaneous static pressure coefficient C_{ps} [-] distribution at 90% span-wise position for dry and equilibrium-steam conditions.

(a). Across the shock wave at the rotor leading edge, the wetness mass fraction drops considerably which is caused by the steep increase in the pressure at the bow shock wave. The wetness decrease downstream of trailing edge shock wave **S3** of the rotor and wetness of up to 12% is seen on the rotor suction surface in the region of flow over-expansion. Circumferentially and time-averaged wetness mass fraction across radial span at the outlet of the stator are increased to 7.5% near the hub and 4.0% near the tip. At the outlet of the rotor domain, wetness is increased up to 10%.

Effect of equilibrium steam modeling on efficiency: Circumferentially and time averaged total-to-total stage efficiencies are compared for dry and wet steam modeling for unsteady simulations in Figure 3.9. Following definitions for total-to-total efficiencies across the stage are used for equilibrium and dry-steam modeling, as given in equation 3.2 and 3.3 respectively.

$$\eta_{tt,wet} = \frac{h_{o,inlet} - h_{o,exit}}{h_{o,inlet} - h_{o,exit,isentropic}} \quad (3.2)$$

$$\eta_{tt,dry} = \frac{h_{o,inlet} - h_{o,exit}}{h_{o,inlet} \left(1 - \frac{P_{o,exit}}{P_{o,inlet}}\right)^{\frac{\gamma-1}{\gamma}}} \quad (3.3)$$

Figure 3.9 (a) shows the total-to-total efficiency difference between dry and equilibrium steam computations. The following observations can be obtained. The wet steam results predict overall lower efficiency across the radial span. From 0-5% of radial span close to the hub, the equilibrium-steam simulation predicts 5% increase followed by 2.5% drop in efficiency compared to dry-steam. Similarly, a sharp increase of 19% and a decrease

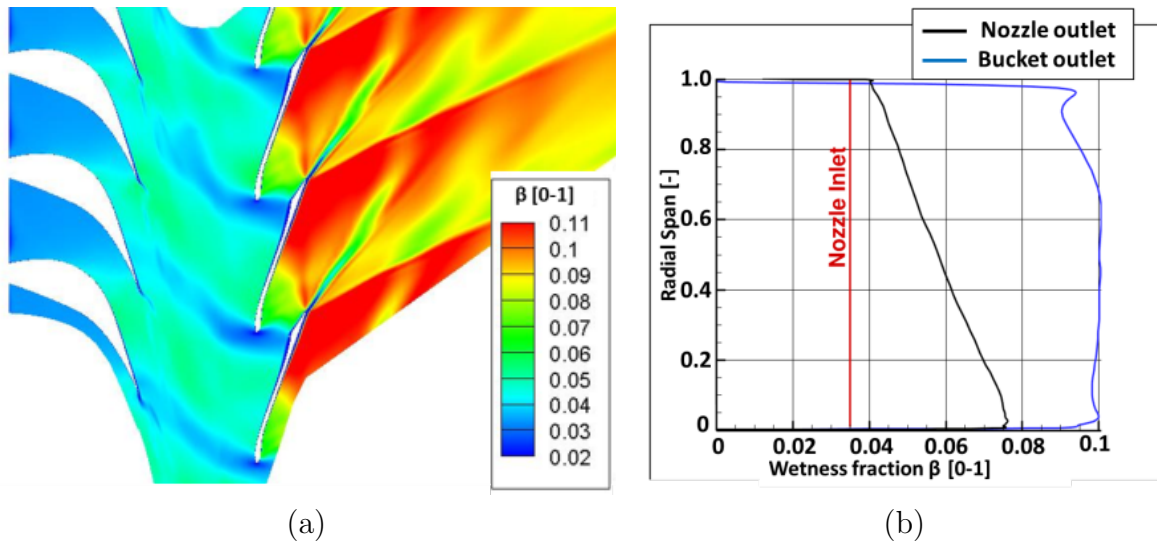


Figure 3.8: Instantaneous wetness mass fraction distribution; (a) blade to blade contour at 90% span-wise position, (b) circumferentially averaged radial wetness fraction at inlet and outlet of stator and rotor.

is seen in the 95%-100% of radial span. Equilibrium steam predicts similar efficiency as dry steam at 5% of span and lower efficiency of about 2% up to 60% of radial span. Efficiency is predicted lower by 2.6% at 60% of span and continuously decrease to 5.3% at 80% span respectively by using equilibrium-steam model. From 80% to 95% of radial span includes the wake downstream of bow-shock region as shown by Entropy distribution in Figure 3.9 (b). Larger entropy from 80% to 95% of the radial span is related to losses introduced by bow-shock wave **S1** interaction between stator and rotor as well rotor blade profile loss introduced by supersonic flow expansion. In conclusion, the dry steam model over-predicts total-to-total stage efficiency by 2.7% on average compared to thermodynamic properties of steam. This indicates a substantial error in prediction introduced by the dry-steam model (ideal gas law assumption) and might significantly impact computational accuracy.

Unsteady pressure loading:

From time-resolved data, instantaneous distributions of static pressure coefficient on the pressure side of the rotor for the full radial span are shown for two different time steps in Figure 3.10. These two time steps are selected at a distance of time period $t/T=0.0$ and $t/T=0.625$, where T is the time period in which a rotor blade cover one stator pitch. Instantaneous rotor pressure levels at different instant in time covering time period T for equilibrium-steam results are shown in Figure 3.11 at 5%, 50% and 97% of radial span. The pressure fluctuations at the rotor are periodic in this time frame of rotor passing one stator pitch in Figure 3.11. The unsteadiness is low at 5% and 50% span of rotor as shown in Figure 3.11 (a) and (b). However, the increase in unsteadiness is observed

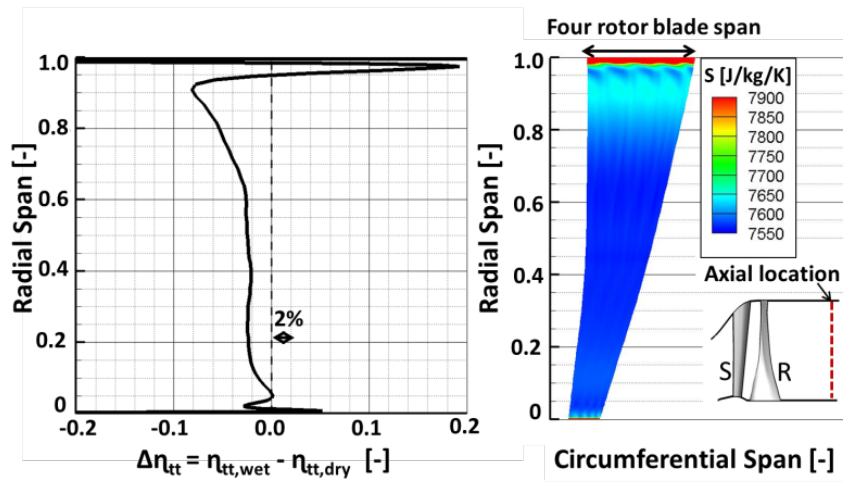


Figure 3.9: (a) Circumferentially and the time-averaged difference in total-to-total stage efficiency for equilibrium and dry steam simulations on the left and (b) Entropy contours from equilibrium steam computations at the stage exit.

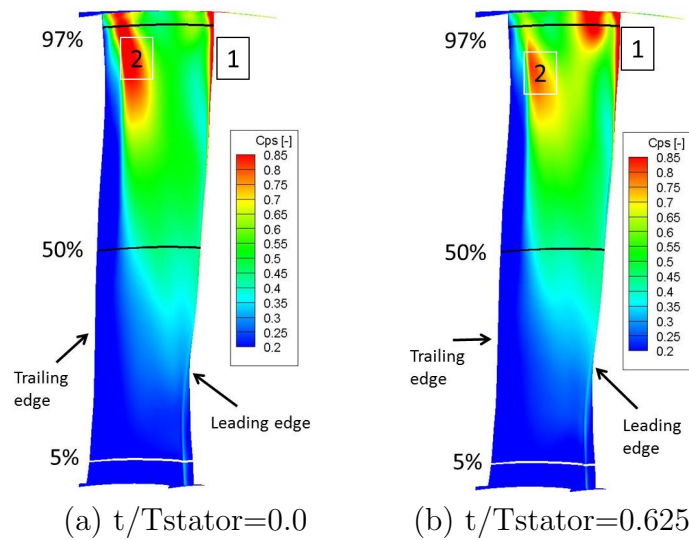


Figure 3.10: Instantaneous static pressure coefficient C_{ps} [-] distribution from equilibrium-steam simulation on the rotor pressure surface at $t/T=0$ in (a) and $t/T=0.625$ in (b).

above 80% of the rotor span on the pressure side. The pressure side is subject to the unique incidence of the flow (incidence angle and relative Mach combined). The yaw and pitch angle unsteadiness introduced by rotor leading edge shock S1 is the driving factor for pressure side unsteadiness, as shown in Figure 3.11 (c), at 97% of span.

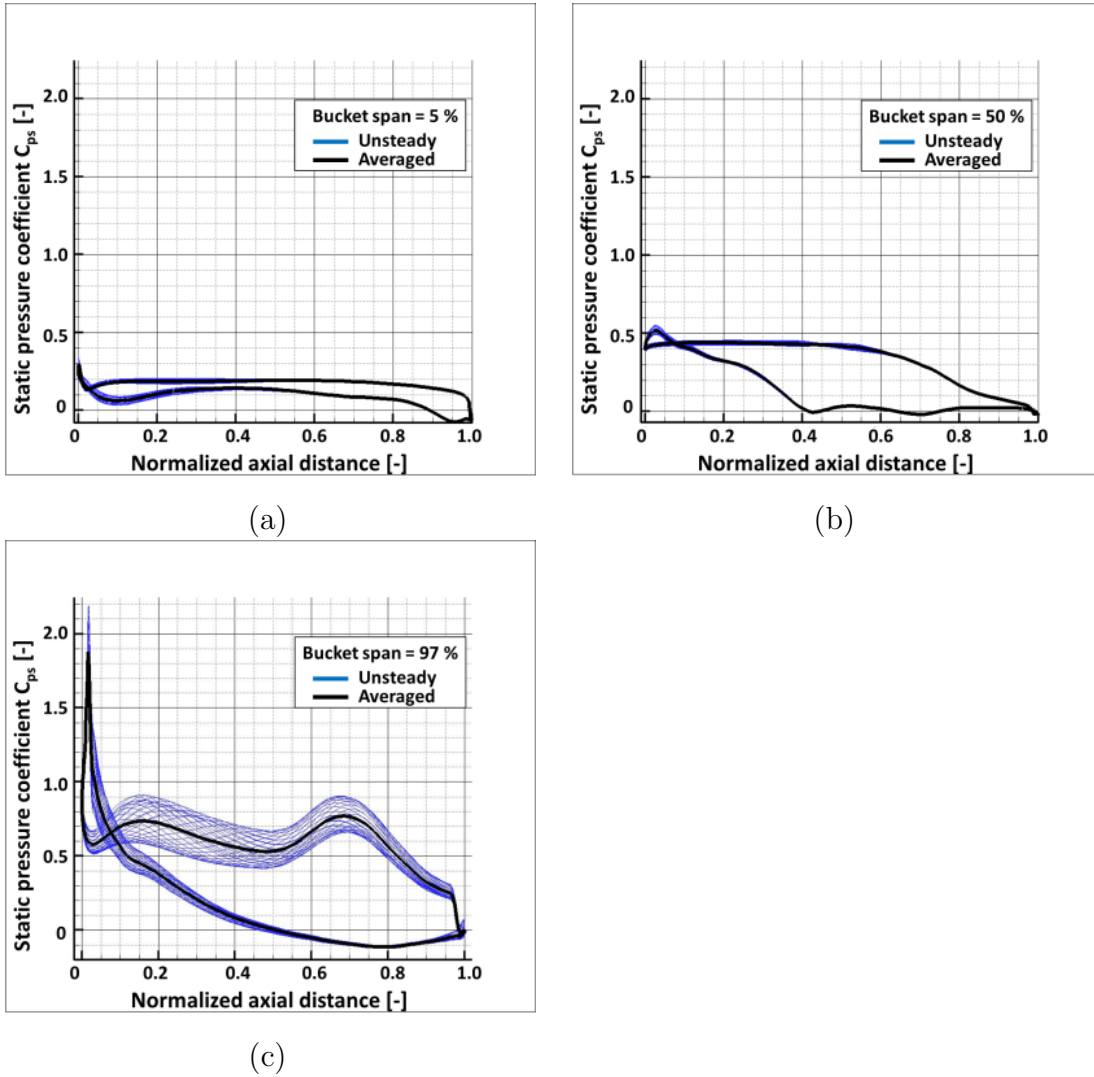


Figure 3.11: Instantaneous rotor surface static pressure coefficient covering a time frame of one rotor passing at (a) 5%, (b) 50% and (c) 97% of span-wise positions for equilibrium-steam simulations.

As seen in Figure 3.10 (a) at $t/T=0$, and Figure 3.11 (c) with unsteady envelop of pressure level at 97% of span, there is a high-pressure region, as shown by caption [2], on the pressure surface upstream of the throat of rotor blade due to an impingement of

the bow shock wave (2) from the leading edge of the adjacent blade. This region of high pressure stays at constant location with time as the blades rotate but the intensity and size of it vary with time as shown in Figure 3.10 (b) at $t/T=0.625$, and Figure 3.11 (c) at 0.68 of axial chord distance. Peak to peak fluctuation of unsteady pressure at 0.68 of axial chord distance is 33% compared to time-averaged pressure level. On Figure 3.10 at $t/T=0.625$, another region of high pressure, as shown by caption [1], appears on the pressure side, close to the tip downstream of leading edge. Pressure in this region is highly unsteady, as observed in Figure 3.11 (c) at 0.15 of axial chord distance. Peak to peak fluctuation of unsteady pressure at 0.15 of axial chord distance is 44% compared to time-averaged pressure level. Results show a much wider envelope of pressure fluctuations on the pressure side from between 0.1 and 0.7 of the axial chord distance. On the other hand, the suction surface of the rotor shows lower unsteadiness compared to the pressure side. At 0.1 of the axial chord distance as shown in Figure 3.11 (c), the suction side of rotor show 35% peak-to-peak pressure fluctuations compared to time-averaged pressure levels, and this gradually decreases towards the trailing edge of the rotor. This indicates a smooth supersonic flow expansion on suction side despite unsteady flow impinging on the pressure side of rotor airfoil. This validates the design intent of supersonic rotor airfoils as the flow turned on the pressure side to enter the throat and expand smoothly on the suction side downstream of the throat. The flow unsteadiness to rotor inlet does not show a pronounced impact on supersonic flow expansion on the suction side. Nevertheless, it must be noted that pressure unsteadiness of 30% and above introduce unsteady forces and may induce high cycle fatigue.

Figure 3.12 shows the instantaneous stator surface static pressure coefficient at 5%, 50% and 97% at different instants in time covering a period of one rotor blade passing. The pressure fluctuations at the stator are periodic in this time frame of one rotor blade passing. At 5% span trailing edge of stator in Figure 3.12 (a) small increase in unsteadiness on the suction side, 0.8-1.0 of axial distance, is a result of oblique shock wave. Peak to peak fluctuations of 13% in pressure level is seen at 0.95 of the axial chord distance compared to a time-averaged pressure. At 50% mid-span of the stator, unsteadiness is reduced as no oblique shock wave is introduced as a result of an increase in exit pressure. High unsteady loading is observed on the suction surface near trailing edge at 97% of the span where the bow shock wave **S1** formed at the rotor leading edge impinges, as shown in Figure 3.12 (c). Peak to peak pressure fluctuations to a maximum of 100%, compared to a time-averaged static pressure coefficient, is seen at 0.97 of axial chord distance on stator suction side in Figure 3.12 (c). Pressure side at the same location sees a 16% peak to peak pressure fluctuation compared to time-averaged static pressure coefficient.

Figure 3.13 shows time averaged rotor static pressure coefficient at 5%, 50% and 97% of span for equilibrium steam and dry steam results. Equilibrium steam results show slightly higher C_{ps} values at 5% and 50% of the span on the suction side. This indicates reduced flow expansion through stator at the hub to mid-span locations. At 97% of rotor

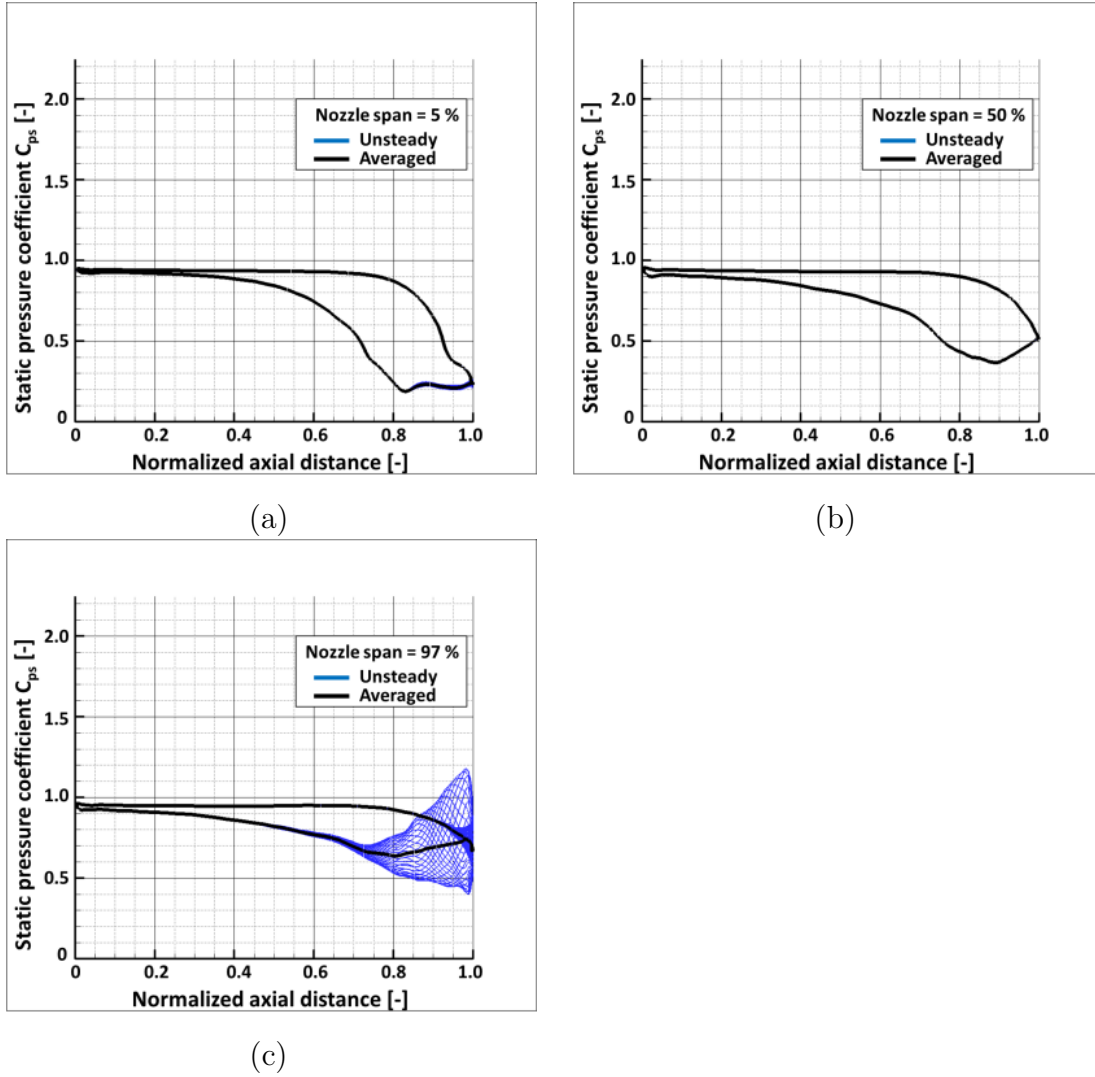


Figure 3.12: Instantaneous stator surface static pressure coefficient covering a time frame of one rotor passing at (a) 5%, (b) 50% and (c) 97% of span-wise positions for equilibrium-steam simulations.

span on the pressure side, equilibrium steam results predict 21% increase in averaged pressure at 0.2 of the axial chord distance. However, 0.4-0.7 of axial chord distance, in the region upstream of the bow shock, wet steam results show a decrease in C_{ps} on pressure side compared to dry steam results. A decrease of 29% is observed at 0.5 of axial chord length. The reduced blade pressure loading indicates lower work extraction by supersonic airfoils compared with dry steam. The increase in adverse pressure gradient introduced by adjacent rotor **S1** bow shock impinging on pressure side at 0.5-0.7 of the axial chord may introduce pronounced boundary layer and entropy generation. Nevertheless, blade surface pressure calculations differ near bow shock regions where pressure change is abrupt.

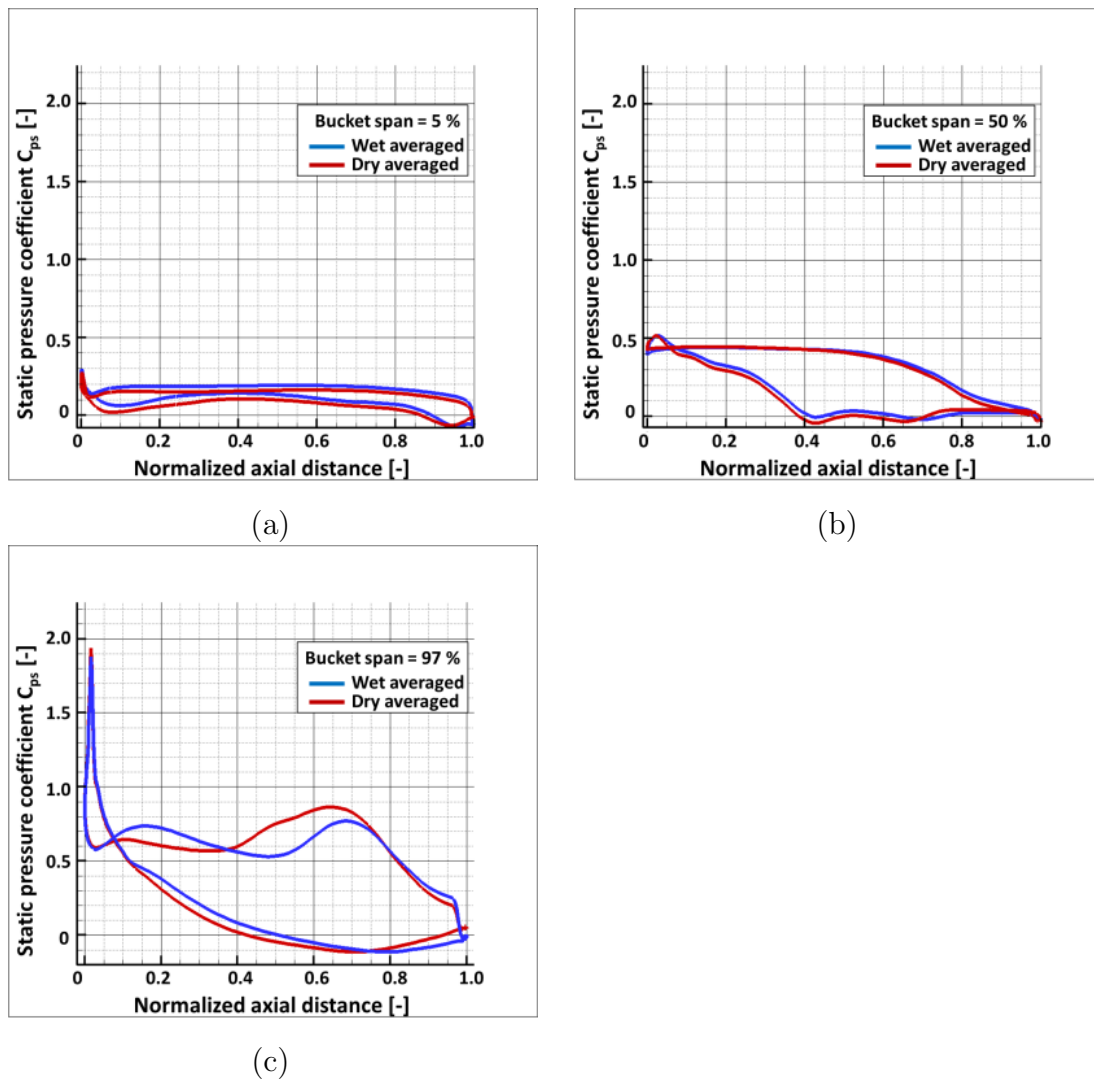


Figure 3.13: Time-averaged rotor surface static pressure coefficient at (a) 5%, (b) 50% and (c) 97% of span-wise positions for equilibrium and dry-steam simulations.

Summary and Conclusions:

The calculations in this study show a bow shock wave at the leading edge of the rotor is formed in the 15% tip span. This bow shock wave interacts with the suction side of upstream stator and pressure side of adjacent rotor blade resulting in increased unsteady loading and a decrease in efficiency near-tip region. A weak shock is also seen at the stator trailing edge in the hub region. This oblique shock wave interacts with downstream rotor leading edge. The stator suction side near the trailing edge and the rotor pressure surface are exposed to the highest unsteady loading in the transonic tip region. The rotor tip leading edge bow shock **S1** is the main mechanism behind unsteadiness in transonic flow. Blade loading at 5%, 50% span shows very low unsteadiness for both stator and rotor blades. Bow shock impinging on the suction side of stator near the trailing edge cause boundary layer modulation; however, no clear evidence of any boundary layer separation is found. The wetness of up to 12% is observed in the supersonic flow expansion at 90% of span downstream of the rotor throat. Circumferentially and time-averaged wetness is increased to 10% at the stage exit.

The following conclusion can be derived from this study.

- The dry and wet steam simulations show similar main flow patterns in terms of shock interaction. In regions with smooth pressure distributions, no major differences are observed between the two results. However, the supersonic flow expansion and rotor leading edge bow shock show substantial differences. The subsonic region downstream of the bow shock wave is smaller for the equilibrium-steam model and introduce steep adverse pressure gradient on the pressure side of the adjacent rotor.
- Dry steam model over-predict total-to-total stage efficiency by 2.7% on average compared to thermodynamic properties of steam. Locally, this value can range from close to zero up to as much as 19%.
- Time-averaged blade unsteady surface pressure on the rotor shows no substantial difference between dry and equilibrium steam results at 5% and 50% of rotor span. Regions on the pressure side of the rotor under influence of bow shock in the tip region, at 97% of span, wet-steam show increase and a decrease of up to 21% and 29% of pressure side C_{ps} respectively compared to dry steam results. This indicates the equilibrium steam predict pronounced front and reduced mid loading of supersonic airfoils on average. Thermodynamic properties of steam are important for accurate prediction of static pressure and unsteady forces on the supersonic tip region of the rotor.
- Span-wise blade to blade contours shows a small increase in entropy as a result of bow shock interaction, however boundary layer, and wake of rotor blades remain the main source of entropy generation.

- Three-dimensional unsteady simulations using equilibrium-steam model for the last stage of a steam turbine with higher resolution of mesh size up to 15 million mesh nodes are feasible, with a wall clock runtime of 58 hours using three Tesla K20X GPUs. GPU parallel solvers overcome large computational runtime requirements for unsteady computation and can be used instead of steady mixing plane solvers as an engineering practice. This allows simultaneous simulation of design features on efficiency as well as unsteady forces which could affect the reliability of the turbine.

3.3 Snubber aerodynamics in the last stage rotor blades of a low-pressure steam turbine

The structural integrity of the last stage rotor is ensured by part span snubber and tip span shroud. The aerodynamic performance of the low-pressure last stage is important, as major work extraction is performed in this stage. The inclusion of snubber geometry in a time-resolved computational model requires additional effort in the meshing. The body-fitted mesh for snubber must be well resolved with y^+ value kept below 5 similar to the blade boundary layer and hub-tip end walls. This not only requires complicated mesh topology but also increase the time to convergence. In this section, the efficiency penalty of snubber and impact on supersonic flow in the rotor tip region is discussed.

Geometry and computational domain: Two separate cases of with and without snubber geometry are setup for the last stage L-0 30° sector. The geometry is scaled by 1/3 to match the size of the test turbine facility described earlier by Haraguchi et al [55]. The stator blade count is modified from 58 to 60 whereas the rotor blade count is unchanged to 48, with a blade count ratio of 5:4 for 30° sector. The mesh is generated using AutoGrid5 and IGG meshing tools by NUMECA. Meridional path mesh clustering, wall files with snubber geometry and mesh clustering are shown in Figure 3.14 (a), (b) and (c) respectively.

The computational domain is sub-divided into four sub-domains each running on a separate GPU, with a total mesh size of 15.6 million mesh nodes. GPU domains and mesh size for each sub-domain is given in the Figure 3.14 (d) and Table 3.3. Each mesh domain is fit into 6 gigabytes of NVIDIA Tesla K20X onboard memory. The multi-block mesh is created with fully matching block and row interfaces in order to retain second-order accuracy in space and eliminate interpolation errors in the regions of highly unsteady flow. Tip cavity and seals are excluded from this study. Single rotor passage mesh consists of 2.1 million mesh nodes, of which about 0.64 million mesh nodes are used in the vicinity of the snubber. The wake region downstream of snubber is as well resolved with increased mesh clustering as shown in Figure 3.14 (a). A test case of L-0 30° excluding snubber geometry consists of 12.87 million mesh nodes running on four GPUs with same domain decomposition.

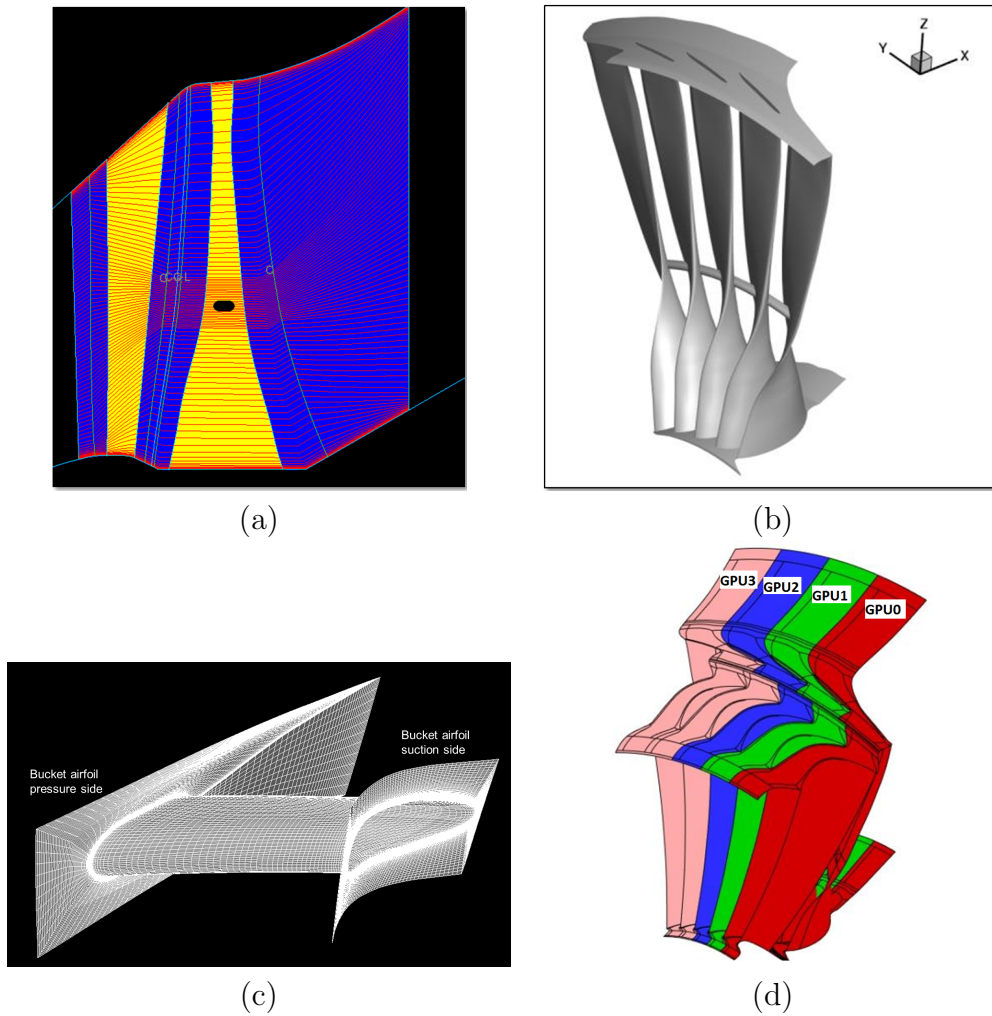


Figure 3.14: L-0 meridional path including snubber (a), wall files with snubber geometry (b) L-0 mesh clustering on snubber wall surface (c) and multi-GPU domain decomposition are shown in (d) respectively.

Table 3.3: L-0 stage (30° sector domain) including snubber geometry is sub-divided into four sub-domains, each running on a separate GPU.

	Stator	Rotor	Mesh size Snubber	w/o Snubber
GPU 0	1	1	3.58	2.9
GPU 1	1	1	3.58	2.9
GPU 2	1	1	3.58	2.9
GPU 3	2	1	4.82	4.17
Total	5	4	15.6	12.87

Boundary conditions, simulation settings, and convergence:

The experimental measurements are performed by MHPS at inlet and exit of each stage, for all four stages, using a five-hole probe resulting in time-averaged radial profiles of flow quantities. The radial profiles of static, total pressure and yaw, pitch angles for design operation are imposed as inlet boundary conditions from 5-hole probe measurements at L-0 inlet. The outlet boundary condition is imposed as a radial equilibrium with static pressure at diffuser hub end-wall measured in the same experiments. The sliding mesh interface is used at the stator-rotor and rotor-diffuser row interfaces.

Unsteady simulations are performed with dual time stepping approach. The 30° rotor revolution is resolved with 120 physical time steps. In order to ensure proper propagation of information through high node clustering regions as snubber and rotor boundary layer mesh, 200 sub-iterations are used per time step. Both simulations are first to run with dry steam (ideal gas law) for flow field to develop and subsequently converged with equilibrium steam model (IAPWS IF97 steam tables).

Simulation is run on Piz-DAINT CRAY XC30 Swiss National Supercomputing Center (CSCS) in Lugano. The simulation has covered 2.77 full annular rotor revolution with the equilibrium-steam model. The 60° rotor revolution take 19 wall clock hours with four GPUs running in parallel. The unsteady periodic solution is achieved for both simulations with a mass error of below 0.25% across rows.

Results and discussion:

The numerical model is validated with experimental measurements conducted by Bos-das et al. [12] at the MHPS low-pressure steam turbine test facility in Hitachi, Ibaraki Japan. Measurements were conducted using novel fast response heated probe (FRAP-HTH). This is the first reported time-resolved measurements in the wet steam environment with the supersonic relative flow at the last stage rotor inlet ever been reported. The

snubber analysis is performed for same design operating condition and time-averaged flow comparison for relative flow yaw angle and Mach number is shown in Figure 3.15 (a) and (b) respectively. The measurements are performed for 70% of tip span shown in the blue curve. The computation flow properties are shown by the red curve for the snubber and black curve for without snubber cases respectively. The relative yaw angle is found to be in agreement from 70% to 90% with about 1.2° over-predicted at 82% of span. The relative Mach is over-predicted by about 0.04 at 82% of span. The differences above 90% of span might be due to the fact that measured values are close to probe's calibration range.

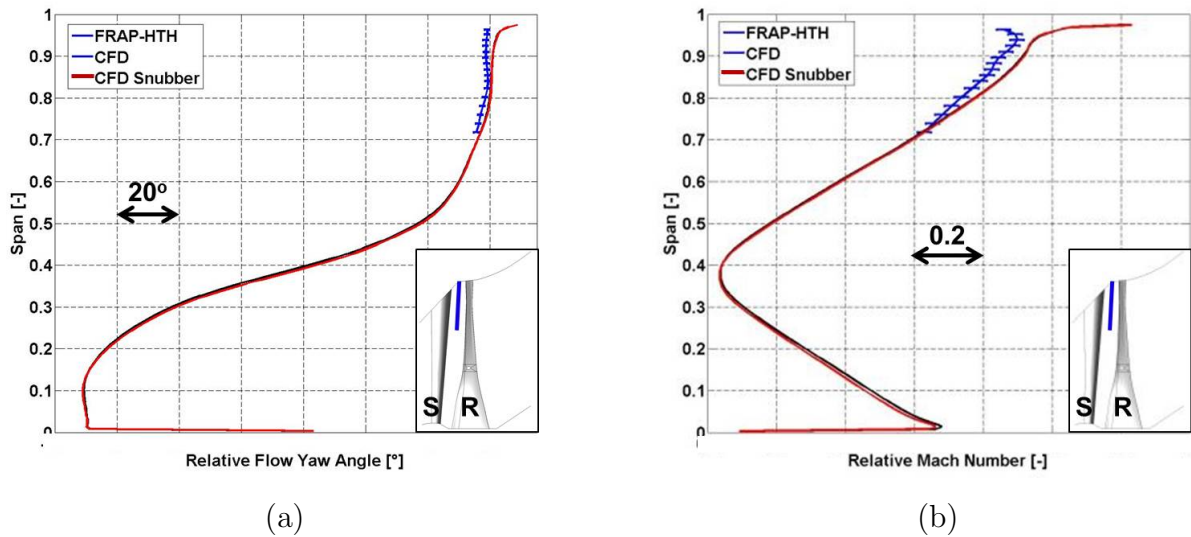


Figure 3.15: Circumferentially mass averaged and time-averaged relative yaw angle (a) and relative Mach (b) at FRAP-HTH plane located at $x/s=0.35$ between L-0 stator and rotor.

The snubber and without snubber comparison of relative flow yaw angle and Mach number in Figure 3.15 (a) and (b) demonstrate clearly that the flow field upstream of L-0 rotor is not affected by blockage introduced by snubber. The unchanged inlet relative conditions indicate a similar flow expansion through rotor without modeling of the snubber. Nevertheless, only a slight over-prediction of about 0.018 appear at about 10% of radial span for relative Mach.

Circumferentially mass averaged and time-averaged total-to-total η_{tt} and total-to-static η_{ts} stage efficiency is shown in Figure 3.16 (a) and (b) respectively. The overall η_{tt} and η_{ts} are reduced by 0.19% and 0.2% respectively. The radial profile of total-to-total efficiency shows a decrease from about 25%-35% and 40%-50%. The increase in efficiency from 35%-40% is a result of mass flow redistribution. The total-to-static efficiency is reduced from 25%-35%. The radial efficiency profiles indicate loss introduced by snubber

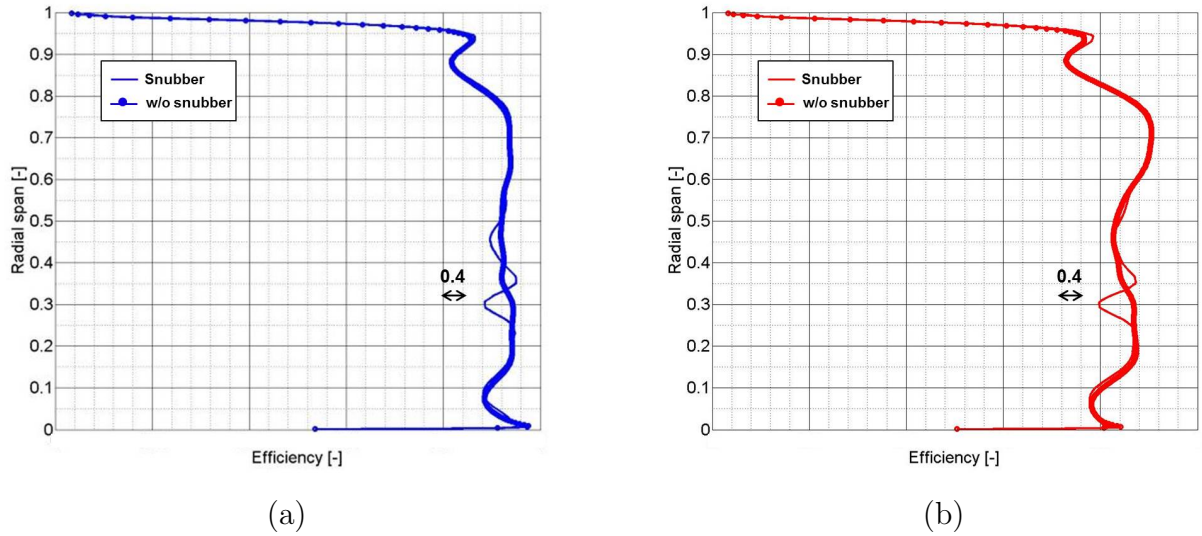


Figure 3.16: Circumferentially mass averaged and time-averaged total-to-total η_{tt} (a) and total-to-static η_{ts} efficiency (b) for L-0 stage. The overall η_{tt} and η_{ts} stage efficiency are reduced by 0.19% and 0.2% respectively with snubber.

wake is locally confined to 25%-50% of radial span even at the exit of the part-diffuser domain. A small increase of about 0.15% in total-to-static efficiency is observed at about 94% of the radial span is a result of a decrease in the adverse pressure gradient introduced by adjacent airfoil leading edge bow shock **S1** on pressure surface, for the snubber case. The decrease in adverse pressure gradient is shown by the reduced slope of the red curve (snubber) compared to black curve (without snubber) from 0.4-0.7 of the axial chord as shown in Figure 3.17 (c).

The static pressure coefficient at rotor wall surface is shown for 41%, 60% and 90% respectively in Figure 3.17 (a), (b) and (c) respectively. The difference in static pressure on pressure and suction side of the airfoil is proportional to airfoil lift or the work done by the fluid on the rotor. The static pressure loading decrease upstream of snubber from 0%-28% of axial chord length for 41% of radial span. The pressure side is about unchanged whereas suction side pressure increase as a result of flow deceleration introduced by snubber blockage. No lift is generated from 28%-55% of the axial chord in the location of the snubber, whereas static pressure loading is decreased by about 25% on the suction side at 66% of axial chord span. This pressure drop is a result of snubber wake interaction with suction side. The snubber introduces a penalty in work extraction as a result of flow blockage and wake interaction with airfoil suction side. The static pressure loading at 60% of rotor radial span is about unchanged from 0%-90%. A small decrease of about 4% of average pressure loading on the suction side at 90%-100% (counter loaded region)

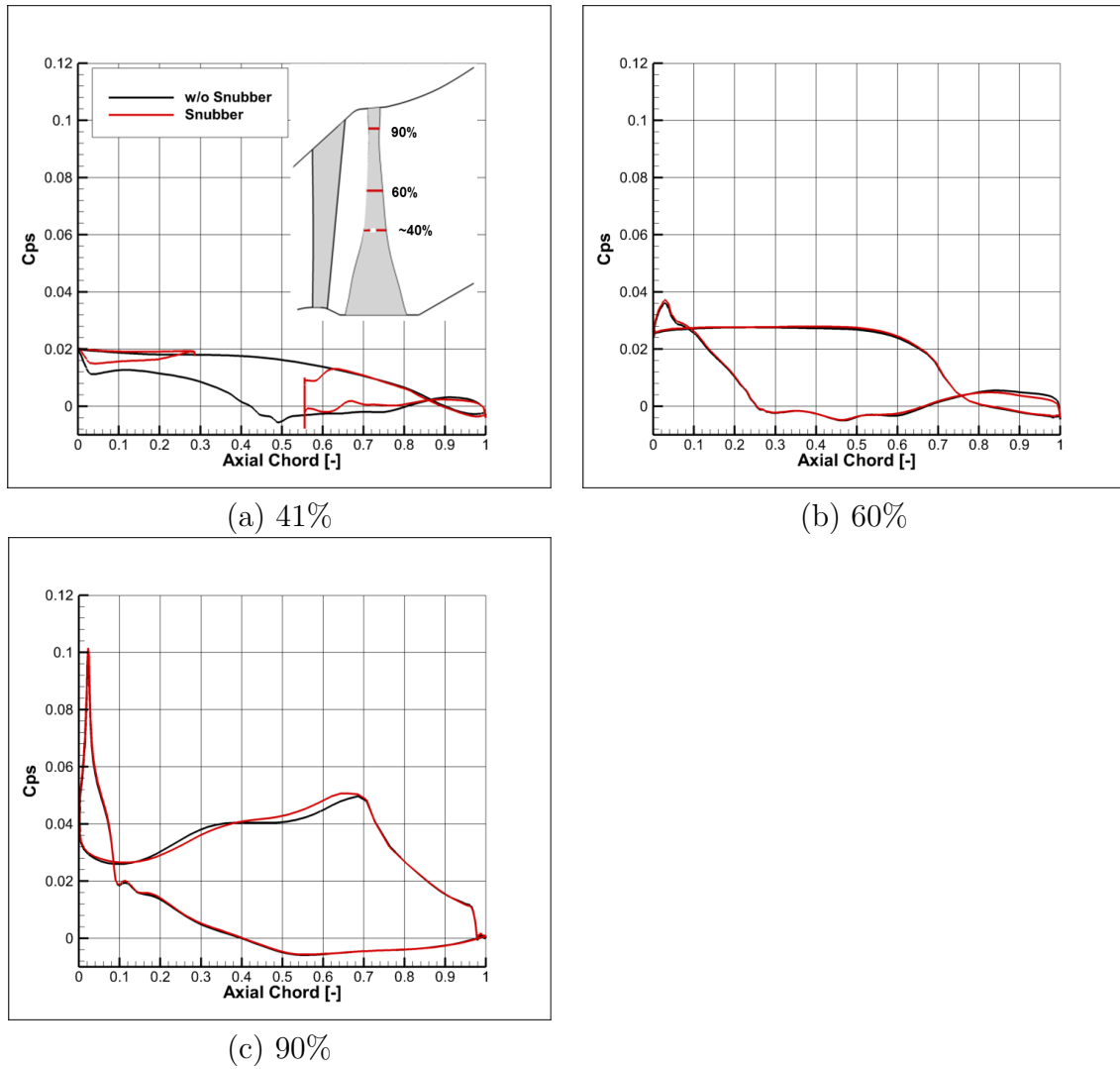


Figure 3.17: Time averaged static pressure distribution C_{ps} at rotor wall surface at 41% (a) 60% (b) and 90% (c) radial span-wise location.

of the axial chord is a result of flow pitching upward in the boundary layer influenced by stator wake at lower span-wise positions. The static pressure loading at 90% of the radial span as shown in Figure 3.17 (c) show un-changed smooth supersonic flow expansion on the suction side. The pressure side, however, shows an increase in static pressure loading of about 7% of local loading, at 60% of blade axial chord span. The snubber blockage decreases the adverse pressure gradient introduced by bow-shock **S1** from adjacent airfoil tip impinging on the pressure side. This introduces decrease in entropy production from the interaction of the shock with adjacent airfoil boundary layer and increases efficiency only slightly by 1.5% locally as shown by the radial profile of total-to-static efficiency at 94% of radial span in Figure 3.16 (b).

Summary and conclusions: A nominal efficiency loss of $\eta_{tt}=0.19\%$ and $\eta_{ts}=0.2\%$ is introduced and local to snubber location. The efficiency loss is introduced by snubber wake mixing downstream and modulation of suction side rotor boundary layer locally in the vicinity of the snubber. The design optimization process requires generating several cases in a short span of time and identification of major efficiency improvements. The quantified efficiency penalty in this study allows a basis to exclude snubber geometry in the following studies. However, designers must be cautious in the proposed optimized designs where an increase in radial velocities at snubber span is expected. The snubber geometry must be included in such cases as the efficiency penalty might be higher with a potential for flow separation, increase in wake mixing losses or potential intensification of secondary flows.

3.4 Influence of blade count modeling on flow aerodynamics

In this section, the analysis of computational cost versus accuracy as a result of blade count modification is established. Results from four stage half annular computations with real blade count are compared with the last two stages (L-1 and L-0) computational model. The four-stage half annular real blade count model consists of 337 airfoils with a total mesh size of 195.9 million mesh nodes running on 57 Tesla K20 GPUs. The last two stage 30° sector model consists of 21 airfoils with a total of 16.9 million mesh nodes running on 2 Pascal P100 GPUs. The tip cavities and snubber geometry are excluded. Both computational models are applied with boundary conditions from design operation experiments (radial profiles at inlet) and run with equilibrium steam model. The difference in run-time for two cases is as much as 13.5 days (6.74 estimated days on Pascal P100) for full four stage and less than a day (21 hours) for the sector last two stage case. The key differences are found to be with workload shift in the computational 30° model. The annular throat area is increased for L-1 stator row as blade count is decreased from 88 to 84. The annular throat area is reduced for L-0 stator as the blade count is increased from 58 to 60. The

rotor count for L-1 and L-0 stages is unchanged. The key difference between the two cases is blade count change and modeling of L-1 upstream stages (L-3 and L-2) in the case of full four-stage configuration.

In addition, for the half annular case, additional smoothing had to be applied for the stability of numerical computations. Several attempts have been made to recover the computation to standard smoothing coefficients, however, the transition of values leads to pressure drop outside the range of steam tables in the superheated steam in L-3 stage. The two-stage modified blade count 30° sector case, on the other hand, use a standard smoothing algorithm developed by Basol [27]. It must be noted that only half annular case discussed in this section required additional smoothing. All other cases discussed in this thesis are run with the standard algorithm. The efficiency values in this section, therefore, must be used with caution. However, relatively well agreement with experiments allows a basis to trust for qualitative analysis. The time-averaged and circumferentially mass averaged radial profiles for relative Mach, relative yaw angle and total pressure are compared at FRAP-HTH plane in the L-0 stage stator-rotor gap as shown in Figure 3.18. The relative flow yaw angles match relatively well in the tip span region with experimental values. The relative Mach match relatively well in the case of 30° sector. Clear reasoning of the half annular real blade count relative Mach deviation in the transonic tip region is not available. However, additional smoothing applied in the case of half annular computations might smooth the supersonic flow features such as **S1** shock front and increase inaccuracy in relative Mach prediction. Nevertheless, total pressure as shown in Figure 3.18 (c) show real blade half annular case in relative agreement with experimental data. The increase of about 9.6% on average, in absolute total pressure at L-0 stator inlet is observed for the modified blade count. This is a result of increased throat area of L-1 stator and decreases in L-0 changing the pressure ratio of both stages in the modified blade count computations. The decrease in L-1 stator blade count by four (from 88 to 84) increase annular throat area and reduce flow expansion in L-1 stage. This results in an increase in absolute total pressure at L-0 stator inlet as shown in Figure 3.18 (c).

Table 3.4: Time-averaged stage efficiency and specific work percentage increase for the last two stages (30° sector - modified blade count) with respect to four stages half annular real blade count.

[%]	L-1	L-0+Diffuser	L-1+L-0+Diffuser
$\Delta\eta_{tt}$	6.8	6.2	6.1
$\Delta\eta_{ts}$	6.5	5.8	5.6
$\Delta h_{o,modified} / \Delta h_{o,real}$	2.88	15.05	9.4

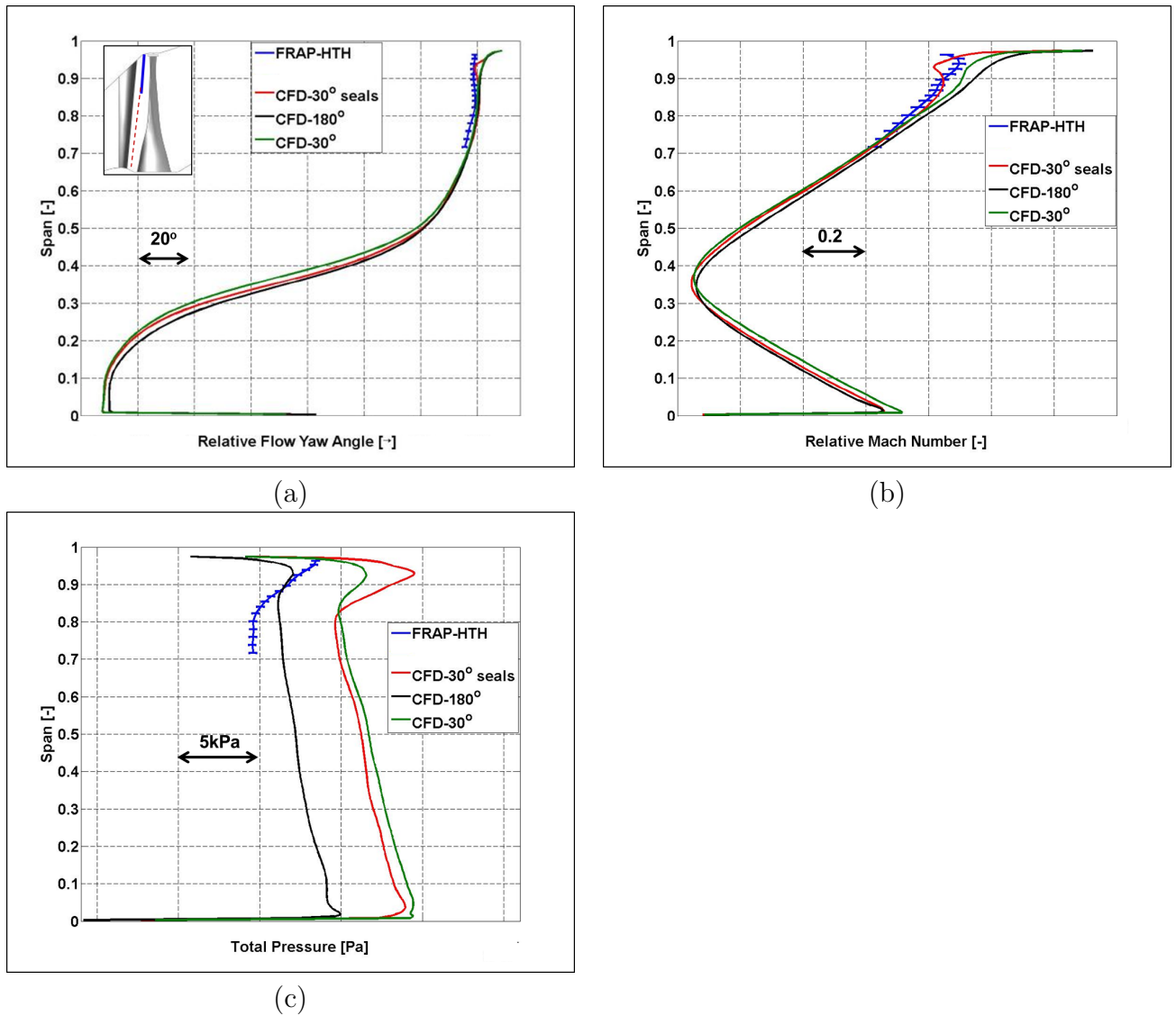


Figure 3.18: Circumferentially mass averaged and time-averaged relative flow yaw angle (a) relative Mach (b) and absolute total pressure P_t (c) at FRAP-HTH plane located at $x/s=0.35$ between L-0 stator and rotor.

Table 3.5: Time-averaged workload shift for stage L-1 and L-0 with respect to last two stages for 30° sector with modified blade count and four stages half annular real blade count.

[%]	Modified blade count	Real blade count	-
$\Delta h_{o,L-1} / \Delta h_{o,2stage}$	56.31	53.54	-
$\Delta h_{o,L-0+Diffuser} / \Delta h_{o,2stage}$	43.68	46.46	-
$\Delta h_{o,modified} / \Delta h_{o,real}$	-	-	109.4

3.5 Influence of the tip cavity and seals modeling on efficiency and losses

In this section computational cost versus accuracy for the tip cavity and seal leakage flow, modeling is discussed. Two separate cases are compared for the last two stages (L-1 and L-0 combined) with and without tip cavity and seals. The case of without cavities is discussed in the last section 3.4 is considered in this study and compared with an improved model including a tip cavity and seal. The mesh size drastically increases for seals case to about 57.6 million (15 GPUs) compared with 16.95 million (2 GPUs). The seal's case running on 15 GPUs converge in about 7 days of runtime (171 clock hours) compared with one day (21 wall clock hours) of runtime for without seals case. The impact of L-1 and L-0 leakage flow is substantial. About 5% of total mass flow accounts for the leakage flow in L-0 tip cavity. The L-1 leakage flow changes the secondary flow through L-0 stator tip region substantially. The L-1 leakage flow spread spanwise in tip region during flow expansion through the L-0 stator passage and part of this high enthalpy leakage flow is used for useful work in L-0 supersonic tip airfoils. Further, for optimization of L-0 stator stacking that may be able to control and reduce leakage flow through L-0 rotor tip cavity, this may result in additional useful work extraction.

Table 3.6: Time-averaged stage efficiency and specific work percentage increase for without seals case (with respect to tip cavity and seal geometry case).

[%]	L-1	L-0+Diffuser	L-1+L-0+Diffuser
$\Delta \eta_{tt}$	2.4	3.6	3.0
$\Delta \eta_{ts}$	3.9	4.6	3.6
$\Delta h_{o,no-seals} / \Delta h_{o,seals}$	3.6	5.0	4.4

The percentage increase (error) in time-averaged, circumferentially and radially mass-averaged stage efficiencies and work extraction for without cavities case is presented in Table 3.6. The computations without modeling cavities over-predict total-to-total η_{tt} and total-to-static η_{ts} by 3.0% and 3.6% respectively. The work extraction is over-predicted by 4.4%. Without seals case over-predict L-1 and L-0 stage specific work by 3.6% and 5.0% respectively with respect to seals case respective stages. This error is substantial and the over-prediction of efficiencies may mislead the designers during the design optimization process. Further, as shown in Figure 3.18, a comparison of seals and without seals cases with FRAP-HTH experiments reveals that L-1 and L-0 tip cavity and seals modeling is essential for accurate prediction of relative yaw and Mach number to L-0 rotor in the supersonic tip region. The modeling of tip-cavities and seals is essential even at the cost of additional runtime and computational resources.

3.6 Flow aerodynamics and loss mechanisms in the last two stages of a low-pressure steam turbine including tip cavities and seals

In this section, a computational setup for last two stage L-1 and L-0 combined with part diffuser is established. The purpose of this study is to understand key loss mechanisms and time-resolved aerodynamics to establish reasoning for further improvements in LP steam turbine design. The computational model is extensively validated with experiments before a detailed flow analysis is presented.

3.6.1 Computational setup and mesh

3.6.1.1 Geometry and mesh

A computational model for 30° including L-1 and L-0 tip cavity and seals is set up according to 1/3 scaled geometry of experiments (Figure 3.2), as shown in Figure 3.19. Geometry and mesh is generated using Auto Grid5 meshing tool by NUMECA.

The mesh of this computational model was created using the real geometry of the tip cavities and seals for L-1 and L-0 rotor. However, in order to achieve matching interfaces in the domain with acceptable mesh quality, the tip shroud had to be extended in both stages. Tip shroud geometry of L-1 rotor is extended by 11.3% and 19.3% of axial chord length at the leading and trailing edge, as shown in Figure 3.20 (a). Mesh in this region between tip-shroud and seals-casing is resolved with about 1.6 million mesh nodes for a single passage, as shown in Figure 3.20 (b). The matching interface between all blocks of cavity region and main flow, as well as between stator and rotor domain interfaces, has been successfully achieved in order to keep second-order accuracy in space.

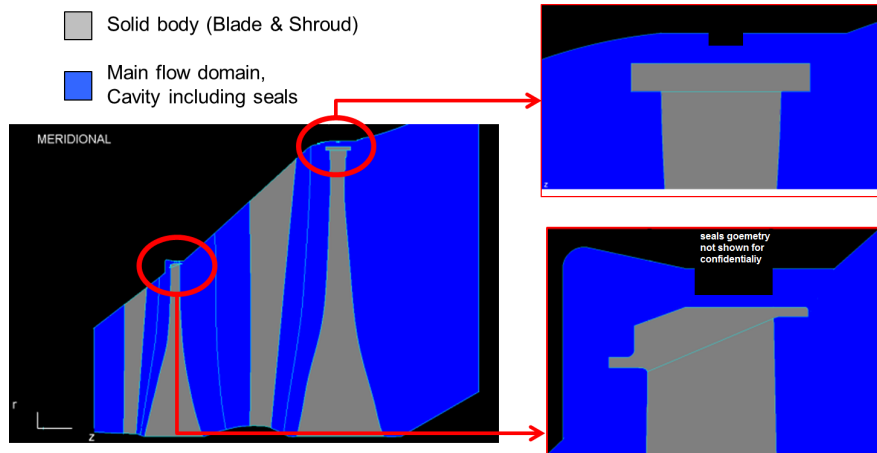


Figure 3.19: Schematic of L-1 and L-0 tip cavity and seals geometry in meridional view. Seals geometry not shown for confidentiality.

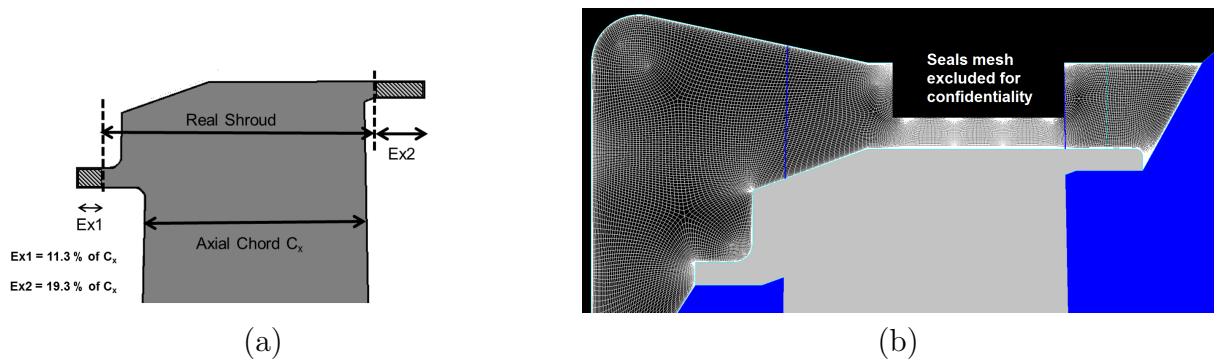


Figure 3.20: (a) Shroud of L-1 rotor had to be extended, both at leading edge and trailing edge to achieve matching interface with the main flow domain. (b) Mesh region between seals and shroud of L-1 rotor is resolved with about 1.6 million mesh nodes. Seals mesh not shown for confidentiality.

Similarly, for L-0 stage rotor, tip shroud geometry of L-0 rotor is extended by 22.6% and 22.3% of axial chord length at the leading and trailing, as shown in Figure 3.21 (a). Mesh in this region between tip-shroud and seals-casing is resolved with about 1.8 million mesh nodes for a single passage as shown in Figure 3.21 (b). Mesh is resolved using 56 mesh nodes in the radial span of the tip-cavity region.

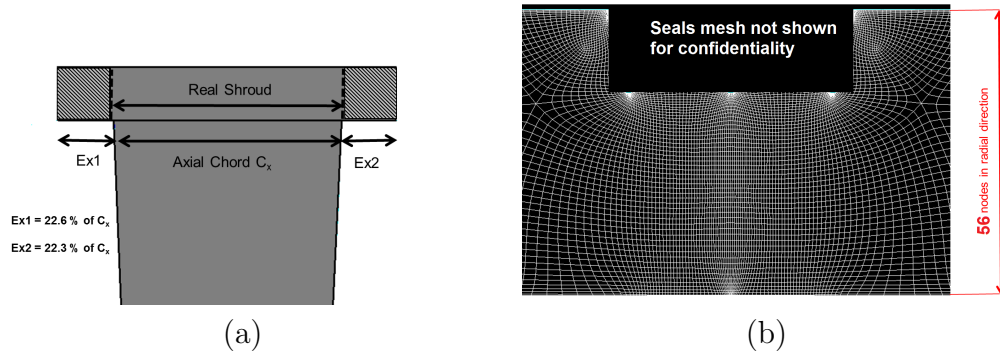


Figure 3.21: (a) Shroud of L-0 rotor had to be extended, both at the leading edge and trailing edge to achieve a matching interface with the main flow domain. (b) Mesh region between seals and shroud of L-0 rotor is resolved with about 1.7 million mesh nodes.

Simulation setup of 30° computational model is set up on 17 GPU's running in parallel. The computational domain is split into rows, and each row is split into circumferential sub-domains to fit onboard GPU memory of 6 gigabytes (for NVIDIA K20X on Piz DAINT).

A total of about 56.7 million nodes were used for the computational domain, of which more than 20 million were used in the region of L-1 and L-0 cavities to resolve the complex geometry and the unsteady flow phenomena.

Table 3.7: Mesh quality report.

Minimum angle	Maximum Aspect Ratio	Maximum Expansion Ratio
4.6	1752	5.21

The quality of the mesh is presented in Table 3.7. Despite the presence of some skewed cells, especially in the region of the tip cavity and seals of L-1 stage, the overall quality is considered well within acceptable range.

A 30° model is created with a change of the original blade count. For L-1 stage blade

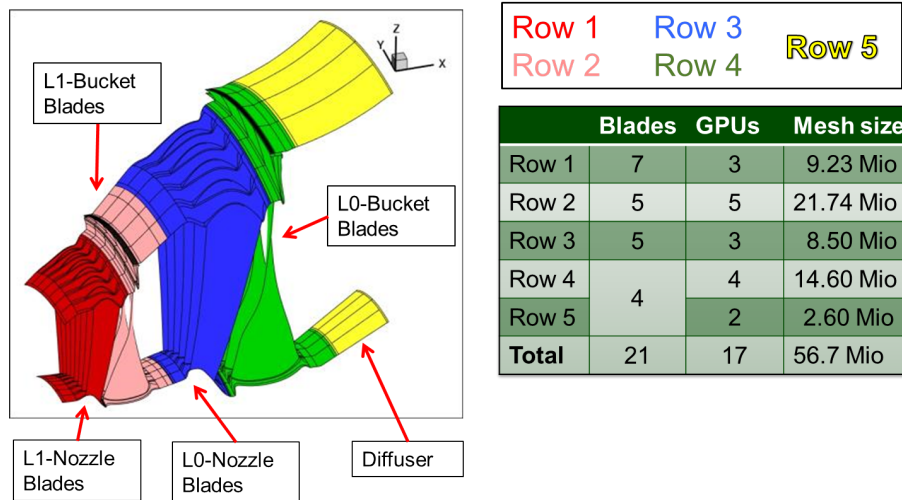


Figure 3.22: L-0, L-1 domain is split into 5 rows shown on left, with mesh size and number GPU's used for each row shown on the right.

count is modified from 88-60 to 84-60 stator-rotor blades. Similarly, for L-0 stage, the blade count had to be modified from 58-48 to 60-48 stator-rotor blades. Eventually, the 30° model of L-1 and L-0 stage including tip cavities and seals was created, to achieve fully matching interfaces between each row.

3.6.1.2 Boundary conditions

Simulation is setup with experimental boundary conditions measured using the five-hole probe for the design operating condition as shown in Table 3.1. Radial profiles of total pressure, total temperature, yaw, and pitch angles are applied at the inlet of the mesh as CFD inlet boundary conditions. For the outlet boundary conditions, measured static pressure is imposed in the hub of the diffuser with radial equilibrium exit boundary conditions. Rotor rotational speed is set as 10800 [rpm]. Radially constant values for turbulence intensity and turbulent length scale are imposed in the inlet of the domain for the $k-\omega$ turbulence model. The values of turbulence intensity and turbulent length scale are set as 5.11% and 2.23×10^{-4} respectively. The values were obtained from the flow field of 4-stage half-annular simulation discussed in section 3.4.

3.6.1.3 Solver setup, runtime and convergence

The solver is setup for unsteady simulation with 120-time steps for a 30° rotation of rotor blade. Wilcox $k-\omega$ with Kato-Launders source term modification is used for turbulence modeling. The simulation is performed with equilibrium-steam modeling in order to predict steam wetness. Due to the extra computational cost of wet-steam compared to dry-steam

simulations, dry-steam conditions are used from initial guess until the flow field is relatively developed and then wet-steam is initialized and used until the simulation reaches convergence. The simulation has completed more than 3 full annular rotor revolutions – 1140 degrees of rotation – since wet-steam was initialized. Convergence history according to mass flow for the whole simulation and for the last period is presented in Figures 3.23 (a) and (b) respectively.

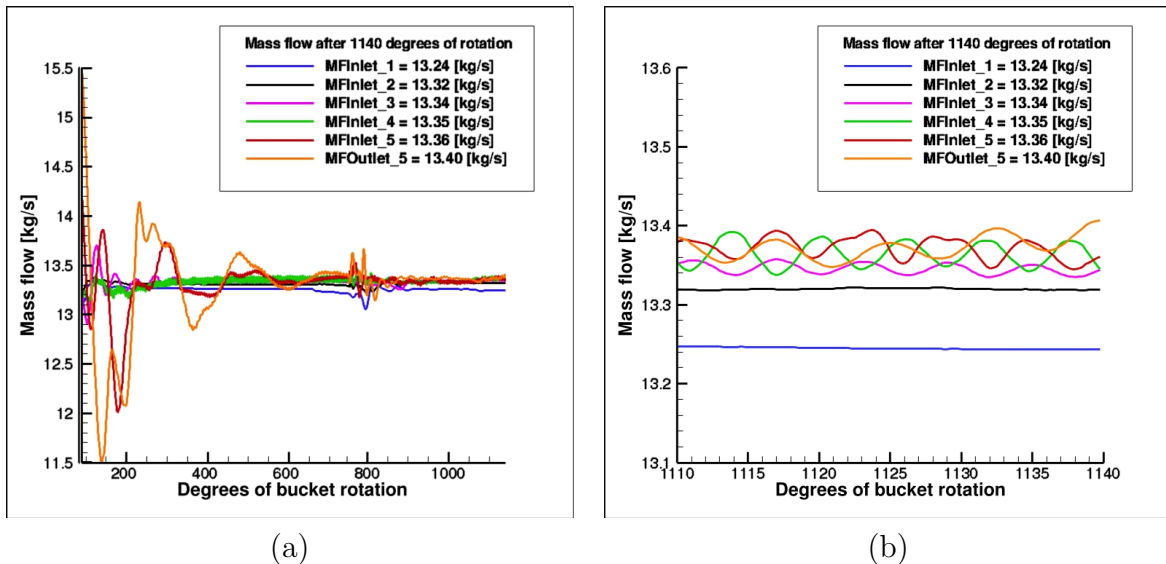


Figure 3.23: (a) Mass flow at the inlet of each row and outlet of the machine for 1140 degrees of rotor revolution. (b) Mass flow at the inlet of each row and outlet of the machine for the last 30 degrees of rotor revolution.

As observed in Figure 3.23 (a), the simulation starts with high mass flow oscillations, which seem to decrease during the last periods of the simulation. In Figure 3.24, it is shown that the difference between inlet and outlet mass flow of each row is kept in low levels between 0.2 – 0.6%. The real mass flow under design operating conditions from experiments is $47.5 \text{ [t/h]} = 13.194 \text{ [kg/s]}$. The mass flow predicted by CFD in the inlet of the L-1 stage is 13.24 [kg/s] and is 0.3% higher compared to experiments. Additionally, mass flow imbalance between the inlet and outlet of the machine is predicted to have a difference in the range of 0.7 – 0.9%.

The simulation is considered to have reached convergence after having completed more than 3 full rotor revolutions, or 1140 degrees of rotation. Computational run-time for 90 degrees rotation required on average 20.8 clock hours, or $17 \cdot 20.8 = 353.6$ node hours. In total, 266 clock hours, or 11 days, were required for the completion of this simulation on Piz DAINTE (CRAY XC30, Nvidia Tesla K20x GPUs). The equivalent node-hours on Piz-DAINT supercomputing cluster were 4522 hours.

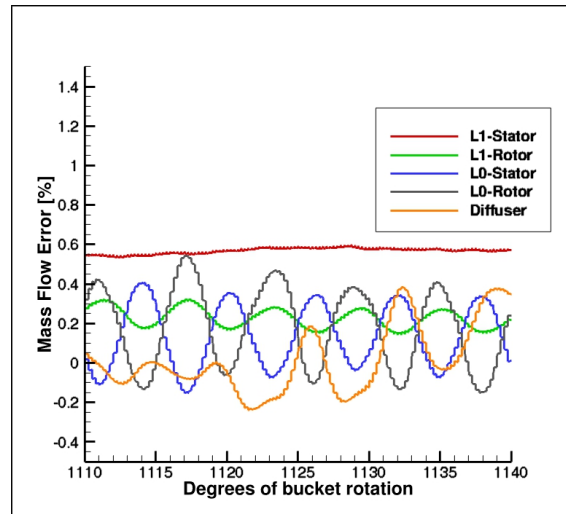


Figure 3.24: Mass flow error in [%] between inlet and outlet of each row.

3.6.1.4 Validation of numerical model

The validity of the numerical model has been extensively evaluated with available experimental measurements conducted in the test facility. More specifically, predictions of the CFD model have been compared with 5HP measurements conducted by MHPS at the outlet of L-1 and L-0 stages. More importantly, numerical results were additionally compared with time-resolved and time-averaged measurements at the stator exit of the last stage of MHPS's LP steam turbine that was conducted (Bosdas et al. [25]). Measurements were conducted in MHPS's test facility in Japan using a novel fast response heated probe (FRAP-HTH) and were the first time that time-resolved measurements in a wet steam environment with the supersonic relative flow at the rotor inlet had ever been reported. Details on FRAP measurement method and uncertainty are available in the original publication (Bosdas et al., [25]). The locations of the experimental measurements that were used for comparison with the current numerical study are presented in Figure 3.25.

Comparison of CFD with 5-hole probe at L-1 rotor exit: Figures 3.26 (a) and (b) show comparison of CFD with 5HP experimental data for absolute yaw angle, as well as total temperature across the blade span at L-1 rotor exit, respectively. CFD results are circumferentially averaged over five rotor pitches and time-averaged over five rotor blade passing periods of L-1 rotor blades with 156 nodes in the spanwise direction, while 5HP measurements were performed along a single radial traverse and averaged over 10 sample data measured at intervals of a second with 20 points in a spanwise direction. For confidentiality reasons, only grid resolution is shown for absolute yaw angle, while total temperature has been normalized by dividing both numerical and experimental data with the mean of experimental values.

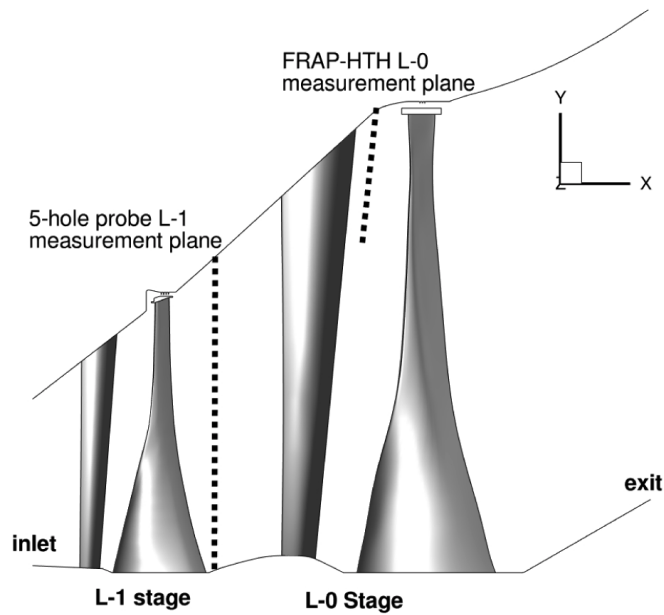


Figure 3.25: Schematic of last two stages of MHPS low pressure steam turbine with probe measurement locations marked with dotted lines.

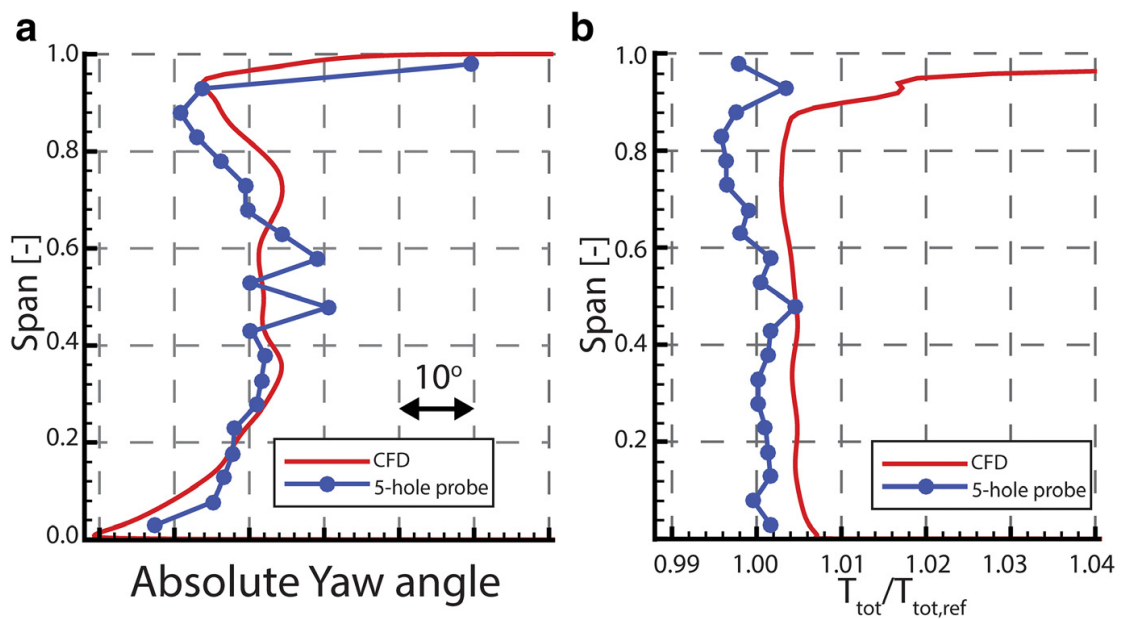


Figure 3.26: Comparison of CFD and 5HP for absolute yaw angle (a) and total temperature (b) at rotor exit of L-1 stage (Papagiannis et al. [1]).

As shown, a good agreement has been achieved between numerical results and experimental data, both in trends and absolute values across the span. The root means square (RMS) deviation between them is 3.8° but the value is increased due to the very high gradient close to the tip. The mismatch in yaw angle between 40% and 60% of the span is due to the presence of the PSC (Part Span Connector), which causes an overturning of the flow at 58% and 48% span. PSCs are not included in the numerical model. Total temperature is well predicted by CFD, with RMS difference from experiments equal to 1.15%. The effect of PSC is also visible on the total temperature that causes a slight increase in the exact same span locations.

Comparison of CFD with time-averaged FRAP-HTH probe at L-0 stator exit: In this section, CFD predictions are compared with time-averaged results of FRAP-HTH measurements at the outlet of L-0 stator. This area is of particular interest because the flow becomes supersonic in the relative frame of reference in the inlet of the last rotor, generating a shock wave upstream of the rotor leading edge (Senoo et al. [23]). Figures 3.27 (a) and (b) show comparison of CFD with FRAP-HTH for delta flow yaw angle and relative Mach number, respectively.

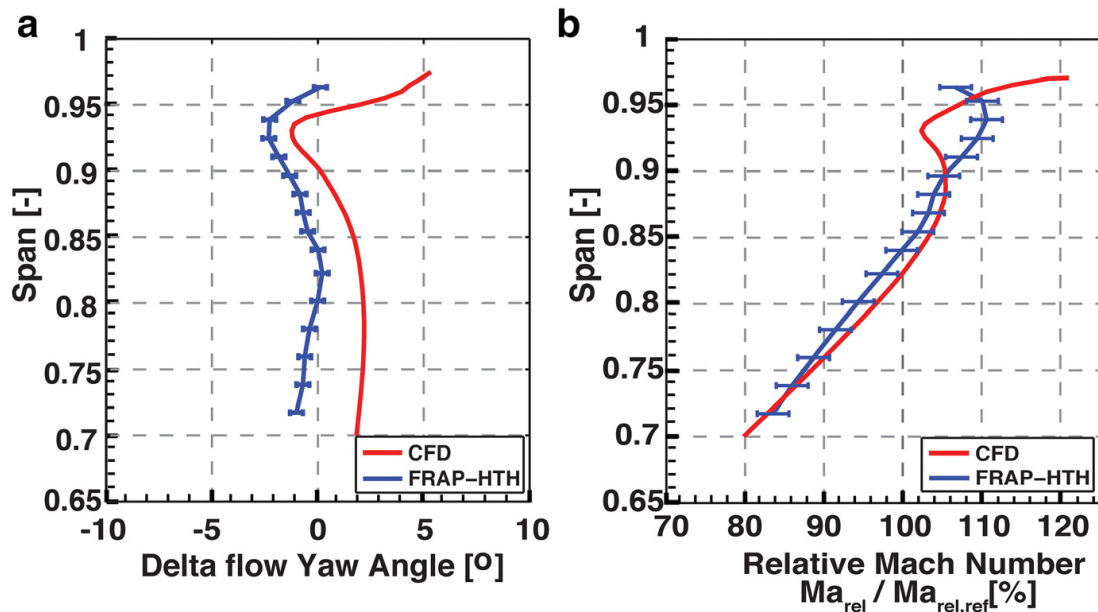


Figure 3.27: Comparison of CFD and time-averaged FRAP-HTH for delta flow yaw angle from the mean blade metal angle (a) and relative Mach number (b) at L-0 stator exit (Papagiannis et al. [1]).

In Figure 3.27 (a) the absolute yaw angle is subtracted from the mean blade metal angle, representing essentially the deviation flow angle at the stator blade exit. Positive

values indicate overturning of the flow, while negative values imply flow under-turning. In Figure 3.27 (b), relative Mach number has been normalized by dividing both numerical and experimental data with the mean of experimental values. CFD results in Figure 3.27 are circumferentially averaged over five L-0 stator pitches and time-averaged over four rotor blade passing periods of L-0 rotor blades with 57 nodes in span-wise direction, while FRAP-HTH measurements are time-averaged and circumferentially area averaged over one L-0 stator pitch with 16 points in a span-wise direction. The comparison shows that yaw angle is slightly overpredicted by 2.4° on average compared to measurements but the trend is captured accurately. The reason of the mismatch could rely on the fact that the computational model has a slightly modified blade count compared to the real, which was done in order to allow the simulation of only a sector of the full annulus. The offset could also be due to probe alignment error during installation.

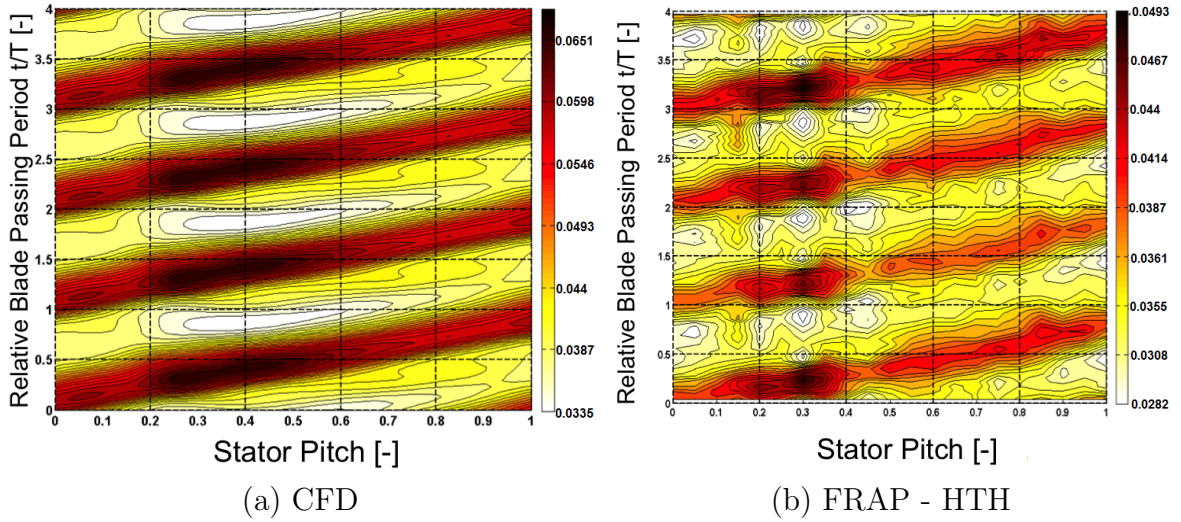


Figure 3.28: Unsteady static pressure coefficient C_{ps} [-] at the outlet at L-0 stator outlet (92% span).

Figure 3.29 shows the comparison of the Absolute Yaw angle relative to the stator exit metal angle in the time-space plots. Comparison of CFD and FRAP-HTH shows that trends are captured relatively accurately but with a small mismatch in the absolute values. The plots have the same contour range, which explains why CFD is slightly darker/lighter in certain regions. The mismatch of maximum values is about $\pm 2^\circ$.

The unsteady static pressure shows the bow shock interaction with the stator of the L-0 stage. Comparison in Figure 3.28 shows that a very satisfactory agreement in terms of capturing the underlying trends of static pressure. However, the intensity of the bow shock is overpredicted compared to FRAP-HTH measurements with a mean value of about.

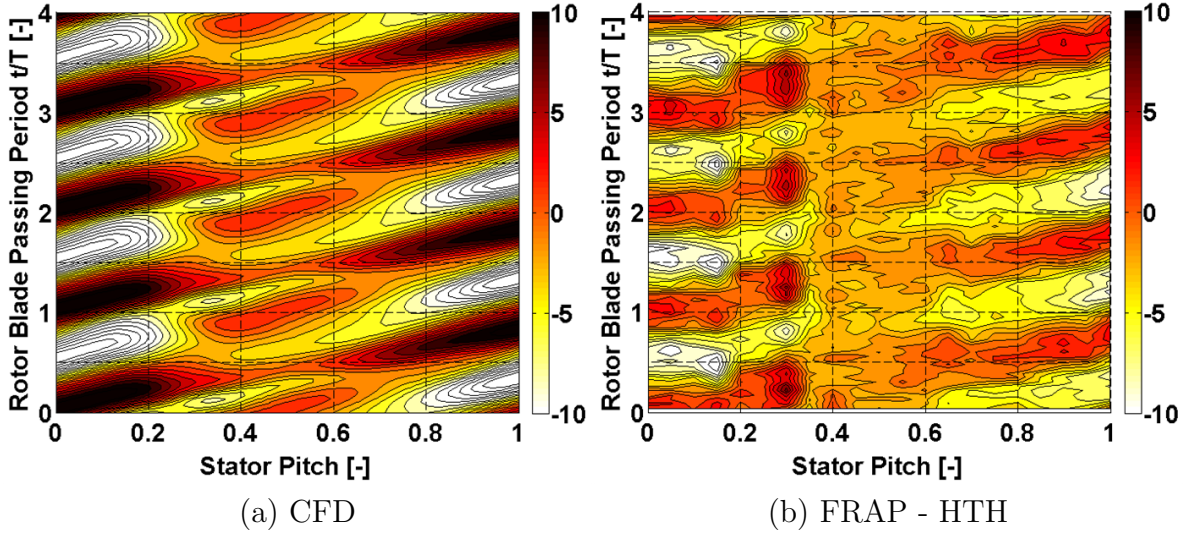


Figure 3.29: Absolute Yaw angle relative to blade metal angle [o] at L-0 stator outlet (92% span).

The mismatch increase of static pressure is related to change in blade count. Half annular multistage real blade count computations predict static pressure with accuracy.

3.6.2 Spanwise entropy loss budget

In this section a spanwise entropy loss for L-0 stator, rotor and diffuser are presented for identification of regions with high entropy loss. In the subsequent sections, an understanding of loss mechanisms in each region is established by looking at time-resolved and averaged flow field. For this purpose, two key parameters are used. First entropy loss coefficient $q[-]$ as defined in equation 3.4 and streamwise vorticity ω_s in equation 3.6. Streamwise vorticity is calculated as scalar product of the vorticity Ω whose components are given in equation (3.7, 3.8, 3.9) and the primary flow vector C_s . The streamwise vorticity is related to secondary flows introduced by flow perpendicular to the direction of the flow. A reduction of streamwise vorticity means a reduction of secondary flows and potential mixing losses or reduction of entropy due to the dissipation of the velocity gradients in shear layers. As presented in the analysis the supersonic flow features such as trailing edge shock or normal shock at leading edge also introduce secondary flows driven by pressure or density gradients. The unsteadiness of the flow is further quantified throughout this work with the definition given in equation 3.5.

$$q = e^{-\left(\frac{S_{in} - S_{out}}{R}\right)} \quad (3.4)$$

$$\frac{rms(\widetilde{Fq}_{max} - \widetilde{Fq}_{min})}{mean(\overline{Fq})} * 100[\%] \quad (3.5)$$

$$\Omega_s = \Omega.C_s \quad (3.6)$$

$$\Omega_x = \frac{1}{r} \left(\frac{\partial r C_\theta}{\partial r} - \frac{\partial C_r}{\partial \theta} \right) \quad (3.7)$$

$$\Omega_x = \frac{1}{r} \left(\frac{\partial C_x}{\partial \theta} - \frac{\partial C_\theta}{\partial x} \right) \quad (3.8)$$

$$\Omega_x = \left(\frac{\partial C_r}{\partial x} - \frac{\partial C_x}{\partial r} \right) \quad (3.9)$$

Figure 3.30 show entropy loss profiles calculated across stator, rotor and diffuser. The stator entropy loss in Figure 3.30 (a) show pronounced entropy generation in the tip region from 80% to 95% of tip span. The entropy loss decrease near casing is associated with mass flow redistribution of L-1 leakage flow at L-0 stator inlet to lower spanwise positions. The second high entropy generation region is near hub end wall from 0%-5% and third from 5%-25% or radial span. These two regions have associated endwall loss and oblique shock wave loss as well as hub passage vortex. The flow in the stator is supersonic in the hub to about mid-span region and the passage employ a convergent-divergent stator design. The flow from mid-span to tip span is near transonic to subsonic and employ convergent passage stator design to expand the flow optimally. The tip region from 85% to 100% of the span is supersonic at rotor tip leading edge and introduce a bow-shock. This bow-shock interact with stator tip trailing edge and suction surface and introduce flow unsteadiness in the presence of adverse pressure gradients introduced by bow-shock. The high entropy loss at rotor tip is associated with tip passage and endwall flows at flared L-0 stator casing as well as boundary layer modulation and unsteadiness introduced by bow shock in the stator-rotor axial gap.

The rotor entropy loss in Figure 3.30 (b) show high entropy losses in the hub region from 0%-20% of radial span. The high entropy levels are associated with rotor hub end-wall flows and suction side separation bubble as a result of low root reaction. The hub region flows are designed as an impulse turbine, with rotor airfoil only turning the flow. The low root reaction problem is well known in steam turbines and appear as a result increase in annulus area and the introduction of very long last stage rotor blades. The high static pressure gradients in stator-rotor gap are unavoidable and can only be managed by controlling hub reaction by different stacking or hub profiling designs. Nevertheless, the

entropy loss from 20% to about 80% consistently increases in transonic rotor airfoils and are related to mainly blade profile losses. The loss from 80% to 95% of span appears lower as a result of mass flow redistribution. Nevertheless, as shown in section 2.2 of equilibrium steam versus dry steam, the absolute entropy contours levels are higher in the tip region indicating a high cumulative loss in the tip region. This section employs a supersonic airfoil design (throat at the rotor passage inlet and divergent profile to expand supersonic flow smoothly). The last stage employs high reaction design in the tip region as the work is extracted with the expansion of flow through supersonic tip airfoils. These supersonic airfoils are carefully designed for a unique incidence (Mach relative and incidence to the rotor) in order to expand the flow optimally. The flow impinges on the pressure side of the airfoil, pass through the throat and expands on the suction side of supersonic airfoils. The loss generation mechanism is driven by flow expansion, blade profile losses and trailing edge shock interaction with expanding flow and wake of an adjacent airfoil. From about 95% to 100% a substantial increase in entropy loss can be seen by two peaks. The first peak at about 97% of the span is the loss introduced by tip shroud end walls (attachment to rotor airfoil tip as well cavity lower-end wall) and wake downstream of the shroud. This feature is labeled in this work as **TS**. The second higher peak at the casing (labeled as **CS**) is introduced by L-0 tip cavity tip-endwall flow and flow separation at diffuser inlet introduced by an increase in casing flare. In between these two peaks, a region of lower entropy represents leakage flow. The leakage flow has high entropy levels compared to passage flow.

The diffuser entropy loss is shown in Figure 3.30 (c). The entropy rise from 60% up to tip span are mixing losses from features such as tip shroud **TS**, cavity endwall and diffuser inlet flare separation **CS** and blade profile and trailing edge shocks as the flow pass through the diffuser. The purpose of the diffuser is pressure recovery from near vacuum conditions especially at the exit of supersonic tip airfoils. Reduced strength of loss features at the exit of the rotor may improve pressure recovery in the diffuser and decrease mixing losses. In conclusion, supersonic tip region is subject to high entropy production and aerodynamic losses, as shown by radial profiles of L-0 stage.

3.6.3 Time-resolved aerodynamics and loss at L-0 stator exit

3.6.3.1 Bow shock interaction in the transonic tip region

In this section, the transonic tip region flow is analyzed in order to develop an understanding of key loss generation mechanism in the presence of leading-edge bow shock **S1**. The instantaneous entropy loss q and streamwise vorticity for two stator pitch from 70% to 100% of radial span are presented in Figure 3.31. The axial plane is located at $x/s=0.39$ between L-0 stator and rotor. x/s represents a fraction of the axial tip gap where x represent distance downstream of stator trailing edge and s represents the distance from trailing edge of the stator to leading edge of the rotor. As clearly seen the high loss is

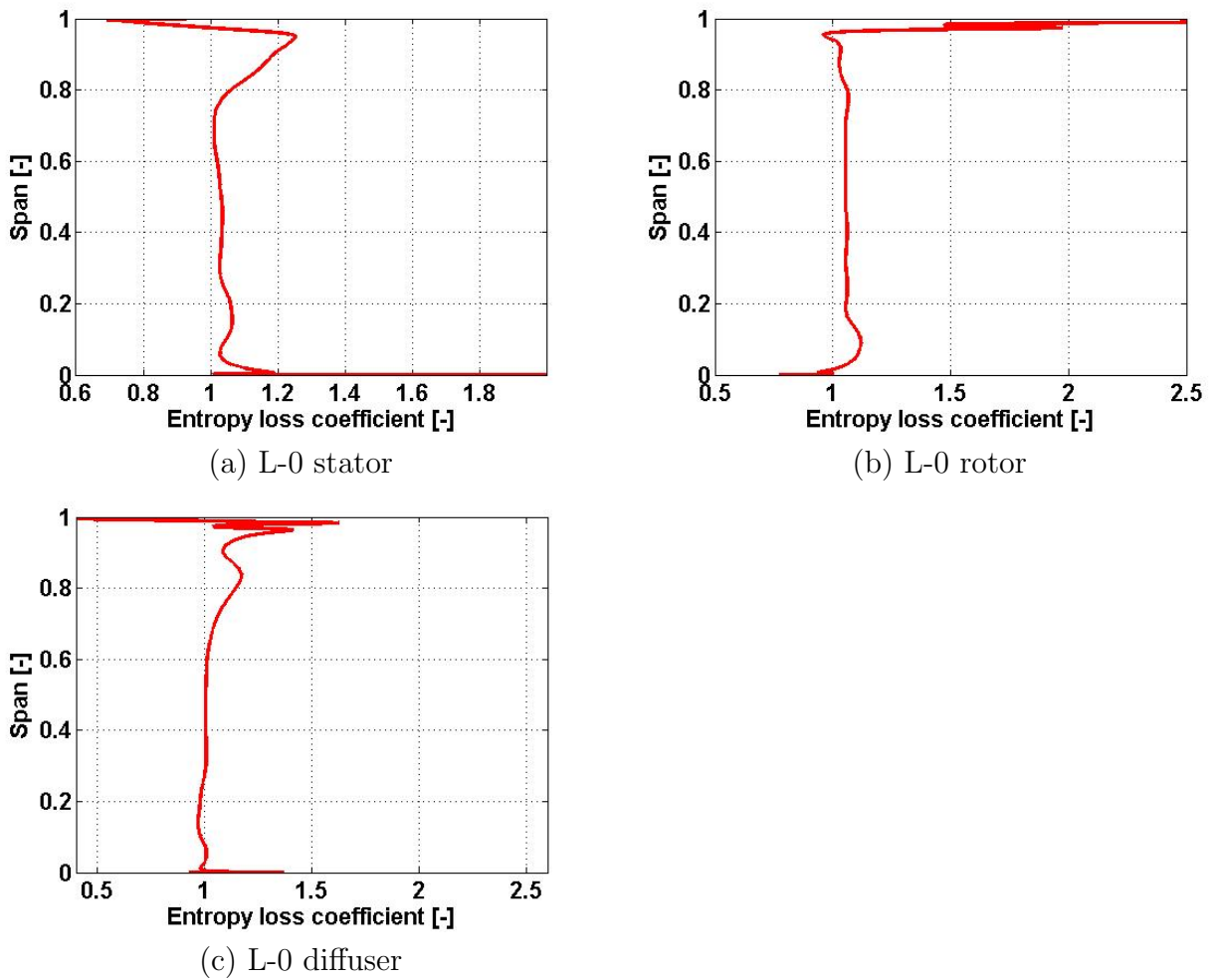


Figure 3.30: Radial profiles of the entropy loss coefficient for stator (a), rotor (b) and diffuser (c) for L-0 stage including tip cavities and seals.

concentrated from 85% to 100% of the span with transonic bow shock. The observer is looking towards rotor leading edge in the direction of flow and rotor rotates from left to right in these figures. Two bow shock fronts are shown with white dotted lines. The pronounced streamwise vorticity gradients are concentrated from about 95% to 100% of tip span. These high streamwise vorticity gradients are introduced on stator suction side and downstream trailing edge wake region introduced by bow shock adverse pressure gradients. Nevertheless, only trends of high streamwise vorticity and entropy loss can be seen in these plots and no individual secondary loss features such as tip passage vortex are identified, as bow shock disturb the flow even within this short distance downstream of L-0 stator.

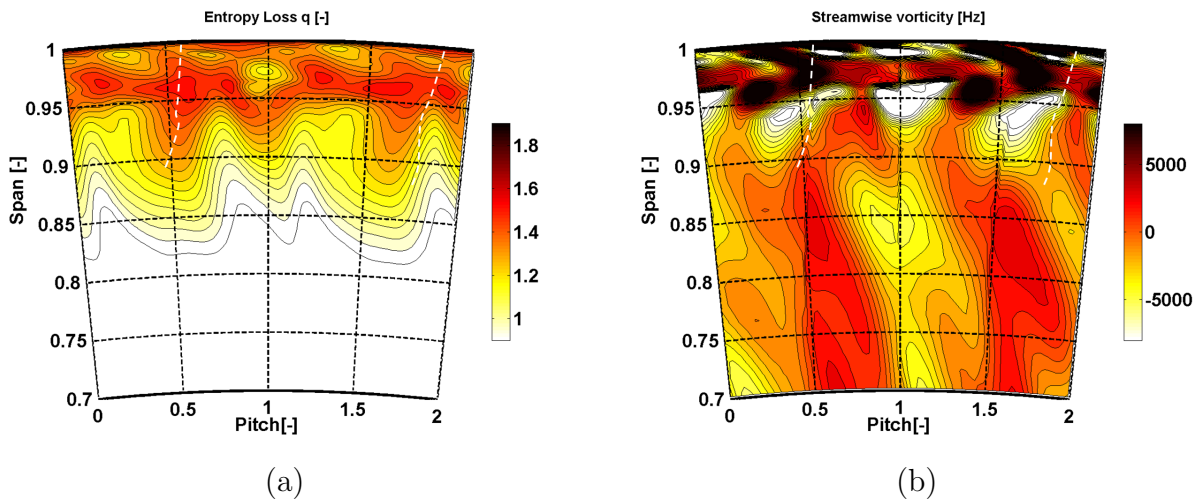


Figure 3.31: Instantaneous contours for (a) Entropy loss $q[-]$ and (b) streamwise vorticity for two stator pitch at the exit of L-0 stator from 70% to 100% of radial span. The white dotted lines are rotor leading edge bow shock front. High entropy loss is seen in the vicinity of 95% of the radial span with pronounced streamwise vorticity gradients.

For a better understanding, time-space plots at 90% of radial span for one stator pitch are presented in Figure 3.32. The entropy loss, streamwise vorticity, and total pressure coefficient are shown in Figure 3.32 (a),(b) and (c) respectively. The rotor rotation is left to right and observer is looking in the direction of the rotor. The rotor features appear as inclined lines whereas stator features are straight. This can be seen in C_{pt} contours where the near trailing edge of stator wake is identified by widening of low C_{pt} region at 0.2 pitch. The bow shock S1 is marked with the dotted thick white line where C_{pt} rise with a steep gradient. The region of high C_{pt} marked with a white thick arrow is introduced downstream of S1 by an increase in static pressure. Downstream of this high C_{pt} region the pressure drop as the shock move further to the right. These pressure gradients are the main source of unsteadiness in the tip region. Nevertheless, the shock in itself does not show a correlation directly with loss features shown in Figure 3.32 (a). There are two high

entropy loss regions labeled as 1 and 2 in Figure 3.32 (a). Feature 1 is introduced loss from suction side boundary layer of L-0 stator. Feature 2 is the loss introduced by suction side of the adjacent stator. The high loss q feature 1 is positioned in the low C_{pt} region. At feature 1 position, indicated by the solid black line, streamwise vorticity gradients from positive to -ve streamwise vorticity are observed. The source of this positive streamwise vorticity is stator suction side. As the bow shock move from the pressure side through the passage and impinges on the suction side, the high C_{ps} at tip span and low C_{ps} towards lower span, introduce a -ve radial velocity at suction side boundary layer. There is also positive tangential vorticity present as a result of high blade turning of 78° . The introduced radial velocity gradients increase the strength of this +ve tangential vorticity and modulate boundary layer to increase the loss. The -ve streamwise vorticity is introduced as a result of flow deceleration in the wake as the bow shock move further through passage after leaving the trailing edge by creating adverse pressure gradient axially. The two regions of high positive vorticity from suction side and -ve vorticity shed at trailing edge side by side as shown in Figure 3.33 (c). The steep gradients introduce additional entropy losses as the features move axially in the stator-rotor axial gap.

In conclusion feature 1 is a combination of loss from suction side boundary layer and downstream mixing losses in the wake. The blade to blade contours are also shown in Figure 3.33. From instantaneous plots, the location of high entropy generated on suction side boundary layer can be seen in figure (b). The positive and -ve streamwise vorticity shedding from trailing edge of L-0 rotor can be seen in Figure (c).

3.6.3.2 Hub passage flow (supersonic in stator frame of reference)

Instantaneous entropy loss and streamwise vorticity at exit of L-0 stator hub is shown in Figure 3.34 (a) and (b) respectively. The pronounced positive streamwise vorticity from 5% to 30% of hub span is trailing shed vorticity from stator blades. Stator hub passage vortex is visible at about 1% of span at 0.5 and 1.7 of stator pitch as negative streamwise vorticity. The positive streamwise vorticity from 0% to 5% is hub trailing shed vortex. Nevertheless, entropy loss contours clearly show the losses in the hub region are dominated by blade profile losses for supersonic flow expansion in stator hub. The loss in the hub region is substantially lower compared to supersonic tip region at L-0 stator exit where unsteadiness is pronounced and rotor leading edge bow shock modulate stator suction side boundary layer.

The time-resolved entropy loss and streamwise vorticity at 2% of radial span is shown in Figure 3.35 (a) and (b) respectively. The region of 0.0-0.4 stator pitch with pronounced positive streamwise vorticity is hub trailing shed vortex, and the entropy loss is consistently high in this location. The region of 0.4-0.9 of stator pitch shows lower levels of entropy loss in the presence of hub passage vortex. Nevertheless, the impact of rotor upstream bow wave is less pronounced in the hub region.

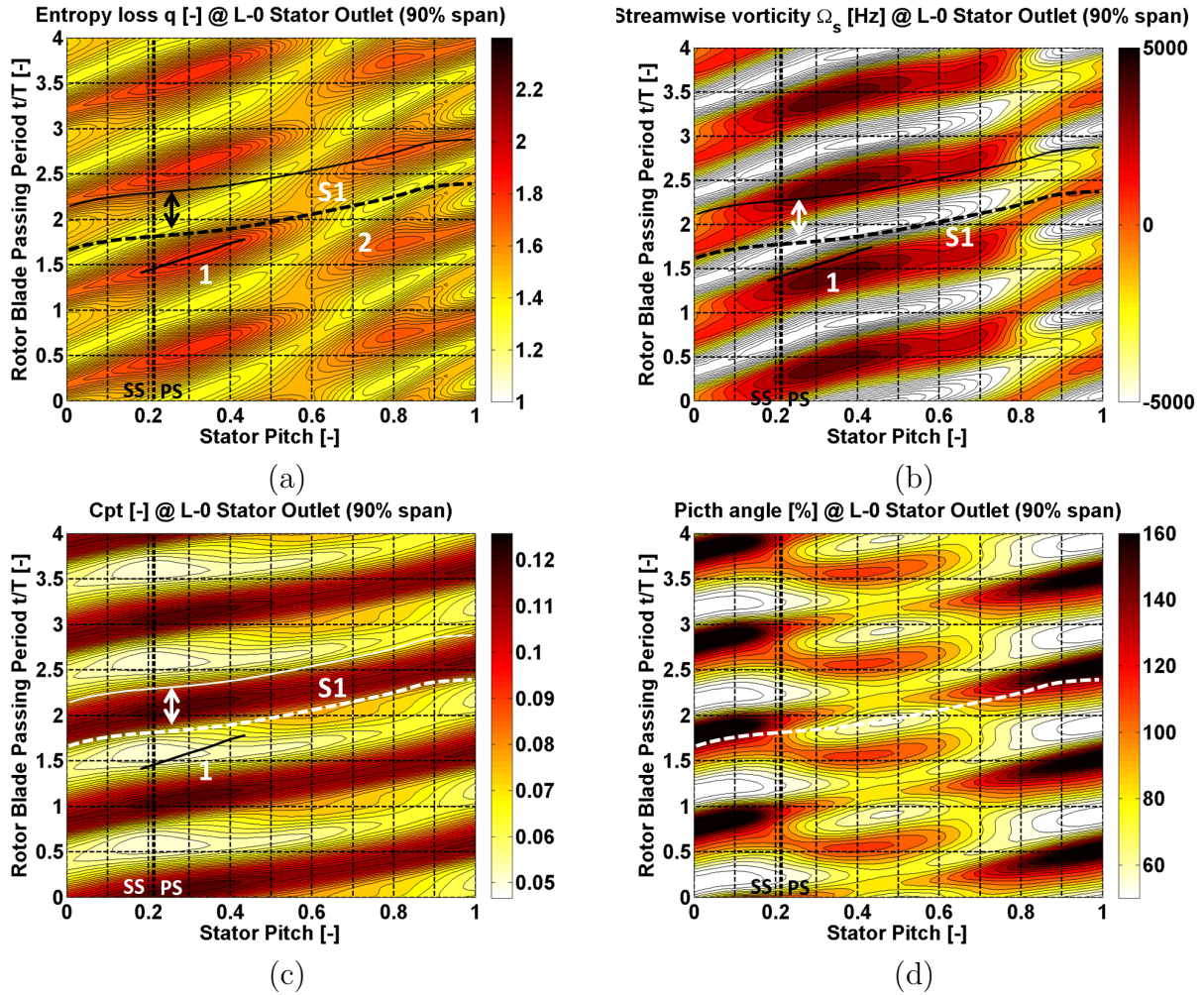


Figure 3.32: Time-space plots for (a) Entropy loss q [-], (b) streamwise vorticity (c) Total pressure coefficient C_{pt} and (d) non-dimensional pitch angle γ (equation 4.8) for one stator pitch at the exit of L-0 stator 90% of radial span. Loss features are labeled as 1 and 2 are introduced at stator suction side boundary layer.

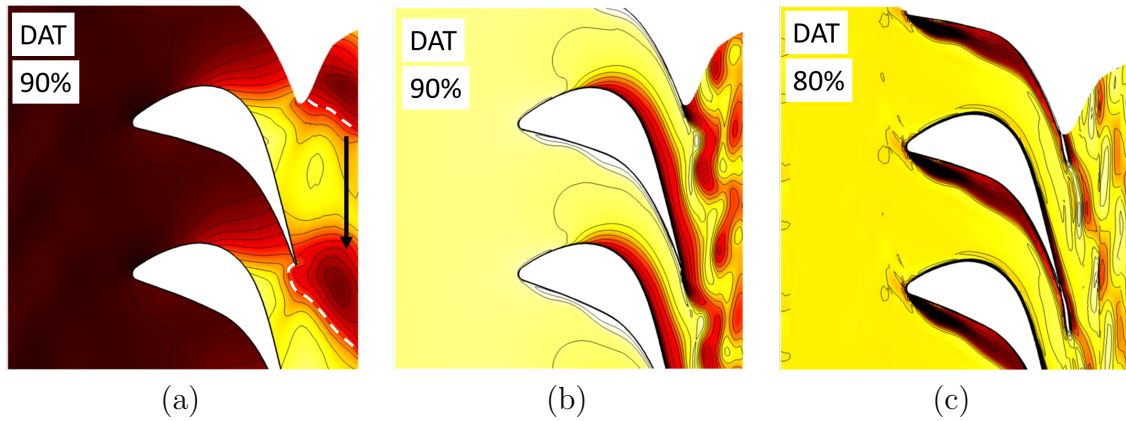


Figure 3.33: Instantaneous blade to blade contours of (a) C_{ps} [-] (b) Entropy loss q [-] and (c) streamwise vorticity at 90% of radial span parallel to flared casing.

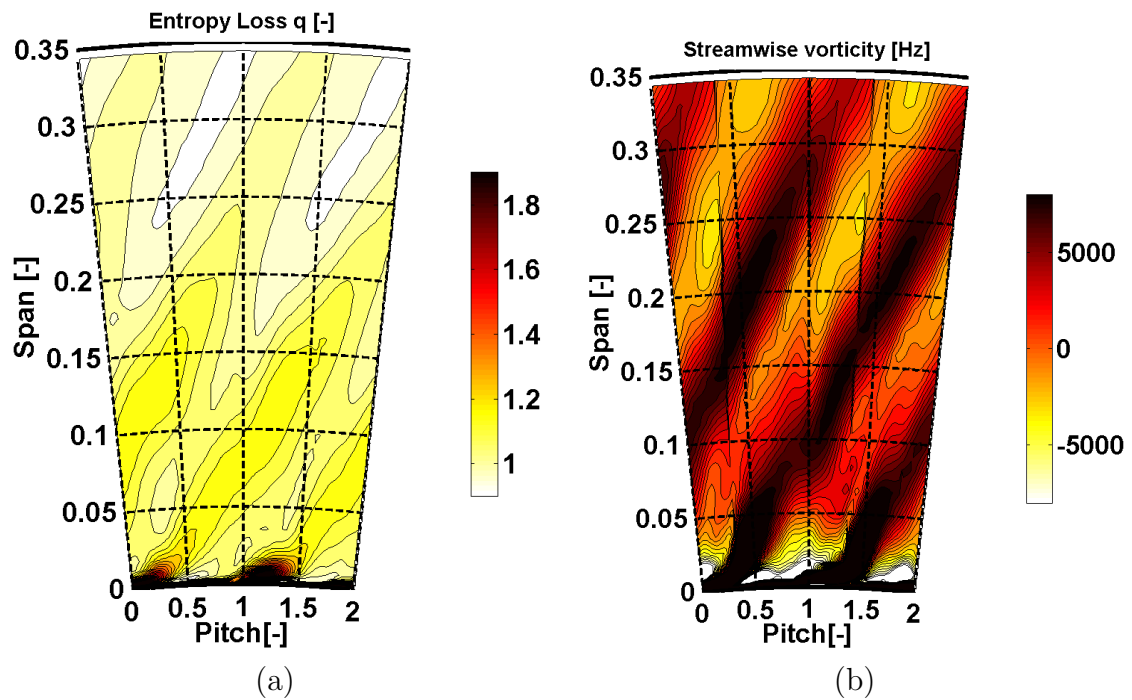


Figure 3.34: Instantaneous (a) Entropy loss q [-], (b) streamwise vorticity Ω_s for two circumferential pitch distance at L-0 stator exit from 0%-35% of radial span.

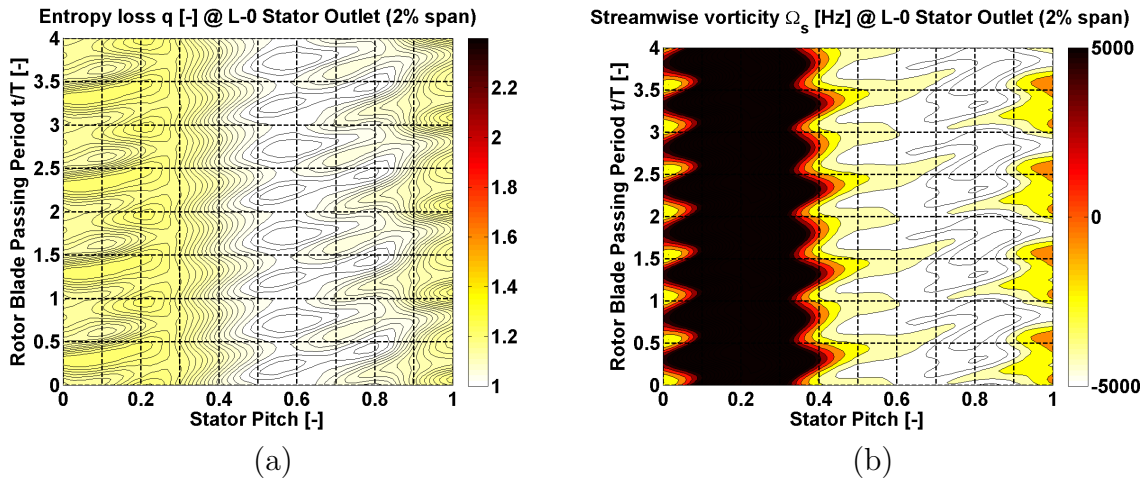


Figure 3.35: Time-resolved plots for (a) Entropy loss q [-], (b) streamwise vorticity ω_s for one stator pitch at L-0 stator exit at 2% of radial span.

3.6.4 L-0 rotor flow aerodynamics and loss generation mechanisms

Time-averaged relative Mach blade-to-blade contours at 91% and 95% of radial span for rotor is shown in Figure 3.36 (a) and (b) respectively. These two locations demonstrate supersonic flow expansion in the rotor. The subsonic region is clearly visible upstream of rotor leading edge, is introduced by **S1** leading edge bow shock. The flow downstream of throat recover and expands on the suction side. The pressure side as shown in both contours is responsible only for flow redirection towards supersonic airfoil throat and flow expansion initiates downstream of the throat on the suction side. The convex curvature and trailing edge introduce expansion waves **E2** responsible for over-expansion of flow on the suction side labeled as **Er2** after reflection. The flow decelerates by convex curvature labeled as **C2** and over-expanding flow is terminated by trailing edge shock **S3**. The intensity of flow expansion and shock waves increase towards tip span as shown by relative Mach contours at 95% of span. The reported loss mechanisms from time resolve flow are consistent with supersonic tip airfoil design reported loss mechanisms by Senoo et al. [24]. As shown in Figure 3.37 by blade-to-blade entropy loss contours, the blade profile and wake losses are the main flow mechanisms for entropy production in the supersonic flow expansion.

Time-averaged entropy loss and streamwise vorticity at the exit of L-0 rotor downstream from 70%-100% tip span are shown in Figure 3.38. The loss features are labeled as wake **W**, trailing edge shock **S3**, tip shroud loss **TS** and cavity exit separation **CS**. The high relative Mach flow near tip span and shroud generate a higher loss in general compared to the hub or mid-span regions at rotor exit. The blade profile and wake mixing loss dominate as shown. The un-avoidable tip shroud loss is high as a result of supersonic flow

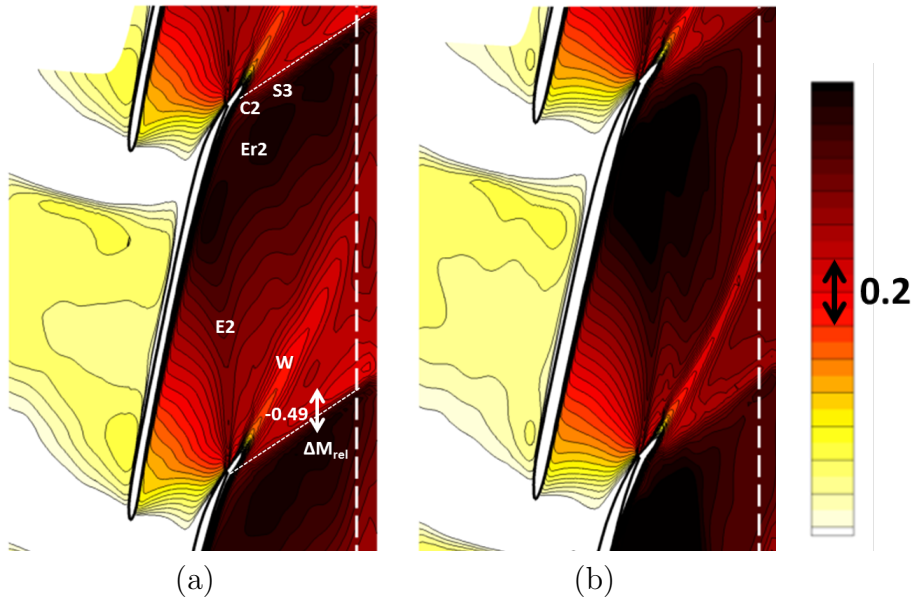


Figure 3.36: Time averaged relative Mach for (a) 91%, (b) 95% of the radial span. White dotted line represent location of rotor outlet plane for data presented in Figure 3.38 - 3.39.

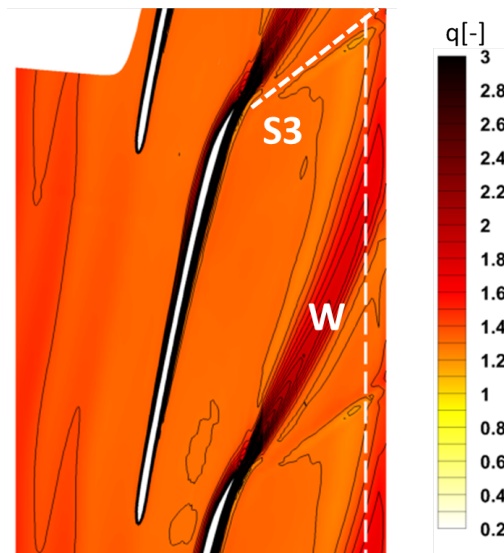


Figure 3.37: Time averaged entropy loss $q[-]$ at 91% of the radial span.

expansion generating higher losses at rotor tip attachment to the shroud. The secondary flows such as rotor tip passage vortex are not visible in supersonic flows. The trailing edge shock **S3** also demonstrate traces of loss with downstream mixing in the flow. The casing flow at the exit show traces of small separation bubble as a result of the casing flare at diffuser inlet. The trailing edge shock also introduces streamwise vorticity in the flow as shown in Figure 3.39 (b). The traces of loss as a result of the wake and trailing edge shock are clearly visible in time-resolved entropy loss contours at rotor exit (91% of span), as shown in Figure 3.39 (a) by labeled features **W** and **S3**.

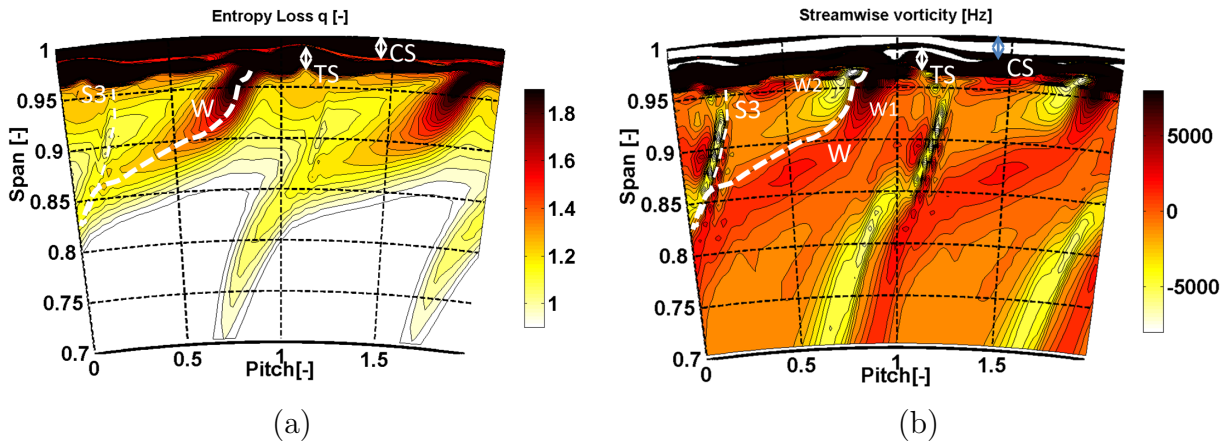


Figure 3.38: Time averaged plots for (a) Entropy loss $q[-]$, (b) streamwise vorticity Ω_s for two rotor pitch at L-0 rotor exit from 70%-100% of radial span.

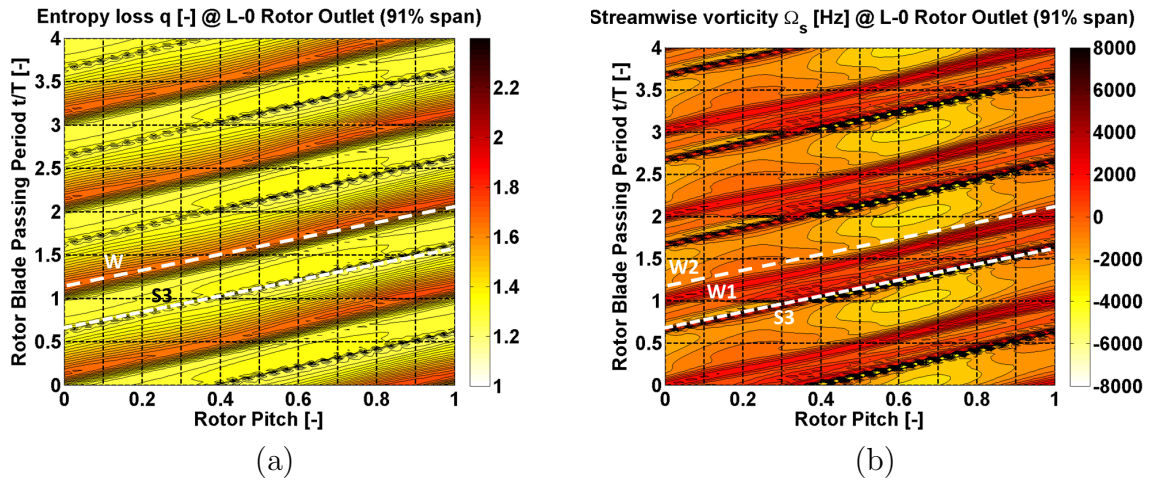


Figure 3.39: Time averaged plots for (a) Entropy loss $q[-]$, (b) streamwise vorticity Ω_s for one rotor pitch at L-0 rotor exit at 91% of radial span respectively.

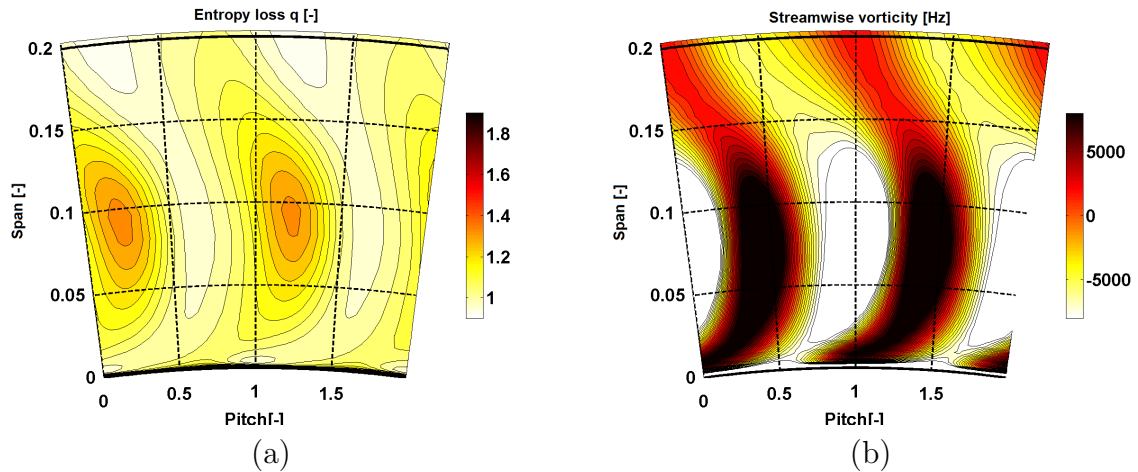


Figure 3.40: Time averaged plots for (a) Entropy loss $q[-]$, (b) streamwise vorticity Ω_s for two rotor pitch at L-0 rotor exit from 0%-20% of radial span.

Time-averaged entropy loss q and streamwise vorticity at L-0 rotor exit plane near hub span from 0%-20% is shown in Figure 3.40 (a) and (b) respectively. Two features with elevated loss profile, visible at 0.25 and 1.25 of stator pitch are the traces of hub separation bubble on the suction side of rotor introduced as a result of low root reaction. As the analysis reveal, at the exit of rotor supersonic tip region flows incur pronounced aerodynamic losses and must be considered during further design optimization stages. L-0 rotor hub separation also generates pronounced loss that cannot be ignored. Increase in stage hub reaction can be used as an effective mechanism to suppress this separation bubble. In the next two chapters, two carefully tailored stator stacking designs are considered in order to control L-0 stage reaction variation, stator loading distribution, and rotor inlet flow conditions in order to explore further aerodynamic improvements in the design.

Chapter 4

L-0 stator stacking redesign: Forward curved sweep

The time-resolved analysis in chapter 3 has provided an understanding of individual loss mechanism of multi-stage MHPS 10 MW low-pressure steam turbine including tip-cavities and seals. These unprecedented set of time-resolved computations are able to well predict experiments and resolve unsteady bow-shock wave interaction in L-0 stator-rotor tip gap. In this chapter effects of the axial gap in the stator-rotor tip region and stator trailing edge orthogonality to flared casing, on L-0 stage loading distribution, reaction variation and time-resolved aerodynamic improvements are explored. Datum and modified forward curved sweep (FCS) computational cases discussed in this chapter consists of combined last two stages L-1 and L-0. Both computational setups consist of 58 million mesh nodes each including tip-cavities and seals. Details on mesh quality, computational setup, convergence and runtime are discussed in chapter 3, section 3.6.

4.1 Forward curved sweep design

The datum or baseline design of L-0 stator employ the so-called advanced vortex nozzle (AVN) design. This AVN design is a form of optimized stator lean with mid-span and hub regions stacked and leaned towards the hub. The tip of stator connects orthogonally at the casing. The purpose of AVN design is to counter low root reaction, by an increase of hub static pressure, from inducing concave outward curvature streamlines in the hub region. The forward curved sweep stacking is employed in addition to AVN design in this work. The modified stator is a compound three-dimensional design with both stator AVN at hub and midspan and FCS at tip region. The spanwise and blade to blade stacking of forward curved sweep modification is shown in Figure 4.1 (a), (b) respectively. The trailing edge of L-0 stator is kept tangent to datum design at about 72% of radial span and curved

towards the tip span with trailing edge connecting flared casing perpendicularly. The stator airfoil at each spanwise location from 72% towards casing span is moved axially away from the L-0 rotor. This aggressive spanwise curvature increase L-0 stator/rotor tip trailing/leading edge gap by 1.8 times of datum design. The stator tip trailing edge connects with the flared casing at a lower span of 92% compared with datum design. This decrease the overall annular theoretical throat area. The constancy of theoretical throat area is ensured by opening the throat by blade twist from hub up to tip span. The blade-to-blade schematic of throat area increase and axial sweep are shown in Figure 4.1 (b) for 72%, 80% and 85% respectively.

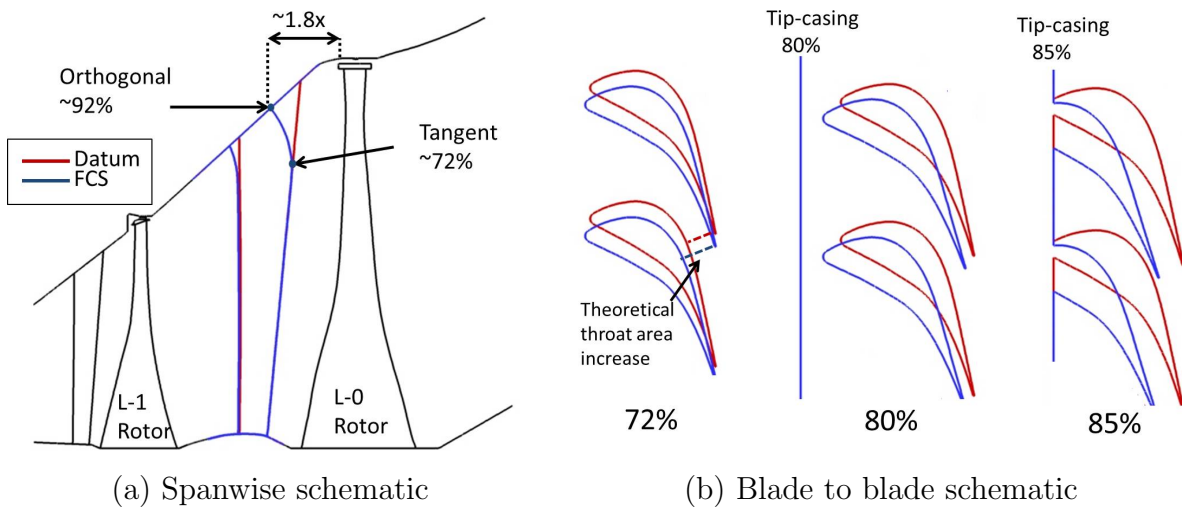


Figure 4.1: Spanwise schematic of L-1, L-0 stages combined with datum (red) and forward curved sweep (blue) stator modification is shown in (a), whereas 72%, 80%, 85% blade to blade schematic are shown in (b) respectively. Blade profiles at each spanwise position are moved axially away from L-0 rotor and throat area increased with blade twist in order to maintain overall constant annular throat area.

4.2 Stage efficiency and specific work

Stage total-to-total η_{tt} and total-to-static η_{ts} efficiency improvements are presented in Table 4.1. The calculations are circumferentially and radially mass averaged and time averaged for 30 degree of rotor rotation. The enthalpy based definition of efficiencies are given in equation 4.1, 4.2 respectively. The inlet and outlet of stage are indicated with subscript labels 1 and 3.

$$\eta_{tt} = \frac{h_{o1} - h_{o3}}{h_{o1} - h_{o3,isen}} \quad (4.1)$$

$$\eta_{ts} = \frac{h_{o1} - h_{o3}}{h_{o1} - h_{3,isen}} \quad (4.2)$$

The total-to-total η_{tt} efficiency is relevant for stage L-1 as leaving kinetic energy is useful. L-1 stage η_{tt} show an improvement of 0.1%. Note that work extraction is increased in L-1 stage by 3.4% (from 44.02% to 47.42% of combined two stage specific-work) as shown in Table 4.2. The increase in L-1 stage work extraction is an indication of increased annular throat area of L-0 stator (Havakechian et al. [56]). Despite the increase in L-1 specific work, the efficiency improvement of $\eta_{tt}=0.1\%$ is an indication of optimized flow expansion in L-1 stage. The last stage L-0 and part diffuser domain show an improved total to static efficiency η_{ts} of 1.0%. The total to static efficiency η_{ts} is relevant for the last stage L-0 as kinetic energy leaving the steam turbine is wasted. The two-stage and part diffuser combined efficiencies η_{tt} and η_{ts} improve by 1.3% and 1.1% respectively.

Table 4.1: Stage efficiency improvements for forward curved sweep stacking. Calculations are time (30° of bucket rotation), circumferentially and radially mass averaged. Both total-to-total and total-to-static efficiency improve for modified FCS case.

	L-1+L-0+Diffuser	L-0+Diffuser	L-1
$\Delta\eta_{tt}[\%]$	+1.3	+1.8	+0.1
$\Delta\eta_{ts}[\%]$	+1.1	+1.0	+1.3

Despite an effort to keep theoretical throat area constant, the workload increase in L-1 is a result of increased annular throat area of L-0 stator as predicted by computations. The flow in tip region is subsonic to near transonic in an absolute frame of reference. The unsteady interaction of rotor leading edge bow shock wave with stator suction side and passage further complicates the identification of exact throat location. Note that the swallowing capacity of the machine is determined by upstream L-3 stage stator with a higher blade count and reduced annular throat area. In the current computational setup, inlet mass flow is defined by L-1 stage inlet boundary conditions. Thus a change in L-0 stator annular throat area does not influence mass flow through the machine and only introduce stage workload shift. An increase of throat area as in this case, increase L-1 stage specific-work by 3.4% and reduce L-0 stage specific-work by 3.5% as shown in Table 4.2. The overall two stages specific work is increased by 1.57% for modified design.

Table 4.2: Stage specific-work (Δh_o) load shift for datum and modified forward curved sweep design. Calculations are time (30° of bucket rotation), circumferentially and radially mass averaged.

	Datum	FCS	-
$\Delta h_{o,L-0} / \Delta h_{o,2stage}$ [%]	55.98	52.48	-
$\Delta h_{o,L-1} / \Delta h_{o,2stage}$ [%]	44.02	47.42	-
$\Delta h_{o,FCS} / \Delta h_{o,Datum}$ [%]	-	-	101.57

Leaving loss:

$$Leaving\ Energy = \frac{1}{2} C_{abs,exit}^2 \quad (4.3)$$

Leaving kinetic energy in equation 4.3 is known as leaving loss and calculated at last stage L-0 rotor exit. The computations predict averaged leaving loss increase by 12.32% for forward curved sweep design. The time and circumferentially mass averaged profiles show increase in leaving energy at hub 0-12% and leakage flow at rotor outlet. Havakechian et al. [56] report similar levels of increase in leaving loss for the orthogonal sweep (of about 11.22% for non-constant throat area orthogonal sweep). The individual contribution to leaving loss is dominated by an increase in spanwise radial velocities throughout the exit span. Tangential absolute velocity component surprisingly decreases from hub to 70% of radial span and increase nominally from 80% to 96% of L-0 rotor exit span. The axial velocity change is less pronounced with only small increase near hub and reduction in the tip region (80%-96%).

4.3 Spanwise aerodynamic performance analysis

4.3.1 Stage reaction variation and spanwise flow aerodynamics

Stage reaction R_p , as defined in equation 4.4 is a key optimization parameter in order to assess improvements by 3D stator stacking. For steam turbine with long rotor blades in the last stage, increase in hub reaction is an effective way to control rotor tip relative inlet Mach as shown by equation 4.5 (Senoo et al. [22]). The relative rotor inlet tip velocity w_{tip} increase in proportion to hub reaction $R_{p,hub}$, blade tip peripheral speed U_{tip} and decrease to the square of hub to tip ratio r_{hub}/r_{tip} . Increase in L-0 hub reaction of about 3.3% (see Figure 4.2 (b)) must increase relative Mach as per equation 4.5. However, the relative inlet Mach number $M_{rel,tip} = w_{tip}/a$ reduce by 0.04 at 95% of tip span (Figure 4.3) (a), where a is the speed of sound. The axial displacement of the blade profile introduces a suction side lean facing towards tip as discussed in the subsequent analysis. In the meridional plane,

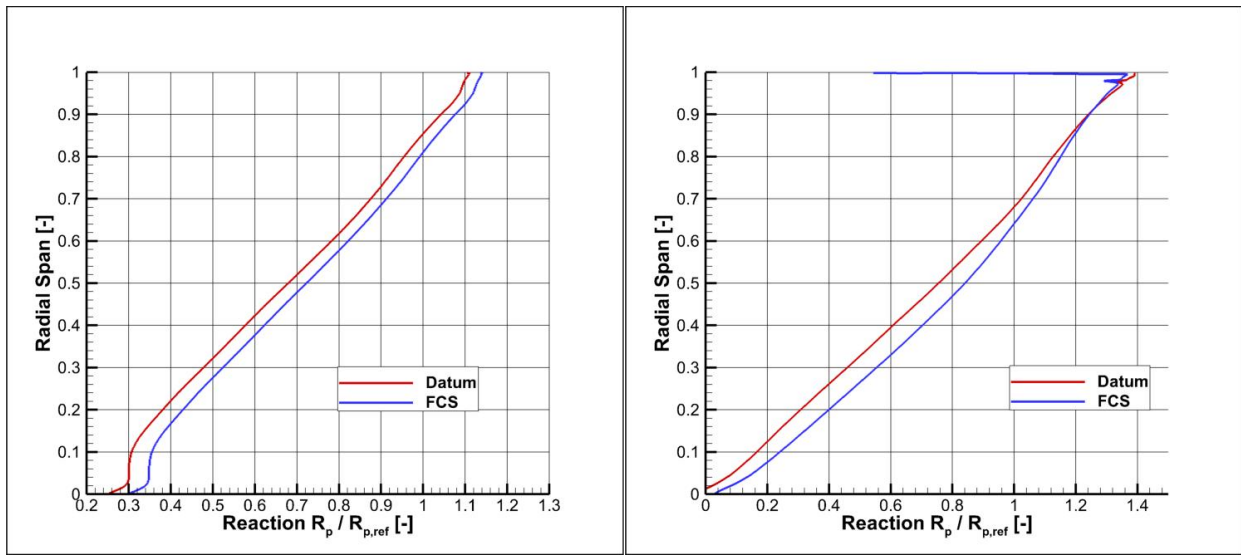
the blade to blade contours shows a closed throat area. The lean as well reduced throat area at the tip in meridional flow path increase absolute Mach and decrease relative Mach to rotor tip. The increase in hub reaction has a positive effect on potential rotor suction side separation in the hub region. This reduces absolute Mach number at hub and stator trailing edge shock losses and potential interaction with rotor leading edge at the hub. The increase of hub reaction by 3.3% reduces absolute Mach by 0.09 at about 2% of hub span. A low hub reaction is however desirable for reduction of leaving energy. Increase in leaving energy deteriorates diffuser performance.

$$R_p = \frac{\Delta P_{rotor}}{\Delta P_{stage}} \quad (4.4)$$

$$w_{tip} = U_{tip}[1 - 2(1 - R_{p,hub})(r_{hub}/r_{tip})^2] \quad (4.5)$$

The stage reaction for L-1 and L-0 are shown in Figure 4.2 (a) and (b) respectively. L-1 stage reaction increase from 2.7% at 10% to 1.8% at 90% of span. The spanwise increase of L-1 stage reaction is a result of stage workload shift as discussed earlier. Havakechian et al. [56] report a constant shift increase in the spanwise reaction for the orthogonal sweep with a non-constant throat area. The throat area in such cases is kept constant by opening up the blade by the twist. A similar observation is made in the current results of L-0 stage reaction. The reaction shows a constant shift throughout span as shown in Figure 4.2 (b). The opening of L-0 stator throat by twist has increased overall effective throat area despite the theoretical throat area being constant in the blade stacking design phase. It must be noted that constant increase in L-0 stage reaction from 0%-83% of radial span decelerates the flow as shown by absolute Mach number in Figure 4.3 (a). The relative Mach is decreased from 0%-32% of radial span and increase onwards up to 87% of radial span. The relative Mach decrease again from 87% up to tip span. The static pressure coefficient C_{ps} increase in the hub to about 47% of span and decrease onward up to tip span. The radial pressure gradient in the axial gap is formed to balance the centrifugal force caused by swirl (tangential velocity). Forward curved sweep ease this strong positive static pressure gradient.

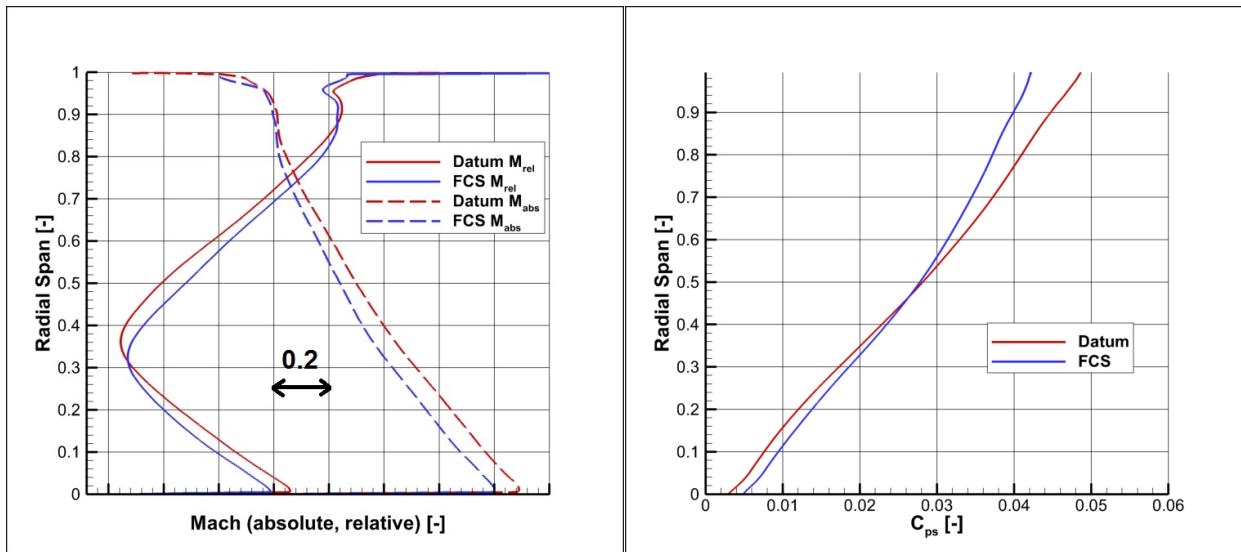
The non-dimensional meridional mass flux show a reduction in the tip region from about 87% to tip span as shown in Figure 4.4. This indicates a potential reduction in L-0 tip cavity flow. The seal leakage flow from L-1 rotor with un-extracted energy pass through L-1 stator tip region and spread in the radial span. The leakage flow further mix with L-0 bow shock **S1** interaction with the stator. A reduction in L-0 seal flow allows redirection of this high enthalpy fluid to pass through L-0 rotor tip region and potentially improve overall work extraction. The meridional mass flux reduced in tip span is redistributed to 30%-87% respectively.



(a) L-1 stage reaction

(b) L-0 stage reaction

Figure 4.2: Circumferentially mass averaged and time-averaged, non-dimensional, spanwise reaction variation for L-1 (a) and L-0 (b) stages respectively.



(a)

(b)

Figure 4.3: Circumferentially mass averaged and time-averaged spanwise Mach absolute, relative (a) and static pressure coefficient C_{ps} (b) in L-0 stator-rotor axial gap.

The pressure ratio $P_e/P_{o,inlet}$ for L-0 stage is increased throughout radial span as shown in Figure 4.5. L-0 rotor supersonic tip airfoils are designed for unique incidence (rotor inlet relative Mach M_{rel} and relative yaw angle to rotor α_1) and pressure ratio. Increase in stage pressure ratio reduces the flow expansion through L-0 rotor with a potential decrease in relative Mach at rotor outlet. This has a positive influence by reduction of leading and trailing edge shock strength and blade profile losses.

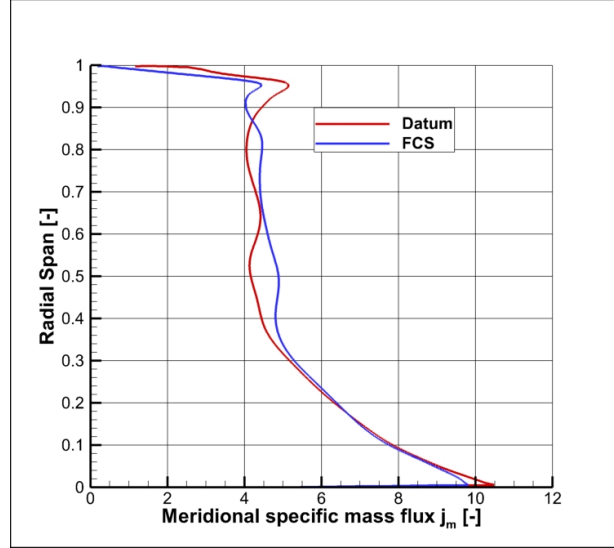


Figure 4.4: Circumferentially mass averaged and time-averaged spanwise non-dimensional meridional mass flux $j_m = \rho C_m / \rho_{ref} C_{m,ref}$ in L-0 stator rotor axial gap.

4.3.2 Spanwise loss profiles

The spanwise distribution of entropy loss, mass flow redistribution and wetness increase across stator, rotor and part diffuser are presented in Figure 4.6. The radial span is further split into three distinct regions of the hub, mid and tip span. The quantities are further radially mass averaged to report change in each region as presented in Table 4.3, 4.4 and 4.5 respectively. Note that the reported values are calculated as percentage change from the outlet to inlet of a particular blade row i.e. change within the row (stator, rotor or diffuser). Forward curved sweep design increase entropy loss by 1.98% in the stator tip region and reduce by 5.69% in rotor tip span from about 70% to 100% as shown in Figure 4.6. The increase in entropy loss is attributed to tangential lean at stator trailing section introduced by forward displacement of stator airfoil profile. The introduced lean is stator suction side facing tip span. The blade profiles further show pronounced suction side curvature in the meridional flow path and a closed throat area. These changes accelerate the flow in the stator tip passage and introduce pronounced streamwise vorticity and entropy loss in the

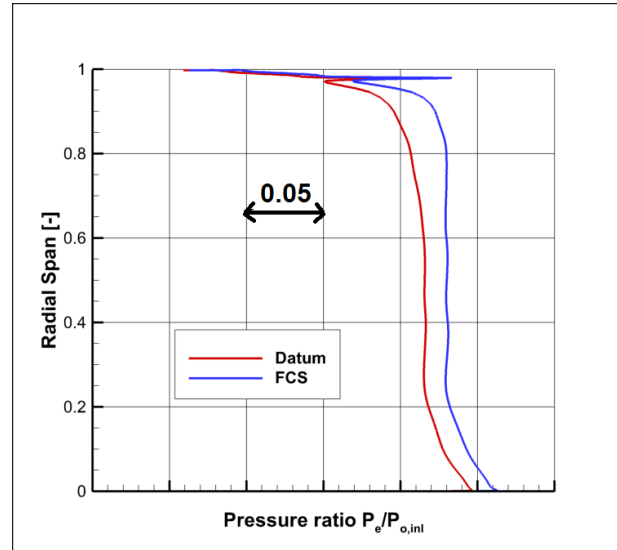


Figure 4.5: Circumferentially mass averaged and time-averaged spanwise L-0 stage pressure ratio. The total pressure drop at the inlet of L-0 stator as a result of increased specific work in L-1 stage.

tip region and at the casing. There are additional features of flow separation at casing introduced by changes in shock interaction with the flow in the axial gap as discussed later in section 4.4.2.

The entropy loss improvements are dominant and is a consequence of reduced flow expansion through supersonic tip airfoils as a result of increase in pressure ratio. The pressure ratio increase result from workload shift introduced by annular L-0 stator throat area increase. A reduced inlet relative Mach and flow expansion through rotor supersonic airfoil result in lower blade profile loss and trailing edge shock loss and its interaction with stator wake. The mass flow reduces by 3.57% in the L-0 stator tip and increases by 4.99% in the rotor tip region. Note that mass flow through the L-0 tip cavity is reduced by 0.49% as discussed later in the analysis. The reduction of mass flow through the L-0 nozzle tip region is a result of a reduction in radial velocities in the tip region. Stator stacking orthogonality to the casing, reduce meridional sweep to incoming flow and improve stream surface twist, by a reduction of radial velocities, as reported by Havakechian et al. [56]. The mass flow increase of 4.99% in the rotor is a result of a reduction in relative Mach through supersonic tip airfoils. In supersonic flow, decrease in Mach increase mass flow rate per flow passage area. In addition, an increase in radial velocities within rotor passage is observed. The wetness fraction decrease by 0.06% in stator tip and 0.15% in rotor tip span.

L-0 stator hub and mid-span region improve entropy loss by 0.86% and 0.78% respec-

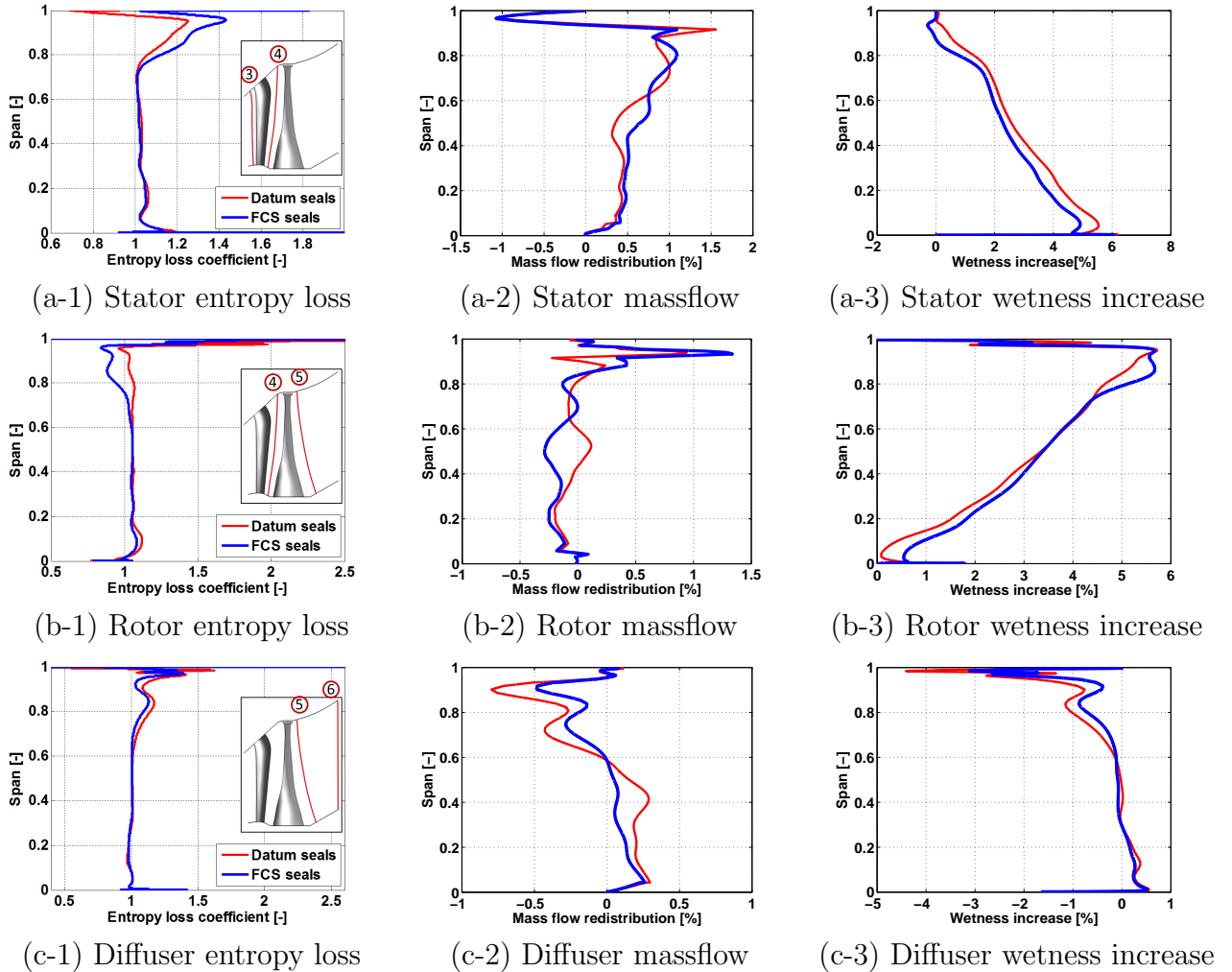


Figure 4.6: Circumferentially mass and time-averaged entropy loss, mass flow redistribution and wetness increase within stator (a), a rotor (b) and part diffuser (c) respectively. The values are calculated as percentage change from the outlet to inlet of a particular row. Entropy loss increase in stator tip region and a decrease in the rotor and part diffuser. Tip region with supersonic airfoils is an area with pronounced loss improvements.

tively (see Table 4.3). The mass flow increase by 1.28%, 2.29% and wetness decrease in both regions by 0.53% and 0.29% respectively. The absolute Mach in stator hub and midspan is decreased (see Figure 4.3) and resulting blade profile loss in midspan and a weak oblique shock as well hub passage vortex are improved respectively. The rotor hub and midspan entropy loss decrease by 1.93%, 0.58%, and mass flow reduce by 0.98% and 4.01% respectively. L-0 rotor hub improvements source from a reduction in flow separation of the suction side with an increase in hub reaction. Improvement in the midspan flow is introduced by a reduction in transonic airfoils blade profile and shock losses. The entropy loss improvement of 0.48% and 7.22% at mid and tip span of the diffuser are reported. The hub region loss is increased by 0.65%.

Table 4.3: L-0 stator: change in entropy loss, mass flow, and wetness in each hub to tip span region across the stator.

[%]	Hub [0-35]	Midspan [35-70]	Tip [70-100]
Δq	-0.86	-0.78	1.96
$\Delta \dot{m}$	1.28	2.29	-3.57
$\Delta \beta$	-0.53	-0.29	-0.06

Table 4.4: L-0 rotor: change in entropy loss, mass flow, and wetness from hub to tip radial span across the rotor.

[%]	Hub [0-20]	Midspan [20-70]	Tip [70-100]
Δq	-1.93	-0.58	-5.69
$\Delta \dot{m}$	-0.98	-4.01	4.99
$\Delta \beta$	0.17	-0.19	-0.15

Table 4.5: L-0 diffuser: change in entropy loss, mass flow, and wetness from hub to tip radial span across part diffuser domain.

[%]	Hub [0-20]	Midspan [20-70]	Tip [70-100]
Δq	0.65	-0.48	-7.22
$\Delta \dot{m}$	-0.58	-2.36	2.94
$\Delta \beta$	-0.07	-0.01	0.53

4.4 Time resolved flow analysis

4.4.1 L-0 Stator exit flow

L-0 rotor leading edge bow shock **S1** unsteady interaction with stator average out individual flow features in time-averaged data. In order to identify individual flow structures, an instantaneous flow snapshot is preferred. Figure 4.7 shows the instantaneous total pressure coefficient C_{pt} , pitch and absolute yaw angles at the exit of L-0 stator. The axial plane is located at $x/s=0.39$ between L-0 stator and rotor (x/s represent datum design axial tip gap). The plots show stator downstream view from 70%-100% of radial tip span and for two stator pitch of circumferential span at the same rotor blade relative position $t/T=0$. The observer is looking towards the axial direction of flow and rotor is rotating in a left to right of circumferential pitch axis. The rotor tip leading edge bow shock is marked with white dotted lines. Two bow shock fronts can be seen clearly as C_{pt} rise in Figure 4.7 (a-1) datum and (a-2) forward curved sweep design.

The flow in the L-0 stator-rotor gap in the tip region shows strong unsteady signature introduced by rotor leading edge bow shock. The bow-shock strength is decreased and maximum C_{pt} regions following the shock front are reduced by as much as 5% in the FCS design. The decrease in shock strength can be attributed to two contributing factors. The first factor is the reduction in absolute total pressure by about 8% on average at the L-0 stage inlet. This is a result of the increase in reaction and consequently increased energy extraction in L-1 stage. The increase in the effective throat area of L-0 stator is the cause of this increased L-1 work extraction. The second contributing factor is the decrease in Mach number relative to rotor inlet from 86% to 100% of span. The total pressure drop across the bow shock is a unique function of total pressure and Mach number before the shock front in the absolute frame of reference (Senoo et al. [24]). This is explained by equation 4.6 for an ideal gas. The relative Mach decrease and absolute Mach increase across the shock **S1** front results in a total pressure rise. Furthermore, shock loss is a strong function of Mach number perpendicular to the shock front (Denton et al. [15]).

$$\frac{P_{02}}{P_{01}} = \left[\frac{(\gamma + 1)M_1^2}{(\gamma - 1)M_1^2 + 2} \right]^{\frac{\gamma}{\gamma-1}} \left[\frac{(\gamma + 1)}{2\gamma M_1^2 - (\gamma - 1)} \right]^{\left(\frac{1}{\gamma-1}\right)} \quad (4.6)$$

The increased stator-rotor gap by 1.8% at tip result in L-0 stator trailing edge moving to a lower radial span. The high C_{pt} core after the bow-shock move away from casing towards stator trailing edge from about 98% to 95% radial span as seen in Figure 4.7 (a-1) and (a-2). The C_{pt} levels in the free-stream flow between two shocks are reduced by about 16% from 88% to 100% at circumferential pitch axis 1.0. The high C_{pt} signature from 70% to 85% of span at 0.6 and 1.8 of circumferential pitch axis is the work done by the rotor upstream potential field, also termed as bow wave. The signature is reduced for the modi-

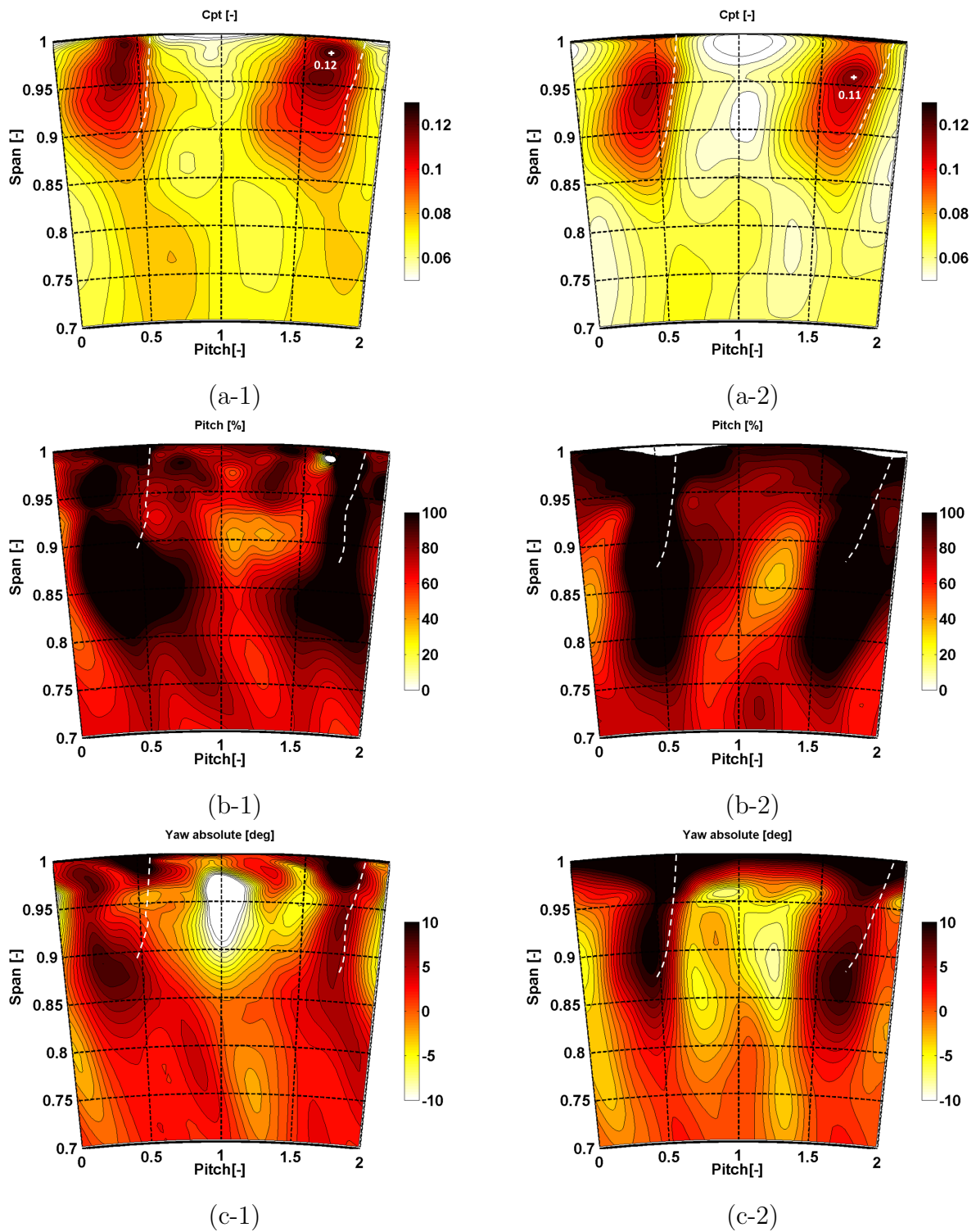


Figure 4.7: Total pressure C_{pt} coefficient, Pitch and Yaw angle at the exit of L-0 stator tip (*-1) Datum on left and (*-2) Forward tip curved sweep design on the right column.

fied design by about 13%. A reduction in the strength of bow-shock and bow-wave in the tip region must result in a reduced shock loss. Nevertheless, the loss introduced by shock **S1** interaction with the stator suction side boundary layer, and the axial gap unsteady flow is dominant in comparison to shock front loss. The density gradients introduced by shock, induce pitch and yaw angle modulation, as explained in the time-resolved flow measurements of datum design by Bosdas et al. [25]. A weaker bow-shock wave interaction with the upstream stator exit flow, however, increases unsteadiness in the modified case. Pitch angles show pronounced overturning directed towards casing with a larger area cover from 75% to 100% span for the modified case compared to datum as shown in Figure 4.7 (b-1) and (b-2). Note that the non-dimensional pitch angle is defined as flow parallel to the axial direction as 0%, whereas parallel to flared casing as 100% as shown in equation 4.8. The pitch angle under-turning next to the casing at 0.5 and 1.8 of circumferential pitch distance is introduced in the modified case (b-2). The flow separates in this region with negative axial velocity and contributes as one of the additional loss sources in the modified case. The flow separates mid of the passage at L-0 stator casing (92% of stator axial chord length), by adverse pressure gradient introduced by downstream bow-shock **S1**. The intensity of flow separation increase and stays attached to the casing as flow covers the axial distance in the presence of rotating bow-shock. The flow separation bubble stays connected to the shock low C_{pt} regions next to the casing. The results show reduced shock intensity in the presence of increased axial distance in the tip axial gap pronounce pitch and yaw angle for the shown time instant in Figure 4.7. Note that absolute yaw angle is defined by subtracting CFD yaw angle from stator exit blade metal angle according to equation 4.7. The overturning of yaw angles after the shock front is increased by about 4° at 98% of span (see Figure 4.7 (c-*)). The flow under-turning in the free stream between two shocks at pitch span 1.0 and radial span 95% is improved by 12.5°. The yaw angle modulation from 70% to 85% of the span is improved in free-stream as well as bow wave region.

$$\Delta\varphi = \varphi_{ma} - \varphi_{abs,CFD} \quad (4.7)$$

$$\gamma = \frac{\gamma_{CFD}}{\gamma_{flareangle}} \times 100 \quad (4.8)$$

Figure 4.8 shows the streamwise vorticity and entropy loss coefficient at the exit of L-0 stator. The entropy loss is increased by about 42% in the tip region near casing at 98% of the radial span. Loss features are diffused as a result of increased axial distance in the forward curved sweep case. The mixed out entropy loss features in Figure 4.8 (b-2) cannot be clearly attributed to individual streamwise vorticity features shown in (a-2). The increased axial distance allows a larger area for the flow to diffuse. The benefit of the relatively weak bow shock and reduced interaction with stator trailing edge are relatively less

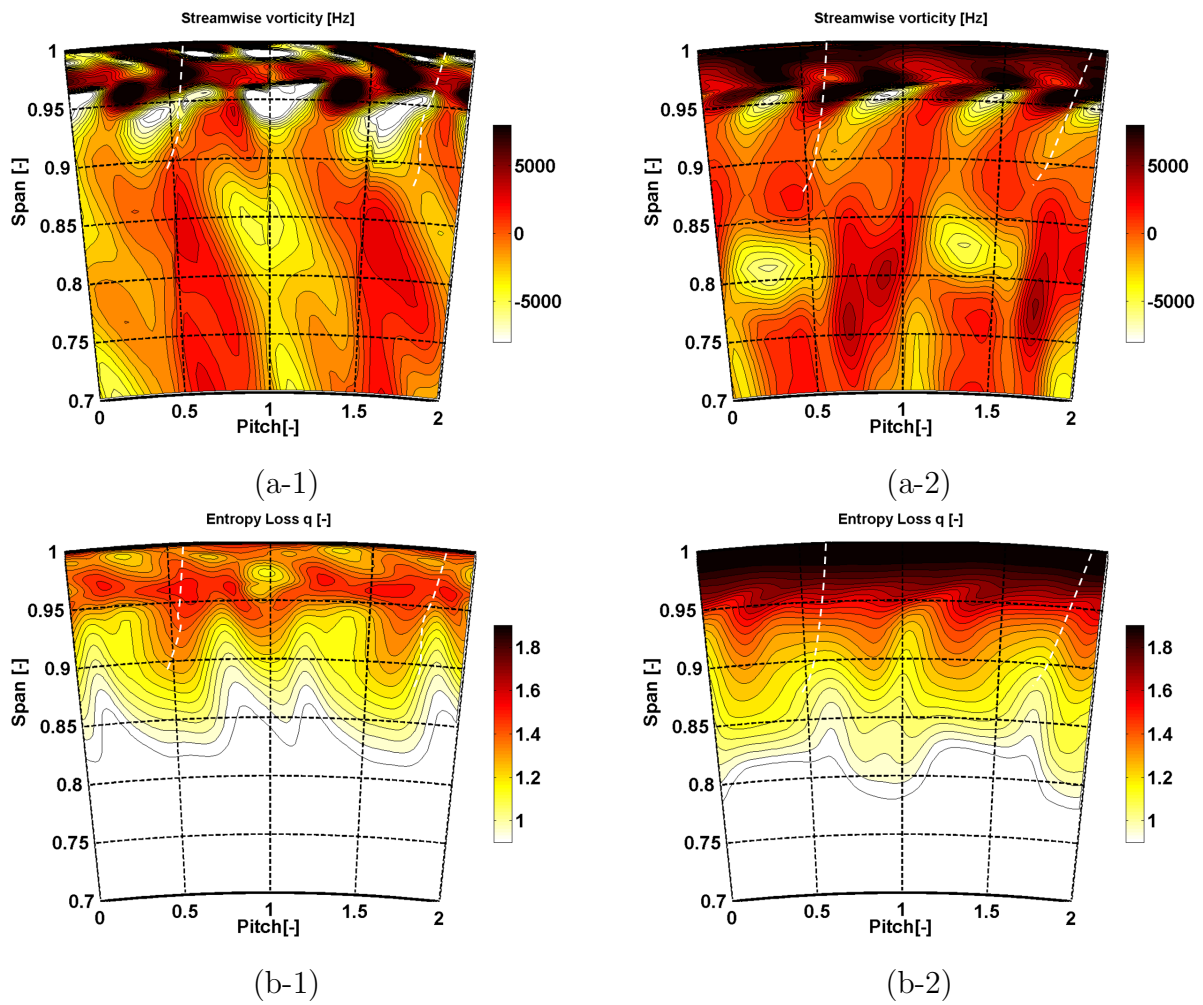


Figure 4.8: Streamwise vorticity and entropy loss at the exit of L-0 stator tip for (*-1) Datum on left and (*-2) Forward tip curved sweep design on the right.

pronounced as compared to pronounced streamwise vorticity and mixing in an increased axial gap. The very high L-0 stator tip turning angles of about 78° induce high levels of tangential vorticity. The tangential vorticity is a dominant component of streamwise vorticity in the tip region. Large turning angles induce high levels of positive tangential vorticity on the suction and negative tangential vorticity on pressure side towards trailing edge. In addition, the adverse pressure gradient induced by bow shock further enhance the intensity of positive streamwise tangential vorticity on the suction side of stator trailing edge. In forward curved sweep case, the suction side vorticity and subsequent interaction with unsteady flow induced by bow shock incur additional entropy loss (see Figure 4.8 (b-2)). The streamwise vorticity is mixed out for modified case (Figure 4.8 (a-2)) and display relatively reduced peak strength from 95% to 100% span in the modified case. The contact interface of positive and negative streamwise vorticity regions (steep vorticity gradients) as indicated in datum case Figure 4.8 (a-1) and (b-1) at 0.5, 1.0 and 1.5 of circumferential pitch span entrain pronounced entropy levels.

Time-resolved aerodynamics of stator-rotor interaction is presented with time-space plots for one stator pitch and four rotor blade passing period at 90% of radial span at stator exit plane. Static pressure coefficient, incidence and relative Mach to L-0 rotor are presented in Figure 4.9. The bow shock **S1** front for one rotor passing is marked with a dotted white line in all figures at 1.6 of blade passing period. The static pressure rise after the shock is reduced in intensity and area cover in forward curved sweep design. This indicates a weaker shock. The interaction with stator trailing edge increase shock strength in datum design (0.1-0.5 of stator pitch), is reduced for forward curved sweep (see Figure 4.9 (a-1),(a-2)). The reduced high static pressure area cover after the shock increase free-stream area between two shock fronts. This low static pressure area between two shock fronts face rotor pressure side subject to a unique incidence (incidence angle and relative Mach). The static pressure unsteadiness is increased from $\pm 38\%$ to $\pm 41\%$ at 0.3 of the pitch span. Cps unsteadiness is also pronounced from $\pm 15\%$ to $\pm 27\%$ at 0.9 of pitch span. This indicates an increase in Cps unsteadiness across the pitch. As explained in the time-resolved experiments of Bosdas et al. [25] the unsteadiness in flow yaw and pitch angles in the stator-rotor gap is driven by pressure gradients introduced by the bow shock. Incidence to the rotor in the datum design as shown in Figure 4.9 (b-1) has two regions. The rotor tip shock **S1** at about 0.7 of the pitch impinges on the suction side and as the rotor rotates towards 1.0 of stator pitch, the distance between the leading edge and stator trailing edge is reduced. The rotor further moves from 0.0-0.2 of stator pitch with even more pronounced unsteadiness in incidence with a lowest axial gap between rotor leading edge and stator trailing edge at 0.2 of the pitch span. In the low unsteadiness region of 0.3 to 0.7 shock is going through passage with increased axial distance. With FCS design the axial gap is increased throughout the pitch span. Nevertheless, the maximum incidence fluctuations of about $\pm 12.5^\circ$ at 0.04 of the pitch span are reduced to a maximum of $\pm 5.65^\circ$ at 0.19 of pitch span in FCS design. The average flow incidence to L-0 rotor, at 90% of the

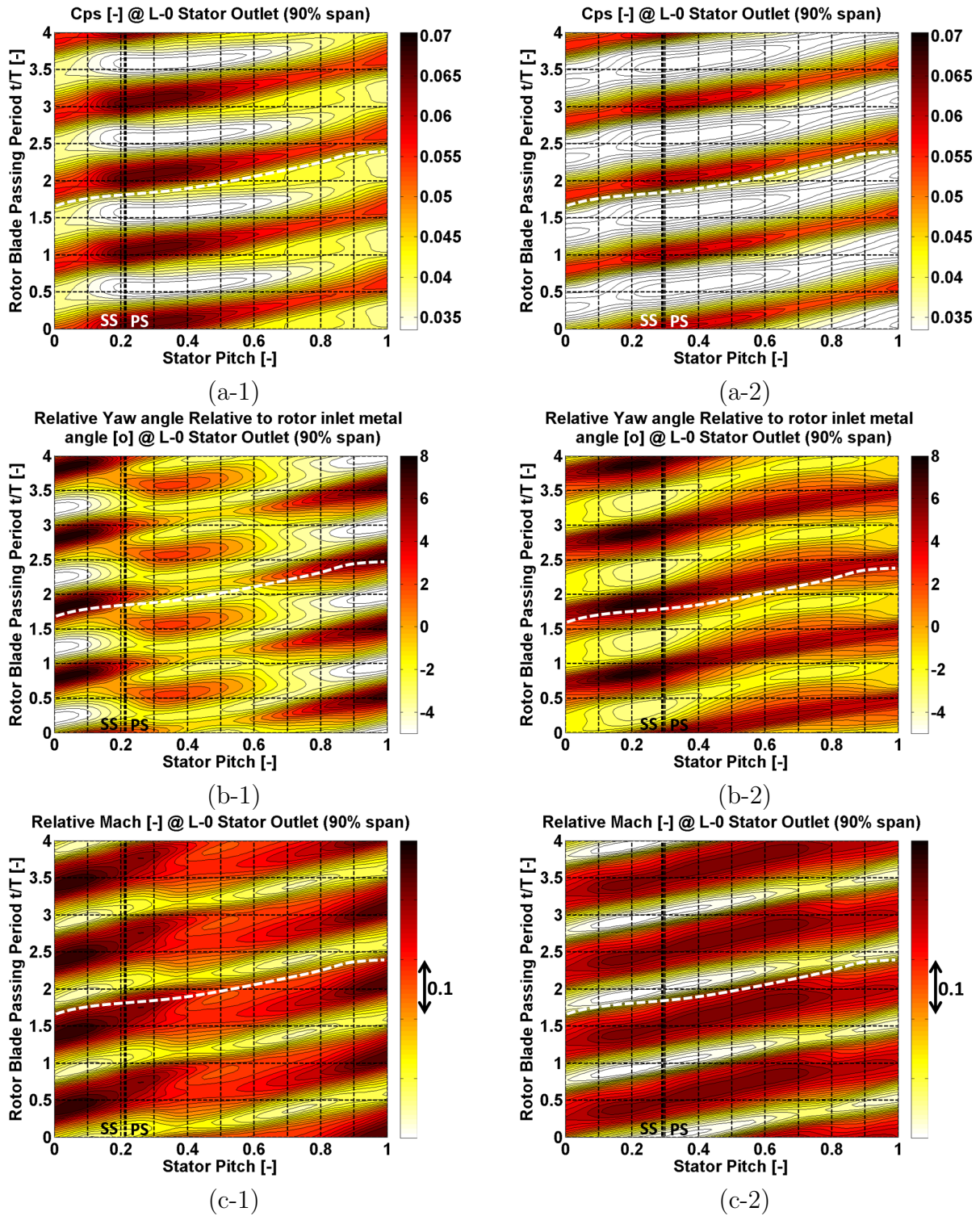


Figure 4.9: Static pressure coefficient C_{ps} , incidence and Mach relative to rotor inlet at 90% of tip span for one stator pitch plotted for four rotor blade passing periods. Datum design is shown on the left (*-1) and forward curved sweep to the right (*-2).

radial span, is improved from -3.5° to a positive incidence of 0.88° . The relative Mach to rotor is shown in Figure 4.9 (c-1) datum and (c-2) FCS design. The region of high static pressure following the shock front reduce relative Mach to the rotor as the flow decelerates after the shock front. The area of low Cps following the high Cps region allow relative Mach increase to free-stream conditions. The region of the reduced axial gap between stator trailing edge and rotor leading edge (0.0-0.2) in the datum design show elevated level of relative Mach (see Figure 4.9 (c-1)) compared with increased axial gap region of about 0.3-0.7 of stator pitch. The relative Mach is decreased by 1.5% on average at 90% of the radial tip span in the FCS design. The variation of relative Mach across the pitch span in datum design Figure 4.9 (c-1) is no more present with an increase in axial distance Figure 4.9 (c-2). Increased axial distance eliminates the effects of pronounced incidence and relative Mach (pitch axis 0-0.2) as the axial gap between rotor leading edge and stator trailing edge reduce; as the rotor rotates from the suction side towards stator trailing edge. This results in a consistent incoming relative Mach to the rotor.

Despite the Cps unsteadiness is increased, an increase in axial gap and reduction in shock strength (pressure gradients) decrease the rotor incidence and unsteadiness. Incoming relative Mach to rotor does not show pitch-wise spatial variation that is present in the datum design as a result of the varying gap between rotor leading edge and stator suction side. Both of these effects improve unique incidence to L-0 rotor.

The time-resolved pitch span analysis at 90% of radial span show improved rotor incidence and relative Mach in the region of 0-0.3 and 0.7-1.0 of stator pitch. The entropy loss averaged radial profiles (see Figure 4.6 (b-1)) report improvements from 70% to the blade tip span of the rotor. As rotor geometry is unchanged, the incoming flow conditions and pressure ratio are two important aspects to influence flow expansion through supersonic airfoils in the rotor tip region. Time-resolved static pressure Cps and relative Mach at 10% of pitch span and 70%-100% of radial span are presented in Figure 4.10 (a-*) and (b-*) respectively. The shock front is highlighted with a white dotted line for datum plots on the left and with a black dotted line for FCS plots on the right. As discussed earlier, the area cover for high Cps region after the shock front is reduced and the area cover of low Cps region is increased for FCS design. The relative Mach rise in the low Cps region between 90%-99% of radial span. The low Cps region after the shock passes the plotted radial location (10% of pitch span) relax the flow to free-stream relative Mach values. The relative Mach in the region of low Cps is reduced along with a reduction in peak-to-peak fluctuations from $\pm 24\%$ to $\pm 19\%$ at about 94% of radial span. A reduction in peak-to-peak fluctuations and average relative Mach in the tip region is a desirable outcome of the modified FCS design for supersonic tip airfoils.

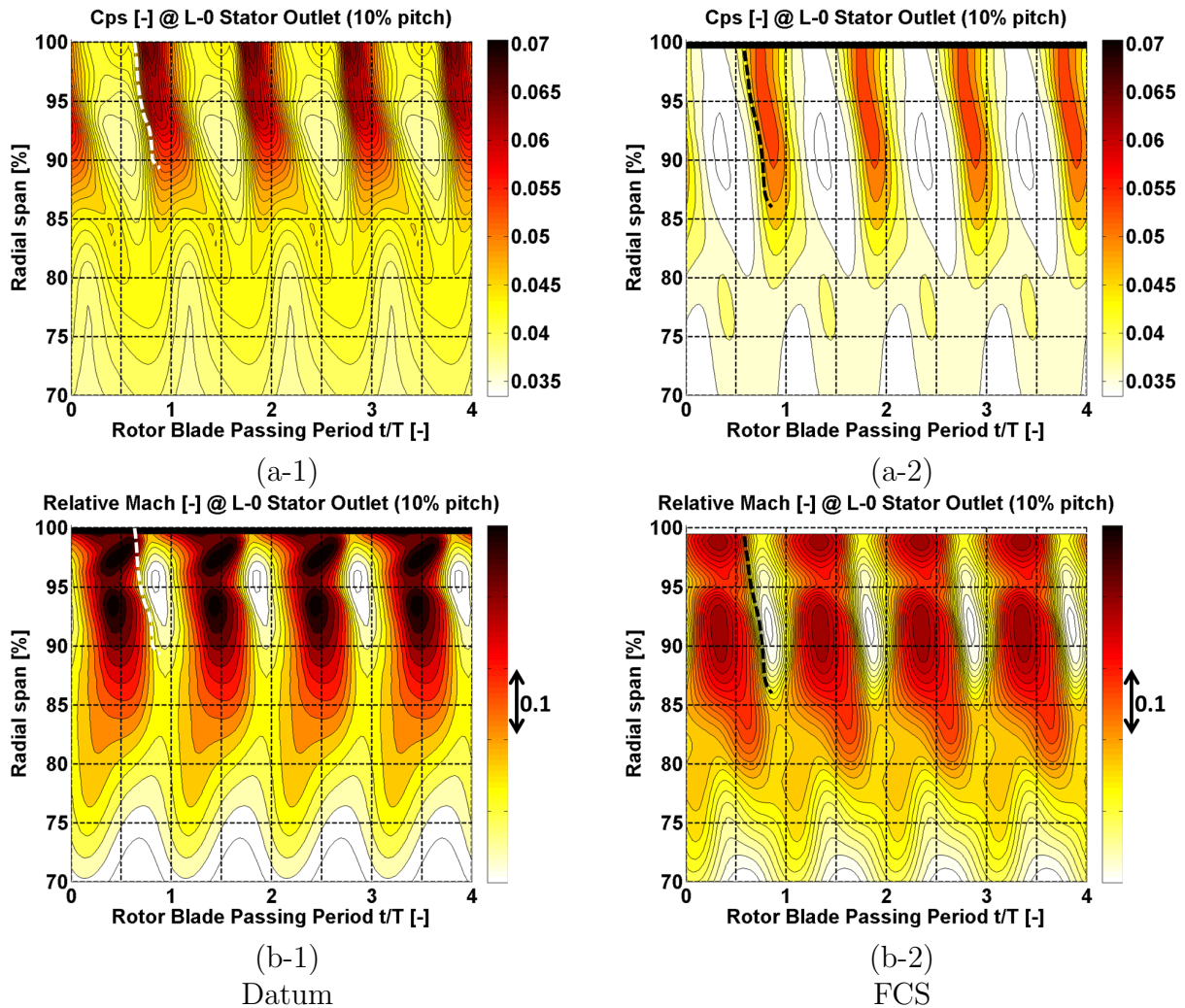


Figure 4.10: Static pressure coefficient C_{ps} and relative Mach at 10% of stator pitch (high unsteadiness region) from 70-100% of tip span. Datum design is shown on the left (*-1) and forward curved sweep to the right (*-2).

4.4.2 Three-dimensional flow through L-0 stator tip passage

In this section, the analysis of L-0 nozzle tip passage and endwall flow is presented. The design intent of forward curved sweep is to improve flow aerodynamics in the L-0 stator tip passage and endwall flow by a reduction of the meridional sweep of the incoming flow. This must improve the orthogonality of flow to the airfoil and loading proportional to ρC_m^2 for FCS design instead of ρC_x^2 of the radially stacked blade in datum design. The computational results show a substantial increase in loss in stator tip region for modified case (see Figure 4.6 (a-1)). The time-resolved flow through nozzle tip region demonstrates a steady behavior from the inlet to about 60%-75% of blade axial surface span. The flow unsteadiness increase on the suction side of the nozzle from about 80%-100% of the radial tip span. The discussed flow unsteadiness can be observed in static pressure distributions on nozzle blade surface as shown in Figure 4.13 and 4.14. The instantaneous blade-to-blade contours are considered sufficient for analysis of L-0 stator inlet and tip-endwall as presented in Figures 4.11 and 4.12.

The instantaneous blade-to-blade contours, parallel to flared casing, for entropy loss q , streamwise vorticity Ω_s , for 90% and 98% of radial span are shown in Figure 4.11. The datum (left) and forward curved sweep (right) contours are plotted side by side whereas the location of tip axial planes in Figure 4.12 are indicated with white solid lines on 98% contour plot at the top. The streamwise vorticity and entropy loss gradually increase from 90% of radial span towards 98% of tip span for both Datum and FCS stacking as shown in Figure 4.11 (a) and (b) respectively. As shown in entropy loss contours (b), two regions of elevated entropy loss are identified, stator suction side with high blade turning angle and axial gap. As blade to blade contours are extracted at a plane parallel to flared casing (meridional plane), axial axis from left to right show contours at higher spanwise positions. The entropy loss, as well the streamwise vorticity is increased in the axial gap for both 90% and 98% respectively. For 98% plane, the streamwise vorticity gradients smooth out in axial gap downstream with pronounced entropy loss in the region. This entropy rise is partly linked to pronounced loss sources in tip passage and further flow mixing downstream in the axial gap. Stator suction side and casing endwall flows are the main sources of this loss. The stator suction side loss is labeled as feature 1. The primary reason for the increase in feature 1 loss is the pronounced convex curvature of the airfoil in the meridional plane, as a result of the axial sweep. The introduced lean with suction side facing towards tip casing (as shown in Figure 4.12 (a-2)) introduce increased flow acceleration on suction side. Increase in absolute Mach is also a result of reduced throat area in the meridional plane at 98% of span. The tip passage vortex is shown by positive streamwise vorticity and labeled as feature 2. Increased flow acceleration delay migration of tip passage vortex to suction side in FCS design. The horseshoe vortex from the suction side is shown by -ve streamwise vorticity, labeled as feature 3.

The changes in flow aerodynamics and loss mechanisms are further explained with

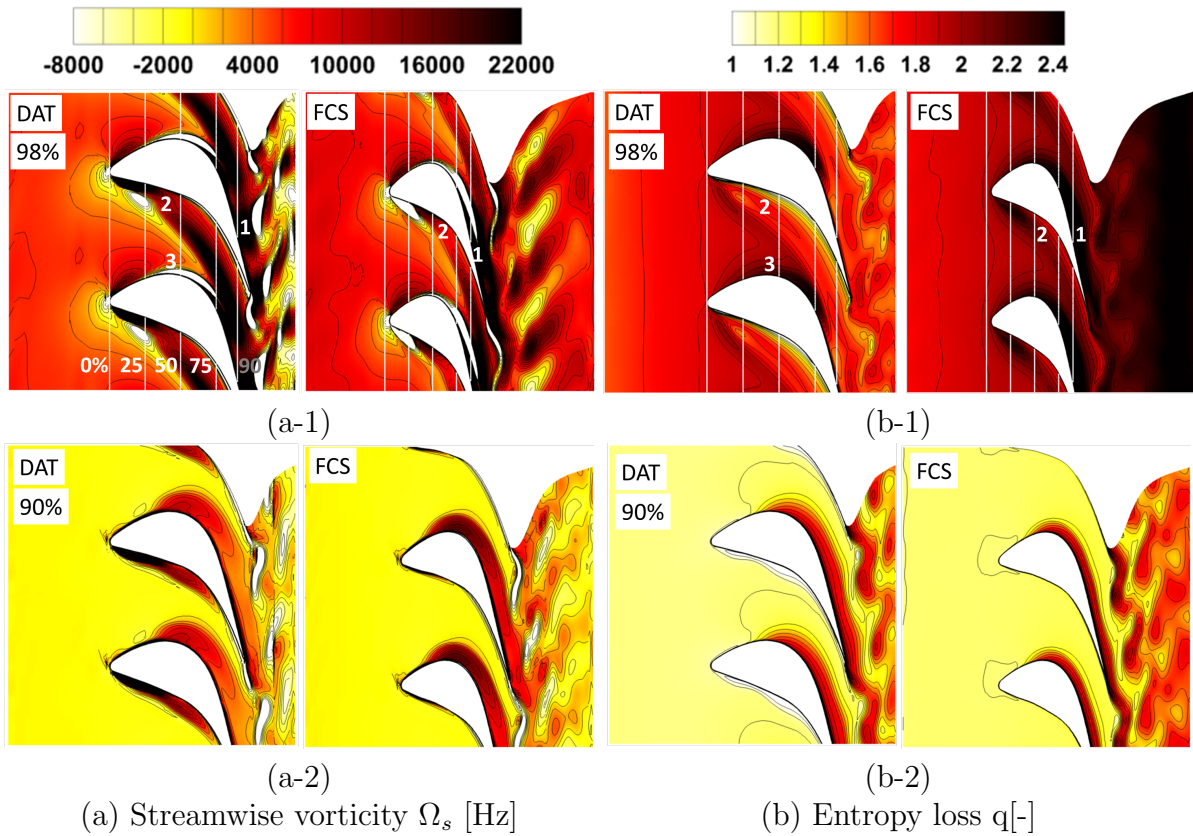


Figure 4.11: Instantaneous blade-to-blade contours from L-0 stator tip region for datum and forward curved sweep case. Streamwise vorticity and entropy loss increase towards stator tip.

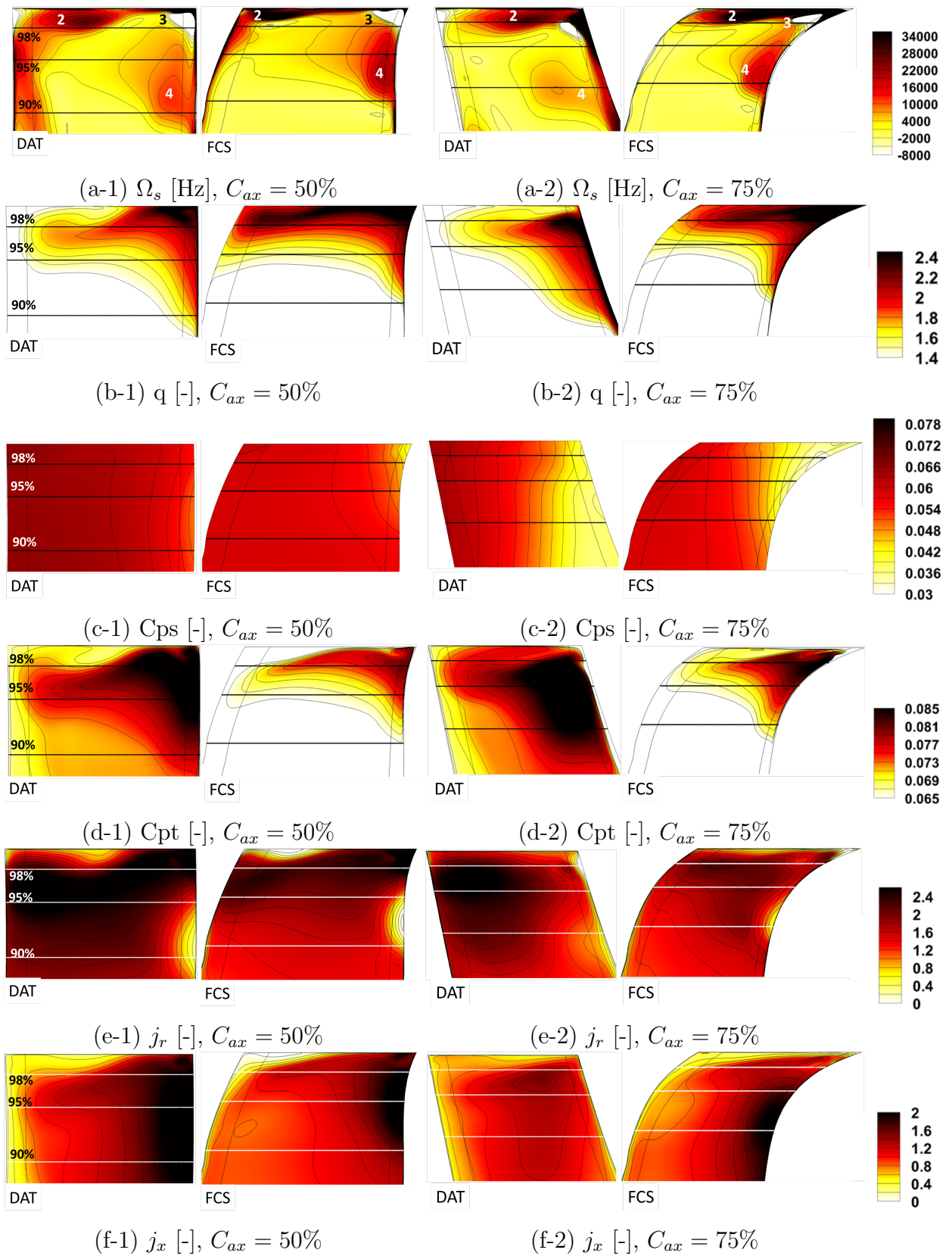


Figure 4.12: Instantaneous contours for L-0 stator tip passage in axial ($r-\theta$) plane at 50% and 75% of axial chord length. The pressure side is on the left and suction side of stator airfoil is on the right in all the figures. Streamwise vorticity and entropy loss increase in tip passage and endwall flow for forward curved sweep design towards stator trailing edge.

blade-to-blade contours in axial ($r - \theta$) plane in the tip region, at 50% and 75% of L-0 stator axial chord length as shown in Figure 4.12. The spanwise location is labeled with a black solid line and labeled with the percentage of radial tip span on the left. The pressure side of the stator airfoil is on the left and suction side on the right in all plots. Streamwise vorticity (a), entropy loss (b), static pressure coefficient C_{ps} (c), total pressure coefficient C_{pt} (d), radial specific mass flux ρC_r (e) and axial specific mass flux ρC_x (f) are shown respectively. The tip passage vortex, feature 2 become more intense at $C_{ax}=50\%$ for sweep design as shown by streamwise vorticity Ω_s in Figure 4.12 (a-1). The increase in positive streamwise vorticity is a result of a reduction in axial and radial mass flux near casing as shown in Figure 4.12 (e-1), (f-1). At $C_{ax}=75\%$ (figure (a-2)) the datum design has a negative lean with pressure surface facing the casing endwall. The forward curved sweep design introduces lean as a result of axial displacement of blade profiles (opposite to datum design). As argued by Denton et al. [15], the lean effects are similar to moving the airfoil in a frozen pressure field. In this scenario, C_{ps} at $C_{ax}=75\%$ (figure (a-2)) display a similar result. The reduction of static pressure on the suction side corner to the casing accelerates the flow (increase in absolute Mach). This is the same region where maximum entropy loss accumulate as shown in Figure 4.12 (b-2) at $C_{ax}=75\%$. Note that, part of this high entropy loss comes from L-1 leakage flow. Nevertheless, at both $C_{ax}=50\%$ and 75% entropy loss contours are pronounced near casing and suction side with increased area cover. The positive streamwise vorticity is more intense next to casing and suction side at both axial locations. The radial specific mass flux j_r (or radial velocities) decrease through tip passage at both axial locations (Figure 4.12 (e-1) and (e-2)). Forward curved sweep is known to reduce stream surface twist (Havakechian et al. [56]), by reduction of meridional flow path's sweep at inlet and exit of L-0 stator.

In conclusion, despite the flow stream surface twist is reduced in the L-0 tip passage, and reduction of radial velocities allow useful flow expansion; instead, the overall loss and streamwise vorticity are increased for FCS design. The phenomena responsible for this loss is found to be the introduction of suction side lean facing towards casing. This not only introduces reduced L-0 throat area in the tip span, as well as introduce strong convex curvature on the suction side in the meridional flow path. The increased absolute Mach (flow expansion) in tip passage pronounce streamwise vorticity at casing endwall and suction side corner. The entropy loss is increased in these regions. The suction side flow after interaction with bow shock shed as stronger streamwise vorticity gradients. These streamwise vorticity gradients are mixed out in the axial gap to introduce further entropy loss. Nevertheless, it is important to note that despite the increase in losses, the increase of absolute Mach decrease relative Mach to rotor tip inlet, and improve flow expansion through supersonic airfoils.

L-0 stator static pressure loading: Figure 4.13 show time-averaged and min/max envelop of static pressure distribution for L-0 stator at 80%, 90% and 98% parallel to flared casing. Forward curved sweep design reduces meridional sweep at leading and trailing

edge. The stator blade profiles at leading and trailing edge become about perpendicular to the incoming and leaving flow. The static pressure loading increase at 98% and 90% of radial span as the loading is proportional to ρC_m^2 as compared to ρC_x^2 for datum design (comparison of Figure 4.13 (a-1) to (a-2)). The L-0 stator is counter loaded at the leading edge as shown by Cps distribution at 80%-98% of radial span. The counter loading is reduced as a result of improved incidence (workload shift, L-1 increase in reaction improve incidence to L-0 stator). The static pressure distribution show unsteadiness at about 0.7-1.0 of meridional surface span at 98% (see Figure 4.13 (a-1) and (a-2)). This unsteadiness is reduced for FCS design at 98%, (Figure 4.13 (a-2)) and increased at 90% of span (b-2). The increase in unsteadiness at 90% span is a result of the **S1** shock moving to a lower spanwise position as a result of the increased axial gap.

Figure 4.14 show time-resolved static pressure distribution for four rotor blade passing period for datum and FCS design at 98% of span. The meridional wall surface span of -1 represents pressure side leading edge whereas 0 represent pressure side trailing edge. The surface span of 0-1 represents trailing edge to leading edge of the suction side. The pronounced unsteadiness is seen on the suction side from 0-0.3 of wall surface span and -0.1 to 0.0 on the pressure side in the datum design as shown in Figure 4.14 (a-1). The bow shock **S1** impinge suction side at about 0.3 of wall surface span. In time, the shock front travel to trailing edge 0.0 and stays attached to the pressure side up to about -0.1 of wall surface span as shown by high Cps values in datum case as shown in Figure 4.14 (a-1). The intensity of static pressure for FCS design is reduced, however, area cover in time is increased. The shock interacts with a suction side for a longer duration of time to increase unsteadiness (at 98% of span). This should introduce additional boundary layer losses on suction side as explained in the previous section.

In conclusion, the static pressure loading (flow expansion) is improved from 90%-100% of span and reduced at 80% of span. The increase in flow expansion is linked to the increase of absolute Mach in the tip region and the reduction of relative Mach to rotor inlet. The reduction of relative Mach is a desirable design improvement. The incidence to L-0 stator is also improved as a result of increased L-1 stage reaction. Together with improved flow expansion and incidence, the counter loading at the leading edge is reduced. The static pressure unsteadiness is also decreased at 98% and increased at 90% of span. Overall flow expansion improvements are desirable, however, increase in loss as explained in this section is an undesirable outcome. The analysis of the rotor in the next section explains the improvements in the rotor supersonic tip airfoils result in reduced entropy loss and improved efficiency.

4.4.3 L-0 rotor aerodynamic improvements

The main flow aerodynamic improvements are observed in the tip span region of the supersonic airfoil as shown in Figure 4.6 (b-1). The loss mechanisms reported for the

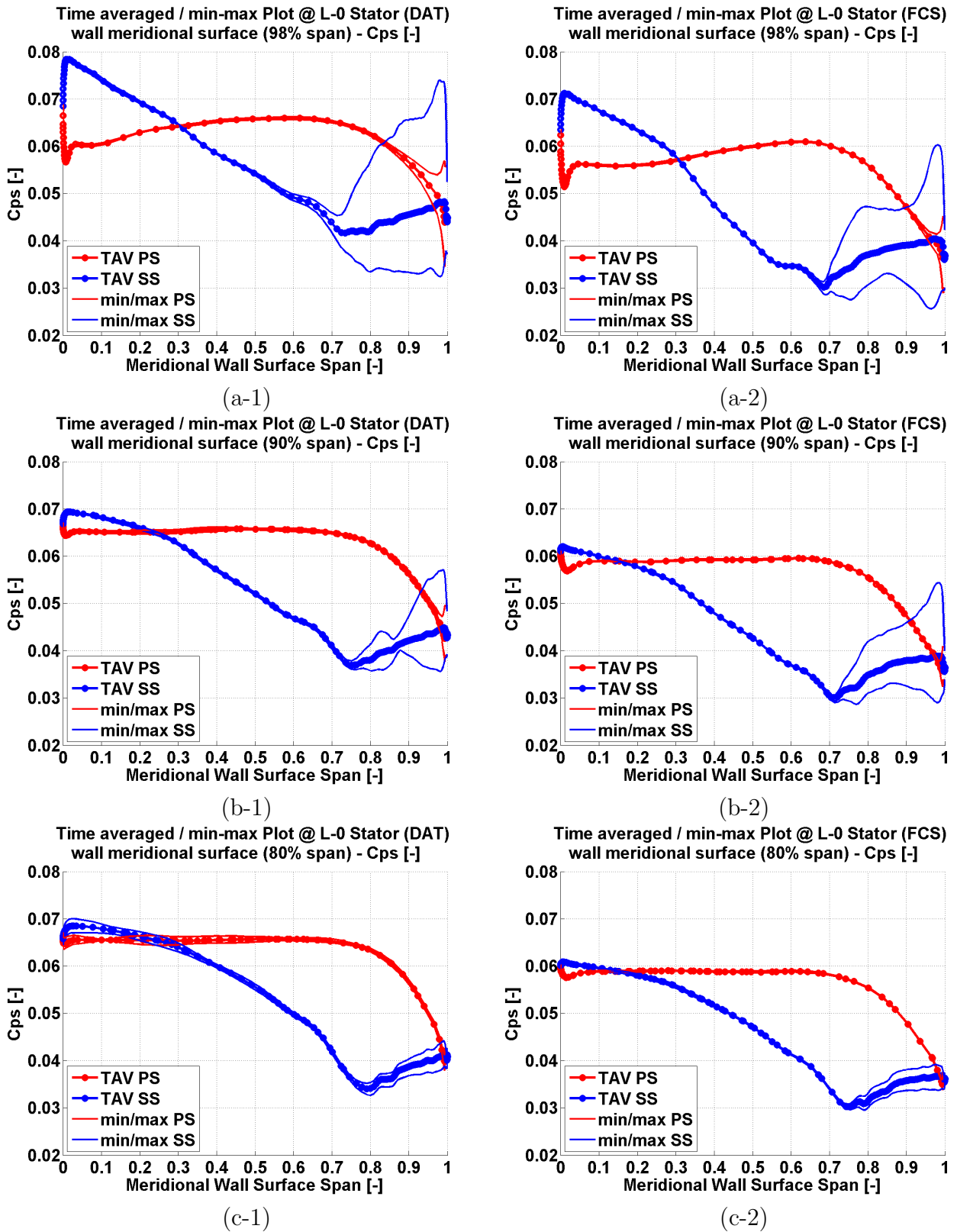


Figure 4.13: The time-averaged and min/max envelope of blade static pressure loading C_{ps} for L-0 stator tip passage at 80%, 90% and 98% of radial span respectively. The forward curved sweep improves flow by reducing blade leading edge counter loading. L-0 stator C_{ps} loading is increased towards tip endwall at 98% of radial span and reduced towards hub span.

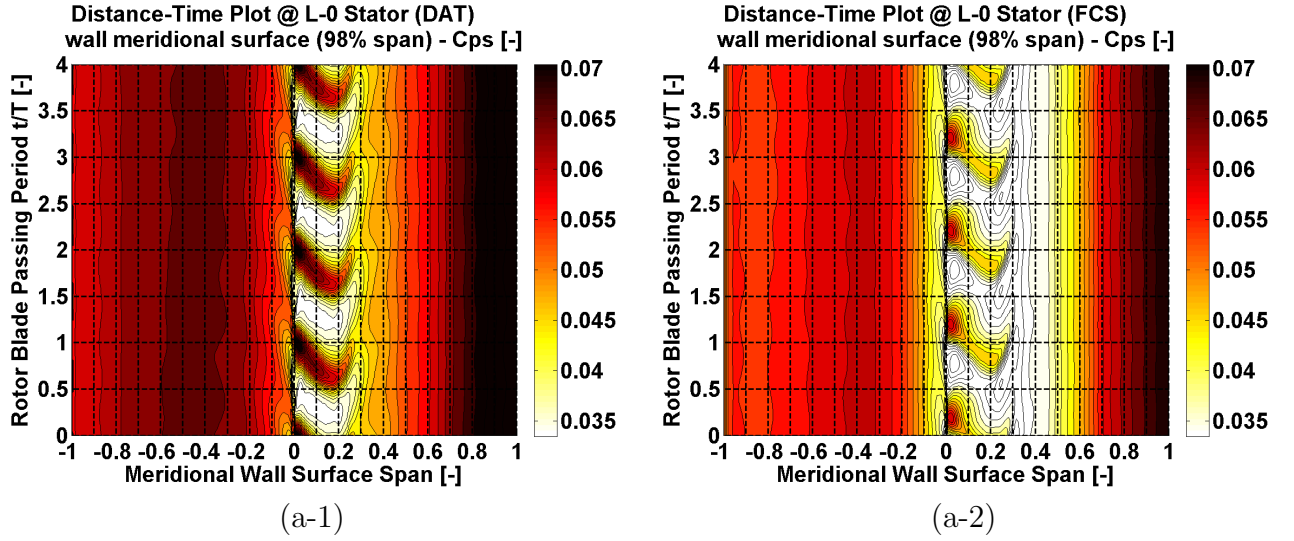


Figure 4.14: Time-resolved static pressure loading C_{ps} for L-0 stator tip passage at 98% of radial span respectively for datum and FCS design.

supersonic airfoil design discussed in this work are shown in Figure 1.6. Senoo et al. [24] report six loss generation mechanisms as explained in chapter 1.

Time-averaged contours for entropy loss and streamwise vorticity at the rotor exit plane located at $x/C_{ax,rotor} = 1.94$ (94% of rotor tip axial chord length downstream of rotor tip trailing edge) are shown in Figure 4.15. The plots show 70-100% of radial span for two rotor pitch. The observer is looking into the axial direction of flow towards the machine exit. Rotor rotation is directed from left to right. Four entropy loss features are identified and labeled as follows. Rotor wake **W**, rotor trailing edge shock **S3**, tip shroud boundary layer loss **TS** and tip cavity and diffuser casing separation loss **CS**.

Two rotor wake features are visible in the contours. The location of wake **W** is marked with thick dotted white line starting from 95% of tip span at about 0.85 of pitch and inclined towards left, interacting with shock **S3** marked with thin white dotted line, at about 85% of radial span, as shown in Figure 4.15 (a-1) and (a-2). Rotor wake at 93%-96% of span shows a positive streamwise vorticity region on the right **W1** and negative streamwise vorticity region on the left **W2**. The feature **W1** and **W2** are both parts of the wake with pronounced intensity at about 95% of span. The source of positive streamwise vorticity **W1** is the compression wave **C1** on the suction side convex curvature region near tip airfoil trailing edge, as shown in Figure 1.6. The adverse pressure gradient introduced by **C1** induce positive tangential vorticity component as a result of shear introduced by axial and radial velocity gradients. The flow is decelerated axially and radial velocities increase. The shock **S3** following compression wave **C1** introduce further adverse pressure gradient. Flow upstream of **S3** shock front reduce radial velocity and downstream shock front radial

velocities increase. The positive tangential vorticity is convected with the rotor wake side by side with feature W2. The feature W2 is created at rotor trailing edge with dominant negative axial vorticity as the dominant component. The wake W carries blade profile loss as shown in entropy loss contours in Figure 4.15 (b-1), (b-2). The forward curved sweep design shows a decrease in loss throughout 70%-96%. The streamwise vorticity gradients for feature W1 and W2 at 92%-95% of span and corresponding entropy contours show a reduced area cover and intensity. The vorticity gradients introduced by S3 shock at 0.2 pitch from 85%-95% of span reduce and resulting entropy loss decrease.

The feature **TS** is spread from 96% to about 98% includes shroud losses. This feature has three components. The first component is loss generation due to supersonic flow expansion at shroud lower wall (attachment to rotor tip). The supersonic flow expansion in shroud endwall generates a thick boundary layer. The second component is shroud wake loss. The third component includes tip shroud endwall losses from the cavity. The fourth feature **CS** includes losses from tip cavity casing and flow separation introduced by diffuser geometry flare downstream of rotor tip cavity. In conclusion, both streamwise vorticity and entropy loss are reduced at rotor exit in the tip span region of supersonic flow expansion.

Time-resolved flow entropy loss \mathbf{q} and relative Mach for one rotor pitch at 91% of radial span at rotor exit plane $x/C_{ax,rotor} = 1.94$ are shown in Figure 4.16. The time-resolved plots show four rotor blade passing period on the vertical axis. Two inclined parallel lines are labeled as W and S3. The feature W show a larger area cover of entropy loss in Figure 4.16 (a-1) as compared to feature S3. The intensity of feature W that represents rotor blade profile and wake loss and S3 for trailing edge shock loss is reduced for FCS design as shown in Figure 4.16 (a-2). The values of relative Mach at rotor exit show flow expansion (or over-expansion) through rotor airfoils. As clearly shown in the Figure 4.16 (b-1), relative Mach increase to maximum values upstream of shock front from about 0.3-0.6 of rotor blade passing period at 0% of rotor pitch span. Pronounced relative Mach values are a result of flow over-expansion on the rotor suction side terminated by shock S3. Immediately, after the shock front S3, the relative Mach decrease to a minimum and then recover to free-stream value and decreased again slightly in the stator wake. Clearly, as shown in Figure 4.16 (b-2), the modified design the flow over-expansion is reduced upstream of the shock front. The analysis shows a reduction in over-expansion of flow through rotor passage results in entropy loss reduction.

The time-averaged and min/max (unsteadiness envelop) static pressure loading C_{ps} for L-0 supersonic airfoil is presented in Figure 4.17 for 90% and 95% of radial span. A decrease in static pressure loading is observed in these plots. This indicates a reduced flow expansion through supersonic airfoils. The increase in pressure ratio across the L-0 stage reduces the flow expansion through supersonic tip airfoils. These supersonic airfoils are designed for a unique incidence (relative inlet Mach and incidence combined). This

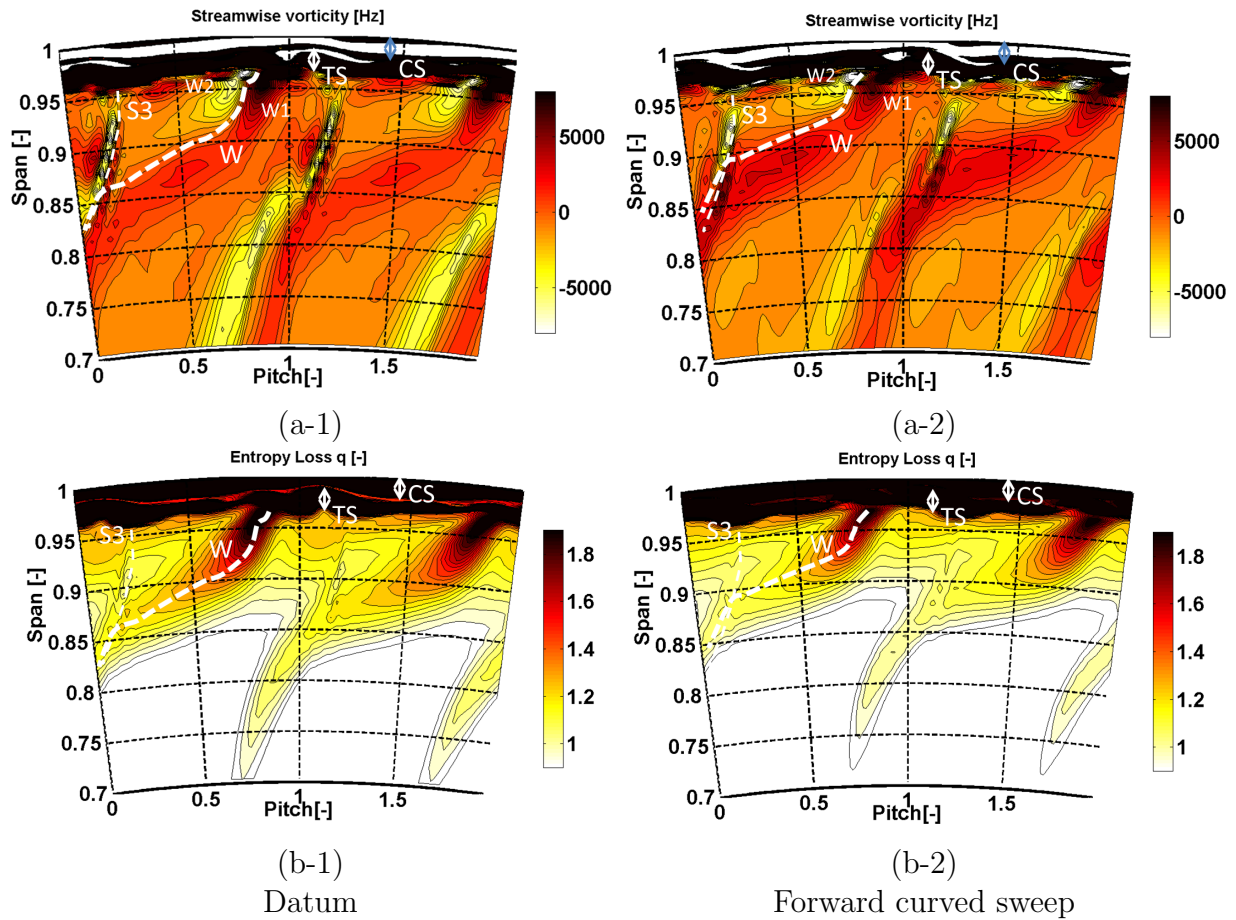


Figure 4.15: Time-averaged entropy loss $q[-]$ and streamwise vorticity $\Omega_s[Hz]$ contours (in relative frame of reference) for Datum on the left and forward curved sweep on the right at L-0 rotor exit tip region (70%-100%).

unique incidence is identified as the flow impinging pressure side of rotor from 0.0 to about 0.5 of rotor axial surface span (see Figure 4.17 (a-1)). The adjacent rotor leading edge shock S1 impinge at about 0.65 of the axial surface span as indicated by elevated static pressure. This is followed by increased flow expansion introduced by convex curvature on the pressure side trailing edge region. On the suction side (0.1 of axial span), at 90% of radial span, concave curvature introduces sudden expansion and afterward a smooth flow expansion up to 0.97 of the axial span. The expanding flow on the suction side is slowed down by compression wave C1 at the trailing edge. The expanding flow through passage is terminated by trailing edge shock S2 downstream. Nevertheless, smooth supersonic flow expansion for the designed airfoils is achieved by a unique incidence and a pressure ratio.

The rotor tip airfoils are counter loaded at tip for both 90% and 95% of radial span

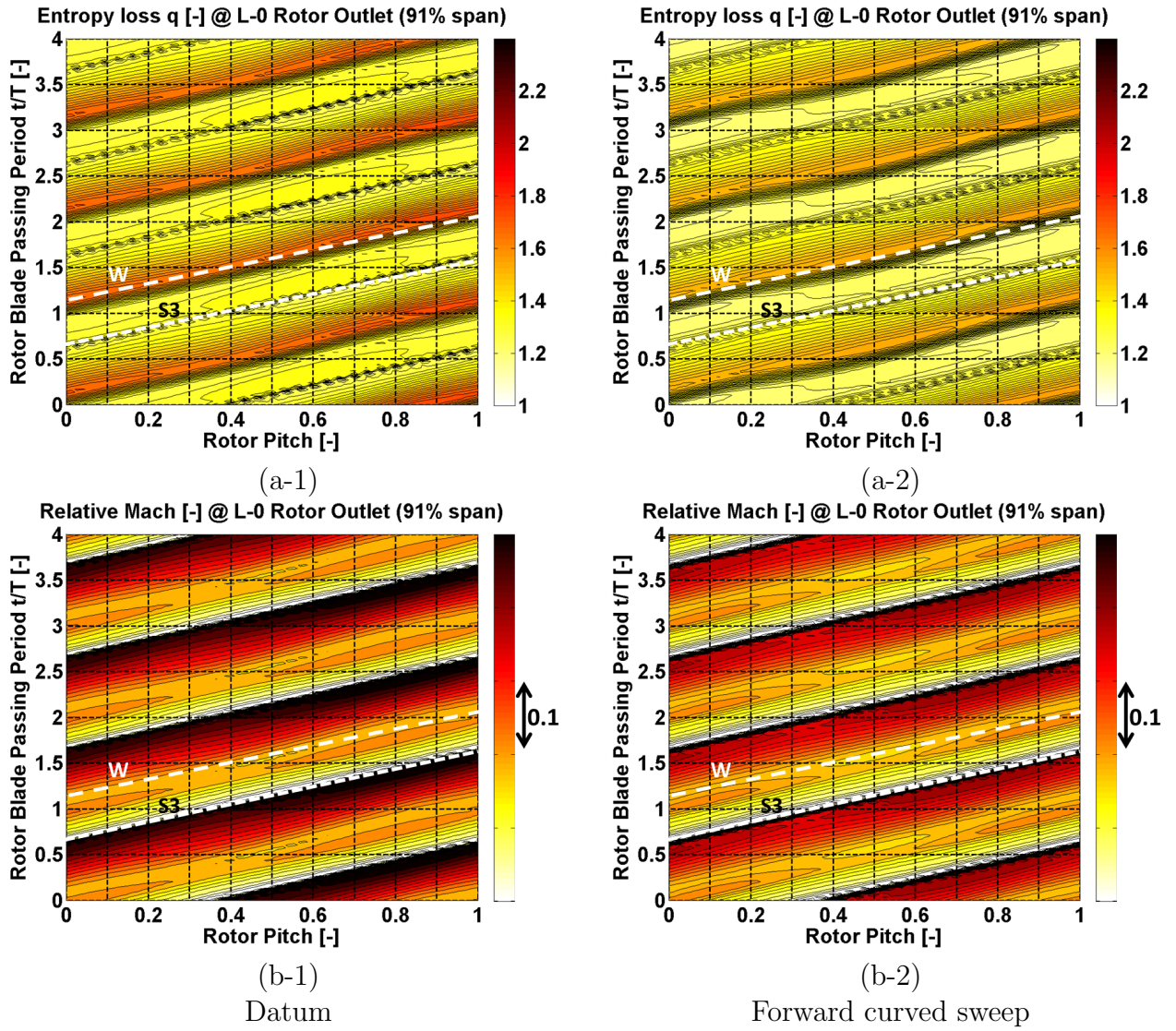


Figure 4.16: Time-resolved entropy loss q [-] and relative Mach M_{rel} [-] contours (in absolute frame of reference) for Datum on the left and forward curved sweep on the right at L-0 rotor exit (91% span).

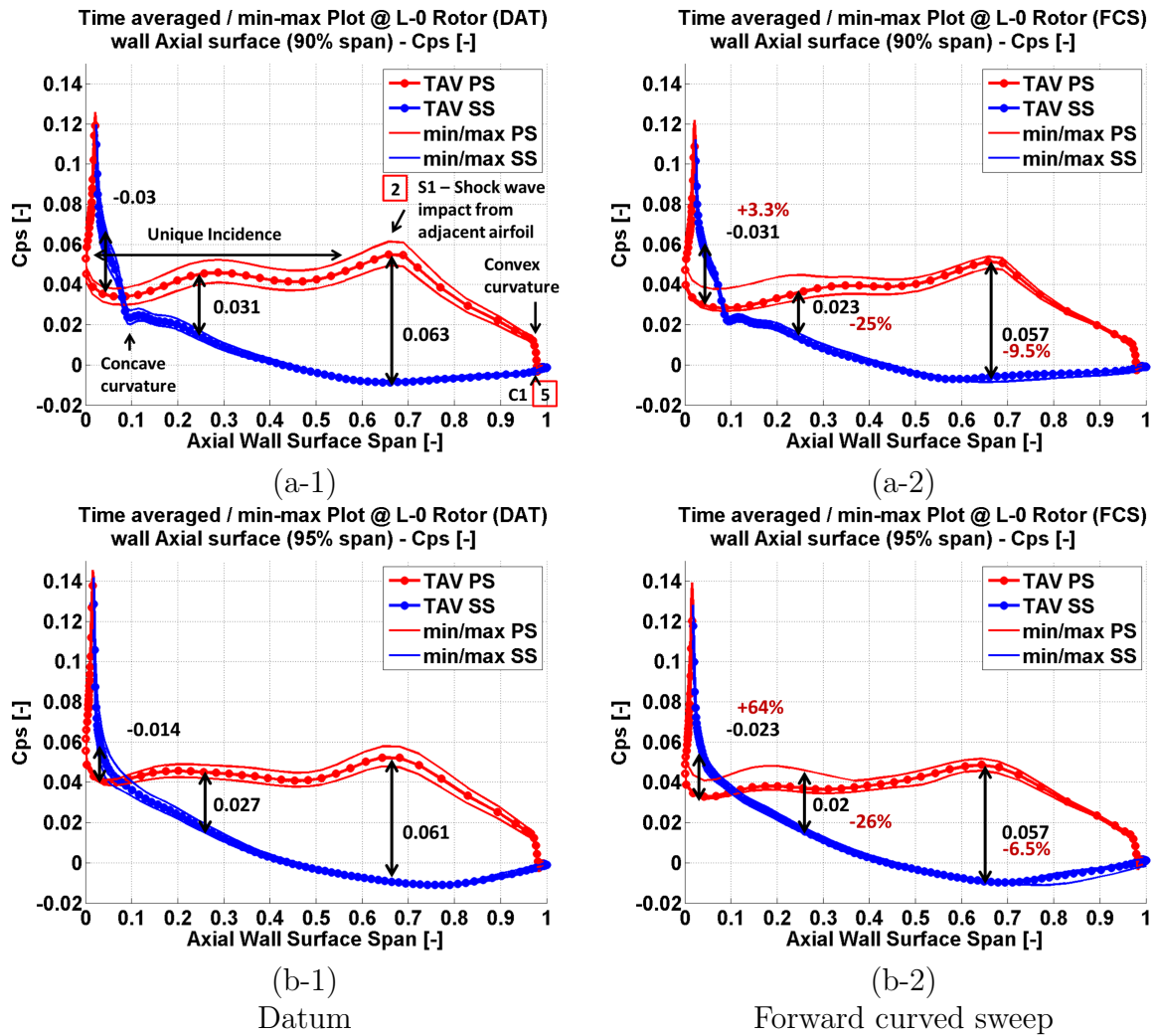


Figure 4.17: Time-averaged and min/max envelop of static pressure C_{ps} distribution on a rotor wall surface at 90% and 95% respectively. Static pressure loading and airfoil lift are reduced in the tip region as a result of increased pressure ratio across rotor $P_e/P_{o,int}$.

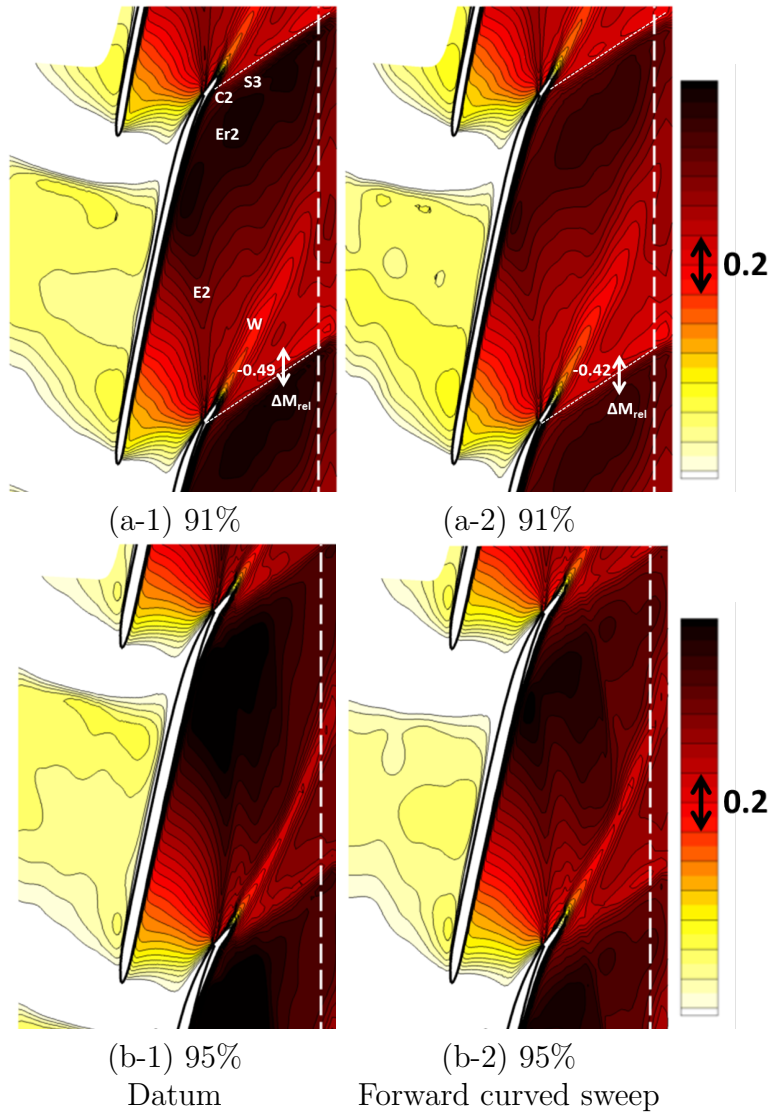


Figure 4.18: Time-averaged relative Mach M_{rel} contours at 91% and 95% for datum on the left and FCS on the right respectively.

shown in Figure 4.17. This counter loading is increased by 3.3% and 64% at 90% and 95% respectively for FCS design. The static pressure loading at 0.25 of the axial surface span is reduced by 25% and 26% respectively for 90% and 95% of the radial span. The loading at 0.65 of the axial surface span is reduced by 9.5% and 6.5% respectively. The flow expansion in the front to mid of axial surface span is reduced predominantly. This region also experiences a pronounced pressure unsteadiness for both 90% and 95% radial span position. The unsteadiness at impinging bow shock S1 to pressure surface is reduced at about 0.65 of the axial span. The overall entropy loss and streamwise vorticity are reduced at the exit of the rotor (see Figure 4.15) despite a pronounced unsteadiness at the inlet of the rotor. The overall unsteadiness on the pressure surface increase from about $\pm 19\%$ to $\pm 25\%$.

Time-averaged blade-to-blade contours of relative Mach at 91% and 95% are shown in Figure 4.18. The datum design is shown on the left and FCS on the right. The white dotted line show the location of rotor exit plane $x/C_{ax,rotor} = 1.94$ for the plots presented earlier in Figure 4.15 and 4.16 respectively. The flow expansion is reduced at both spanwise locations 91% and 95% as shown. At 91% the strength of expansion wave E2 is reduced and resulting flow over-expansion on the suction side of the rotor is reduced by a 0.09 decrease in relative Mach. The shock S3 strength is also reduced as a result. The inlet values of relative Mach at throat are about 0.01 low in the modified design locally. At 95% the expansion wave result in even more pronounced over-expansion compared to 91% of rotor tip span as shown in datum design Figure 4.18 (a-1), (b-1). The flow over-expansion is reduced at 95% of the rotor radial tip span for FCS design.

In conclusion, despite a pronounced static pressure unsteadiness in inlet conditions, the entropy loss and streamwise vorticity are reduced in the supersonic flow expansion through L-0 rotor tip. The decrease in loss is attributed to reduced flow expansion as a result of an increase in stage pressure ratio, as a result of L-0 stator annular throat area increase. This also results in overall last stage workload decrease.

Tip cavity mass flow: The averaged mass flow for L-0 tip cavity is decreased from 5% in the datum to 4.51% in the FCS design. The mass flow unsteadiness at L-0 cavity inlet is increased from $\pm 0.2\%$ in the datum design to $\pm 0.23\%$ in the forward curved sweep design.

4.5 Concluding summary and remarks

The important findings in this chapter are as follows.

- Forward curved sweep design improves η_{tt} and η_{ts} for two-stage combined, by 1.3% and 1.1% respectively. The last stage η_{ts} efficiency with part diffuser increase by 1.0%.

- The design increase two stages combined work extraction by 1.57%.
- The forward curvature sweep reduces L-0 stator annular throat area. In an attempt to retain constant theoretical throat area a blade twist is applied with throat opening throughout the span. However, computations predict an increase in the annular throat area. The exact location of the throat in the stator tip span is difficult to establish for two reasons. The flow is subsonic and adverse pressure gradients by rotating bow shock introduce unsteadiness in mass flow passing through L-0 stator tip region.
- Increase in throat area introduces workload shift (L-1 stage extract 3.4% more specific work Δh_o). This decrease inlet total pressure to L-0 stage and increase the L-0 stage pressure ratio.
- Increase in L-0 stator annular throat area increases the reaction of both L-1 and L-0 stage.
- Leaving loss at L-0 rotor exit increase by 12.32%. This leaving loss is contributed by an increase in radial velocities at rotor exit.
- Axial displacement of blade profile in FCS introduces a lean on stator suction side (mid-span to trailing edge) facing towards tip casing. The stator throat in the meridional plane is reduced. Both of these geometrical changes increase absolute Mach at stator exit (improved flow expansion). The increase in absolute Mach reduces relative Mach to rotor inlet. This is a desirable improvement.
- FCS design increase L-0 stator tip region entropy losses by 1.98%, whereas the rotor losses in supersonic tip airfoil decrease by 5.69%.
- The introduced L-0 suction side lean and reduced throat area in a meridional plane in the L-0 tip span region increase flow expansion and losses. The main losses are introduced at tip passage endwall and suction side corner (leaned suction side). In addition, the pronounced streamwise vorticity gradients increase losses in the increased axial gap.
- Increase in axial gap decrease rotor leading edge shock strength. The bow shock adjusts the radial position to come in contact with L-0 stator trailing edge at a lower spanwise location. This introduces a pressure gradient between high Cps after bow shock front and the casing. A casing separation is introduced that rotates along with the bow-shock.
- A weak bow shock in increased axial gap pronounces static pressure unsteadiness.
- In the datum design, the axial distance between rotor and stator vary as the rotor rotates from the suction side towards stator trailing edge. This decrease in axial gap introduces pronounced incidence and relative Mach (as well as unsteadiness). With

an increase in the axial gap, both the average values and unsteadiness of incidence and relative Mach to rotor decrease. These are the desired outcome by FCS design.

In conclusion, forward curved sweep design even with non-constant throat area is able to introduce desirable efficiency improvements in the last stages of a low-pressure steam turbine with the supersonic flow in the tip region. The trailing edge suction side lean as well reduced throat area in meridional flow path introduced by forward curvature increase the stator losses. However, flow expansion through stator tip is improved resulting in Mach relative decrease (M_{abs} increase) at rotor inlet. The improvements in flow expansion through supersonic tip airfoils decrease entropy loss. The supersonic flow expansion improvements are introduced by either increase in the last stage pressure ratio or relative Mach at rotor inlet. A further investigation is required with constant throat area to individuate improvements by workload shift (increased L-0 pressure ratio) or inlet relative Mach decrease (Forward curved sweep design). The role of reduction in unsteadiness of unique incidence to supersonic rotor inlet is unclear and require further investigation.

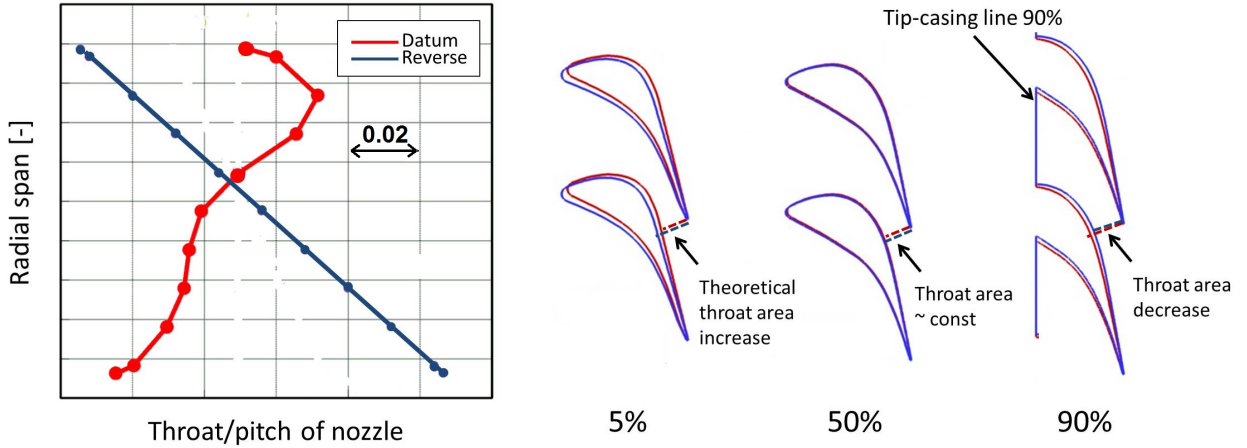
Chapter 5

L-0 stator stacking redesign: Blade twist-controlling throat to pitch ratio

In the previous chapter 4, a forward curved sweep design is analyzed in order to predict the influence of increased axial stator-rotor gap on shock **S1** aerodynamics and performance of the last stage (L-0). The flared casing of L-0 stator results in a reduced annular throat area. Despite an effort to keep throat area constant by blade twist, the throat area change (increase) in forward curved sweep design. Nevertheless, stator twist as a blade stacking option allows blade design to ensure a constant throat area as well as change stage reaction variation and L-0 stator loading distribution. In this chapter, L-0 stator twist design is analyzed with the aid of time-resolved computations and impact on **S1** shock and stage aerodynamic performance is discussed. The same mesh of two-stage (L-1, L-0, part diffuser combined) including tip cavities and seals is used in this analysis.

5.1 Stator twist design

The stator twist stacking is employed in addition to advance vortex nozzle (AVN) design in this work. L-0 stator throat to pitch ratio is increased at the hub and decreased at the tip on datum AVN design as shown in Figure 5.1 (a). An increase in the throat to pitch ratio at the hub is enabled by opening up of throat area (TA) by twist whereas pitch is kept constant. The stacking line is set at trailing edge of L-0 stator. The TA is increased at hub 5%, about constant at mid-span 50% and decreased at 90% as shown in Figure 5.1 (b) respectively. The opening up of throat area in the hub region is expected to reduce flow expansion through the stator, lower absolute Mach, increase static pressure and hub reaction. The effect should revert in the tip region with flow absolute Mach increase and reaction decrease.



(a) Spanwise throat-to-pitch ratio

(b) Blade-to-blade schematic

Figure 5.1: Spanwise throat to pitch ratio variation datum (red) and Reverse throat-to-pitch ratio (blue) stator modification in (a) whereas 5%, 50%, 90% blade to blade profile schematic (b) are shown respectively.

5.2 Stage efficiency and specific-work

Stage efficiency total-to-total η_{tt} and total-to-static η_{ts} improvements are presented in Table 5.1. L-1 stage η_{tt} show an improvement of 0.2%. The work extraction increase in L-1 stage by 0.23% (from 44.02% to 44.25% of two-stage specific-work combined) as shown in Table 5.2. The last stage L-0 and part diffuser domain show an improved total to static efficiency η_{ts} of 1.3%. The workload of the L-0 stage improves by 0.23%. The two-stage and part diffuser combined efficiencies η_{tt} and η_{ts} improve by 1.1% and 0.9% respectively. The modified case of Reverse design extract 1.36% of additional specific work for two-stage and part diffuser combined compared with datum design, whereas the workload shift between L-1 and L-0 stage is nominal in the modified reverse design.

Table 5.1: Stage efficiency improvements for stator twist stacking.

	L-1+L-0+Diffuser	L-0+Diffuser	L-1
$\Delta\eta_{tt}[\%]$	+1.1	+1.6	+0.2
$\Delta\eta_{ts}[\%]$	+0.9	+1.3	+0.3

Leaving loss: The computations predict averaged leaving loss increase by 30.55% for Reverse design. High leaving loss is observed in the seal jet and hub 0-12% of the

Table 5.2: Stage specific-work (Δh_o) load shift for datum and modified design. Calculations are time (30° of bucket rotation), circumferentially and radially mass averaged.

	Datum	Reverse	-
$\Delta h_{o,L-0} / \Delta h_{o,2stage}$	55.98	55.75	-
$\Delta h_{o,L-1} / \Delta h_{o,2stage}$	44.02	44.25	-
$\Delta h_{o,FCS} / \Delta h_{o,Datum}$	-	-	101.36

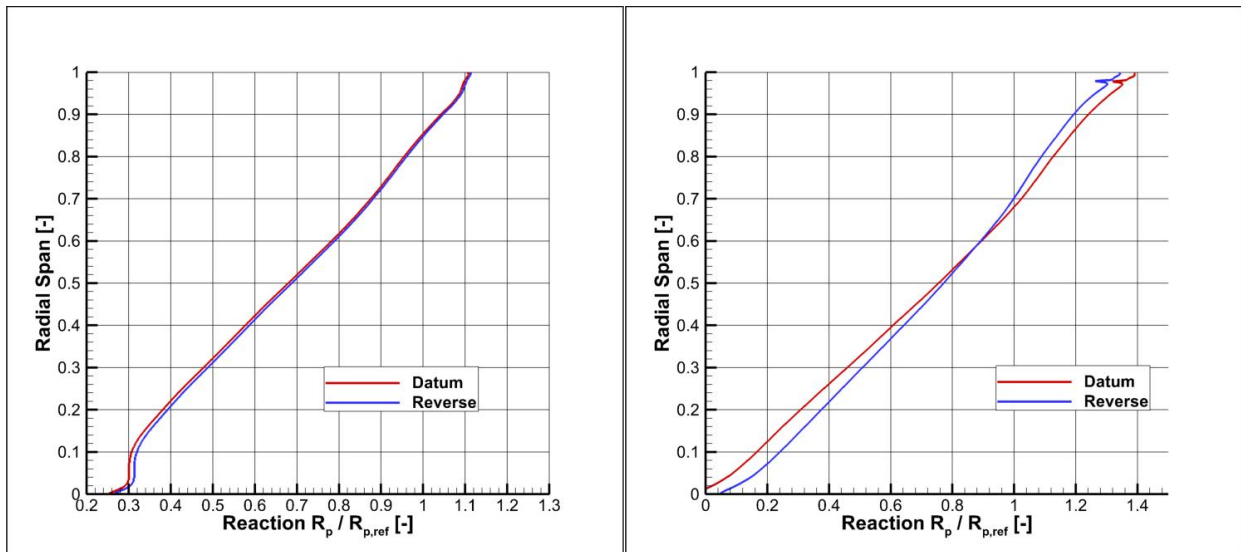
span as well 58%-85% of span at rotor exit. The individual contribution to leaving loss is dominated by an increase in spanwise radial velocities throughout the rotor exit span.

5.3 Spanwise aerodynamic performance analysis

5.3.1 Stage reaction variation and spanwise flow aerodynamics

L-0 hub reaction increase about 4% at hub (1% span) and decrease by 2.77% at the tip (99% span) as shown in Figure 5.2 (b). The L-1 reaction is about unchanged as shown in Figure 5.2 (a). The increase in static pressure Cps at hub reduce Mach absolute by 0.07 and decrease relative Mach by 0.05 as shown in Figure 5.3 (a). At 90% of tip span absolute Mach increase by 0.06 and relative Mach decrease by 0.04. The flow in tip region is near transonic and even a decrease of 0.04 relative Mach on average may have a substantial impact on shock aerodynamic and flow expansion through supersonic rotor tip airfoils. Increase in hub reaction is expected to improve potential flow separation on suction side in the rotor hub. Note that stator twist allows measurable control of reaction variation. The increase in the throat-to-pitch ratio in the hub and decrease in the tip is effectively able to control flow acceleration through L-0 stator by reducing absolute Mach at the hub and increasing at the tip in proportion to throat area change throughout radial span. The results are in agreement with the ideas presented by Havakechian et al. [57]. Opening throat area at hub and closing at tip generate concave upward streamline curvature in the stator-rotor gap to lower absolute Mach at the hub and increase near tip respectively.

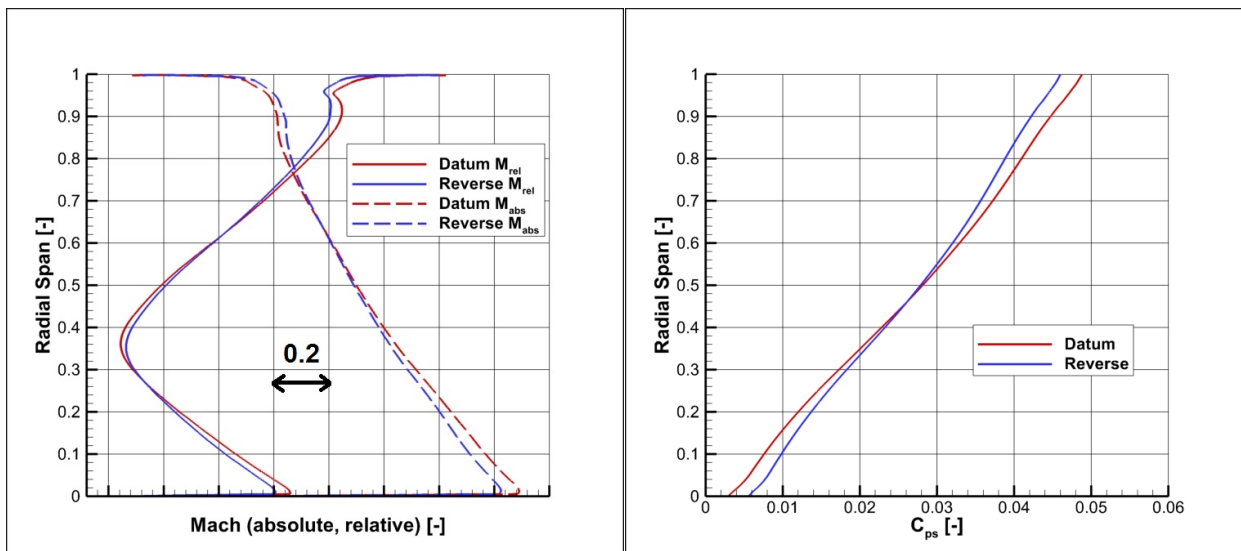
The meridional specific mass flux increase from hub to about 60% of span and decrease onwards up to tip span as shown in Figure 5.4. This is a similar trend as reaction variation in L-0 stage (see Figure 5.2), an increase in the hub to about 60% of radial span and decrease onwards to tip span. The time-averaged results show that throat-to-pitch ratio variation is an effective control mechanism for both mass flow redistribution in the stator-rotor gap and L-0 stage reaction variation.



(a) L-1 stage reaction

(b) L-0 stage reaction

Figure 5.2: Circumferentially mass averaged and time-averaged spanwise reaction variation for L-1 (a) and L-0 (b) stages respectively.



(a)

(b)

Figure 5.3: Circumferentially mass averaged and time-averaged spanwise Mach absolute, relative (a) and static pressure coefficient C_{ps} (b) in L-0 stator-rotor axial gap.

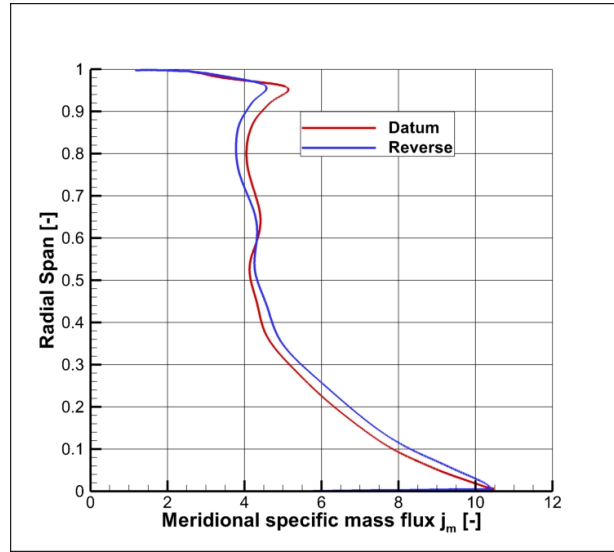


Figure 5.4: Circumferentially mass averaged and time-averaged spanwise non-dimensional meridional mass flux $j_m = \rho C_m / \rho_{ref} C_{m,ref}$ in L-0 stator-rotor axial gap.

5.3.2 Spanwise loss profiles

The spanwise distribution of entropy loss, mass flow redistribution and wetness increase across stator, rotor and part diffuser are presented in Figure 5.5. The change in each region of hub, midspan and tip are presented in Table 5.3, 5.4 and 5.5 respectively. Reverse design increase entropy loss by 3.15% in the stator tip region and reduce by 4.72% in rotor tip span from about 70% to 100% (see Figure 5.5). The increase in entropy loss is attributed to flow acceleration (Mach absolute increase) in L-0 tip region. A decrease in the relative Mach to rotor tip improves flow expansion and result in lower entropy losses. The mass flow is reduced by 3.10% in the L-0 stator tip and increase by 4.12% in the rotor tip region. Note that mass flow through the L-0 tip cavity is reduced by 0.19% as discussed later. This cavity mass flow is redistributed to rotor tip region and result in an increased work extraction. The mass flow increase of 4.12% in the rotor is related to relative Mach decrease in supersonic tip airfoils. The wetness fraction is decreased by 0.03% in stator tip and increased by 0.03% in rotor tip span.

L-0 stator hub and mid-span region improve entropy loss by 0.04% and 0.08% respectively (see Table 5.3). The mass flow increase by 2.10%, 1.00% and wetness decrease in hub region by 0.27% respectively. The wetness is about unchanged at stator mid-span. The absolute Mach in stator hub and mid span is decreased (see Figure 5.3) and resulting blade profile loss in midspan region and a weak oblique shock as well hub passage vortex are improved in the hub region respectively.

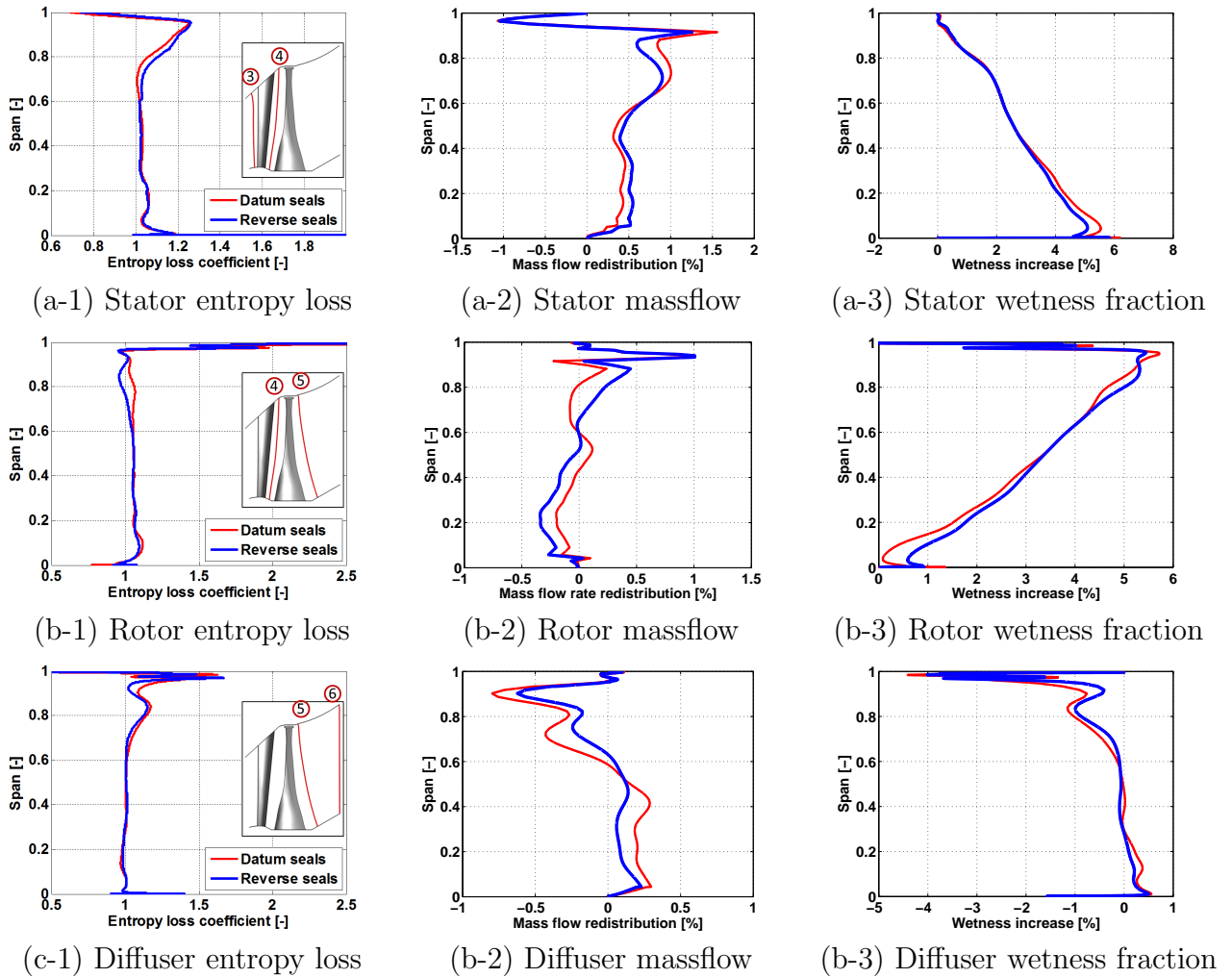


Figure 5.5: Circumferentially mass and time-averaged entropy loss, mass flow redistribution and wetness increase within stator (a), rotor (b) and part diffuser (c) respectively. Entropy loss increase in stator tip region and a decrease in the rotor and part diffuser.

The rotor hub and midspan entropy loss decrease by 0.88%, 0.43%, and mass flow reduce by 2.56% and 1.56% respectively. L-0 rotor hub improvements result from a reduction in flow separation of the suction side with an increase in hub reaction. Improvement in the midspan flow is introduced by a reduction in transonic airfoils blade profile and shock losses. The entropy loss improvement of 0.34% and 5.10% at mid and tip span of the diffuser are reported. The part diffuser hub loss is increased by 0.91%.

Table 5.3: L-0 stator: change in the loss, mass flow and wetness in each hub to tip span region

[%]	Hub [0-35]	Midspan [35-70]	Tip [70-100]
Δq	-0.04	-0.08	3.15
$\Delta \dot{m}$	2.10	1.00	-3.10
$\Delta \beta$	-0.27	6×10^{-4}	-0.03

Table 5.4: L-0 rotor: change in the loss, mass flow and wetness from hub to tip radial span

[%]	Hub [0-20]	Midspan [20-70]	Tip [70-100]
Δq	-0.88	-0.43	-4.72
$\Delta \dot{m}$	-2.56	-1.56	4.12
$\Delta \beta$	0.20	-0.23	0.03

Table 5.5: L-0 diffuser: change in the loss, mass flow and wetness from hub to tip radial span

[%]	Hub [0-20]	Midspan [20-70]	Tip [70-100]
Δq	0.91	-0.34	-5.10
$\Delta \dot{m}$	-1.04	-1.39	2.43
$\Delta \beta$	-0.12	-9.3×10^{-3}	0.37

5.4 Time resolved flow analysis

5.4.1 L-0 Stator exit flow

Figure 5.6 shows the instantaneous streamwise vorticity and entropy loss at the exit of L-0 stator. The axial plane is located at $x/s=0.39$ between L-0 stator and rotor (FRAP measurement plane). The plots show stator downstream view from 70%-100% of radial tip span and for two stator pitch of circumferential span at the same rotor blade relative position. The observer is looking towards the axial direction of flow and rotor is rotating in a left to right of circumferential pitch axis. The rotor tip leading edge bow shock is marked with white dotted lines. The entropy loss clearly increases from about 80% to 100% of span. The streamwise vorticity gradients near tip span reduce in strength and indicate pronounced mixing with increased flow expansion in the stator-rotor gap.

Figure 5.7 show time space flow field for four rotor blade passing period and one stator pitch at 90% of radial span on FRAP-HTH plane shown in Figure 5.6. One rotor tip leading edge bow shock **S1** is indicated with a white dotted line out of four visible in the plots. Clearly, the shock strength is reduced as indicated by a decrease in static pressure Cps after the shock front. The decrease in relative Mach at rotor inlet results in a reduced shock strength. The Cps unsteadiness does not show a pronounced change and increase to a maximum of ± 3.94 at 0.9 of the pitch. A decreased shock strength visibly increase incidence to the rotor leading edge. The flow incidence to supersonic tip airfoil is increased in both high (0-0.3 and 0.07-1.0) and low (0.3-0.7 of pitch) unsteadiness regions. The incidence unsteadiness at 0.11 of the pitch is increased from $\pm 7^\circ$ to about $\pm 9^\circ$ and in the region of low unsteadiness at 0.5 pitch increased from $\pm 2^\circ$ to $\pm 6^\circ$. The relative Mach is reduced in strength in the high Cps region after the shock front and reduced as well in the free stream region of low Cps. The region of high unsteadiness from 0.0-0.3 as the rotor approaches trailing edge and the distance between rotor leading edge and stator trailing edge reduces show the highest relative Mach throughout the pitch span in datum design. This feature is introduced by a decrease in absolute Mach as the rotor approaches trailing edge. With the increase in flow acceleration through the stator tip region by the closing throat, the absolute Mach increase at the trailing edge when the rotor-stator gap is minimum. The resulting relative Mach reduce. On average relative Mach is decreased by 3.7%. The unsteadiness is however increased from $\pm 20\%$ to $\pm 22\%$ at 0.1 pitch and $\pm 9\%$ to $\pm 15\%$ at 0.5 pitch. A reduction in relative Mach at rotor tip inlet as a result of blade twist (closing throat and increase in absolute Mach) results in a weaker shock **S1** and pronounced unsteadiness of both incidence and relative Mach (a pronounced unique incidence).

Figure 5.8 show time space flow field for four rotor blade passing period and from 70%-100% of radial span at 0.1 of pitch span (the pitch axis shown in Figure 5.7). One rotor tip leading edge bow shock **S1** is indicated with a white dotted line on datum (right)

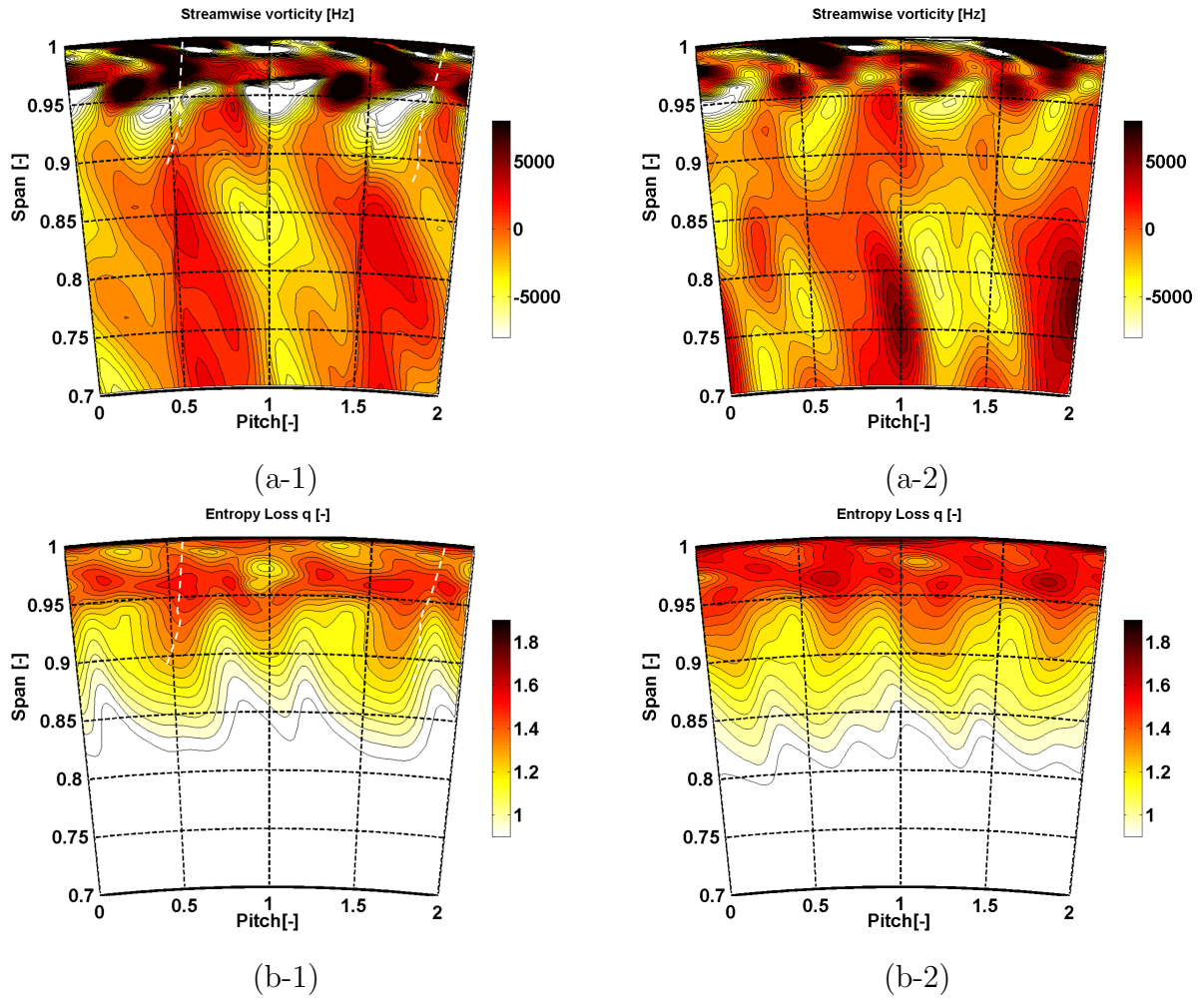


Figure 5.6: Instantaneous streamwise vorticity Ω_s [Hz] and entropy loss q [-] at the exit of L-0 stator tip for (*-1) Datum on left and (*-2) Reverse design on the right.

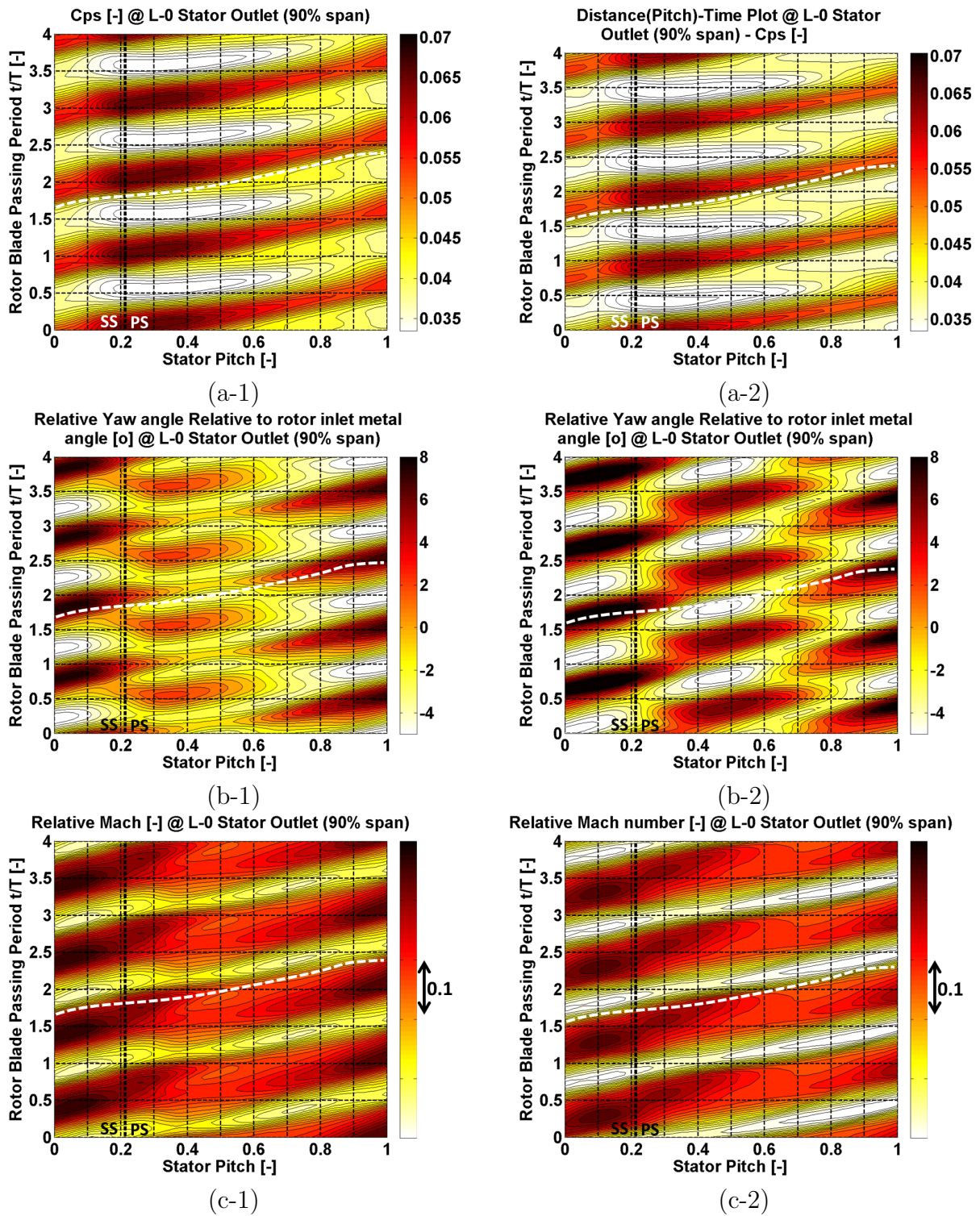


Figure 5.7: Static pressure coefficient Cps, incidence and Mach relative to rotor inlet at 90% of tip span for one stator pitch plotted for four rotor blade passing periods. Datum design is shown on the left (*-1) and Reverse design to the right (*-2).

and black for Reverse design (left) out of four visible shock fronts in the plots. The shock strength is visibly reduced from 85% to 100% of the radial span. The shock S1 is stronger near casing. Nevertheless, the relative Mach show pulsating jets of flow by increase before and decrease after the shock front. The Cps unsteadiness at 95% of radial span increase only slightly from $\pm 24\%$ to $\pm 25\%$ however, at 75% decrease from $\pm 4.9\%$ to $\pm 2.4\%$. The unsteadiness of relative Mach increase from $\pm 23\%$ to $\pm 25\%$ at 97% of radial span and decrease $\pm 7\%$ to $\pm 3\%$ at 75% or radial span. In conclusion, both the high (radial span 85%-100% with S1 shock) and low unsteadiness (70%-85%) regions of radial span show an increase and a decrease of Cps and relative Mach unsteadiness respectively.

5.4.2 L-0 rotor aerodynamic improvements

Time-averaged contours for entropy loss and streamwise vorticity at the rotor exit plane location $x/C_{ax,rotor} = 1.94$ (94% of rotor tip axial chord length downstream of rotor tip trailing edge) are shown in Figure 5.9. The plots show 70% to 100% of radial span for two rotor pitch. The observer is looking into the axial direction of flow towards the machine exit. Rotor rotation is directed from left to right. Four entropy loss features as explained earlier are labeled.

Two rotor wake features are visible. The location of wake W is marked with thick dotted white line starting from 95% of tip span at about 0.85 of pitch and inclined towards left, interacting with shock S3 marked with thin white dotted line, at about 85% of radial span, as shown in Figure 5.9 (a-1) for datum case. Rotor wake at 93%-96% of span shows a positive streamwise vorticity region on the left **W1** and negative streamwise vorticity region on the right **W2**. The feature W1 and W2 are both part of the wake and intense at about 95% of span. The source of positive streamwise vorticity W1 is the compression wave C1 on the suction side convex curvature region near tip airfoil trailing edge, as shown in Figure 1.6. The adverse pressure gradient introduced by C1 induce positive tangential vorticity component as a result of shear introduced by axial and radial velocity gradients. The flow is decelerated axially and radial velocities increase. This observation is similar to be observed in the forward curved sweep case. The common aspect of the two design is a reduction of flow expansion in supersonic airfoils. Both features W1 and W2 are reduced in strength in reverse design. The wake W interact with S3 shock at about 90% of radial span compared with 85% of span for datum design. Nevertheless, the streamwise vorticity gradients are reduced for trailing edge shock S3.

The wake W carries blade profile loss as shown in entropy loss contours in Figure 5.9 (b-1), (b-2). The reverse design shows a decrease in loss throughout 70%-96%. The streamwise vorticity gradients for feature W1 and W2 at 92%-95% of span and corresponding entropy contours show a reduced area cover and intensity. The S3 trailing edge shock loss feature disappear from entropy loss contours at about 0.2 of rotor pitch and 90% of radial span (see Figure 5.9 (b-2)).

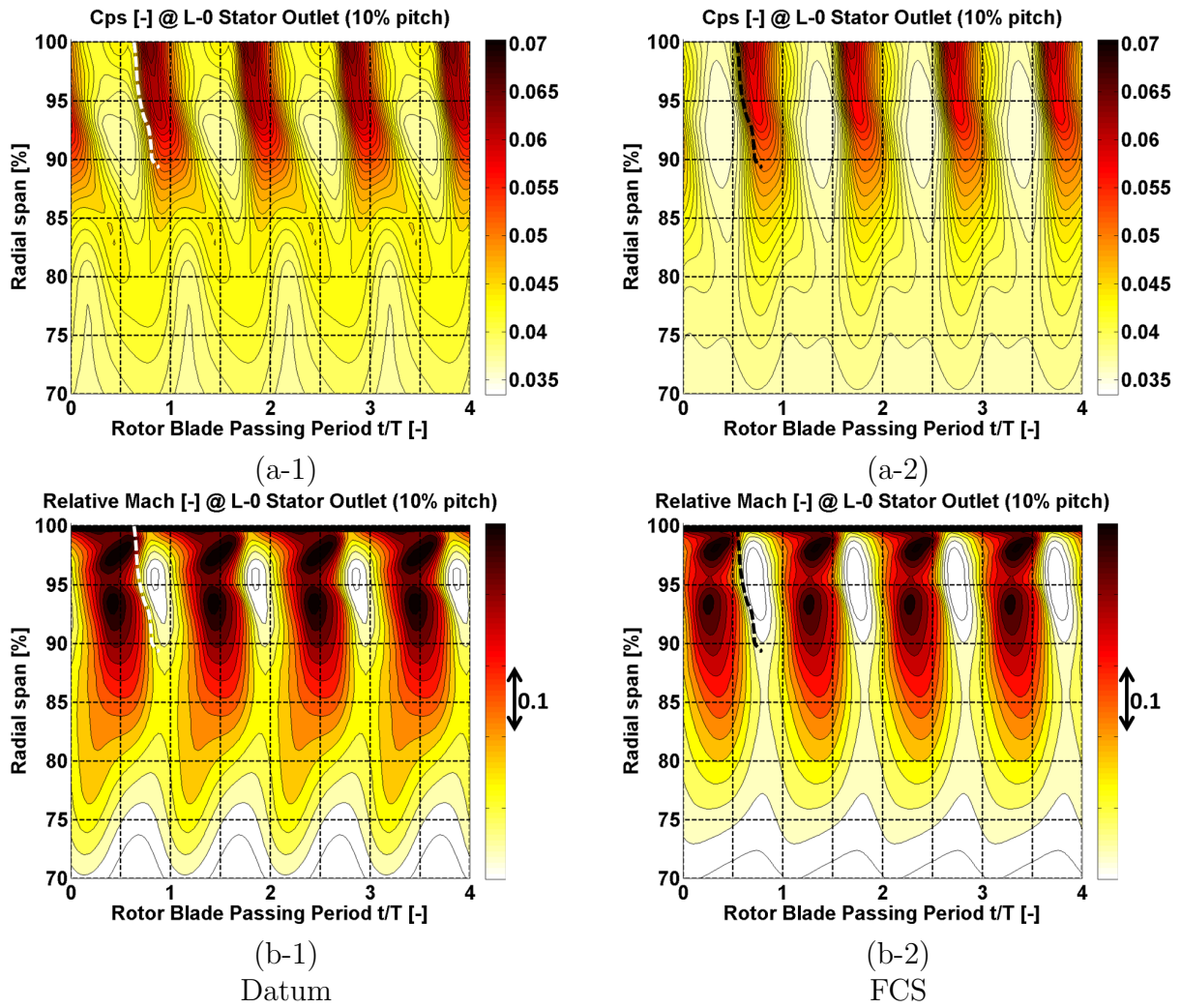


Figure 5.8: Static pressure coefficient C_{ps} and relative Mach at 10% of stator pitch (high unsteadiness zone) from 70-100% of tip span. Datum design is shown on the left (*-1) and Reverse to the right (*-2).

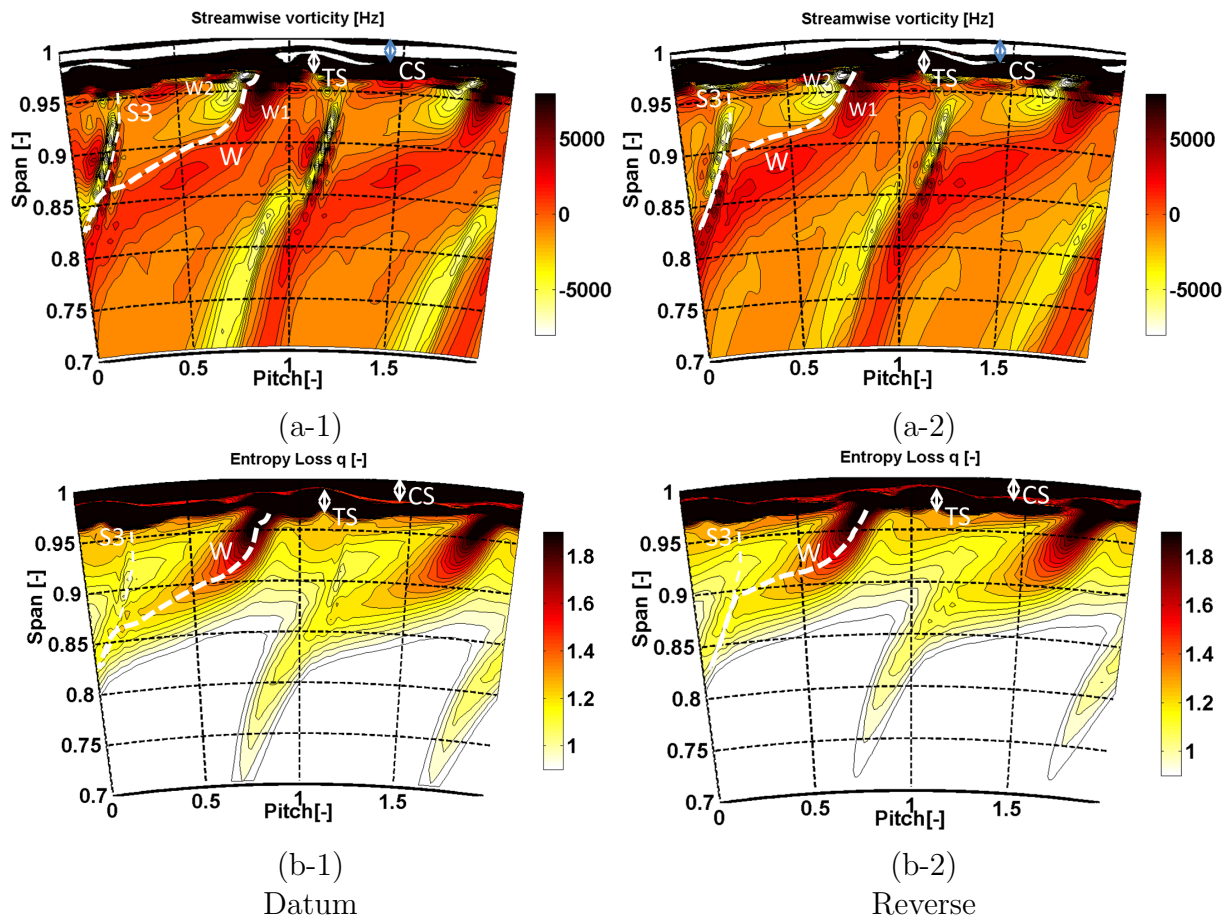


Figure 5.9: Time-averaged entropy loss $q[-]$ and streamwise vorticity $\Omega_s[Hz]$ contours (in relative frame of reference) for Datum on the left and reverse stacking on the right at L-0 rotor exit tip region (70%-100%).

Figure 5.10 shows time averaged blade-to-blade contours for relative Mach and entropy loss $q[-]$ at 91% of rotor radial span. The decrease in relative inlet Mach influence flow expansion through supersonic tip airfoils. The relative Mach shows reduced contour levels for suction side flow expansion in reverse design. The reduced flow expansion is terminated by a relatively weaker trailing edge shock $S3$, whose location is marked with a dotted white line in Figure 5.10 (b-1) and (b-2). The corresponding entropy levels are reduced as shown in Figure 5.10 (b-2). The entropy loss reduces by 1% locally at the marked position in the wake downstream. The loss improvements primarily result from blade profile and wake losses as a result of reduced flow expansion.

In conclusion, despite an increase of unsteadiness (rotor incidence and relative Mach) in stator-rotor gap, the flow expansion through supersonic airfoils in the tip region is opti-

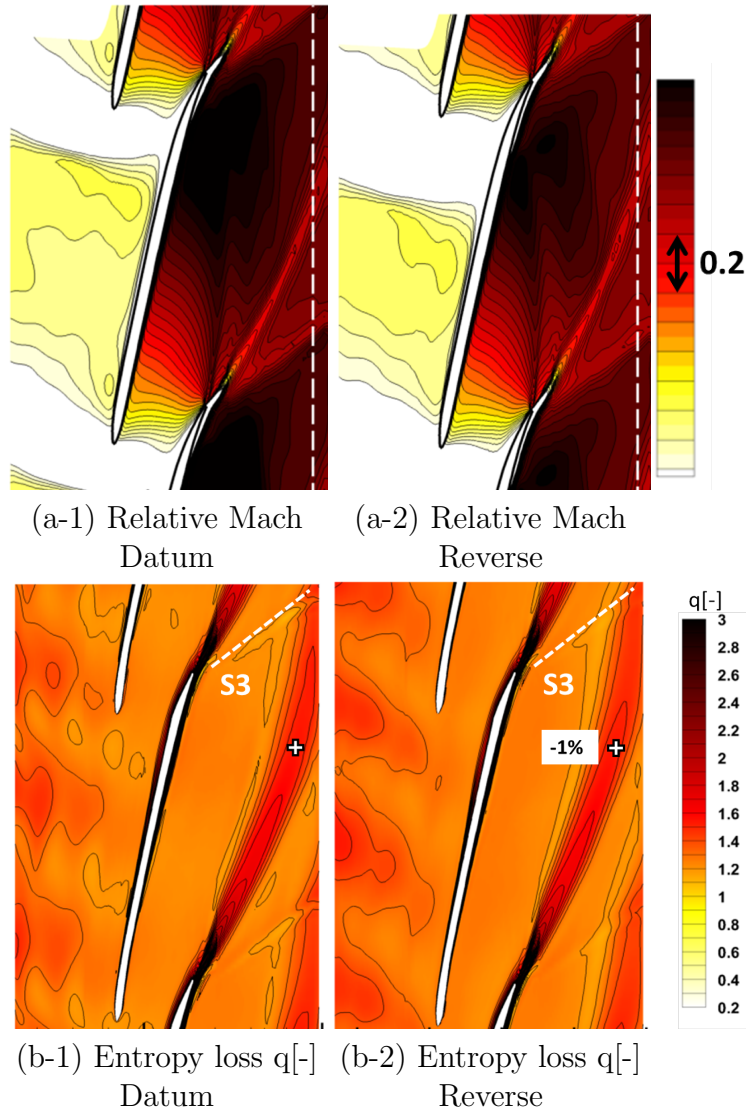


Figure 5.10: Time-averaged blade-to-blade contour of relative Mach and entropy loss coefficient $q [-]$ at 91% of rotor tip span. The trailing edge shock S3 strength is reduced with decreased flow expansion through the rotor tip region. The entropy in the wake is decreased by 1% locally at a marked position downstream.

mized as a result of a decrease in relative Mach on average. The relative Mach reduction in the stator-rotor tip gap reduces shock strength of both S1 (rotor leading edge bow shock) and S3 (rotor trailing edge shock).

Tip cavity mass flow: Mass flow is decreased from 5% in datum to 4.81% in reverse design. The mass flow unsteadiness at L-0 cavity inlet decrease from $\pm 0.2\%$ in datum to $\pm 0.15\%$ for reverse blade twist design.

5.5 Comprehensive flow model - Reduction of losses in supersonic rotor tip airfoils in the low-pressure steam turbine by controlling stator throat-to-pitch ratio

The main drivers that have been identified in order to improve the performance of supersonic airfoils at rotor tip are as follows.

- Increasing throat to pitch ratio at the hub and decreasing at the tip "Reverse" twist stacking increase hub and lowers tip reaction.
- The change in absolute Mach and mass flow redistribution through stator and rotor can effectively be controlled in the same proportion as the increase in hub and reduction in tip reaction.
- Decrease in the throat to pitch ratio at the tip reduce relative inlet Mach to the rotor as well as meridional mass flux. This effectively reduces mass flow through the L-0 rotor tip cavity.
- A reduction in relative Mach on average in rotor-stator tip axial gap reduce leading edge bow shock strength and pronounce unsteadiness in the flow (unique incidence to rotor supersonic airfoils).
- The effects of relative Mach reduction on average reduce the flow expansion through supersonic tip airfoils. This results in a decrease of rotor leading and trailing edge shock strength as well as blade profile losses, despite a pronounced flow unsteadiness at rotor inlet.

5.6 Concluding summary and remarks

The summary of important findings in this chapter is as follows.

- Increase in the throat to pitch ratio at the hub and decrease at tip improve two stages combined efficiency (L-1, L-0 and part diffuser) by 1.1 and 0.9 for η_{tt} and η_{ts} respectively. The L-0 and part diffuser combined total to static efficiency η_{ts} increase

by 1.3%. Surprisingly L-1 also demonstrate total-to-total efficiency η_{tt} improvements of 0.2.

- Stage specific-work Δh_o increase by 1.3% for two-stage combined.
- The L-1 stage reaction is about unchanged and workload shift of only 0.23% is reported. This indicates a constant annular throat area for L-0 stator (unchanged by blade twist stacking).
- The opening of the throat area at hub reduce flow acceleration in the stator hub passage, lower absolute Mach and increases static pressure at the outlet. The closing of the throat area at tip induce opposite effects by increasing absolute Mach and reduction of static pressure resulting in a decrease of tip reaction.
- L-0 stator tip shows entropy loss increase of 3.15% and the rotor tip region improve entropy loss by 4.72%.
- L-0 stator report reduction in the mass flow from 60% to 100% and increase from hub to 60% of radial span. In L-0 rotor the mass flow through 60% to rotor tip span is increased and hub to 60% of the radial span is decreased. This is effectively controlled by the throat to pitch ratio change as a result of a change in Mach number in the respective regions. A reduction in supersonic tip airfoil relative Mach, for example, increase mass flow per unit passage area.
- The reduction of relative Mach at the rotor inlet reduce shock strength and pronounce flow unsteadiness. Despite an increase in unique incidence unsteadiness in the stator-rotor gap (85%-100% radial span) a reduction in relative Mach on average reduce the flow expansion and subsequent losses in supersonic rotor airfoil and downstream flow.

Chapter 6

Conclusions and outlook

In this work, a comprehensive understanding of time-resolved flow mechanism for a multi-stage transonic low-pressure steam turbine is developed with the aid of high performance computational fluid dynamics. The time-resolved computations of datum design are extensively validated with experiments. The analysis reveals a transonic tip region introduce pronounced losses compared with mid-span and hub flow in L-0 (last) stage. Rotor leading edge bow-shock interaction with the stator, rotor supersonic airfoils, and tip cavity-shroud flow are pronounced loss regions. A carefully tailored design of forward curved sweep and throat-to-pitch ratio variation are proposed in order to understand the role of axial distance in the tip region and stage reaction variation respectively. The time-resolved computations of the proposed design show an increase in efficiency and work extraction as reported in conclusions. The necessary computational capability is developed by parallelization of in-house CFD code "MULTI3" for a cluster of GPUs. For the prediction of wetness and relative accuracy of computations, the solver is extended with equilibrium steam model (IAWPF-IF97 steam tables). Further, an inaccuracy introduced by approximation of geometrical details such as cavities, multi-stage model, snubber, and blade count modification for sector domain model is predicted and guidelines for computations, for a low-pressure steam turbine design process are proposed.

6.1 Impact of thermodynamic properties of steam on computational accuracy

The computations with ideal gas law assumption and thermodynamic properties of steam show similar main flow patterns in terms of shock interaction. In regions with smooth pressure distributions, no major differences are observed between the two results. However, the supersonic flow expansion and rotor leading edge bow shock show substantial differences. The subsonic region downstream of the bow shock wave is smaller for the

equilibrium-steam model and introduce steep adverse pressure gradient on the pressure side of the adjacent rotor. Ideal gas law over-predict total-to-total stage efficiency by 2.7% on average compared to thermodynamic properties of steam. Computations with thermodynamic properties of steam show reduced static pressure loading, consequently a decrease in airfoil lift for supersonic tip airfoils. Thermodynamic properties of steam are important for accurate prediction of static pressure and unsteady forces on the supersonic tip region of the rotor.

6.2 Impact of geometrical model on computational accuracy

The computational cost of full four stages including tip cavities and seals is very high as the mesh size exceed 1.37 billion mesh nodes. The developed multi-GPU capability allow this scale of computation. However, a mesh with matching interface across all blocks, rows and cavity boundaries might not be possible due to restriction criterion from different blade count in each row and matching node condition in tip-cavities as explained in the thesis. This necessitates identification of simplified models with an estimate of computational cost versus accuracy and identification of physical phenomenon not captured by simplified models. Following conclusions are established from a comparative analysis of different geometrical approximations.

- **Last stage rotor part span connector:** The part span connector located at about 40% of radial span (subsonic inlet flow in rotor frame of reference) reduce total-to-total η_{tt} and total-to-static η_{ts} efficiency by 0.19% and 0.2% respectively. The unsteady flow introduced by snubber is within $\pm 15\%$ of radial span. The blockage introduced by snubber, however, does increase static pressure loading at about 40%-70% of axial chord on average for the supersonic tip airfoil. The reduced adverse pressure gradient, as introduced by rotor leading edge bow-shock impinging on the adjacent airfoil's pressure side, decreases the entropy production as a result of boundary layer modulation and increases the total-to-static efficiency by 0.15% locally at 94% of radial tip span.
- **Influence of blade count modification and multi-stage modeling (30° last two stage sector versus half annular four-stage model):** The half annular computational model with real blade count (337 airfoils ~ 195 million mesh nodes) require a run-time of 13.5 days with 57 GPUs in comparison to 21 hours for 30° last two stage (21 airfoils ~ 16.9 million nodes) with 2 GPUs. The key difference as a result of blade count change is a workload shift as annular throat area for L-1 increase (88->84 airfoils) and L-0 decrease (58->60 airfoils). As found in the results of stator stacking, multi-stage computational model is necessary in order to predict the effects of throat area change on upstream stages.

- **Importance of modeling tip cavities:** The last two stages computational model (30° domain) without tip cavity and seals over-predict total-to-total η_{tt} efficiency by 3.4% and total-to-static by 4.32%. The without cavity case over predict two stages specific-work by 4.41%. The mass flow through the last stage cavity is about 5% on average of the total mass flow. The L-1 tip leakage flow with high enthalpy and swirl change secondary flows within the last stage stator tip region.

The analysis reveals the importance of tip cavity modeling as the difference in error is substantial. The snubber can be excluded from the model (additional complexity in mesh generation). The real blade count full annular computations including tip cavities are the best model for accuracy, however, restrictions imposed by matching mesh interface criterion does not allow a viable mesh size. For several design cases (optimization algorithms) a multi-stage sector model including cavities is proposed as a viable solution.

6.3 Aerodynamic improvements of low-pressure steam turbine by last stage stator stacking

6.3.1 Forward curved sweep - Tip axial distance

Forward curved sweep of last stage stator is analyzed in order to develop an understanding of axial distance on the rotor tip leading edge shock and flow unsteadiness in the stator-rotor axial gap in the transonic tip region. The modified design introduce axial distance of 1.8 times the datum design with stator trailing edge orthogonal to flared casing, and sweep is introduced at 72%-100% of radial span. The design annular throat area is kept constant with the opening of stator throat by the twist.

The following conclusions are established.

- **Effects of non-constant throat area:** The time-resolved computations predict an increase in the effective annular throat area of last stage modified stator. This is introduced by two factors. First, the flow in the last stage stator tip region is subsonic to near transonic and flow might not be choked. In time with the rotation of the rotor, the rotor tip leading edge shock introduce adverse pressure gradients to the flow in stator tip region passage and influence the effective throat area. The second aspect is related to the geometrical changes as the stator blade profiles are moved axially towards the penultimate stage (L-1) from 72%-100%. This introduces pronounced suction side curvature and close throat area in the meridional plane. Nevertheless, several iterations of time-resolved three dimensional CFD might be required to find an FCS design with a constant throat area. The opening of the throat at stator lower span-wise positions can be restricted with each iteration step. The increase in last stage stator annular throat area increases reaction for both

penultimate L-1 and last stage L-0. The penultimate stage extract 3.4% additional specific work Δh_o compared with the last stage. The overall two stages specific work is however increased by 1.57%.

- **Aerodynamic efficiency improvements:** Despite an increase in the annular throat area, efficiency improvements of total-to-total $\eta_{tt} = 1.3\%$ and total-to-static $\eta_{ts} = 1.1\%$ are predicted for two-stage and part diffuser combined. The last stage η_{ts} efficiency is improved by 1.0%. The key aerodynamic efficiency improvements are observed in the last stage tip region flows. The entropy loss increase in the curved stator tip passage by 1.98%, however, decrease by 5.69% in rotor supersonic tip airfoils.
- **Loss introduced within forward curved stator tip passage:** The forward curved sweep introduces a lean from midspan of the axial chord to trailing edge with suction side facing towards casing in the stator tip region. This lean effect introduces flow acceleration on the suction side and results in loss increase on suction side boundary layer. The suction side is also exposed to incoming rotor leading edge shock. The streamwise vorticity and loss are further pronounced with the interaction of shock for a longer duration of time. In addition, the loss at the casing is also increased as a result of pronounced tangential vorticity (shear introduced by axial deceleration of flow at casing). Note that the losses are introduced despite the fact that flow expansion through forward curved stator is improved and blade surface pressure loading increase proportional to ρC_m^2 compared to ρC_x^2 .
- **Loss introduced by bow shock relocation to a lower spanwise position:** The rotor leading edge bow shock weakens with an increase in axial distance, and relocates to a lower spanwise position to come in contact with forward curved stator trailing edge. The gap between high pressure introduced by bow shock and casing, introduce a pressure gradient towards casing. Flow separation is introduced and rotates with rotor bow shock between high static pressure and casing. This is an additional loss feature introduced by an axial gap.
- **Loss introduced by mixing in axial gap:** Pronounced streamwise vorticity on forward curved stator suction side and trailing shed vorticity further introduce viscous and mixing losses in the increased axial gap.
- **Impact of an axial gap on rotor inlet flow unsteadiness:** As explained earlier in the datum design, a decrease of the axial distance between stator suction side and rotor tip leading edge as the rotor approaches stator trailing edge, induce pronounced unsteadiness in the flow. With the axial distance increased with a forward curved sweep, this unsteadiness in the flow is reduced. The maximum incidence fluctuations of about $\pm 12^\circ$ as the rotor is in the vicinity of stator trailing edge is reduced to $\pm 5^\circ$ at 90% of span. The average incidence is improved from -3.5° to a positive 0.88° .

The relative Mach on average decrease by 1.5% at 90% of span. The maximum peak to peak relative Mach fluctuations observed at 94% of the radial span is decreased from $\pm 24\%$ to $\pm 19\%$. In conclusion, the axial gap is able to decrease peak to peak fluctuations of relative Mach and incidence to supersonic rotor tip airfoils.

- **Reduction of rotor tip leakage mass flow:** Forward curved stator reduces radial velocities in the tip axial gap from 85%-100% of radial tip span. This is able to reduce rotor tip leakage flow by 0.49% (from 5% to 4.51%) on average. However, the unsteadiness of mass flow through leakage is increased nominally from $\pm 0.2\%$ to $\pm 0.23\%$.
- **Loss improvement in last stage rotor supersonic tip airfoils:** The increase in stage pressure ratio and a decrease in relative inlet Mach to rotor reduce the flow expansion through the rotor tip region. The front-loading ($C_{ax}=0.25$) of the rotor airfoil are decreased by as much as 25% and 26% for 90% and 95% of rotor span respectively. Despite an increase in unsteadiness of static pressure (from $\pm 19\%$ to $\pm 25\%$) on pressure surface (area subject to unique incidence), the entropy loss at rotor exit is reduced. The decrease in relative Mach (flow expansion downstream of rotor throat) reduce trailing edge shock strength. The streamwise vorticity induced by suction side convex curvature (compression wave) and trailing edge shock is reduced. In conclusion, despite the pronounced unsteadiness in pressure at the inlet, a decrease in relative inlet Mach and pressure ratio increase reduce losses in the supersonic flow expansion.
- **Increase in hub reaction improves last stage rotor hub flow separation:** Increase in hub reaction improve suction side flow separation in the last stage rotor hub.

6.3.2 Blade twist - controlling stage reaction by variation of the throat to pitch ratio

Last stage blade twist is an effective parameter to control reaction variation and mass flow redistribution as shown in this study. The throat is opened from hub span towards 60% span (increase in the throat to pitch ratio) and closed from 60% to the tip span (decrease in the throat to pitch ratio). The condition of a constant annular throat area is ensured in a stator twist design. The key conclusions on the flow aerodynamic improvements are established as follows.

- **Throat to pitch ratio control on flow expansion in the stator and resulting reaction and mass flow redistribution:** An increase in throat area at the hub and closing of the throat at the tip is able to alter flow expansion through stator proportionally i.e. reduced absolute Mach at the hub and increase at the tip. The reaction increases at the hub and decreases at the tip. The mass flow shows a similar

trend by redistributing through the stator, an increase in the hub and reduction in the tip. The mass flow within the rotor redistribute with a decrease in the hub and increase in the tip region. In conclusion, throat to pitch ratio variation can be used as an effective optimization parameter.

- **Decrease of the throat to pitch ratio in the tip region reduce bow shock strength and increase incidence unsteadiness to rotor:** A decrease in the throat to pitch ratio increase absolute Mach through stator tip region (Increased flow expansion). An increase in absolute Mach results in a decrease in relative Mach inlet to rotor tip and results in a reduced shock strength. A weak bow shock introduces pronounced incidence unsteadiness. In the high unsteadiness region where the axial gap between rotor leading edge and stator trailing edge is minimum and unsteadiness is high, the incidence is further pronounced by $\pm 2^\circ$ (from $\pm 7^\circ$ to $\pm 9^\circ$). In the region of low unsteadiness, the incidence to the rotor is pronounced by $\pm 4^\circ$ (from $\pm 2^\circ$ in datum to $\pm 6^\circ$ in modified design). The relative Mach decrease by 3.7% on average. The relative Mach unsteadiness is increased by $\pm 2\%$ (from $\pm 20\%$ to $\pm 22\%$) in high unsteadiness region and $\pm 6\%$ (from $\pm 9\%$ to $\pm 15\%$) in low unsteadiness region at 90% of radial span. In conclusion, unique incidence (relative Mach and incidence) to the rotor is pronounced in the tip axial gap.
- **Increased flow expansion in the stator tip region increase stator losses:** The increased flow expansion in the stator tip as a result of throat area reduction increase entropy loss by 3.15% on average.
- **Decrease of throat area at tip reduces tip leakage mass flow:** The decrease in meridional mass flow in the tip region reduces tip leakage mass flow by 0.19% (from 5% to 4.81%) on average. The unsteadiness in mass flow through last stage rotor tip leakage flow is reduced from $\pm 0.2\%$ to $\pm 0.15\%$.
- **Efficiency improvements:** The modified design improve two stage combined efficiency total-to-total η_{tt} by 1.1% and total-to-static η_{ts} by 0.9% respectively. The last stage with part diffuser total to static efficiency η_{ts} increase by 1.3%.
- **Improved flow expansion in supersonic tip airfoils by reduction of relative inlet Mach:** Despite an increase in stator entropy loss of 3.15% in the tip region, rotor entropy loss decrease by 4.72% in the supersonic tip airfoils. The reduction of inlet relative Mach reduces flow expansion through supersonic rotor airfoil, as well as trailing edge shock strength. The resulting streamwise vorticity and entropy loss in the wake and trailing edge shock is reduced.

General conclusions from last stage stator stacking

- Relative Mach to rotor inlet is the key parameter to optimize in order to mitigate supersonic rotor tip passage losses.

- Despite a pronounced unsteadiness in the flow, a reduction of relative Mach to rotor inlet on average is able to improve flow expansion through rotor supersonic airfoils and mitigate entropy loss by weakening trailing edge shock. The positive influence of relative Mach reduction dominates the potentially negative impact of pronounced unsteadiness introduced by stacking methods discussed in this work.
- In both the stator stacking design, decrease in rotor relative inlet Mach weakens the leading edge bow shock. The presence of weak shock in the forward curved sweep design (increase in tip axial gap) show reduced peak-to-peak fluctuations of flow properties. Whereas, without a change in the axial gap (stator throat-to-pitch ratio decrease in transonic tip region) the peak-to-peak fluctuations increase in the presence of weak bow shock. This is an important aspect to consider in the design optimization process as pronounced unsteadiness in transonic tip region is not only driven by leading edge bow shock as reported in literature, as well depends on the stator-rotor axial gap in the transonic tip region.

6.4 Future work

The future work in continuation of discussed results is proposed on the following fronts.

- The MULTI3 performance for a cluster of GPUs can be improved by the development of load-balancing architecture for sub-domain interface treatment. This requires the elimination of row master node concept by introducing run-time node interface matching calculations for sliding mesh interface method for every physical time step. The second step of high-performance computing optimization is re-structuring of parallelization by replacing synchronous inter-GPU data transfer with asynchronous data transfer. A careful code restructuring is required, and conceptually as the row or sector interface computations are underway, the GPU processing should continue with further computations in the iteration loop.
- A comprehensive three-dimensional time-resolved analysis of two aggressive stator stacking modifications are analyzed in this work. Increase in the leaving loss and wetness, despite the improvements in aerodynamic efficiency, requires further analysis and exploration of an optimized compound stator stacking design driven by optimization algorithms. The computational capability allows multi-stage computations for several design optimization cases for the training of artificial intelligence frameworks (such as neural networks) and allows subsequent prediction of optimized compound stacking design by keeping leaving losses and wetness within acceptable limits.
- The forward curved sweep and stator twist design improve aerodynamic efficiency. However, the condensing steam in last stage stator builds a water film on stator surface and breaks into droplets shedding from trailing edge. A film and droplet model

is developed in MULTI3 as a separate project. This model with some additional developments i.e. generalized for multi-stage and multi-row parallelization may give additional insight into droplet formation, impact energy and erosion for proposed stator stacking designs.

- The time-resolved unsteady blade forces available with MULTI3 for the multi-stage low-pressure steam turbine are useful for the assessment of mechanical strength and reliability of long blades. The necessary software modules can be developed in order to import unsteady data to available commercial non-linear finite element method (FEM) solvers. This will provide the necessary details on ductile strength under centrifugal forces, vibratory strength, high cycle, and low cycle fatigue strength.

Bibliography

- [1] I. Papagiannis, A. Raheem, A. Basol, A. Kalfas, R. S. Abhari, H. Fukushima, and S. Senoo, “Unsteady flow mechanisms in the last stage of a transonic low pressure steam turbine—multistage effects and tip leakage flows.,” *J. Eng. Gas Turbines Power*, vol. GPPF, October 2017.
- [2] W. R. Anderegg, J. W. Prall, J. Harold, and S. H. Schneider, “Expert credibility in climate change,” *Proceedings of the National Academy of Sciences*, vol. 107, no. 27, pp. 12107–12109, 2010.
- [3] M. van der Hoeven, “Energy and climate change—world energy outlook special report,” *Int. Energy Agency*, vol. 2015, - 2015.
- [4] R. Adib, H. Murdock, F. Appavou, A. Brown, B. Epp, A. Leidreiter, C. Lins, H. Murdock, E. Musolino, K. Petrichenko, *et al.*, “Renewables 2018 global status report,” *Paris: REN21 Secretariat*, 2018.
- [5] M. J. Moore and C. Sieverding, “Two-phase steam flow in turbines and separators: theory, instrumentation, engineering,” 1976.
- [6] X. Cai, D. Ning, J. Yu, J. Li, L. Ma, C. Tian, and W. Gao, “Coarse water in low-pressure steam turbines,” *Proceedings of the Institution of Mechanical Engineers, Part A: Journal of Power and Energy*, vol. 228, no. 2, pp. 153–167, 2014.
- [7] Y. A. Cengel and M. A. Boles, “Thermodynamics: an engineering approach,” *Sea*, vol. 1000, p. 8862, 2002.
- [8] S. Dixon *et al.*, *Fluid Mechanics and Thermodynamics of Turbomachinery By SL Dixon: Fluid Mechanics and Thermodynamics of Turbomachinery*. Digital Designs, 2005.

-
- [9] S. Senoo, K. Segawa, H. Hamatake, T. Kudo, T. Nakamura, and N. Shibashita, “Computations for unsteady compressible flows in a multistage steam turbine with steam properties at low load operations,” *J. of Eng. for Gas Turbines and Power*, vol. 133, 2011.
- [10] A. Gerber, R. Sigg, L. Völker, M. Casey, and N. Sürken, “Predictions of non-equilibrium phase transition in a model low-pressure steam turbine,” *Proceedings of the Institution of Mechanical Engineers, Part A: Journal of Power and Energy*, vol. 221(6), pp. 825–835, 2007.
- [11] S. Miyake, I. Koda, S. Yamamoto, Y. Sasao, K. Momma, T. Miyawaki, and H. Ooyama, “Unsteady wake and vortex interactions in 3-d steam turbine low pressure final three stages,” in *ASME Turbo Expo 2014: Turbine Technical Conference and Exposition*, pp. V01BT27A013–V01BT27A013, American Society of Mechanical Engineers, 2014.
- [12] I. Bosdas, M. Mansour, A. Kalfas, R. Abhari, and S. Senoo, “Unsteady Flow Field and Coarse Droplet Measurements in the Last Stage of a Low Pressure Steam Turbine With Supersonic Airfoils Near the Blade Tip,” *ASME. J. Eng. Gas Turbines Power*, vol. 139(9), pp. 091601–091601–11, 2017.
- [13] P. Rossi, A. Raheem, and R. Abhari, “Numerical model of liquid film formation and breakup in the last stage of a low-pressure steam turbine,” *Journal of Engineering for Gas Turbines and Power*, pp. GTP–17–1189, 2018.
- [14] O. Sharma and T. Butler, “Predictions of endwall losses and secondary flows in axial flow turbine cascades,” in *ASME 1986 International Gas Turbine Conference and Exhibit*, pp. V001T01A098–V001T01A098, American Society of Mechanical Engineers, 1986.
- [15] J. Denton and X. L., “The exploitation of three-dimensional flow in turbomachinery design,” *Proceedings of the Institution of Mechanical Engineers, Part C: Journal of Mechanical Engineering Science*, vol. 213(2), p. 125–137, - 1998.
- [16] L. Langston, “Secondary flows in axial turbines—a review,” *Annals of the New York Academy of Sciences*, vol. 934, no. 1, pp. 11–26, 2001.
- [17] T. Behr, *Control of rotor tip leakage and secondary flow by casing air injection in unshrouded axial turbines*. PhD thesis, ETH Zurich, 2007.
- [18] H.-F. Vogt and M. Zippel, “Sekundärströmungen in turbinengittern mit geraden und gekrümmten schaufeln; visualisierung im ebenen wasserkanal,” *Forschung im Ingenieurwesen*, vol. 62, no. 9, pp. 247–253, 1996.

- [19] H. Stuer, F. Truckenmuller, D. Borthwick, and J. D. Denton, "Aerodynamic concept for very large steam turbine last stages," in *ASME Turbo Expo 2005: Power for Land, Sea, and Air*, pp. 673–687, American Society of Mechanical Engineers, 2005.
- [20] S. Havakechian and J. Denton, "Three-dimensional blade-stacking strategies and understanding of flow physics in low-pressure steam turbines—part i: Three-dimensional stacking mechanisms," *Journal of Engineering for Gas Turbines and Power*, vol. 138, no. 5, p. 052603, 2016.
- [21] G. Gyarmathy and W. Schlachter, "On the design limit of steam turbine last stages," *Technology of Turbine Plant Operating with Wet Steam, BNES, London*, vol. volume 6, pp. pp. 55–63, 2014.
- [22] S. Senoo, H. Ono, T. Shibata, S. Nakano, Y. Yamashita, K. Asai, K. Sakakibara, H. Yoda, and T. Kudo, "Development of Titanium 3600rpm-50inch and 3000rpm-60inch Last Stage Blades for Steam Turbines.," *J. Eng. Gas Turbines Power*, vol. volume 6, October 2014.
- [23] S. Senoo, "Development of design method for supersonic turbine aerofoils near the tip of long blades in steam turbines: Part 1—overall configuration," in *ASME Turbo Expo 2012: Turbine Technical Conference and Exposition*, pp. 355–365, American Society of Mechanical Engineers, 2012.
- [24] S. Senoo and H. Ono, "Development of design method for supersonic turbine aerofoils near the tip of long blades in steam turbines: Part 2 — configuration details and validation.," in *ASME Turbo Expo: Power for Land, Sea, and Air, Volume 5B: Oil and Gas Applications; Steam Turbines ()* (A. T. Expo, ed.).
- [25] I. Bosdas, "Time resolved flow field and droplet measurements in wet steam turbine flows," *Doctoral Thesis*, 2016.
- [26] M. Parvizinia, C. Berlich, F. Truckenmuller, and H. Stuer, "Numerical and experimental investigations into the aerodynamic performance of a supersonic turbine blade profile," in *ASME Turbo Expo 2004: Power for Land, Sea, and Air*, pp. 1349–1358, American Society of Mechanical Engineers, 2004.
- [27] M. A. Basol, "Turbine Design Optimizations using High Fidelity CFD," *ETH Zurich*, vol. Diss. No. 21559, - 2014.
- [28] J. Denton and X. L, "Some Limitations of Turbomachinery CFD," *ASME*, vol. GT2010-22540, - 2010.

- [29] A. Basol, A. Raheem, M. Huber, and A. R.S., “Full-Annular Numerical Investigation of the Rim Seal Cavity Flows Using GPU’s,” *ASME Turbo Expo 2014: Turbine Technical Conference and Exposition*, vol. Volume 2D: Turbomachinery, p. V02DT44A034, - 2014.
- [30] R. Schädler, A. Kalfas, R. Abhari, G. Schmid, and S. Voelker, “Modulation and Radial Migration of Turbine Hub Cavity Modes by the Rim Seal Purge Flow,” *ASME. J. Turbomach*, vol. 011011-011011-10, p. 139(1), - 2016.
- [31] J. Starzmann, M. Casey, and J. Mayer, “Unsteady numerical study of wet steam flow in a low pressure steam turbine,” *In High Performance Computing in Science and Engineering 11, Springer Berlin Heidelberg*, vol. 221(6), pp. 437–450, 2012.
- [32] J. Starzmann, M. Schatz, M. Casey, J. Mayer, and F. Sieverding, “Modelling and validation of wet steam flow in a low pressure steam turbine,” *ASME 2011 Turbo Expo: Turbine Technical Conference and Exposition*, pp. 2335–2346, january 2011.
- [33] J. Hesketh and P. Walker, “Effects of wetness in steam turbines,” *Proceedings of the Institution of Mechanical Engineers, Part C: Journal of Mechanical Engineering Science*, vol. 219(12), pp. 1301–1314, - 2005.
- [34] “<https://www.nvidia.com/en-us/data-center/tesla-p100/>,” -.
- [35] M. Wolfe, “The PGI Accelerator Programming Model on NVIDIA GPUs,” - 2009.
- [36] “<https://www.openacc.org/>,” -.
- [37] “<https://www.nvidia.de/object/cuda-parallel-computing-de.html>,” -.
- [38] “<https://www.open-mpi.org/>,” -.
- [39] T. Brandvik and G. Pullan, “An Accelerated 3D Navier-Stokes Solver for Flows in Turbomachines,” *ASME J. of Turbomachinery*, vol. 133, no. 021025, pp. 1–9, - 2011.
- [40] E. Phillips, R. L. Davis, and J. Owens, “Unsteady Turbulent Simulations on a Cluster of Graphics Processors,” *AIAA*, vol. 2010-5036, - 2010.
- [41] R. Ni, “A Multiple Grid Scheme for Solving the Euler Equations,” *AIAA Journal*, vol. 20, no. 3, p. 1565–1571, - 1981.
- [42] A. S. Leizerovich, *Steam turbines for modern fossil-fuel power plants*. The Fairmont Press, Inc., 2008.

- [43] A. Jameson, “Time Dependent Calculations using Multigrid with Applications to Unsteady Flows Past Airfoils and Wings,” *AIAA*, pp. 91–1596, - 1991.
- [44] M. Giles, “Non-reflecting Boundary Conditions for Euler Equation Calculations,” *AIAA Journal*, pp. 89–1942–CP, - 1989.
- [45] A. Burdet, “A computationally efficient feature based jet model for prediction of film cooling flows,” *ETH Zurich*, - 2005.
- [46] B. Baldwin and H. Lomax, “Thin Layer Approximation and Algebraic Model for Separated Turbulent Flows,” *AIAA*, pp. 78–257, - 1978.
- [47] P. R. Spalart and S. R. Allmaras, “A one-equation turbulence model for aerodynamic flows,” *La Recherche Aérospatiale*, vol. 1, p. 5, - 1994.
- [48] D. Wilcox, “Reassessment of the Scale-Determining Equation for Advanced Turbulence Models,” *AIAA*, vol. 26, 11, pp. 1299–1310, 1988.
- [49] M. Kato and B. E. Launder, “The Modeling of Turbulent Flow Around Stationary and Vibrating Square Cylinders,” *Proc. 9th Symposium on Turbulent Shear Flows, Kyoto*, vol. 1, pp. 10.4.1–10.4.6., - 1993.
- [50] R. Chima, “A k-omega Turbulence Model for Quasi-Three-Dimensional Turbomachinery Flows,” *NASA*, vol. TM 107051, - 1996.
- [51] M. Holmgren, “X Steam, Thermodynamic properties of water and steam,” -.
- [52] M. Huber, “GPU Acceleration of a Fluid Flow Solver for Turbomachinery Applications,” *LEC - ETH Zurich*, - 2014.
- [53] “<https://www.cscs.ch/computers/piz-daint/>,” -.
- [54] I. Papagiannis, “Unsteady Steam Turbine Optimization Using High Fidelity CFD,” *Doctoral Thesis*, vol. 25781, - 2019.
- [55] M. Haraguchi, T. Nakamura, H. Yoda, T. Kudo, and S. Senoo, “Nuclear Steam Turbine With 60 inch Last Stage Blade,” *ASME. International Conference on Nuclear Engineering, Volume 1: Plant Operations, Maintenance, Engineering, Modifications, Life Cycle and Balance of Plant; Nuclear Fuel and Materials; Radiation Protection and Nuclear Technology Applications ()*, vol. volume 6, p. V001T01A042, 2014.
- [56] S. Havakechian and J. Denton, “Three-Dimensional Blade Stacking Strategies and Understanding of Flow Physics in Low-Pressure Steam Turbines—Part II: Stacking Equivalence and Differentiators,” *J. Eng. Gas Turbines Power*, p. 138(6), Nov 2015.

- [57] S. Havakechian and J. Denton, “Three-Dimensional Blade Stacking Strategies and Understanding of Flow Physics in Low-Pressure Steam Turbines—Part I: Three dimensional stacking mechanisms,” p. 138(6), Nov 2015.

A. Nomenclature

Letters and symbols

β	wetness fraction
η_{tt}	efficiency total-to-total
η_{ts}	efficiency total-to-static
γ	specific heat ratio
ρ	density
e	internal energy
C_{ps}	static pressure coefficient
C_{pt}	total pressure coefficient
P	static pressure
P_o	total pressure
Ω_s	stream-wise vorticity
Ω_x	axial vorticity
Ω_θ	tangential vorticity
Ω_r	radial vorticity
h_o	total enthalpy
q	entropy loss coefficient
M	Mach number
M_{rel}	relative Mach number
AVN	Advanced Vortex Nozzle
C	velocity
C_x	axial velocity
C_m	meridional velocity
C_{ax}	axial chord length
\dot{j}_m	meridional specific mass flux (ρC_m)
\dot{m}	mass flow rate
R_p	stage reaction (pressure based definition $\frac{\Delta P_{rotor}}{\Delta P_{stage}}$)
ω_{tip}	relative rotor inlet tip velocity
U_{tip}	blade tip peripheral speed
$S1$	leading edge bow shock
$S2$	trailing edge pressure side shock
$S3$	trailing edge suction side shock

W	rotor wake
TS	Tip shroud loss feature
CS	casing separation loss feature at diffuser inlet
TA	throat area
x	axial distance
r	radial height
$C1$	compression wave at suction side trailing edge of supersonic airfoil
α_1	relative yaw angle at rotor inlet

Abbreviations

2D	two dimensional
3D	three dimensional
MHPS	Mitsubishi Hitachi Power Systems, Ltd.
GPU	Graphic Processing Unit
GP-GPU	General Purpose - Graphic Processing Unit
CSCS	Swiss National Supercomputing Centre
LEC	Laboratory for Energy Conversion
CFD	Computational Fluid Dynamics
URANS	Unsteady Reynolds Averaged Navier-Stokes
MPI	Message Passing Interface
IAPWS-IF97	The International Association for the Properties of Water and Steam - Industrial Formulation 1997
LP	Low Pressure
PSC	Part Span Connector (Snubber)
FCS	Forward Curved Sweep
DAT	Datum design

B. List of publications

- Rossi, P., Raheem, A., Abhari, R.S., 2018, "Numerical model of liquid film formation and breakup in the last stage of a low-pressure steam turbine" *Journal of Engineering for Gas Turbines and Power*, **GTP-17-1189**.
- Papagiannis, I., Raheem, A., Basol, A., Kalfas A.I., Abhari, R.S., Fukushima, H., Senoo, S., 2017, "Unsteady flow mechanisms in the last stage of a transonic low pressure steam turbine – multistage effects and tip leakage flows" *Journal of the global Power and Propulsion Society*, **JGPPS-00029-2017-01**.
- Basol, A.M., Raheem, A., Huber, M., Abhari, R.S, 2014, "Full annular numerical investigation of the rim-seal cavity flows using GPUs" *ASME Turbo Expo 2014: Turbine Technical Conference and Exposition*, **GT2014-26755**.

C. Curriculum Vitae

Asad Raheem

Born 15.08.1983 in Lahore, Pakistan



Education

2013-2019 Dr. Sc. ETH, High performance computing for turbo-machinery

2009-2012 MSc. ETH. RW, Computational Science and Engineering (CGPA 5.0/6.0, Thesis 6.0/6.0)

2001-2005 BS. (CS). UAAR, Majors in Computer Science and Software Engineering (CGPA 3.83/4.00)

Professional Experience

2013-2018 Doctoral Research – Laboratory for Energy Conversion [LEC](#), ETH Zurich



Development of novel supercomputing software

- Developed scalable **supercomputing software** “[MULTI3](#)” (100+ GPUs of order 1.0 billion nodes).
- Developed **large-scale scientific data analysis** software (20+ Terabyte for 100+ GPUs).

Research project supervision and teaching

- Teaching assistant for “[Aerospace Propulsion](#)” and “[Anatomy of Turbocharger](#)” with 60+ enrolled students.
- Thesis supervision of four (MSc, BSc) students in scientific software development and large-scale data analysis.

2014-2017 Research collaboration – Mitsubishi Hitachi Power Systems [MHPS](#) Japan



Aerodynamic design improvements of transonic steam turbine ([MHPS 1000 MW class steam turbine](#))

- Performed quantified time resolved aerodynamic analysis of MHPS 50-inch (3600 rpm) low-pressure steam. The analysis consists of **0.5 billion**-mesh nodes, 670+ airfoils running on **114 GPUs**.
- Reported detailed time resolved analysis of aerodynamic efficiency improvements and underlying flow mechanisms.

2010-2012 Consultant – CFD/CAE - [ASCOMP](#) GmbH, Zurich, Switzerland



- Developed computational framework for two-phase multi-component flows in [TransAT suite](#), used by software developers at ASCOMP to develop application specific flow models including oil & gas, process plants, microfluidic reactors.
- Developed GUI for pre-processing, mesh generation and run-time simulation status on supercomputing cluster.

2009-2010 Software Developer – [Disney Research](#), Zurich, Switzerland



- Software development of NVIDIA CUDA kernels for performance optimization of numerical solver for visual de-ghosting in 3D movies. Integrated numerical algorithm with 13x speedup to the rendering engine.

2006-2009 Software Engineer – [Bentley systems](#), Islamabad



- Served as lead architect and implemented [OpenPlant](#) modeling framework (Object Oriented Design) using AGILE (SCRUM) product development. The framework serves as basis for five products in [OpenPlant](#) solution portfolio.
- Developed 2D and 3D primitive geometry objects (using computational geometry and MicroStation graphics engine) that serve as building blocks for complex shapes (Condenser, Piping system, Tanks, valves, compressor etc.) in a processing plant.
- Implemented object dynamic interaction and collision detection in a 3D space. Framework data storage is integrated with cloud platform [ProjectWise](#) for centralized access of data to geographically distributed product users.
- Developed [OpenPlant PID](#) from inception to release in 2009 in a team of 10+ engineers. This involved design and implementation of library of 2D schematic components with associated specification data, intelligent drawings with integration to physical plant models, as well cloud based storage of data with ProjectWise integration for distributed access across engineering teams.

- Developed [OpenPlant Modeler](#) as part of team of 10+ engineers working on 3D physical model piping components and plant equipment. Involved in overall design and effective access to plant objects for quick drawing workflow. Implemented fast collision detection algorithm of piping and plant objects for the accuracy of physical model.

2008-2009 Scientific Software Developer – Comsats Institute of Information Technology, Islamabad



- Implemented numerical solver for compressible flows for Multi-dimensional batch crystallization models with size independent growth rates. The software is used in chemical and particulate processes engineering analysis (food products, pharmaceuticals).

2005-2005 Software Engineer – Signals Research and Development [NUST](#), Rawalpindi



- Developed secure email communication system with advanced encryption techniques. Email and information exchange platform can transfer encrypted data via various channels including exchange servers, peer-to-peer telephone TAPI and wireless/radio communication. Platform is deployed at various federal establishments in Pakistan including clients from Middle East.

2004-2005 Software Engineer – [XorLogics](#), Islamabad / Belgium



- Developed logistic management information system for clients in transportation and trading. This involved software automation of Logistic procedures, inventory and items delivery status and comprehensive database management system.
- Developed Microsoft office document reader for Nokia 6600. Implemented custom data format and optimized on-chip memory management module in order to make document lightweight for limited on-chip memory and processing power.

Languages

English (Bilingual C2), Urdu (Native), Punjabi (Native), German (Basic knowledge A2), Hindi (Proficient C1)

Scholarships & Awards

- Secured distinction within top 1% in higher secondary school examination at district level (canton Rawalpindi).
- Secured full admission scholarship for BS (CS) studies, and additional merit scholarship in six consecutive semesters for high score.

Sports and hobbies

- Rock climbing (multi-pitch) and high altitude alpine expeditions (5000 meters) in Himalayas.
- Reading news / articles / books about new topics and breakthroughs in science and its potential impact on human society.